# Metamaterials for energy harvesting at small scale

Marco Moscatelli

INSTITUT POLYTECHNIQUE DE PARIS

NNT : 2022IPPAX024

Thèse de doctorat

ÉCOLE POLYTECHNIQUE

IP PARIS

POLITECNICO MILANO 1863

# Metamaterials for energy harvesting at small scale

Thèse de doctorat de l'Institut Polytechnique de Paris
préparée en cotutelle entre l'École polytechnique et le Politecnico di Milano

École doctorale n°626 École doctorale de l'Institut Polytechnique de Paris (EDIPP)
Spécialité de doctorat : Mécanique des fluides et des solides, acoustique

Thèse présentée et soutenue à Palaiseau, le 01 avril 2022, par

**MARCO MOSCATELLI**

Composition du Jury :

| | |
|---|---|
| Agnès Maurel<br>Directrice de recherche CNRS, ESPCI (Institut Langevin) | Président |
| Habib Ammari<br>Professeur, ETH Zürich (Departement of Mathematics) | Rapporteur |
| Luigi Gambarotta<br>Professeur, Università di Genova (DICCA) | Rapporteur |
| Kim Pham<br>Professeur, ENSTA Paris (IMSIA) | Examinateur |
| Claudia Comi<br>Professeure, Politecnico di Milano (DICA) | Directrice de thèse |
| Jean-Jacques Marigo<br>Professeur, École polytechnique (LMS) | Directeur de thèse |

# Metamaterials for energy harvesting at small scale

Ph.D. Thesis
submitted by

Marco MOSCATELLI

Thesis directors: Prof. Claudia COMI
Prof. Jean-Jacques MARIGO

Laboratoire du Méchanique des solids

École Polytechnique
Institute Polytechnique de Paris

# Abstract

The increasing demand of energy-autonomous small electronic sensors and devices has propelled the emergence of energy harvesting technologies as a prominent area of interest for research both in academia and industry. One of the key features of this new generation of sensors is their low-power electricity demand. This characteristic has promoted the development of small scale integrated solutions as alternatives to the periodic replacement or recharging of commonly used batteries, eliminating, or at least reducing, the costs associated to these procedures (both in terms of economical resources and environmental waste).

In this framework, one of the most effective methods for the energy harvesting is to use ambient vibrations, due to the ease of finding this source of mechanical energy. Nevertheless, ambient vibrations are generally largely distributed in space and characterized by a low energy content. Therefore, for an efficient harvesting of energy, it is required to develop systems that are able to convey and trap the vibrations (and the energy they carry with them) in a small region, where they can then be collected and converted into electrical energy by means of, for instance, piezoelectric devices.

Among the possible solutions, the artificial materials that go under the name of "metamaterials", if properly designed, have proved to possess excellent properties in terms of waves control and can be used to develop vibration-based energy harvesting systems. Here, we will concentrate on a specific attribute that characterizes the dynamic behavior of a class of these composite materials, namely the presence of band gaps in the spectrum, *i.e.* intervals of frequencies corresponding to attenuated waves. Phononic crystals and locally resonant materials with a periodic structure belong to this class and are the main subjects of this work. Using a mass-in-mass crystal, we first individuate the roles of the main parameters of the problem of wave propagation in these two typologies of metamaterials. Then, we employ a two-scale homogenization technique to derive their effective behavior at a sub-wavelength scale. In particular, locally resonant materials are analyzed, being characterized by the presence of band gaps already at a sub-wavelength regime.

With the idea of focusing the mechanical energy in a confined area, we analyze the effect of a defect of periodicity. We show that this can result in the formation of localized modes at frequencies inside a band gap. By using locally resonant materials, we then develop a system (based on the resonant tunneling phenomenon in physics) that

allows us to trap mechanical waves in a cavity, *i.e.* in the region of the metamaterial with a defect of periodicity, where the energy will pile up and thus focus. We make here use of the derived effective material properties.

In the final part of the manuscript, we study and experimentally validate the attenuation and localization phenomena on a one dimensional metastructure. For this, we employ a taut cable with a family of hanging masses periodically repeated along its length. First, we theoretically study its dynamic behavior and then we compare the results with an experimental test, validating the attenuation and localization effects.

The objective of this thesis is twofold: on one hand we aim to treat the elasto-dynamic problem associated to defective periodic media presenting band gaps (*i.e.* metamaterials), and on the other hand we also want to give some proofs of efficiency of these systems for the localization of mechanical energy. Our results provide new insights on the dynamic behavior of defective periodic media to be used in energy harvesting systems, which makes this work relevant to both theoretical and practical fields.

# Résumé

La demande croissante de petits capteurs et dispositifs électroniques autonomes en énergie a propulsé l'émergence des technologies de récupération d'énergie en tant que domaine d'intérêt de premier plan pour la recherche, tant dans l'academique que dans l'industrie. L'une des principales caractéristiques de cette nouvelle génération de capteurs est leur faible demande en électricité. Cette caractéristique a favorisé le développement de solutions intégrées à petite échelle comme alternatives au remplacement périodique ou à la recharge des batteries couramment utilisées, éliminant, ou du moins réduisant, les coûts associés à ces procédures (à la fois en termes de ressources économiques et de déchets environnementaux).

Dans ce cadre, l'une des méthodes les plus efficaces pour la récupération d'énergie est d'utiliser les vibrations ambiantes, en raison de la facilité à trouver cette source d'énergie mécanique. Néanmoins, les vibrations ambiantes sont généralement largement réparties dans l'espace et caractérisées par un faible contenu énergétique. Par conséquent, pour une récupération efficace de l'énergie, il est nécessaire de développer des systèmes capables de transmettre et de piéger les vibrations (et l'énergie qu'elles transportent avec elles) dans une petite région, où elles peuvent ensuite être collectées et converties en énergie électrique. l'énergie au moyen, par exemple, de dispositifs piézoélectriques.

Parmi les solutions possibles, les matériaux artificiels qui portent le nom de "méta-matériaux", s'ils sont bien conçus, se sont avérés posséder d'excellentes propriétés en termes de contrôle des vagues et peuvent être utilisés pour développer des systèmes de récupération d'énergie basés sur les vibrations. Ici, on se concentrera sur un attribut spécifique qui caractérise le comportement dynamique d'une classe de ces matériaux composites, à savoir la présence de bandes interdites dans le spectre, *i.e.* des intervalles de fréquences correspondant à des ondes atténuées. Les cristaux phononiques et les matériaux localement résonnants à structure périodique appartiennent à cette classe et sont les principaux sujets de ce travail. A l'aide d'un cristal masse dans masse, on précise d'abord les rôles des principaux paramètres du problème de la propagation des ondes dans ces deux typologies de métamatériaux. Ensuite, on utilise une technique d'homogénéisation à deux échelles pour dériver leur comportement effectif à une échelle inférieure à la longueur d'onde. En particulier, les matériaux localement résonnants sont analysés, étant caractérisés par la présence de bandes interdites déjà à un régime inférieur à la longueur d'onde.

Avec l'idée de focaliser l'énergie mécanique dans une zone confinée, nous analysons l'effet d'un défaut de périodicité. on montre que cela peut entraîner la formation de modes localisés à des fréquences à l'intérieur d'une bande interdite. En utilisant des matériaux localement résonnants, on développe alors un système (basé sur le phénomène de tunneling résonant en physique) qui permet de piéger des ondes mécaniques dans une cavité, c'est à dire dans la région du métamatériau avec un défaut de périodicité, où l'énergie va s'empiler vers le haut et ainsi se concentrer. On utilise ici les propriétés matérielles effectives dérivées.

Dans la dernière partie du manuscrit, nous étudions et validons expérimentalement les phénomènes d'atténuation et de localisation sur une métastructure unidimensionnelle. Pour cela, on utilise un câble tendu avec une famille de masses suspendues périodiquement répétées sur sa longueur. Dans un premier temps, nous étudions théoriquement son comportement dynamique puis on compare les résultats avec un test expérimental, validant les effets d'atténuation et de localisation.

L'objectif de cette thèse est double: d'une part nous visons à traiter le problème élasto-dynamique associé aux milieux périodiques défectueux présentant des bandes interdites (*i.e.* métamatériaux), et d'autre part on veut également donner des preuves d'efficacité de ces systèmes de localisation de l'énergie mécanique. Nos résultats fournissent de nouvelles informations sur le comportement dynamique des milieux périodiques défectueux à utiliser dans les systèmes de récupération d'énergie, ce qui rend ce travail pertinent à la fois pour les domaines théoriques et pratiques.

# Acknowledgments

A PhD is a journey full of difficulties and obstacles that can be overcome only if one has the chance of encountering good travel companions. In my case, I was lucky enough to meet the best travel companions a could ever ask for. As this journey has now come to an end, I would like to reserve some words to acknowledge them.

First of all, I want to warmly thank my thesis directors, Claudia Comi and Jean-Jacques Marigo. It has been a great pleasure and honor for me to have them as guides. Beyond their profound scientific knowledge and outstanding pedagogy, I am enormously in dept with them for their unconditioned support, kindness, humor and for their interest to my work.

My acknowledgments are equally addressed to all the members of the committee of my defense, for their precious comments and questions. I am so grateful to Habib Ammari and Luigi Gambarotta for accepting to review my thesis and for the nice words used in their reports on this work. I also owe my gratitude to the other two members of the jury, Agnès Maurel and Kim Pham. As I first met them during a summer school they had organized in Cargèse, I have never stopped reading and appreciating their work.

I had the opportunity to pursue this thesis in two prestigious laboratories, namely the LMS at the École polytechnique and the DICA at the Politecnico di Milano. In this regard, I would like to thank all the people working there for their hospitality and for making these places such perfect environments for doing research. In particular, I thank Alexandra Joly, Anna Johnsson and Elena Raguzzoni from the administrative staffs of the two laboratories, for being always there in case of any type of need. I also thank Marco Cucchi for his help in the setup of the experimental tests. His technical knowledge and advice were fundamental for making this part of the present work possible.

A special thank goes to all the PhDs and postdocs that have been part of this journey. In particular, I would like to thank Filippo, Tullio, Othmane, Lucas, Alice, Matteo, Martina and David. I feel so lucky to have met them. All the adventures we had together will always be part of my best memories.

I finally thank my parents, Anna and Paolo, my grandparents, Mariagrazia and Giuseppe, my brother and sister, Samuele and Elena, and my girlfriend, Laura. Grazie per essere sempre al mio fianco.. Grazie per essere fonte d'ispirazione.. Grazie per il vostro amore incondizionato che mi spinge oltre a qualsiasi ostacolo.. Questo traguardo è stato possibile solamente grazie al vostro incessante supporto.

*To my parents.*

# Contents

Chapter 1

# Introduction

## 1.1 General context: the world of metamaterials

During the last decades, the field of metamaterials has experienced an evolution that has lead them from being confined merely as academic curiosity, to become an active field with several possible applications. The term "*metamaterials*", with the Greek prefix *meta-* meaning beyond, is normally used for denoting artificial (*i.e.* man-made) composite materials that are constructed by repeating a unit cell, most often periodically. The particular arrangement and the peculiar design of their micro-structure confer them some unusual properties, which is unlikely to find in more common materials. In contrast, taken individually, each constituent has a standard behavior. It is in this sense that the composite material becomes a metamaterial.

Often in the literature, the above definition is completed by the statement that the unusual behavior is expected to modify the macroscopic response of the composite; in that case, the term metamaterial would be used only for denoting a sub-wavelength regime. It is recognized in the literature that a commonly established definition of this typology of materials does not exist yet (see *e.g.* the review by Lu et al. (2009)) and in this work, when referring to a metamaterial, we decided to avoid the latter restriction, if not explicitly specified.

### 1.1.1 Classification based on the problem of waves propagation

When dealing with the propagation of waves, a widely studied feature of metamaterials is their dispersive behavior that enables for the control and manipulation of propagating waves.

The most exploited property is the presence of band gaps affecting their dynamic response, *i.e.* gaps of frequencies at which waves cannot propagate without attenuation. Inspired from the behavior of crystals in solid state physics, this feature was first studied in the field of electromagnetism, leading to the development of the so-called "*Photonic*

*Crystals*" (PtCs) (Sakoda, 2005; Joannopoulos et al., 2008). Very soon, the exact same concept was extended to the fields of elasticity and acoustics, with the emergence of the so-called "*Phononic Crystals*" (PnCs) (Sigalas et al., 1992; Kushwaha et al., 1993; Sigalas et al., 1995). From a mathematical point of view, these frequency gaps come from the banded structure of the spectrum of the differential operator that is involved in the problem (Kuchment, 1993; Figotin et al., 1996a,b). These two subclasses of metamaterials are composed of structures with a spatial periodic modulation of their material properties. Band gaps can appear when subjected to waves with a wavelength comparable to the period.

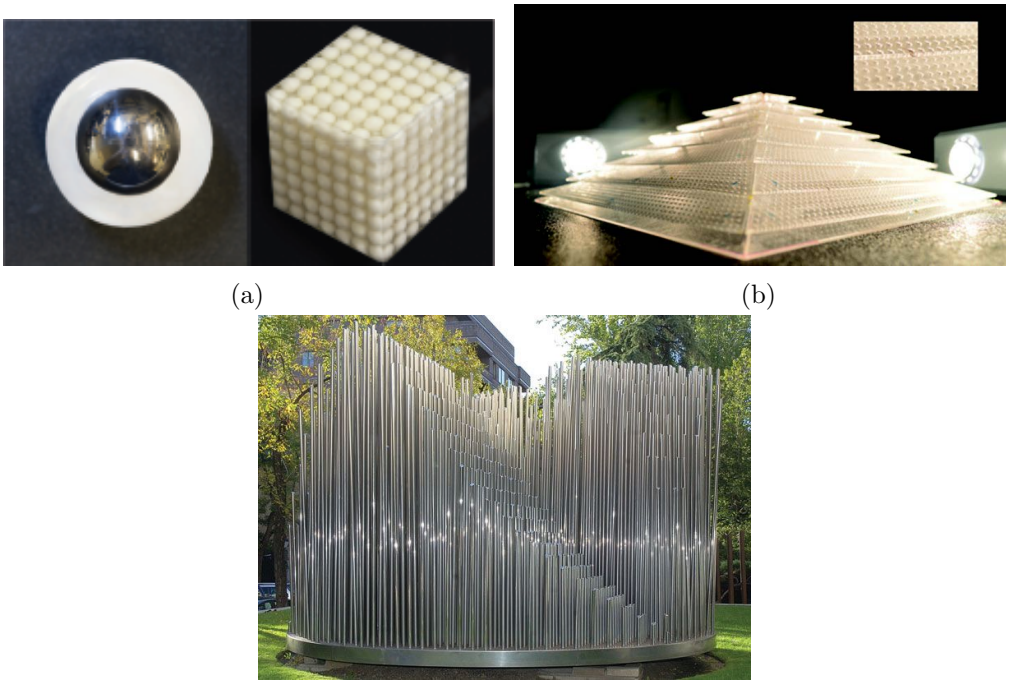

(a) (b)

(c)

Figure 1.1: *(a) A LRM whose basic unit structure is composed of a lead sphere coated with silicone rubber and inserted in an epoxy matrix (source: Sheng et al. (2003)). (b) An acoustic cloak whose unit cell is made up of an air-filled cube that has in the middle an acrylic perforated plate (source: Zigoneanu et al. (2014)). (c) Eusebio Sempere's sculpture in Madrid (Spain) represents a famous example of a 2D phononic crystal for acoustic waves (source: Martínez-Sala et al. (1995)).*

In problems characterized by large wavelengths ranging from centimeters to meters, PtCs and PnCs are hardly employed because low frequencies band gaps would require rather large samples. It is at this stage that the so-called "*Locally Resonant Materials*" (LRMs) broken through: they not only resolved the sample size problem, but also introduced new functionalities, as *e.g.* superlensing (Pendry, 2000; Fang et al., 2006)

and cloaking (Milton et al., 2006a; Milton et al., 2006b).

The present work contributes towards the objective of designing materials with unusual response to elastic (and acoustic) waves. PnCs and LRMs for applications in elastodynamic problems will thus be our field of interest and we will refer to them whenever the term "metamaterials" will be encountered in the following of this work.

In the literature, PnCs and LRMs come in several possible configurations (*cf.* figure 1.1 for some examples), nevertheless, in the most general case, they are composed of a matrix with periodically distributed inclusions that constitute their micro-structure. The interested reader is referred to (Deymier, 2013; Laude, 2015; Romero-García et al., 2019), where a detailed review and numerous applications of these two subclasses of metamaterials are given.

The distinction between PnCs and LRMs is related to the different nature of the mechanism responsible for the attenuation of propagating waves. The dynamic problem is characterized by the presence of two length scales: the size $\ell$ of a unit cell (*i.e.* the period) and the wavelength $\lambda$ of the propagating wave. As stated before, in PnCs the two scales are comparable ($\ell/\lambda = \mathcal{O}(1)$). The inclusions contained in each unit cell behave exactly as the rectangular potential wells in a Kronig-Penney model, commonly employed for studying the motion of electrons in solids (Kronig et al., 1931). Band gaps are induced by a mechanism that resembles Bragg scattering and, therefore, the basic physical reason for the existence of gaps lies in the coherent interference of waves. PtCs have exactly the same functioning, but interact with electromagnetic waves. In LRMs, $\ell \ll \lambda$ and wave cancellation is due to Fano-like interactions (Goffaux et al., 2002; Limonov et al., 2017) between the long-wavelength waves propagating in the matrix and the local eigenvibrations of the micro-structural elements (Auriault et al., 1985; Auriault, 1994; Milton et al., 2007).

### 1.1.2 Energy harvesting through defective metamaterials

Energy harvesting (EH) is the technology that pursues to scavenge electrical energy from ambient sources. Over the past few years, this field has received a great deal of attention due to the increasing desire to produce portable and wireless electronics with extended lifespans, getting rid of chemical batteries that need to be replaced or recharged constantly, decreasing the costs and the environmental impact (Elvin et al., 2013). Potential applications of energy harvesting technologies include: wireless sensor networks employed to survey civil infrastructure systems, sensors for monitoring tire pressure in automobiles, powering unmanned aerial vehicles, medical sensors implanted in the human body (such as pacemakers), and remote location sensors (Priya et al., 2009). Numerous sources can be harvested, such as heat, wind, flowing water, and solar energy. Nevertheless, one of the most effective ways of implementing a compact energy harvesting system is to use ambient vibrations, being one of the most accessible energy sources.

Among different methods that can be used for converting vibrations energy into electric energy, piezoelectric transduction (Erturk et al., 2011) is the most popular one

due to the easy application, the high power density, and the relative maturity of the manufacturing methods of piezoelectric materials at different scales (Anton et al., 2007; Priya, 2007; Tol et al., 2016b). More specifically, piezoelectric energy harvesting is most often based on the so-called "*direct piezoelectric effect*": the deformation of these materials due to external vibrations produces electric polarization.

Ambient vibration sources are always distributed on a broad surface. It is thus difficult for the generators to collect and convert such vibration energy. To obtain an efficient energy harvester, one has to trap and focus the energy produced by external vibrations in a given compact region, where it can be then converted in electricity exploiting the piezoelectric effect.

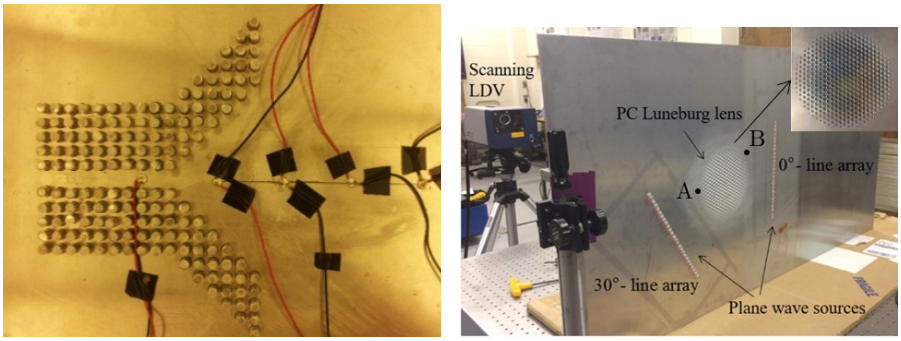


(a) (b)

Figure 1.2: *(a) Array of acoustic scatterers arranged to form an acoustic funnel to channel and focus the propagating waves (source: Carrara et al. (2013)). (b) Experimental setup showing the PC Luneburg lens, with points A and B indicating the positions of two piezoelectric harvester (source: Tol et al. (2017a)).*

To this purpose metamaterials are very attractive, thanks to their abilities to modify the behavior of propagating waves. Several approaches can be found in the literature, relying on different mechanisms and geometries. With the awareness of not being exhaustive, we list some examples herein. The reader is referred to the work of Hu et al. (2021) for a detailed review. Focusing can be attained by using *elliptic* and *parabolic acoustic mirrors* or by guiding and channeling propagating waves using *acoustic funnels* (Carrara et al., 2013). With the same objective, gradient-index lenses have also been employed in different configurations (Tol et al., 2016a, 2017a; Tol et al., 2017b), in analogy to optical lenses. Aiming to increase the interaction time between waves and the harvesting system to amplify the power output, graded arrays of resonators relying on the so-called "*rainbow effect*" have been developed (De Ponti et al., 2020; De Ponti et al., 2021). We report in figure 1.2 two of the listed examples.

All the harvesting systems listed above deals with waves that are not propagating in the bulk (*i.e.* surface and plate waves). Another approach that in principle enables for the focusing of all kinds of waves is based on the excitement of so-called *defect*

*modes*, that can appear due to a perturbation of the periodicity of the domain under consideration, by means of point or line defects.

As stated earlier, metamaterials are generally characterized by a periodic domain and can possess band gaps in their continuous spectra due to the sequential scattering initiated in each unit cell that composes them. A defect of this periodicity can result in the appearance of eigenmodes at frequencies that belong to a band gap. The corresponding field will then be localized around the defect and will decay exponentially outside it (*i.e.* in the unperturbed part of the domain). The defect will thus behave as a resonant cavity.

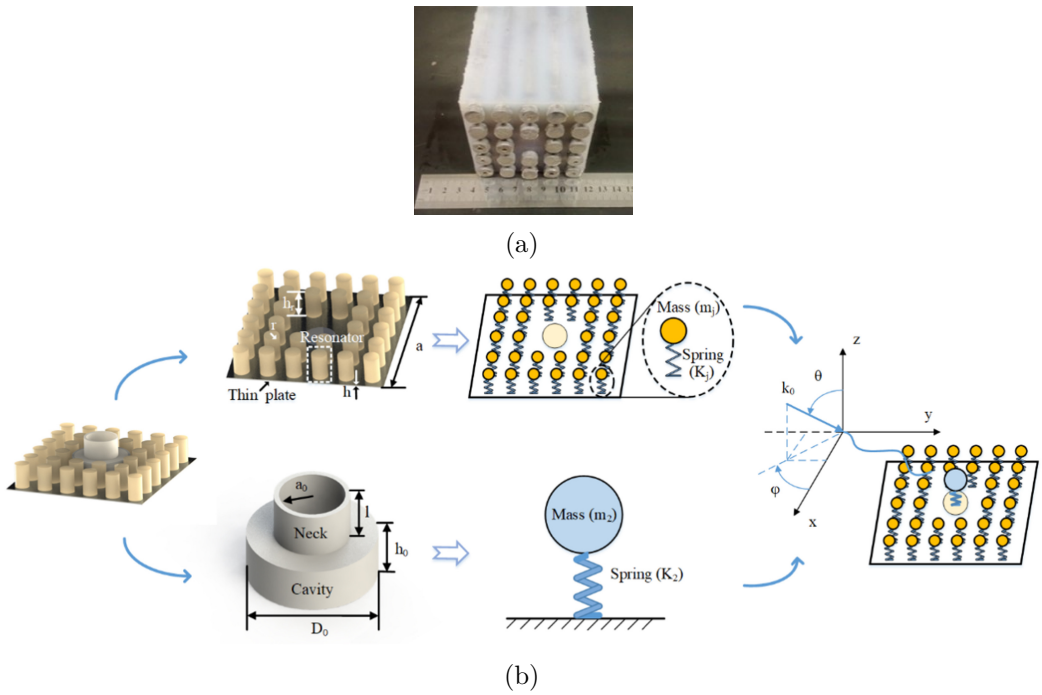


Figure 1.3: *(a) A phononic crystal for mechanical with a central defect generated by the removal of the central scatter element from the period array (source: Lv et al. (2013)). (b) A metamaterial plate mounts an array of resonating stubs, with a Helmholtz resonator placed in a central defect; acoustic waves directed as the vector* $\boldsymbol{k}_0$ *hit the metamaterial and the generated oscillations are localized in the defect (source: Ma et al. (2021)).*

The central idea is that of creating a match between the defect resonance frequency and the excitation frequency, inserting a device for harvesting the energy that is focused in the defect as a result of the localization process. We will call this methodology "*Defective Energy Harvesting*" (DEH).

The first attempts towards the development of DEH devices were conducted in acoustics. In the work of Wu et al. (2009a,b), the authors considered a point defect

obtained by removing the central rod in a sonic crystal[1], placing a piezoelectric element inside. In order to enhance the harvesting capabilities of their system, they later added an Helmholtz resonator in the defect obtaining a stronger focusing of the external vibrations (Wu et al., 2010). Placing the piezoelectric element inside the Helmholtz resonator, a DEH device was later tested confirming the increasing of the scavenged energy (Yang et al., 2013).

Concerning applications for mechanical waves, the harvesting capabilities of the defective phononic crystal reported in figure 1.3a have been experimentally validated in the work of Lv et al. (2013).

In all the DEH devices mentioned until now, the metamaterials considered base their attenuating capabilities on a Bragg's scattering phenomenon. Their dimensions are thus intrinsically connected with the frequencies of interest. This aspect is a possible issue when dealing with low frequency ambient vibrations[2]. There is thus a need of sub-wavelength DEH systems. To this regard, preliminary results exist and cope with the conversion of acoustic sources first into mechanical motion and then into electrical energy, by considering defective LRMs composed of plates with a periodic distribution of softer pillars that can resonate (Qi et al., 2016; Oudich et al., 2017; Ma et al., 2020). An example of such systems is reported in figure 1.3b.The present work is intended to contribute in this direction.

## 1.2 Scope of the present work

Keeping in mind the variety of possible applications previously described, the main objective of this work is to provide a detailed study on the localization phenomenon that can occur in metamaterials, when their periodic structure is altered by the introduction of a compact defect or cavity. Specifically, this thesis addresses the propagation of mechanical waves in discrete and continuous metamaterials.The focus is that of exploiting the aforementioned phenomenon to develop systems behaving as defective energy harvesting devices, both using PnCs and LRMs.

We mainly analyze the harmonic regime: if the source of the time dependent problem under consideration is harmonically varying in time, then the solution is expected to become itself harmonic after a sufficiently long time. Accordingly, we always look for solutions that periodically vary in time.

We propose two lines of research, that are nevertheless strongly related. The first one consists in treating the problem of wave propagation in microstructured media, with the scope of shedding light on how the parameters involved affect the dynamic behavior of this type of systems. In particular, for LRMs, we can use the two-scale homogenization technique (Bensoussan et al., 1978). This method bears on the idea of replacing the periodic (and usually heterogeneous) domain of the problem with an

[1] In acoustics, PnCs are also called *sonic crystals*.

[2] The dimensions of a unit cell is indeed inversely proportional to the frequencies composing the band gap of interest.

effective homogeneous medium, that is easier to deal with. When applied to LRMs, one finds that the effective mass density can become negative for some intervals of frequencies, corresponding to band gaps (Auriault et al., 1985). General results valid for LRMs with a resonating element composed of an inner inclusion embedded inside a coating layer (such as the one depicted in figure 1.1a) have already been considered in the literature (Auriault et al., 2012). Nevertheless, we have not found a comprehensive description of the resonating behavior of the two inclusions. We thus here revisit the problem from a different point of view, that enables us to give more insights on the dispersive behavior of these type of LRMs.

Following these results, we study the dynamic response of defective systems, by introducing a cavity in a periodic LRM. To the best of our knowledge, although the localization phenomenon has been already theoretically demonstrated to occur (Ammari et al., 2017), applications of this particular behavior to DEH apparatus for bulk mechanical waves in LRMs are still missing in the literature. This being interesting for the design of sub-wavelength devices.

Concerning our second line of research, we explore the dynamics of suspended cables, such as the ones used in suspension bridges or overhead lines. Quite often in engineering applications these systems present a family of hanging elements, periodically distributed along their length. Their linearized dynamics could be in principle characterized by many similarities with the typical behavior of the metamaterials described in this thesis. We here aim to give a demonstration of this latter assertion, by considering the problem of a cable in tension between two supports, presenting equally distant attached masses along its length. Our purpose is also that of comparing these theoretical results with those coming from an experimental test. Finally we intend to give an experimental validation of the localization phenomenon previously described by employing the aforementioned cable systems: the periodic set of masses can indeed be altered for instance by removing one mass from the array and a defect is thus formed.

## 1.3 Organization of the thesis

Following this introduction, we divide the thesis in five chapters (plus a final chapter of conclusions), whose content is here briefly described.

**Chapter 2.** The problem of wave propagation in periodic domains is introduced and the Bloch-Floquet approach is presented. A mass-in-mass 1D lattice is used to show and explain the mechanisms of Bragg scattering and local resonance, that are responsible for the formation of band gaps.

**Chapter 3.** The effective behavior of LRMs is derived exploiting the two-scale homogenization technique. Some new results concerning the resonating behavior of three-phase systems are proposed. The effective mass density of two example cases is analytically obtained.

**Chapter 4.** The problem of wave (and energy) localization in defective metamaterials

is established. A new method for trapping mechanical waves is presented by using the aforementioned mass-in-mass chain in a 1D discrete system. The functioning is based on the resonant tunneling phenomenon known from quantum mechanics,

**Chapter 5.** A continuous DEH device based on the same mechanism described in chapter 4 is developed by introducing a cavity in LRMs of the type outlined in chapter 3. The efficiency of this system in localizing and enhancing the mechanical energy carried by propagating waves is also studied.

**Chapter 6.** The dynamic problem associated with the motion of cables hanging between two supports is presented both for the case with and without periodically attached masses. Several approximations concerning the static behavior of these systems are shown and used as a starting point for the problem of small oscillations around the equilibrium configuration of the cable. Theoretical and experimental results are compared and the localization phenomenon obtained by the removal of one mass from the periodic array is experimentally demonstrated.

## 1.4 Notation

Throughout this work, normal-face letters ($a$) stand for scalars; Latin boldface letters ($\boldsymbol{a}$) denote vectors; Greek boldface letters ($\boldsymbol{\alpha}$) designate second-order tensors, while boldface upper-case sans-serif Latin letters ($\mathbf{A}$) designate fourth-order tensors. Vectors and tensors components are indicated normal-face (being scalars), followed by subscripts defining the indexes within squared brackets ($a_{[i]}$, $\alpha_{[ij]}$, $\mathsf{A}_{[ijkh]}$). It will be clear from the number of indexes if either a vector (one index), or a second order tensor (two indexes), or a fourth order tensor (four indexes) will be under investigation. Operators are specified with upper-case normal-face script Latin letters ($\mathscr{A}$). Calligraphic letters ($\mathcal{A}$) are reserved for sets.

The following specific notations do not respect the general rules indicated here-above: the letter V, in absence of any further specifications, will always denote a regular open region in $\mathbb{R}^n$ of class $\mathcal{C}^1$, with $n \in \{1, 2, 3\}$, whose boundary will be designated by $\partial$V; each time it will be clear from the context if the domain is bounded, unbounded, periodic and so on; the letter Y is used to denote a unit cell of a periodic domain V and its volume (or area) is indicated as |Y|; the boldface letter $\boldsymbol{I}$ denotes the second-order unit tensor, whereas the non-italic $\mathbf{I}$ stands for the tensor of inertia; the symbol $\delta_{ij}$, with $i, j \in \{1, 2, 3\}$, is reserved for the $ij$-component of the *Kronecker delta*.

The spatial and time averages of a field ($\bullet$) are given as:

$$\langle(\bullet)\rangle = \frac{1}{|\mathrm{V}|}\int_{\mathrm{V}}(\bullet)\,d\mathrm{V}, \quad \langle(\bullet)\rangle_p = \frac{1}{|\mathrm{V}|}\int_{\mathrm{V}_p}(\bullet)\,d\mathrm{V}_p, \quad \langle(\bullet)\rangle_t = \frac{1}{T}\int_0^T(\bullet)\,dt,$$

where $\mathrm{V}_p$ and $T$ denote respectively a bounded region of V and a period of time. Subscripts $p$ and $t$ might be skipped when no confusion between spatial and time averages can arise.

When a function $(\bullet)(x,t)$ of a generic space variable $x$ and time $t$ is under consideration, we often use $(\bullet)'(x,t) := \partial(\bullet)/\partial x$ and $\dot{(\bullet)}(x,t) := \partial(\bullet)/\partial t$ for the differentiations of $(\bullet)$ with respect to its variables.

The conjugate of a complex number $u$ is denoted $\overline{u}$, its modulus $|u|$, its real part $\mathcal{R}e(u)$ and its imaginary part $\mathcal{I}m(u)$.

The outward normal to a boundary $\partial\mathrm{V}$ is the unit vector $\boldsymbol{n}$, that is normal to any of the points composing the plane tangent to $\partial\mathrm{V}$.

the Greek letter $\sigma$, alone or with a subscript not contained in squared brackets, is reserved for the spectrum of a linear operator.

We denote by $L^2(\mathrm{V},\mathbb{C}^n)$, with $n \in \{1,2,3\}$, the Hilbert space of square-integrable functions from V into $\mathbb{C}^n$, with the usual norm

$$\|(\bullet)\|_{L^2} = \left[\int_{\mathrm{V}} |(\bullet)|^2 \, d\mu\right]^{1/2},$$

where $\mu$ is the Lebesgue's measure in V. We often use $[L^2(\mathrm{V})]^n$ or $[L^2]^n$, in place of $L^2(\mathrm{V},\mathbb{R}^n)$, for real-valued functions. The space $\ell^2$ is the Lebesgue space of square-summable sequences. The same considerations are valid for the Sobolev space $H^1(\mathrm{V},\mathbb{C}^n)$, endowed with the usual norm

$$\|(\bullet)\|_{H^1} = \left[\|(\bullet)\|^2_{L^2} + \|\nabla(\bullet)\|^2_{L^2}\right]^{1/2},$$

with $\nabla(\bullet)$ being the gradient of the function $(\bullet)$, where the derivatives have to be understood in the weak sense. We use $H^1_0$ to denote the closure in $H^1$ of the space of infinitely differentiable functions with compact support in V. When not specified, functions will be either in $[L^2(\mathrm{V})]^n$ or $[H^1(\mathrm{V})]^n$ and the norm $\|(\bullet)\|$ is used, in general, to denote their usual norms. We denote as $W^{1,\infty}(\mathrm{V})$ the Sobolev space of functions $(\bullet) \in L^\infty$ such that $\nabla(\bullet) \in L^\infty$, with the derivatives to be understood in the weak sense. In one-dimension $W^{1,\infty}(\mathrm{V})$ corresponds to the space of Lipschitz continuous functions. We finally use $[L^2_\#(\mathrm{Y})]^n$ and $[H^1_\#(\mathrm{Y})]^n$ for the following Lebesgue and Sobolev spaces:

$$\begin{aligned}[L^2_\#(\mathrm{Y})]^n := \{(\bullet) \in [L^2_{loc}(\mathbb{R}^n)]^n \text{ such that } &(\bullet)(\boldsymbol{x}+\boldsymbol{p}) = (\bullet)(\boldsymbol{x}) \\ &\text{for almost everywhere } \boldsymbol{x} \in \mathbb{R}^n, \forall \boldsymbol{p} \in \mathbb{Z}^n\}\end{aligned}$$

$$[H^1_\#(\mathrm{Y})]^n := \{(\bullet) \in [L^2_\#(\mathrm{Y})]^n \text{ such that } \nabla(\bullet) \in [L^2_\#(\mathrm{Y})]^n\}$$

with Y here standing for the unit cell $(0,1)^n$ and $[L^2_{loc}]^n$ being the space of $[L^2]^n$ functions locally. A function belonging to these spaces is said to be Y-periodic.

Einstein's summation rule will be used throughout the manuscript for vectors and tensors components, with repeated indexes implicitly denoting a sum.

CHAPTER

# 2

# Preliminaries

Chapter summary: *This chapter aims to give an introductory description of the problem of waves propagation in homogeneous and periodically heterogeneous media. The Bloch-Floquet method is presented and general features characterizing the behavior of periodic bodies are derived. Band gaps are then defined and their physical origins are studied by means of a mass-in-mass one-dimensional lattice.*

## Contents



Metamaterials are most often constructed from a periodic repetition of a single unit cell. Their dynamic behavior can be strongly simplified by considering the propagation of waves in infinite periodically heterogeneous media and, consequently, by exploiting the "*Bloch-Floquet (BF) method*". We thus initially give a short introduction on this subject, that is based on the existing literature (Conca et al., 1995, 1997; Comi et al.,

2020). The study of wave propagation in metamaterials generally aims to determine the dispersive properties and the presence of band gaps. The BF approach is then particularly useful since it reduces the effort for the determination of the spectrum of the problem.

The objective of this chapter is to show and describe which are the main ingredients that govern the peculiar elastodynamic behavior of metamaterials. In particular, we are interested in determining under what conditions frequency band gaps can appear. We consider as starting point a one-dimensional periodic structure constituted by the repetition of masses connected by springs in series, each one containing an internal mass-spring resonator. This enables us to analytically fully determine its dynamic response by characterizing the formation of band gaps and by introducing the concept of "*effective mass*" for a discrete system. This notion turns out to be another useful tool for the characterization of the dynamic behavior of periodic structures. Moreover, the concept of effective mass will also be central in chapter 3, where its definition will be extended to continuous bodies.

As stated in the introduction, we recall that in our work we use the term "metamaterials" to indicate both Phononic Crystals (PnCs) and Locally Resonant Materials (LRMs). This further subdivision comes from the two very different physical mechanisms responsible for the formation of band gaps in their spectrum: respectively Bragg scattering and local resonance. We thereafter justify our choice to group them in one class of materials by showing that both mechanisms can (and in general they do) take place in the same structure.

Part of this chapter was the subject of the following publication: Moscatelli et al., 2021.

## 2.1 Propagation of waves in infinite periodic media

The propagation of waves in a periodic structure is a generalization of what happens in homogeneous media. Starting from the characterization of the elastodynamic problem in unbounded domains, we then analyze the problem of free waves[1] when the medium is homogeneous. The spatial periodicity is subsequently established, the Bloch-Floquet approach presented and the behavior of free waves in unbounded periodic domains characterized.

### 2.1.1 The infinite medium

Let us consider an elastic body V occupying the $n$-dimensional Euclidean space $\mathbb{R}^n$ with $n \in \{1, 2, 3\}$ and whose points are denoted as $\boldsymbol{x}$. By fixing an arbitrary origin $\boldsymbol{x}_0$, the points space V can be identified as a subset of the (normed) linear space $\mathbb{R}^n$. The coordinates $\{x_{[n]}\}_{n\in\{1,2,3\}}$ of a point $\boldsymbol{x}$ can thus be defined as the projections of the

[1] We use the term "*free*" to mark the fact that waves of this type are not generated by an external source.

corresponding vector $\boldsymbol{x}$ onto a Cartesian frame with origin in $\boldsymbol{x}_0$. We will call $\boldsymbol{e}_n$, with $n \in \{1, 2, 3\}$, the unit vectors directed as the axes of the Cartesian frame and we will refer to a specific direction of that reference system as either $x_n$ or $\boldsymbol{e}_n$. In what follows, we will generally consider $\mathrm{V} = \mathbb{R}^n$.

We assume that the motion of V is completely described by a displacement vector field $\boldsymbol{u}(\boldsymbol{x}, t)$ function of position $\boldsymbol{x}$ and time $t$, defined on $\mathrm{V} \times \mathbb{R}^+$. The solid is supposed to behave as a linearly elastic material.

Under the hypothesis of small perturbations, the (symmetric) infinitesimal strain tensor $\boldsymbol{\varepsilon}$ is given by the following compatibility condition:

$$\boldsymbol{\varepsilon}(\boldsymbol{x}, t) = \nabla \odot \boldsymbol{u}(\boldsymbol{x}, t). \tag{2.1}$$

In the framework of linear elasticity, the (symmetric) stress tensor $\boldsymbol{\sigma}$ is given by the constitutive law

$$\boldsymbol{\sigma}(\boldsymbol{x}, t) = \mathsf{E}(\boldsymbol{x}) \,:\, \boldsymbol{\varepsilon}(\boldsymbol{x}, t), \tag{2.2}$$

where the fourth order stiffness tensor $\mathsf{E}$ defines the elastic properties of the material under consideration. Its components $\mathsf{E}_{[ijkh]} \in \mathbb{R}$ are at least piecewise smooth functions of $\boldsymbol{x}$, verifying symmetry and (strong) ellipticity conditions:

$$\begin{cases} \mathsf{E}_{[ijkh]} = \mathsf{E}_{[ijkh]} = \mathsf{E}_{[ijkh]} & \text{(symmetry)}, \\ \exists \alpha > 0 \mid \mathsf{E}_{[ijkh]}(\boldsymbol{x}) \xi_{[kh]} \xi_{[ij]} \geq \alpha \xi_{[ij]} \xi_{[ij]}, \quad \forall \boldsymbol{\xi} \mid \xi_{[ij]} = \xi_{[ji]}, \ \forall \boldsymbol{x} & \text{(ellipticity)}. \end{cases} \tag{2.3}$$

The elastodynamic problem is governed by the following motion equation

$$\nabla \cdot \boldsymbol{\sigma}(\boldsymbol{x}, t) + \boldsymbol{f}(\boldsymbol{x}, t) = \rho(\boldsymbol{x}) \ddot{\boldsymbol{u}}(\boldsymbol{x}, t), \tag{2.4}$$

where the source term $\boldsymbol{f}$ denotes the body forces density and $\rho$ designates the *scalar* mass density.

To complete the problem statement, initial conditions on the displacement $\boldsymbol{u}$ and on the velocity $\dot{\boldsymbol{u}}$ must be defined as follows

$$\begin{cases} \boldsymbol{u}(\boldsymbol{x}, 0) = \boldsymbol{u}_0(\boldsymbol{x}), \\ \dot{\boldsymbol{u}}(\boldsymbol{x}, 0) = \dot{\boldsymbol{u}}_0(\boldsymbol{x}). \end{cases} \tag{2.5}$$

In many physical problems $\boldsymbol{f}$ may be considered harmonic in time with angular frequency $\omega > 0$. The excitation is thus monochromatic and may be represented as

$$\boldsymbol{f}(\boldsymbol{x}, t) = \boldsymbol{F}(\boldsymbol{x}) \exp\{\mathrm{i}\omega t\}. \tag{2.6}$$

The solution can then be expressed as

$$\boldsymbol{u}(\boldsymbol{x}, t) = \tilde{\boldsymbol{u}}(\boldsymbol{x}, t) + \boldsymbol{U}(\boldsymbol{x}) \exp\{\mathrm{i}\omega t\}, \tag{2.7}$$

where the first term on the right-hand side is the *transient solution* and the second one is the *steady-state solution*. It is expected that, after a sufficiently long period, the

transient part of equation (2.7) satisfying the initial conditions (2.5) decays to zero and that only the steady-state solution survives.

As stated in the introduction, we are here mainly interested in the steady-state regime, consequently we can neglect $\tilde{\boldsymbol{u}}$ in relation (2.7) and consider a wave function harmonically dependent on time. Correspondingly, the motion equation in terms of $\boldsymbol{U}$ becomes the inhomogeneous Helmholtz equation[1]

$$\nabla \cdot (\mathsf{E}(\boldsymbol{x}) \,:\, (\nabla \odot \boldsymbol{U}(\boldsymbol{x}))) + \boldsymbol{F}(\boldsymbol{x}) = -\omega^2 \rho(\boldsymbol{x}) \boldsymbol{U}(\boldsymbol{x}). \tag{2.8}$$

### 2.1.2 Free waves in homogeneous unbounded domains

So far we have assumed the body to be heterogeneous. In this subsection we consider a homogeneous medium, with $\mathsf{E}$ and $\rho$ to be $\boldsymbol{x}$-independent functions. We are interested to study the problem when no source terms are present.

We seek for solutions of equation (2.8) under the form of propagating plane waves of wavevector $\boldsymbol{k} \in \mathbb{R}^n$:

$$\boldsymbol{U}(\boldsymbol{x}) = \boldsymbol{U}_{\boldsymbol{k}} \exp\{\mathrm{i}\boldsymbol{k} \cdot \boldsymbol{x}\}, \tag{2.9}$$

where $\boldsymbol{k} = k\boldsymbol{p}$, with $k$ being the wave number and $\boldsymbol{p}$ the unit vector defining the direction of propagation of the wave. The motion equation (2.8) then becomes

$$\left[\boldsymbol{p} \cdot \mathsf{E} \cdot \boldsymbol{p} - c^2\, \rho\, \boldsymbol{I}\right] \cdot \boldsymbol{U}_{\boldsymbol{k}} = \boldsymbol{0} \tag{2.10}$$

with $c = \omega/k$ being the *phase velocity* (also denoted *wave speed*) and $\boldsymbol{I}$ the identity second order tensor.

Defining the tensor

$$\boldsymbol{\Gamma} := \boldsymbol{p} \cdot \mathsf{E} \cdot \boldsymbol{p} \tag{2.11}$$

with the indexes contraction $\Gamma_{[jk]} = \mathsf{E}_{[ijkh]}\, p_{[i]}\, p_{[h]}$, solutions exist only if

$$\det\left[\boldsymbol{\Gamma} - c\,\rho\,\boldsymbol{I}\right] = 0. \tag{2.12}$$

Condition (2.12) corresponds to the map $\boldsymbol{k} \to \omega(\boldsymbol{k})$ and represents the so-called *dispersion relation*, defining the (continuous) spectrum of the operator associated to the problem of free waves propagating in unbounded homogeneous domains.

For a given direction, in an $n$-dimensional medium there can be $n$ phase velocities $c_i$, each one corresponding to a specific eigenvector $\boldsymbol{U}_{\boldsymbol{k},i}$ defining the direction of the motion, *i.e.* the *wave polarization*, with $i$ here spanning from 1 to $n$. Propagation is thus anisotropic in general, but since the phase velocities are constant along a specific direction $\boldsymbol{p}$ (*i.e.* they do not depend on the frequency $\omega$), then the medium is defined to be *non-dispersive*.

Due to assumptions (2.3), $c_i$ are real and positive, and $\boldsymbol{U}_{\boldsymbol{k},i}$ are orthogonal in the $\mathbb{R}^n$ sense (*i.e.* in the Euclidean norm).

[1] For unbounded domains, the uniqueness of the solution is guaranteed by requiring that the wave function satisfies the *Sommerfeld radiation condition* at infinity, as indicated in Eringen et al. (1974).

For *isotropic* solids, the constitutive relation (2.2) can be rewritten as

$$\boldsymbol{\sigma}(\boldsymbol{x}) = \lambda(\boldsymbol{x})\,\mathrm{tr}(\boldsymbol{\varepsilon}(\boldsymbol{x}))\boldsymbol{I} + 2\mu(\boldsymbol{x})\boldsymbol{\varepsilon}(\boldsymbol{x}), \tag{2.13}$$

where $\lambda$ and $\mu$ are the Lamé's constants. Considering the homogeneous domain here studied, equation (2.8) takes the form:

$$\mu\Delta\boldsymbol{U}(\boldsymbol{x}) + (\lambda+\mu)\,\nabla\nabla\cdot\boldsymbol{U}(\boldsymbol{x}) + \boldsymbol{F}(\boldsymbol{x}) = -\omega^2\rho(\boldsymbol{x})\boldsymbol{U}(\boldsymbol{x}), \tag{2.14}$$

Plane waves solutions of the form (2.9), can be readily derived. Typically, one finds one *longitudinal (or pressure) wave* and two *transversal (or shear) waves* whose polarizations are respectively aligned and perpendicular to the direction of propagation of the plane wave and whose phase velocities are

$$c_\ell = \sqrt{\frac{\lambda+2\mu}{\rho}}, \quad c_s = \sqrt{\frac{\mu}{\rho}}, \tag{2.15}$$

independently from the direction $\boldsymbol{p}$.

### 2.1.3 Spatial periodicity

We now consider V to be a *periodic domain*. With this, we intend to describe a body whose elastic stiffness $\mathbf{E}$ and scalar mass density $\rho$ are both invariant with respect to a set $\{\boldsymbol{a}_i\}_{i\in\{1,\dots,n\}} \subset \mathbb{R}^n$ of rigid translation vectors that compose the so-called *primitive basis*. This means that, defining $\boldsymbol{\mathcal{A}} \subset \mathbb{R}^n$ as the vector space of all the translation vectors $\boldsymbol{a}$ satisfying

$$\boldsymbol{a} = \sum_{i=1}^{n} p_i\boldsymbol{a}_i, \quad \forall p_i \in \mathbb{Z}, \tag{2.16}$$

the body will look the same when viewed from the point $\boldsymbol{x}$ as when viewed from every point $\boldsymbol{x}'$ such that

$$\boldsymbol{x}' = \boldsymbol{x} + \boldsymbol{a}, \quad \forall \boldsymbol{a} \in \boldsymbol{\mathcal{A}}. \tag{2.17}$$

The set of points $\boldsymbol{x}'$ calculated from relation (2.17) defines the so-called *Bravais lattice* associated to V (Kittel, 2004).

The periodicity is thus obtained from an infinite repetition of an identical *unit cell* Y, defined as

$$\mathrm{Y} = \{\boldsymbol{x} \in \mathrm{V} \,:\, \boldsymbol{x} = \boldsymbol{x}_0 + \sum_{i=1}^{n} \alpha_i\boldsymbol{a}_i,\ -1/2 \le \alpha_i < 1/2 \quad \forall i \in \{1,\dots,n\},\ \boldsymbol{x}_0 \in \mathrm{V}\} \tag{2.18}$$

and a function $\boldsymbol{f} : \mathbb{R}^n \to \mathbb{R}^m$ with $n, m \in \{1,2,3\}$ is said Y-*periodic*, any time

$$\boldsymbol{f}(\boldsymbol{x}') = \boldsymbol{f}(\boldsymbol{x}), \quad \forall \boldsymbol{x}, \boldsymbol{x}' \in \mathrm{V} \text{ fulfilling relation (2.17)}, \tag{2.19}$$

*i.e.* any time it is invariant under $\boldsymbol{a}$.

Following this definition, both $\mathbf{E}$ and $\rho$ are Y-periodic functions. Such periodicity creates an ideal situation for Fourier analysis. Considering wavevectors $\boldsymbol{b} \in \mathbb{R}^n$ of the plane waves that compose the Fourier expansions of such periodic functions, they all respect the following condition

$$\boldsymbol{a} \cdot \boldsymbol{b} = 2\pi p, \quad p \in \mathbb{Z}, \quad \forall \boldsymbol{a} \in \boldsymbol{\mathcal{A}}, \tag{2.20}$$

that ensures the fulfillment of the periodicity requirements[1]. The set $\boldsymbol{\mathcal{B}}$ of all the vectors $\boldsymbol{b}$ defined in the Fourier space associated to the periodic domain V and satisfying condition (2.20) is called *reciprocal lattice*. Its primitive basis is composed of the set of vectors $\{\boldsymbol{b}_j\}_{j\in\{1,\dots,n\}}$ such that

$$\boldsymbol{a}_i \cdot \boldsymbol{b}_j = 2\pi\delta_{ij}, \quad \forall i, j \in \{1, \dots, n\}, \tag{2.21}$$

with $\delta_{ij}$ being the Kronecker's delta.

We are now in position to determine what is known in the literature as *First Brillouin Zone* (FBZ), defined as the unit cell $\mathrm{Y}^*$ dual to Y whose points are closer to the point $\mathbf{0}$ than to any other element of $\boldsymbol{\mathcal{B}}$, such that:

$$\mathrm{Y}^* = \{\boldsymbol{k} \in \mathbb{R}^n \,:\, \boldsymbol{k} = \sum_{i=1}^{n} \alpha_i^* \boldsymbol{b}_i, \quad -1/2 \leq \alpha_i^* < 1/2 \quad \forall i \in \{1, \dots, n\}\}. \tag{2.22}$$

We report in figure 2.1 a sketch representing a generic Bravais lattice, together with its reciprocal lattice, and their associated bases.

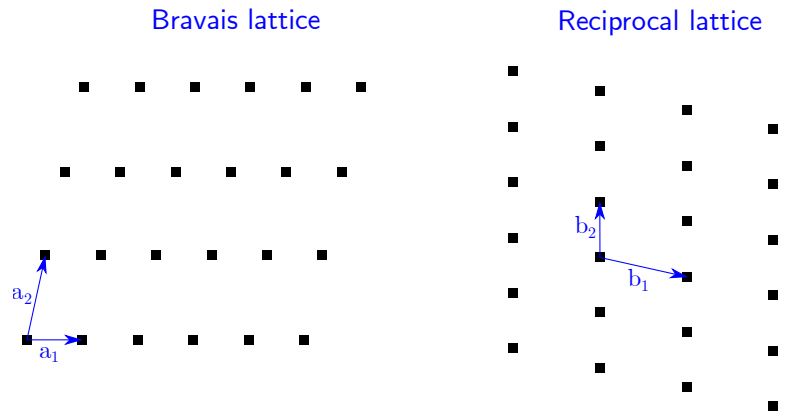


Figure 2.1: *Sketch of a generic 2D Bravais lattice and its reciprocal lattice, with their corresponding primitive bases.*

[1] Before we used the letter $\boldsymbol{k}$ for denoting a wavevector of a generic plane wave. Here, instead, we use the letter $\boldsymbol{b}$ to stress out its function as wave number of plane waves that build up the Fourier expansion of a Y-periodic function and to cope with the existing literature. Note that, as stated in the text, $\boldsymbol{b} \in \mathbb{R}^n$ since $\mathbf{E}$ and $\rho$ are both real functions.

### 2.1.4 Bloch-Floquet approach

When dealing with a domain V composed of a repetition of unit cells Y, the equation (2.8) governing the motion of the body in the harmonic regime is characterized by periodic coefficients. We again look for free waves and, thus, we consider no source terms. Contrary to the homogeneous case analyzed in subsection 2.1.2, considering "simple" plane waves (*i.e.* applying a Fourier transform with respect to the spatial variable) does not result to be an effective tool for transforming the motion differential equation into a set of algebraic equations. Nevertheless, this problem can be tackled by exploiting the periodicity of V, resulting in what is known as *Bloch-Floquet method*[1].

The core of this approach is the use of the so-called *Bloch waves* and *Bloch transform*, that play the same role respectively of plane waves and Fourier transform in homogeneous media.

Specifically, the objective is that of defining the spectrum of an operator $\mathscr{L}$ on $[L^2(\mathrm{V})]^n$ invariant with respect to the translation vectors $\boldsymbol{a} \in \boldsymbol{\mathcal{A}}$, such that

$$\mathscr{L}(\bullet) := -\frac{1}{\rho(\boldsymbol{x})} \nabla \cdot (\mathbf{E}(\boldsymbol{x}) \,:\, (\nabla \odot (\bullet)))\,. \tag{2.23}$$

In order to take into account the translation invariance on its spectrum, the method consists of introducing a family of spectral problems parameterized by a wavevector $\boldsymbol{k} \in \mathbb{R}^n$, such that

$$\mathscr{L}(\mathbf{u}(\boldsymbol{x}, \boldsymbol{k})) = \lambda \mathbf{u}(\boldsymbol{x}, \boldsymbol{k}) \quad \text{in V},\ \lambda \in \mathbb{C} \tag{2.24a}$$

$$\mathbf{u}(\boldsymbol{x} + \boldsymbol{a}, \boldsymbol{k}) = \mathbf{u}(\boldsymbol{x}) \exp\{\mathrm{i}\boldsymbol{k} \cdot \boldsymbol{a}\} \quad \forall \boldsymbol{x} \in \mathrm{V},\ \forall \boldsymbol{a} \in \boldsymbol{\mathcal{A}}. \tag{2.24b}$$

A function $\mathbf{u}$ respecting condition (2.24b) is called $(\mathrm{Y}, \boldsymbol{k})$-*periodic*.

Note that problem (2.24) is invariant when $\boldsymbol{k}$ is replaced by $\boldsymbol{k} + \boldsymbol{b}$ and thus the eigenvectors $\boldsymbol{k}$ can be confined in $\mathrm{Y}^*$. While equation (2.24a) is a typical eigenvalue problem, a justification of the form (2.24b) of the solution can be found in the work of Conca et al. (1997) and comes from group theoretic arguments, by considering the discrete translational symmetry of the solid. The eigenvalues and the eigenvectors of problem (2.24) are respectively known as *Bloch eigenvalues* and *Bloch waves*. To simplify the boundary conditions of the problem, Bloch waves are generally taken in the following form:

$$\begin{cases} \mathbf{u}(\boldsymbol{x}, \boldsymbol{k}) = \tilde{\mathbf{u}}(\boldsymbol{x}, \boldsymbol{k}) \exp\{\mathrm{i}\boldsymbol{k} \cdot \boldsymbol{x}\}, \\ \tilde{\mathbf{u}}(\boldsymbol{x}, \boldsymbol{k}) \quad \text{is Y-periodic.} \end{cases} \tag{2.25}$$

Accordingly, given a function $\boldsymbol{f}(\boldsymbol{x}) \in [L^2(\mathrm{V})]^n$, Bloch waves allows for the definition of

[1] In the mathematical literature, for the case of ordinary differential equations, this problem was treated by Floquet (1883). For partial differential equations, corresponding results were first established by Bloch (1929), who presented what is known in physics as *Bloch wave method*. It is for this reason that the latter approach generally goes under the name of *Bloch-Floquet method*.

its (unique) Bloch transform $\boldsymbol{f}_b(\boldsymbol{x},\boldsymbol{k}) \in [L^2(\mathrm{Y}\times\mathrm{Y}^*)]^n$, such that:

$$\boldsymbol{f}_b(\boldsymbol{x},\boldsymbol{k}) = \sum_{i=1}^{\infty} \boldsymbol{f}_b^i(\boldsymbol{k})\tilde{\mathbf{u}}_i(\boldsymbol{x},\boldsymbol{k}), \tag{2.26}$$

with $\boldsymbol{f}_b^i$ being the projection of the function $\boldsymbol{f}_b$ onto the $i$-th Bloch wave $\tilde{\mathbf{u}}_i(\boldsymbol{x},\boldsymbol{k})$. The function $\boldsymbol{f}$ can then be retrieved through the *inverse Bloch transform* defined as:

$$\boldsymbol{f}(\boldsymbol{x}) = \int_{\mathrm{Y}^*} \boldsymbol{f}_b(\boldsymbol{x},\boldsymbol{k}) \exp\{\mathsf{i}\boldsymbol{k}\cdot\boldsymbol{x}\}\, d\boldsymbol{k}. \tag{2.27}$$

### 2.1.5 Free waves in periodically heterogeneous unbounded domains

Following the discussion in the previous subsection, the problem of free waves propagating in periodic media can be solved by employing the Bloch-Floquet method. The transformation (2.25) is thus applied to the displacement field $\boldsymbol{U}(\boldsymbol{x})$. It maps the equation of motion (2.8) without the source term to the following problem with simplified boundary conditions: find $\lambda = \omega^2(\boldsymbol{k})$ and $\widetilde{\boldsymbol{U}}(\boldsymbol{x},\boldsymbol{k})$ not identically zero such that

$$\begin{cases} (\nabla + \mathsf{i}\boldsymbol{k})\cdot\mathbf{E}(\boldsymbol{x}) \,:\, \left[(\nabla+\mathsf{i}\boldsymbol{k})\odot\widetilde{\boldsymbol{U}}(\boldsymbol{x},\boldsymbol{k})\right] = -\lambda\rho(\boldsymbol{x})\widetilde{\boldsymbol{U}}(\boldsymbol{x},\boldsymbol{k}) \quad \forall\boldsymbol{x}\in\mathrm{Y},\ \forall\boldsymbol{k}\in\boldsymbol{Y}^*, \\ \widetilde{\boldsymbol{U}}(\boldsymbol{x},\boldsymbol{k}) \quad \text{is Y-periodic.} \end{cases} \tag{2.28}$$

The operator $\mathscr{L}_{\boldsymbol{k}}$ on $[L^2(\mathrm{Y}\times\mathrm{Y}^*)]^n$ defined from the above problem as:

$$\mathscr{L}_{\boldsymbol{k}}(\bullet) := -\frac{1}{\rho}(\nabla+\mathsf{i}\boldsymbol{k})\cdot\mathbf{E} \,:\, [(\nabla+\mathsf{i}\boldsymbol{k})\odot(\bullet)] \tag{2.29}$$

is generally known as *shifted (or translated) operator*.

The advantage of the Bloch-Floquet method lives in the reduction of a spectral problem in the unbounded domain V with oscillating coefficients, to a family of eigenvalue problems in the unit cell Y.

At given $\boldsymbol{k}\in\mathrm{Y}^*$, problem (2.28) enjoys the following properties:

1. The eigenvalues $\lambda_p(\boldsymbol{k})$ constitute a sequence of non-negative real numbers $\{\lambda_p(\boldsymbol{k})\}_{p\in\mathbb{N}^*}$, which tends to infinity without accumulation points;
2. The eigenvectors $\widetilde{\boldsymbol{U}}_p(\boldsymbol{x},\boldsymbol{k})$ associated to an eigenvalue $\lambda_p(\boldsymbol{k})$ constitute a subspace (eigenspace) of $[L^2_\#(\mathrm{Y})]^n$ of finite dimension;
3. The eigenspaces are orthogonal to each other in the sense of the scalar product

$$(\boldsymbol{u},\boldsymbol{v}) = \frac{1}{2}\int_{\mathrm{Y}} \rho\,(\boldsymbol{u}\cdot\overline{\boldsymbol{v}} + \boldsymbol{v}\cdot\overline{\boldsymbol{u}})\, d\boldsymbol{x} \quad \forall\boldsymbol{u},\boldsymbol{v}\in[L^2_\#(\mathrm{Y})]^n \tag{2.30}$$

   and constitute a countable basis of $[L^2(\mathrm{V})]^n$.
4. Changing the unit cell from $\mathrm{Y}^*$ to $\alpha\,\mathrm{Y}^*$ and the wave vector from $\boldsymbol{k}$ to $\boldsymbol{k}/\alpha$, simply scale the spectrum of $1/\alpha$ without affecting its structure.

Note that point 3 justifies relation (2.26).

By varying $\boldsymbol{k} \in \mathrm{Y}^*$, one obtains the spectral resolution of the shifted operator in $[L^2(\mathrm{V})]^n$, such that:

1. the spectrum $\sigma$ of $\mathscr{L}$ coincides with the *Bloch spectrum* $\sigma_b$ of $\mathscr{L}_{\boldsymbol{k}}$, the latter being defined as
$$\sigma_b := \bigcup_{p=1}^{\infty} \left[ \inf_{\boldsymbol{k}\in \mathrm{Y}^*} \lambda_p(\boldsymbol{k}), \sup_{\boldsymbol{k}\in \mathrm{Y}^*} \lambda_p(\boldsymbol{k}) \right]; \tag{2.31}$$
2. $\forall p \geq 1$, the map $\boldsymbol{k} \to \lambda_p(\boldsymbol{k})$ is a Lipschitz function and defines the *dispersion relation* of the medium;
3. $\lambda = 0$ is always a solution of problem (2.28);
4. when $\boldsymbol{k} \in \mathrm{Y}^*$ and $\boldsymbol{k} \neq 0$, then $\lambda = 0$ is not a solution of problem (2.28).

Following the above properties, the spectrum $\sigma$ of a body V unbounded and periodic is composed of an infinite and countable number of branches. The dispersion relation is in general not linear, therefore the medium can become *dispersive*. In contrast to the homogeneous case, $\sigma$ does not need to fill up the entire space $\mathbb{R}^+$ and so-called *band gaps* (BGs) might appear. Whenever $\omega \in$ BGs, then solutions can still be found in the form of Bloch waves by allowing $\boldsymbol{k}$ to become complex valued. In that case, the corresponding wave has an amplitude that decreases in space and is said to be *attenuated*. A band gap is thus an interval of frequencies at which propagating waves are attenuated.

## 2.2 The discrete mass-in-mass chain

The physical explanation for the formation of band gaps resides in two mechanism, namely Bragg scattering and local resonances. A rather common and efficient way to demonstrate the previous assertion consists in using discrete systems. Lattice systems composed of lumped masses connected by springs, thoroughly studied by Brillouin (1946), have been constructed for analyzing the behavior of crystals when subjected to elastic waves. Their dynamic response is very similar to that of PnCs, being governed by the superimposition of multiple reflected waves, that can behave in a coherent way for either constructive or destructive interference. These systems are thus characterized by a Bragg scattering phenomenon. LRMs are instead generally modeled with so-called "*mass-in-mass lattices*" of the type shown in figure 2.2, where local resonances can be activated due to the presence of the internal oscillator of mass $m_2$ and stiffness $k_2$.

Our objective in this section is twofold.

- Firstly, we intend to give a better explanation of what is meant by Bragg scattering and local resonance. Most often in the literature mass-in-mass chains are used only for describing their local resonant behavior. Nevertheless, we show here that these systems are instead also influenced by Bragg reflections, that are normally

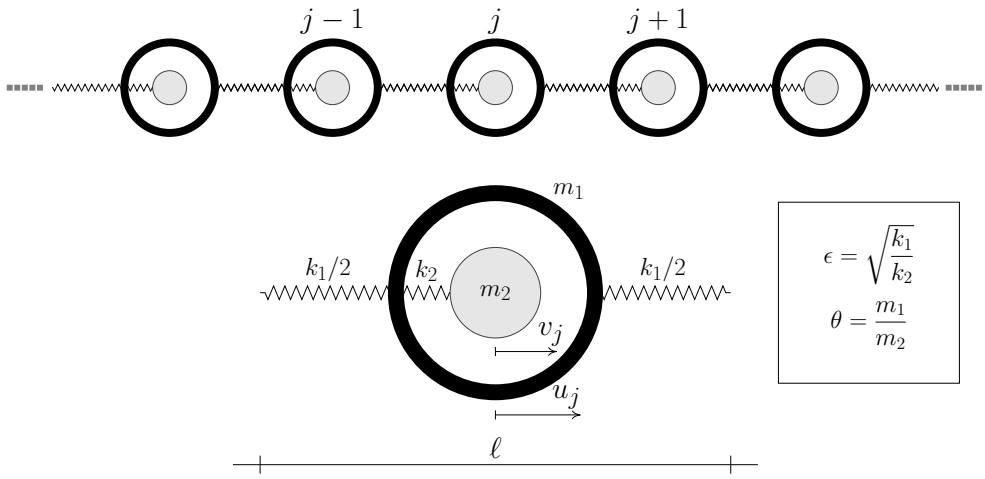


Figure 2.2: *Sketch of the mass-in-mass chain and zoom over its microstructure. Masses $m_1$ are connected to the nearest neighbors with springs $k_1$ on both sides. Each mass $m_1$ contains a resonator of mass $m_2$ and stiffness $k_2$. The chosen unit cell includes mass $m_1$ with the internal resonator and two springs of stiffness $k_1/2$. We call $\ell$ the size of the unit cell.*

not taken into account. We thus employ the lattice shown in figure 2.2 to comment on the two mechanisms responsible for the formation of band gaps.

- Then we show how the parameters involved in the motion problem of a mass-in-mass lattice affect its dynamic behavior. The simplicity of the considered structure allows for a closed form solution to be found, giving insights on the behavior of more general periodic bodies that will be analyzed in the rest of this work.

Our considerations are based both on the BF method and on the definition of an "*effective mass*" for discrete lattices.

For the current section, the angular frequency $\omega$ will be called just "*frequency*".

### 2.2.1 Formulation of the motion problem

Let us consider the mass-in-mass chain in figure 2.2. In this case, the domain V of definition of the problem is discrete and embedded in the one dimensional space $\mathbb{Z} \subset \mathbb{R}$. The primitive basis is thus here composed only by one vector $\boldsymbol{a}_1$.

The system is composed of a periodic repetition of external masses $m_1$ which are connected to the nearest neighboring masses with springs $k_1$ and contain internal resonating masses $m_2$, attached with springs $k_2$. With the aim of keeping the symmetry, the chosen unit cell shown in figure 2.2 includes mass $m_1$ with the internal resonator (of mass $m_2$ and stiffness $k_2$) and two springs of stiffness $k_1/2$. The size of the unit cell

is $\ell$. Each spring is considered as massless. The index $j \in \mathbb{Z}$ is used for referring to a particular cell in the chosen numbering. The displacements of the external and internal masses are denoted by $u_j$ and $v_j$ respectively.

The motion[1] of the mass-in-mass chain is governed by the following differential system of equations:

$$\begin{cases} m_1 \ddot{u}_j = k_1 \Delta_j u + k_2(v_j - u_j) \\ m_2 \ddot{v}_j = k_2(u_j - v_j) \end{cases} \tag{2.32}$$

where $\Delta_j$ denotes the discrete differential operator

$$\Delta_j u = u_{j+1} + u_{j-1} - 2u_j \tag{2.33}$$

and superposed dots mark time derivatives.

We are interested in the steady-state response, therefore we will only consider motions at a given frequency $\omega$, so that the variation in time $t$ of the displacement can be expressed as

$$u_j(t) = U_j \exp(\mathrm{i}\omega t), \qquad v_j(t) = V_j \exp(\mathrm{i}\omega t)$$

and hence the system (2.32) becomes:

$$\begin{cases} m_1 \omega^2 U_j + k_1 \Delta_j U + k_2(V_j - U_j) = 0 \\ m_2 \omega^2 V_j + k_2(U_j - V_j) = 0 \end{cases} \tag{2.34}$$

Let us introduce the eigenfrequencies of each mass-spring part as

$$\omega_1 = \sqrt{\frac{k_1}{m_1}}, \quad \omega_2 = \sqrt{\frac{k_2}{m_2}}$$

and the following dimensionless (positive) quantities:

$$\Omega = \frac{\omega^2}{\omega_2^2}, \qquad \epsilon = \sqrt{\frac{k_1}{k_2}}, \qquad \theta = \frac{m_1}{m_2}, \tag{2.35}$$

with $\Omega$ being the frequency of the wave under consideration normalized with respect to the eigenfrequency of the internal resonators, $\epsilon$ is the square root of the stiffness ratio, and $\theta$ is the mass ratio.
Inserting the above dimensionless quantities into equations (2.34) leads to:

$$\begin{cases} \theta \Omega U_j + \epsilon^2 \Delta_j U + (V_j - U_j) = 0 \\ \Omega V_j + (U_j - V_j) = 0 \end{cases} \tag{2.36}$$

[1] We here formulate the problem in an elastodynamic framework, nonetheless, everything that follows applies also to the problem of waves propagation in acoustics, with a suitable reinterpretation of the quantities.

The second of equations (2.36) gives $V_j$ in terms of $U_j$ (provided that $\Omega \neq 1$):

$$V_j = \frac{U_j}{1-\Omega} \tag{2.37}$$

and inserting this relation into the first of equations (2.36) gives the discrete differential equation governing the motion of $U$:

$$\epsilon^2 \Delta_j U + \mu_\theta(\Omega) U_j = 0 \quad \text{with} \quad \mu_\theta(\Omega) = \theta\Omega + \frac{1}{1-\Omega} - 1. \tag{2.38}$$

The first of the relations (2.38) is the equation governing the motion of a one-dimensional mass-spring chain composed of only one type of particles. Therefore, the function $\Omega \to \mu_\theta(\Omega)$ can be interpreted as a (dimensionless) effective mass, multiplied by a dimensionless (positive) frequency $\Omega$. For clarity, we will simply call it *effective mass*.

At given $\Omega$, the motion depends on the two parameters $\theta$ and $\varepsilon$. The arrangement of a stiff inclusion embedded in a soft matrix ("*stiff-in-soft*") is typically used for PnCs and corresponds to small $\epsilon$. The opposite case ("*soft-in-stiff*"), commonly employed for LRMs, is instead represented by a large $\epsilon$. Consequently, this system can in principle be used as a simplified model for analyzing the behavior of both cases.

### 2.2.2 General solutions

We are now interested in describing the spectrum of the problem and in finding its solutions.

Let us start from the BF approach. Using this method, the motion is searched under the form $U_{j+1} = U_j \exp\{\mathrm{i}\kappa\}$, where $\kappa$ is the given wave number normalized with respect to the cell size. Inserting this form into equations (2.36) gives the dispersion equation relating the frequency to the wave number:

$$4\epsilon^2 \sin^2 \frac{\kappa}{2} = \mu_\theta(\Omega). \tag{2.39}$$

Therefore, at given $\kappa$, a solution exists for $\Omega$ only if

$$0 \leq \mu_\theta(\Omega) \leq 4\epsilon^2. \tag{2.40}$$

This condition determines the *pass bands*, *i.e.* the gaps of frequencies corresponding to propagating waves. In particular, one obtains the dispersion plot shown in figure 2.3a

Thanks to BF method, this result is straightforward; however it is also unsatisfactory, since we do not known the response of the system for waves with a frequency outside the pass bands (*i.e.* inside a band gap). This information is fundamental in order to give a physical interpretation of the mechanisms responsible for the formation of band gaps and can be obtained by investigating the problem in terms of the effective mass $\mu_\theta$[1]. Let us first study the properties of this function at given mass ratio $\theta$. From the

[1] Actually the motion of the chain for $\Omega \in$ band gap could be defined also by using the BF approach; nevertheless, with the concept of effective mass we believe to gain in clarity and simplicity. Moreover, this concept will be again used later on in other parts of this work.

second of relations (2.38), one sees that $\mu_\theta$ is monotonically increasing in its domain of definition, as shown in figure 2.3b. Specifically, one obtains that $\mu_\theta$ is always increasing with $\Omega$ and is negative in the interval $(1, 1+1/\theta)$ of $\Omega$.

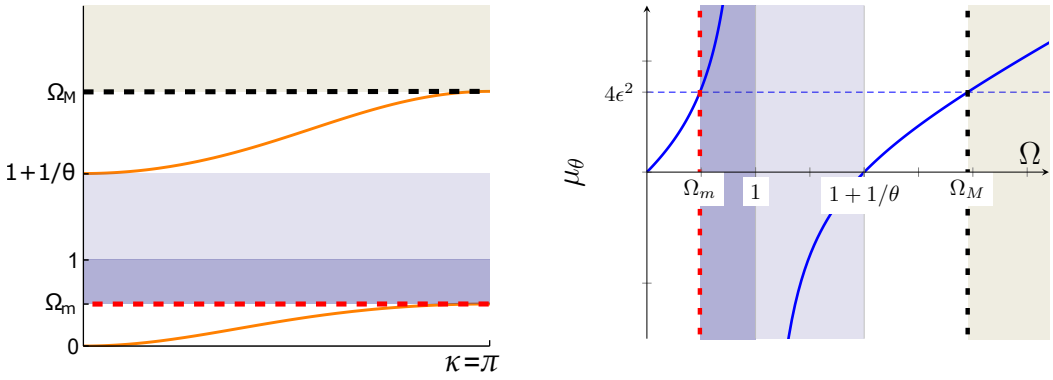


(a) (b)

Figure 2.3: *Dispersion plot* ($\Omega$ vs $\kappa$) *from BF approach (a) and variation of* $\mu_\theta(\Omega)$ *with* $\Omega$ *(b). Intervals* $[\Omega_m, 1+1/\theta]$ *and* $[\Omega_M, +\infty)$ *denote the two band gaps:* $\Omega_A = [\Omega_m, 1]$ *(darker blue) and* $\Omega_C = [\Omega_M, +\infty)$ *(gray) are due to Bragg scattering;* $\Omega_B = [1, 1+1/\theta]$ *(lighter blue) is due to local resonances.* $\Omega_m$ *and* $\Omega_M$ *are given by relations (2.49). By varying* $\epsilon$*, the vertical dashed lines move and the band gaps due to Bragg scattering get either wider or narrower when* $\epsilon$ *becomes respectively smaller and larger. The part of the first band gap generated by local resonances can be modified only by varying* $\theta$*.*

The general solution of equation (2.38) can be obtained in closed form. Let us search the solution as $U_j = r^j$ with $r$ to be determined. Inserting it into equation (2.38) gives the following second degree equation for $r$:

$$r^2 - 2br + 1 = 0 \quad \text{with} \quad b = 1 - \frac{\mu_\theta(\Omega)}{2\epsilon^2}. \tag{2.41}$$

Therefore the roots will be real for $|b| \geq 1$ and complex for $|b| < 1$. Let us consider each case separately.

(i) $0 < \mu_\theta(\Omega) < 4\epsilon^2$. In that case, $|b| < 1$ and the two roots are complex conjugate. Let us set

$$b = \cos \mathsf{K}^* \quad \text{with} \quad \mathsf{K}^* \in (0, \pi). \tag{2.42}$$

Then the two roots are $r = \cos \mathsf{K}^* \pm \mathsf{i} \sin \mathsf{K}^* = \exp\{\pm \mathsf{i} \mathsf{K}^*\}$ and the general solution of equation (2.38) reads

$$U_j = a_1 \cos j\mathsf{K}^* + a_2 \sin j\mathsf{K}^*, \tag{2.43}$$

where $a_1$ and $a_2$ are two arbitrary constants fixed by boundary conditions.

(ii) $\mu_\theta(\Omega) < 0$. In that case, $b > 1$ and the two roots are real numbers. Let us set

$$b = \cosh \mathsf{K}^* \quad \text{with} \quad \mathsf{K}^* > 0. \tag{2.44}$$

Then the two roots are $r = \cosh \mathsf{K}^* \pm \sinh \mathsf{K}^* = \exp\{\pm \mathsf{K}^*\}$ and the general solution of equation (2.38) reads

$$U_j = a_1 \cosh j\mathsf{K}^* + a_2 \sinh j\mathsf{K}^*. \tag{2.45}$$

(iii) $\mu_\theta(\Omega) > 4\epsilon^2$. In that case, $b < -1$ and the two roots are real numbers again. Setting

$$b = -\cosh \mathsf{K}^* \quad \text{with} \quad \mathsf{K}^* > 0 \tag{2.46}$$

the two roots are $r = -\cosh \mathsf{K}^* \pm \sinh \mathsf{K}^* = -\exp\{\pm \mathsf{K}^*\}$ and the general solution of equation (2.38) reads

$$U_j = a_1(-1)^j \cosh j\mathsf{K}^* + a_2(-1)^j \sinh j\mathsf{K}^*. \tag{2.47}$$

Note that, when $|b| = 1$ (*i.e.* when $\mu_\theta(\Omega) = 0$ or $\mu_\theta(\Omega) = 4\epsilon^2$), the solutions of equation (2.41) are double roots. For this particular case, one can check that the general solution of equation (2.38) becomes:

$$U_j = \begin{cases} a_1 + ja_2 & \text{when } \mu_\theta(\Omega) = 0 \\ (-1)^j(a_1 + ja_2) & \text{when } \mu_\theta(\Omega) = 4\epsilon^2 \end{cases}$$

This can be verified either by looking at the limiting behaviors of relations (2.43), (2.45) and (2.47), or by directly looking for a second solution of equation (2.38) in the form $U_j = jr^j$.

In the above relations, $\mathsf{K}^*$ represents a wave number and can be thought of as a function of the frequency $\Omega$ by using the second of the relations (2.41) into relations (2.42), (2.44) and (2.46).

### 2.2.3 Physical interpretation of the band gaps

Let us now describe more in details the three different behaviors (i), (ii) and (iii). The solution corresponds to propagating waves only in case (i). The two other cases (ii) and (iii) designate the band gaps. This result coincides with that of the BF approach (as one can check from condition (2.40)). Accordingly, band gaps are given by the intervals of $\Omega$ such that $\mu_\theta(\Omega) < 0$ or $\mu_\theta(\Omega) > 4\epsilon^2$.

The first condition is verified by the interval $\Omega_B = (1, \Omega_0 = 1 + 1/\theta)$ where the effective mass is negative (lighter blue band in figure 2.3). In this case, by using relation (2.37), one finds that masses $m_2$ move in phase opposition with respect to the motion of masses $m_1$. As frequencies in this interval are close to $\Omega = 1$, *i.e.* to the frequency of resonance of the internal resonators, this spectrum gap is thus generated by the local

resonances of the internal masses $m_2$, that inhibit the *global* movement of the external masses $m_1$.

Concerning the second condition, there exist two values of $\Omega$, say $\Omega_m$ and $\Omega_M$, such that $\mu_\theta(\Omega) = 4\epsilon^2$. Specifically, $\Omega_m$ and $\Omega_M$ are the two roots of the second degree equation

$$\theta\Omega^2 - (1 + \theta + 4\epsilon^2)\Omega + 4\epsilon^2 = 0 \tag{2.48}$$

and read:

$$\begin{cases} \Omega_m = \dfrac{1}{2\theta}\left(1 + \theta + 4\epsilon^2 - \sqrt{(1 + \theta - 4\epsilon^2)^2 + 16\epsilon^2}\right), \\ \Omega_M = \dfrac{1}{2\theta}\left(1 + \theta + 4\epsilon^2 + \sqrt{(1 + \theta - 4\epsilon^2)^2 + 16\epsilon^2}\right). \end{cases} \tag{2.49}$$

The first root $\Omega_m$ belongs to the interval $(0, 1)$ and the second one $\Omega_M$ is greater than $\Omega_0$. When $\Omega = 1$, one sees directly in system (2.36) that $U_j = V_j = 0$ and no motion is possible. Hence, the band gaps correspond to the two intervals $\Omega_A = [\Omega_m, 1]$ and $\Omega_C = [\Omega_M, +\infty)$, shown in figure 2.3 respectively by the darker blue and gray bands. In this case, the external masses $m_1$ do not move in-phase; in particular, the motion of consecutive masses is in phase opposition. This means that for $\Omega \in \Omega_A$ and $\Omega_C$, the solution has the form of an attenuated wave that is trying to propagate throughout the system with a wave length two times the period of the chain. This coincides with the Bragg scattering condition, as it will be shown in the next subsection. Accordingly, band gaps from case (iii) above are to be interpreted as generated by Bragg reflections.

Let us note that, concerning the motion of masses $m_2$, one has to distinguish between $\Omega_A$ and $\Omega_C$ (relation (2.37) is again employed). When $\Omega \in \Omega_A$, masses $m_2$ move in-phase with masses $m_1$ and no local resonances are present. When $\Omega \in \Omega_C$, masses $m_2$ move out-of-phase with respect to masses $m_1$ (as for band gap $\Omega_B$) and it would seem that local resonances were present; nonetheless their motion is not generated by a resonant behavior, as frequencies $\Omega \in \Omega_C$ are far away from $\Omega = 1$ (*i.e.* from the frequency of resonance for the internal mass $m_2$). In particular, masses $m_2$ are kept in motion by masses $m_1$, but their movement do not cause the formation of the band gap, that is instead generated by a Bragg scattering mechanism.

To sum up, we report in figure 2.4 the motion of the masses composing the mass-in-mass chain at some significant frequencies.

### 2.2.4 On the Bragg scattering phenomenon

Let us give here a more detailed definition of what is meant by Bragg scattering. Bragg reflection (or Bragg scattering) refers to the condition for which electromagnetic waves can be selectively reflected from some atomic planes in crystal lattices. Specifically, let us consider for simplicity a $2D$ crystal as the one represented in figure 2.5, where black circles denote the atoms that compose the crystal and vertical dashed lines correspond to a family of parallel atomic planes. A plane wave inclined of an angle $\Phi$ with respect

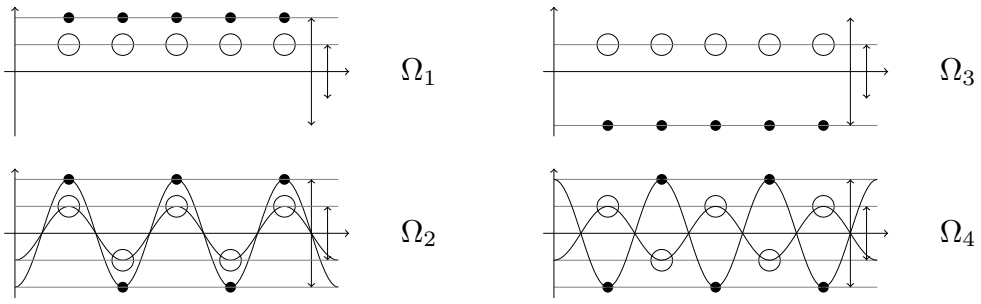


Figure 2.4: *Frames representing the motion of the masses $m_1$ (empty circles) and $m_2$ (black dots) at frequencies $\Omega_1 \approx 0$, $\Omega_2 \approx \Omega_m$, $\Omega_3 \approx \Omega_0$ and $\Omega_4 \approx \Omega_M$. Arrows denote the variation of the amplitudes of the fields $U_j$ and $V_j$ in time, for $j \in \mathbb{Z}$.*

to the horizontal is traveling through the crystals and is reflected by each atom. We identify a specific family of reflected waves with the angle $\Phi^*$ with the horizontal.

Bragg reflection can occur when:

- the angles $\Phi$ and $\Phi^*$ are equal;
- Waves reflected from two successive rows are in phase, such that:

$$d(A,0) + d(0,B) = 2\delta \cos\Phi = q\lambda \quad q \in \mathbb{N}^* \tag{2.50}$$

where $d(P1, P2)$ denotes the distance between points $P1$ and $P2$, $\delta$ is the distance between successive atomic planes and $\lambda$ is the wave length of the incoming wave (*cf.* figure 2.5).

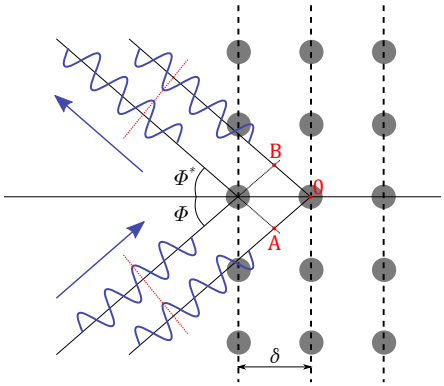


Figure 2.5: *Sketch of a crystal lattice. Black circles denote atoms. Dashed lines identify specific atomic planes. Incoming waves inclined of angle $\Phi$ and a reflected waves inclined of angle $\Phi^*$ are considered.*

Coming back to our problem, sufficiently far from the resonance condition of the inner resonators, masses $m_1$ can be seen as scatter elements in a background homogeneous material. Accordingly, the behavior of the mass-in-mass lattice resembles very much

that of a crystal under electromagnetic waves. In particular, for a 1D lattice of period $\delta = \ell$, the angle $\Phi$ in relation (2.50) is always null and thus Bragg scattering condition is verified whenever

$$2\ell = q\lambda \quad q \in \mathbb{N}^*.$$

The smallest $\lambda$ for which the above relation is verified is

$$\lambda = 2\ell,$$

that in our problem corresponds to a wave whose wave length is twice the period of the lattice.

In the work of Brillouin (1946), it is shown that a condition coinciding with Bragg's formula is indeed valid also for *continuous* materials with a periodic microstructure. The locally resonant behavior and a phenomenon similar to the Bragg scattering for elctromagnetic waves in crystals are thus the two mechanisms responsible for the formation of band gaps in the dynamics of phononic crystals and locally resonant materials.

### 2.2.5 Influence of the parameters of the problem

The dependence of $\Omega_m$, $\Omega_0$ and $\Omega_M$ on the two parameters $\epsilon$ and $\theta$ is studied respectively in figures 2.6 and 2.7. Each subfigure contains three curves representing the behavior of the three frequencies under consideration, in particular: $\Omega_m$ is indicated in red, $\Omega_0$ in blue and $\Omega_M$ in black. The filled areas denote instead the two band gaps previously defined. Two different colors have been used for the first band gap, in order to distinguish between the part of the band gap where the effective mass is positive (darker region) from that where it is negative (lighter region). In the following, we will refer to the lower part $\Omega_A$ and upper part $\Omega_B$ of the first band gap as "band gap A" and "band gap B", respectively.

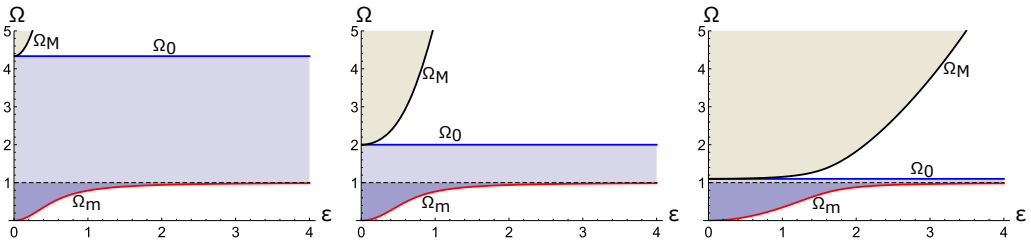


(a) $\theta = 0.3$. (b) $\theta = 1$. (c) $\theta = 10$.

Figure 2.6: *Dependence of $\Omega_m$ (in red), $\Omega_0$ (in blue) and $\Omega_M$ (in black) on $\epsilon$. The parameter $\theta$ is fixed to* 0.3 *(a),* 1 *(b) and* 10 *(c). Filled areas correspond to band gaps.*

As it is clear in both figures 2.6 and 2.7, the frequency $\Omega_0$ is independent from the ratio $\epsilon$ between the stiffnesses of the springs and decreases as the mass ratio $\theta$ increases. In particular, it is responsible for the width of band gap B. As stated before, this band

gap is indeed caused by the presence of local resonances. It is thus reasonable that, when $\theta$ is large, *i.e.* when the mass of the resonator $m_2$ is small with respect to $m_1$, the effect of the resonance is reduced, resulting in a thinner band gap B.

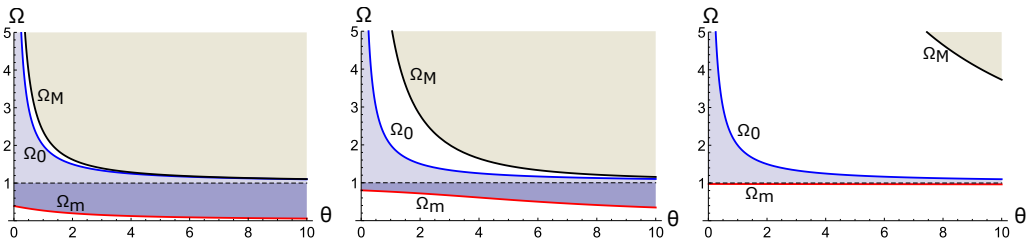


(a) $\epsilon = 0.4$. (b) $\epsilon = 1$. (c) $\epsilon = 3$.

Figure 2.7: *dependence of* $\Omega_m$ *(in red),* $\Omega_0$ *(in blue) and* $\Omega_M$ *(in black) on* $\theta$*. The parameter* $\epsilon$ *is fixed to* 0.4 *(a),* 1 *(b) and* 3 *(c). Filled areas correspond to band gaps.* $\Omega_0$ *is independent from* $\epsilon$*, hence the same curve appears in the three plots.*

Frequency $\Omega_m$ governs the width of band gap A. As specified before, the presence of this band gap is generated by a mechanism of Bragg scattering and it appears connected with a band gap coming from local resonances[1]. From figure 2.6, one can note that $\Omega_m$ tends to 1 as $\epsilon$ grows, causing the reduction of the width of band gap A: in the limit, band gap A vanishes. This can be explained as follows: increasing $\epsilon$, the stiffness $k_2$ of the internal resonator becomes smaller than $k_1$ and the system resembles very much a discrete version of a *locally resonant material* (LRM), whose dynamic response is well known to be governed by local resonances. The behavior of the frequency $\Omega_M$, responsible for the opening of the second band gap, confirms the last remark: its value increases with $\epsilon$, for a fixed $\theta$; therefore, the second band gap opens at higher frequencies and in the limit tends to disappear. If high values of the stiffness ratio $\epsilon$ were considered, as often done in the literature (see *e.g.* the works of Yao et al. (2008), Huang et al. (2009) and Kulkarni et al. (2016)), only this latter case is of interest.

The influence of the parameter $\theta$ on $\Omega_m$ is limited (see figure 2.7), especially for large values of $\epsilon$. $\Omega_M$, similarly to $\Omega_0$, decreases with $\theta$.

We have shown here that a mass-in-mass chain, whose usage is generally confined to the modeling of LRMs, is actually a metamaterial where Bragg scattering and local resonances can take place: if properly tuned, the lattice in figure 2.2 can thus be used to study systems governed by either one of the two wave canceling mechanisms or both. This justifies our choice of grouping PnCs and LRMs under the name of *metamaterials*.

[1]This feature is typical of the so-called "*hybrid metamaterials*" (HMs), where the phenomena of Bragg scattering and local resonance are coupled to enlarge the band gap width Kaina et al., 2013.

### 2.2.6 Asymptotic analysis

It is particularly interesting to discuss the structure of the stop and pass bands in the limit cases of $\epsilon$ tending to $\infty$ or $\epsilon$ tending to zero. The asymptotic behavior of $\Omega_m$ and $\Omega_M$ can be obtained directly from equation (2.48). When $\epsilon$ is large, the solution(s) of equation (2.48), denoted by $\Omega^\epsilon$, can be expanded as follows:

$$\Omega^\epsilon = \epsilon^2\Omega^{(2)} + \Omega^{(0)} + \epsilon^{-2}\Omega^{(-2)} + \cdots$$

and inserting into equation (2.48) gives:

$$\begin{cases} \Omega^{(2)}\left(\theta\Omega^{(2)} - 4\right) = 0 & \text{at the order of } \epsilon^4 \\ 2\theta\Omega^{(2)}\Omega^{(0)} - (1+\theta)\Omega^{(2)} - 4\Omega^{(0)} + 4 = 0 & \text{at the order of } \epsilon^2 \\ \theta{\Omega^{(0)}}^2 + 2\theta\Omega^{(2)}\Omega^{(-2)} - (1+\theta)\Omega^{(0)} - 4\Omega^{(-2)} = 0 & \text{at the order of } \epsilon^0 \end{cases}$$

The expansion of $\Omega_m$ corresponds to $\Omega^{(2)} = 0$ and hence

$$\Omega_m = 1 - \frac{1}{4\epsilon^2} + \cdots$$

whereas the expansion of $\Omega_M$ corresponds to $\Omega^{(2)} = 4/\theta$ and hence

$$\Omega_M = \frac{4\epsilon^2}{\theta} + \frac{1}{\theta} + \frac{1}{4\epsilon^2}\cdots$$

When $\epsilon$ goes to infinity, the first band gap tends to the interval $[1, \Omega_0]$ which corresponds to negative effective mass. One recovers the results obtained in the soft-in-stiff case, with band gaps generated by local resonances. In terms of the physical quantities, this (asymptotic) band gap is given by

$$\text{band gap in the soft-in-stiff case:} \quad \omega \in \left[\omega_2, \omega_2\sqrt{1 + \frac{m_2}{m_1}}\right].$$

When $\epsilon$ is small, $\Omega^\epsilon$ can be expanded as $\Omega^\epsilon = \Omega^{(0)} + \epsilon^2\Omega^{(2)} + \cdots$. Inserting it into equation (2.48) gives:

$$\begin{cases} \Omega^{(0)}\left(\theta\Omega^{(0)} - 1 - \theta\right) = 0 & \text{at the order of } \epsilon^0, \\ 2\theta\Omega^{(0)}\Omega^{(2)} - (1+\theta)\Omega^{(2)} - 4\Omega^{(0)} + 4 = 0 & \text{at the order of } \epsilon^2. \end{cases}$$

The expansion of $\Omega_m$ corresponds to $\Omega^{(0)} = 0$ and hence

$$\Omega_m = \frac{4\epsilon^2}{1+\theta} + \cdots,$$

whereas the expansion of $\Omega_M$ corresponds to $\Omega^{(0)} = 1 + 1/\theta = \Omega_0$ and hence

$$\Omega_M = 1 + \frac{1}{\theta} + \frac{4\epsilon^2}{\theta(1+\theta)} + \cdots.$$

Therefore, almost all frequencies are forbidden except two small intervals of allowed frequencies, the first close to 0 and the other to $\Omega_0$, see figure 2.6. In terms of the physical quantities, the allowed intervals are (approximately) given by

$$\text{first propagating band in the stiff-in-soft case:} \quad \omega \in \left(0, \frac{2\omega_1}{\sqrt{1+\dfrac{m_2}{m_1}}}\right),$$

$$\text{second propagating band:} \quad \omega - \omega_2\sqrt{1+\frac{m_2}{m_1}} \in \left(0, \frac{2\omega_1}{\sqrt{1+\dfrac{m_1}{m_2}}}\right).$$

In this case, band gaps are generated not only by local resonances (for which the effective mass is negative) but also by Bragg reflections of the propagating waves.

### 2.2.7 Comparison with the continuous model

Let us now consider the wave propagation in the one dimensional continuous counterpart of the discrete mass-in-mass chain. The continuous model can be thought of as the limit of the discrete one when the internal length is small with respect to the wave length. The Helmholtz equation in this case can be obtained by replacing in equation (2.36) the discrete differential operator $\Delta_j U$ by the second derivative with respect to the spatial variable $x$, obtaining

$$\epsilon^2 \ell^2 U''(x) + \mu_\theta(\Omega) U(x) = 0 \tag{2.51}$$

where $\ell$ is a characteristic length, which is introduced for dimensional reasons and is related to the size of the microstructure. The general solution of equation (2.51) depends on the sign of $\mu_\theta(\Omega)$: (i) if the effective mass is positive, then the general solution is sinusoidal in space; (ii) if the effective mass is negative, then the general solution is exponential in space. Therefore, the band gap is given by the interval $[1, \Omega_0]$, closure of the interval where the effective mass is negative, whatever the value of $\epsilon$. This result is completely different from that of the discrete model, especially for small values of $\epsilon$. The reason can be understood by considering the Bloch-Floquet approach.

Let us start from the discrete model. As previously stated, in the Bloch-Floquet approach the motion is searched in the form $U_{j+1} = U_j \exp\{\mathrm{i}\kappa\}$. Inserting this solution into equations (2.36) gives the dispersion equation (2.39), relating the frequency to the wave number. Therefore, at given $\kappa$, a solution exists for $\Omega$ only if $0 \leq \mu_\theta(\Omega) \leq 4\epsilon^2$.

If we consider now the continuous model (2.51) and motions of the form $U(x+\ell) = U(x)\exp\{\mathrm{i}\kappa\}$, the dispersion relation becomes

$$\epsilon^2 \kappa^2 = \mu_\theta(\Omega). \tag{2.52}$$

At given $\kappa \neq 0$ there exist two solutions for $\Omega$, one in the interval $(0, 1)$, the other in the interval $(\Omega_0, +\infty)$. When $\kappa$ goes from 0 to infinity, the two solutions describe those two intervals, therefore the (unique) band gap corresponds to the interval $[1, \Omega_0]$.

If we compare equation (2.39) with equation (2.52), it appears that equation (2.52) can be seen as an approximation of equation (2.39) for small values of $\kappa$. So the continuous model is a good representation of the discrete model for small wave numbers (large wave lengths) but not for small wave lengths. It should be used only when the ratio $\kappa/2\pi$ is small (with respect to 1). If it is used for any value of $\kappa$, there are some differences with the discrete model, that depend on $\epsilon$. Specifically, let us consider the two cases according to $\epsilon$ is large or small.

- *Large* $\epsilon$. In this case the whole interval $(0, +\infty)$ of the left hand side of equations (2.39) and (2.52) can be spanned by small values of $\kappa$ (for instance $\kappa \sim \epsilon^{-1/2}$). Hence, when $\epsilon$ goes to infinity both models give $[1, \Omega_0]$ as the band gap.

- *Small* $\epsilon$. For the discrete model, the left hand side of equation (2.39) remains small for any value of $\kappa$ and hence $\Omega$ must be close to the two roots of $\mu_\theta$. But for the continuous model, if one considers any value of $\kappa$, then the left hand side of equation (2.52) describes all the interval $(0, +\infty)$ even if $\epsilon$ is small and the band gap is still $[1, \Omega_0]$.

CHAPTER

# 3

# Effective description of continuous metamaterials

Chapter summary: *The asymptotic homogenization technique is applied to LRMs and relations enabling the calculation of the effective material properties are given. Cylindrical and spherical inclusions allow for the analytical derivation of the effective mass density, that can become negative in certain intervals of frequencies corresponding to band gaps. The results are then compared with numerical calculations carried out by exploiting the BF method.*

## Contents

We showed in chapter 2 how the concept of effective mass can be used for the description of the elastodynamic behavior of a discrete periodic structure. The generalization of this notion to the study of periodic composite materials is well known in the literature: when the size of the period is small compared to the characteristic length of the ongoing phenomenon, then the problem can be treated asymptotically to obtain a *macroscopic* description of the underlying microstructure. This procedure goes under the name of *homogenization theory*, whose objective (in mechanics) is thus that of deducing the *effective material properties* governing the macroscopic behavior of the composite. The term *homogenization* typically comes from the fact that the heterogeneous medium is replaced by a homogenized continuum.

Mathematically, defining an operator $\mathscr{L}^\varepsilon$ with spatially varying coefficients of period $\varepsilon$ such that

$$\mathscr{L}^\varepsilon u^\varepsilon = f \quad \text{in } \mathrm{V}^\varepsilon,$$

with $\mathrm{V}^\varepsilon$ being the periodic domain under consideration, the *homogenization process* consists in searching for the *homogenized solution* $u^0$ of the problem

$$\mathscr{L}^0 u^0 = f \quad \text{in } \mathrm{V},$$

in the limit case of $\varepsilon \to 0$. The operator $\mathscr{L}^0$ is what is called *homogenized operator*, whose coefficients are the *effective coefficients* (Bensoussan et al., 1978). The strength of this technique stands in the possibility to substitute a problem with microscopically heterogeneous coefficients, with one whose coefficients are homogeneous. For this reason, homogenization is an *upscaling method*.

There exist different methods to get the homogenized material properties. The requirement common to all the approaches is the existence of (at least) two scales that must be well separated, namely the *slow scale* of the physical mechanism under study and the *fast scale* associated to the microstructure of the domain.

A metamaterial appears to be composed of a repetition of a unit cell. Consequently, a sub-wavelength regime would fulfill the above requirement essential for the application of an upscaling method. In particular, we presented in chapter 2 the two physical mechanisms that generally take place in this class of materials and that are responsible for their peculiar behavior: while with Bragg scattering no scale separation exists, local resonances might be activated by a slowly varying propagating wave that sequentially interacts with the microstructure inside each unit cell. As previously stated for the mass-in-mass chain in figure 2.2, the first band gap is mainly generated by local resonances when the contrast between the stiffnesses of the external spring $k_1$ and the internal spring $k_2$ is high enough (large values of $\epsilon$)[1]. This suggests that homogenization methods could be effectively applied in continuous metamaterials composed of a matrix-inclusions

[1] In chapter 2, we used the letter $\epsilon$ to denote the ratio between the stiffnesses $k_1$ and $k_2$, whose value could be large or small. We instead employ $\varepsilon$ to indicate a small parameter of the problem.

configuration, providing that high contrast between the rigidity of the matrix and the inclusions is present. Specifically, the stiffer matrix has to be crossed by a propagating wave at low frequency (long wavelength) that interacts with the softer inclusions, initiating fast oscillations inside them and causing the formation of band gaps.

In this framework, the theory of *two-scales asymptotic expansion* is generally employed. This technique was first developed in the fundamental works of Bensoussan et al. (1978), Sanchez-Palencia (1980), and Bakhvalov et al. (1989) and later on reestablished for composite materials (and, in particular, for metamaterials) characterized by the presence of soft inclusions embedded in a stiffer matrix, respecting the condition previously specified (Auriault et al., 1985; Auriault et al., 2012). The method consists in considering a multiple scale perturbation of the field of interest, by construction of asymptotic expansions and by studying its limit behavior.

In this chapter, we aim to revisit the two-scale asymptotic expansion method for general three-dimensional LRMs, following the work and notations of Comi et al. (2020) and Comi et al. (2019). In particular, we consider LRMs that are composed of a matrix containing a periodic array of unconnected inclusions (bi-phase LRMs), that can themselves embed another inner inclusion unconnected with the outer matrix (three-phase LRMs).

Initially, we derive the definitions of the two effective material properties governing the elastodynamic behavior of the homogenized body, namely the *effective mass density* and the *effective stiffness tensor*. Part of these results are known from the literature (see *e.g.* Auriault et al. (2012)), especially concerning bi-phase LRMs. Nonetheless, here we proceed with a different point of view that allows us to point out some general properties of the dispersive behavior, such as the presence of flat bands, and of the effective mass density tensor, such as its symmetry and monotony. This latter property is important for the detection of band gaps in the spectrum of the propagation problem. To the best of the authors knowledge, these results are relatively new for the three-phase LRMs.

Eventually, we specialize the treatment for two-dimensional (2D) and three-dimensional (3D)[1] LRMs with respectively cylindrical and spherical inclusions, for which the effective mass density can be analytically derived and becomes negative at certain gaps of frequencies corresponding to band gaps. Finally, we show some results and compare them to numerical calculations.

Part of this chapter was the subject of the following publication: Comi et al., 2019.

[1] "2D" and "3D" are referred to the periodicity of the solid that is respectively in two and three dimensions.

## 3.1 Asymptotic homogenization of the elastodynamic problem for composite materials with inclusions

In this section we formally apply the two-scales asymptotic technique to derive the effective properties of composite materials. Specific requirements on the material and geometric properties of the composite must be fulfilled and are initially introduced. As stated before, part of these results are already existing in the literature. The scope here is to present our revisited treatment, particularized for the three-phase LRMs, and to argue on some general properties that characterize the effective mass density tensor, *i.e.* its symmetry and monotony. This latter feature being fundamental for the identification of band gaps.

### 3.1.1 Problem formulation

Let us consider the Y-periodic domain V presented in subsection 2.1.3, for $n = 2$ or 3. Its unit cell Y (shown in figure 3.1) is composed by a matrix $\mathrm{Y}_m$ and by one inclusion $\mathrm{Y}_c$ that *might* contain also another embedded inclusion $\mathrm{Y}_f$, that is not connected with the matrix. In this latter case, $\mathrm{Y}_c$ represents the coating of the inner inclusion (or fiber) $\mathrm{Y}_f$ (see figure 3.1). At this point, no restriction is placed on the shape of

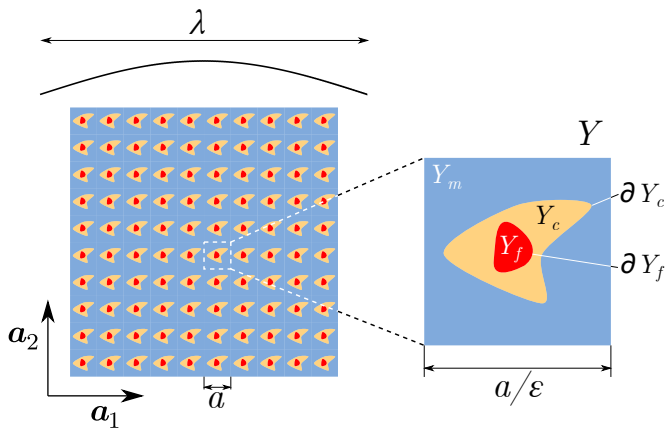


Figure 3.1: *A 2D three-phase periodic domain with a zoom over its unit cell. The 2D primitive basis* $\{\boldsymbol{a}_i\}_{i=\{1,2\}}$ *is given. The characteristic length* $\lambda$ *of the of the macroscopic phenomenon under study is such that* $\lambda \gg a$.

the inclusions. The matrix is connected between adjacent cells, while part $\mathrm{Y}_c$ is not connected with the matrix. All the components are supposed to be made of isotropic linearly elastic materials and perfectly bonded together. The interfaces matrix-inclusion and inclusion-inclusion (if present) are respectively denoted as $\partial\mathrm{Y}_c$ and $\partial\mathrm{Y}_f$. Here we

introduce the fast variable $\boldsymbol{y}$ to denote the points that compose V[1]. The medium is crossed by an incident elastic wave of wavelength $\lambda \gg a$, with $a = (\boldsymbol{a}_1 \wedge \boldsymbol{a}_2) \cdot \boldsymbol{a}_3$ being the macroscopic size of the unit cell Y. The above notation is shown in figure 3.1.

We look at the propagation of free waves in V, with a large wave length. To remain as much general as possible, the displacement field is supposed to have the same dimension $n$ of the domain V under consideration. The problem is thus characterized by the presence of two scales: a slow scale represented by the macroscopically (and periodically) varying phenomenon and a fast scale composed of the periodic repetition of the unit cells. Consequently, we can define a small parameter $\varepsilon = a/\lambda$ such that $\varepsilon \ll 1$.

We now consider the problem from a macroscopic point of view, therefore we scale the domain with $\varepsilon$ to obtain a $\varepsilon$Y-periodic body that we call $\mathrm{V}^\varepsilon$, with the superscript here used to explicitly take into account of this fact. More specifically, the superscript $\varepsilon$ is used to remind the dependence on this (small) parameter. We employ the variable $\boldsymbol{x} = \varepsilon \boldsymbol{y}$ to denote the points composing the domain $\mathrm{V}^\varepsilon$. We are interested in defining the spectrum of the homogeneous (*i.e.* with $\boldsymbol{F} = \boldsymbol{0}$) Helmholtz equation (2.8), that is here rewritten as:

$$\nabla \cdot \boldsymbol{\sigma}^\varepsilon(\boldsymbol{x}) + \omega^2 \rho^\varepsilon(\boldsymbol{x}) \boldsymbol{U}^\varepsilon(\boldsymbol{x}) = \boldsymbol{0} \quad \text{in } \mathrm{V}^\varepsilon. \tag{3.1}$$

For isotropic linearly elastic components and in harmonic regime, the constitutive relation (2.13) can be rewritten eliminating the time dependence as[2]:

$$\boldsymbol{\sigma}^\varepsilon(\boldsymbol{x}) = \boldsymbol{E}^\varepsilon(\boldsymbol{x}) \,:\, \boldsymbol{\varepsilon}^\varepsilon(\boldsymbol{x}) = \lambda^\varepsilon(\boldsymbol{x}) \operatorname{tr}(\boldsymbol{\varepsilon}^\varepsilon(\boldsymbol{x}))\, \boldsymbol{I} + 2\mu^\varepsilon(\boldsymbol{x}) \boldsymbol{\varepsilon}^\varepsilon(\boldsymbol{x}), \tag{3.2}$$

with

$$\boldsymbol{\varepsilon}^\varepsilon(\boldsymbol{x}) = \nabla \odot \boldsymbol{U}^\varepsilon(\boldsymbol{x}).$$

### 3.1.2 Scaling assumptions

The homogenization process through two-scales expansions is based on the decomposition of the original problem into different scales. The scaling of the geometrical and physical quantities is thus fundamental and can lead to different results depending on the assumptions made. In the work of Auriault et al. (1985) the authors show that local inertial phenomena can enormously affect the overall dynamic behavior of composites of the type shown in figure 3.1, when the inclusions $\mathrm{Y}_c$ are much softer than the matrix $\mathrm{Y}_m$. Specifically, this is predicted by the homogenization technique when the material properties respect the following relations:

$$\lambda^\varepsilon(\boldsymbol{x}) = \begin{cases} \lambda_m & \text{in } \mathrm{Y}_m^\varepsilon \\ \varepsilon^2 \lambda_c & \text{in } \mathrm{Y}_c^\varepsilon \end{cases}, \quad \mu^\varepsilon(\boldsymbol{x}) = \begin{cases} \mu_m & \text{in } \mathrm{Y}_m^\varepsilon \\ \varepsilon^2 \mu_c & \text{in } \mathrm{Y}_c^\varepsilon \end{cases}, \quad \rho^\varepsilon(\boldsymbol{x}) = \begin{cases} \rho_m & \text{in } \mathrm{Y}_m^\varepsilon \\ \rho_c & \text{in } \mathrm{Y}_c^\varepsilon \end{cases}, \tag{3.3}$$

[1] This change of notation with respect to section 2.1 is necessary to cope with the existing and consolidated literature: we are indeed here looking at the problem from a microscopic point of view.

[2] Note that letters $\boldsymbol{\sigma}$ and $\boldsymbol{\varepsilon}$ were used in subsection 2.1.1 for denoting stress and strain tensors varying both in space and time. For simplicity, we keep here the same notation, although stresses and strains are no more time dependent now.

where $\lambda_m$, $\mu_m$ and $\rho_m$ have the same order of magnitude of $\lambda_c$, $\mu_c$ and $\rho_c$, respectively.

Note that up to now we have made no hypotheses regarding the internal inclusion $\mathrm{Y}_f$. Nevertheless, with the aim of modeling a LRM, it is clear that the configuration with a resonant inclusion $\mathrm{Y}_f$ stiffer than the surrounding medium $\mathrm{Y}_c$ is the most suitable one. Therefore, we will assume that the elastic coefficients are at most one order higher than those of the inclusions $\mathrm{Y}_c$. Specifically, one has:

$$\lambda^\varepsilon(\boldsymbol{x}) = \varepsilon^{2-\ell}\lambda_f, \quad \mu^\varepsilon(\boldsymbol{x}) = \varepsilon^{2-\ell}\mu_f, \quad \rho^\varepsilon(\boldsymbol{x}) = \rho_f \quad \text{in } \mathrm{Y}_f^\varepsilon,$$

with $\ell \geq 1$, where $\lambda_f$, $\mu_f$ and $\rho_f$ have the same order of magnitude of $\lambda_c$, $\mu_c$ and $\rho_c$, respectively.

The precise scaling of the material properties (*i.e.* the value of $\ell$) will be specified later on. Note however that the inner parts $\mathrm{Y}_f$ of the inclusions $\mathrm{Y}_c$ need not to be present for the composite to behave like a LRM.

Concerning the geometric variables $\boldsymbol{x}$ and $\boldsymbol{y}$, they are related by $\boldsymbol{x} = \varepsilon\boldsymbol{y}$, as indicated in the previous subsection.

Throughout the entire chapter, we consider that frequencies $\omega$ are fixed and independent of $\varepsilon$.

### 3.1.3 Asymptotic expansions

Following the two-scales asymptotic method, the displacement and stress fields $\boldsymbol{U}^\varepsilon$ and $\boldsymbol{\sigma}^\varepsilon$ in equation 3.1 are classically expanded in the following form:

$$\begin{cases} \boldsymbol{U}^\varepsilon(\boldsymbol{x}) = \boldsymbol{U}^0(\boldsymbol{x}, \boldsymbol{x}/\varepsilon) + \varepsilon\boldsymbol{U}^1(\boldsymbol{x}, \boldsymbol{x}/\varepsilon) + \varepsilon^2\boldsymbol{U}^2(\boldsymbol{x}, \boldsymbol{x}/\varepsilon) + \dots \\ \boldsymbol{\sigma}^\varepsilon(\boldsymbol{x}) = \varepsilon^{-1}\boldsymbol{\sigma}^{-1}(\boldsymbol{x}, \boldsymbol{x}/\varepsilon) + \boldsymbol{\sigma}^0(\boldsymbol{x}, \boldsymbol{x}/\varepsilon) + \varepsilon\boldsymbol{\sigma}^1(\boldsymbol{x}, \boldsymbol{x}/\varepsilon) + \dots \end{cases}, \tag{3.4}$$

where the fields $\boldsymbol{U}^i(\boldsymbol{x}, \boldsymbol{x}/\varepsilon)$ and $\boldsymbol{\sigma}^i(\boldsymbol{x}, \boldsymbol{x}/\varepsilon)$ with $i \in \mathbb{Z}$ are obtained from the fields $\boldsymbol{U}^i(\boldsymbol{x}, \boldsymbol{y})$ and $\boldsymbol{\sigma}^i(\boldsymbol{x}, \boldsymbol{y})$, that are Y-periodic in the variable $\boldsymbol{y}$, whose domain of definition can be therefore restricted to the unit cell Y. This means that we are here postulating the existence of smooth functions $\boldsymbol{U}^i(\boldsymbol{x}, \boldsymbol{y})$ and $\boldsymbol{\sigma}^i(\boldsymbol{x}, \boldsymbol{y})$, defined in $(\mathrm{V} \times \mathrm{Y})$, $\mathrm{Y}-$*periodic* in the variable $\boldsymbol{y}$, such that for $\boldsymbol{y} = \boldsymbol{x}/\varepsilon$ the right-hand sides of relations (3.4) are asymptotic expansions of the corresponding left-hand sides. The upper-right indexes of the right-hand side terms denote their ordering in the expansion. Note that the expansion of the stress field starts from the order $-1$.

The whole idea of the two-scales expansion is to insert expressions (3.4) into equation (3.1) and to identify powers of $\varepsilon$ (Bensoussan et al., 1978). For simplifying the process, the usual "trick" consists in considering the spatial variables $\boldsymbol{x}$ and $\boldsymbol{y}$ as independent. In this way, the following derivation rule applies:

$$\frac{\partial(\bullet)}{\partial \boldsymbol{x}} \longrightarrow \frac{\partial(\bullet)}{\partial \boldsymbol{x}} + \varepsilon^{-1}\frac{\partial(\bullet)}{\partial \boldsymbol{y}}. \tag{3.5}$$

This is the reason why the expansion of the stress field starts a priori at order $-1$[1]. Accordingly, a generic function $\boldsymbol{f}(\boldsymbol{x},\boldsymbol{y})$ can be derived independently in the two variables. In particular, we will denote as $\nabla_{\boldsymbol{x}}\boldsymbol{f}$ and $\nabla_{\boldsymbol{x}}\cdot\boldsymbol{f}$ the gradient and divergence of $\boldsymbol{f}$ with respect to $\boldsymbol{x}$ and as $\nabla_{\boldsymbol{y}}\boldsymbol{f}$ and $\nabla_{\boldsymbol{y}}\cdot\boldsymbol{f}$ the gradient and divergence of $\boldsymbol{f}$ with respect to $\boldsymbol{y}$. Following this rule, we will call $\boldsymbol{\varepsilon}_{\boldsymbol{x}}(\boldsymbol{f})$ and $\boldsymbol{\varepsilon}_{\boldsymbol{y}}(\boldsymbol{f})$ the symmetric part of the gradients of $\boldsymbol{f}$ respectively with respect to $\boldsymbol{x}$ and $\boldsymbol{y}$.

### 3.1.4 Effective material description

Substituting the expansions (3.4) into the original Helmholtz equation (3.1) and expanding it as well in different powers of $\varepsilon$, the coefficients of the various powers must be zero, such that

$$\nabla_x\cdot\boldsymbol{\sigma}^i(\boldsymbol{x},\boldsymbol{y})+\nabla_y\cdot\boldsymbol{\sigma}^{i+1}(\boldsymbol{x},\boldsymbol{y})+\rho(\boldsymbol{y})\omega^2\boldsymbol{U}^i(\boldsymbol{x},\boldsymbol{y})=\boldsymbol{0}\quad\text{in Y},\tag{3.6}$$

with

$$\begin{cases}\boldsymbol{\sigma}^{j+p}(\boldsymbol{x},\boldsymbol{y})=\mathbf{E}^j(\boldsymbol{y})\,:\,(\boldsymbol{\varepsilon}_{\boldsymbol{x}}(\boldsymbol{U}^p)+\boldsymbol{\varepsilon}_{\boldsymbol{y}}(\boldsymbol{U}^{p+1})) & \text{in Y}\\ [\![\boldsymbol{U}^p(\boldsymbol{x},\boldsymbol{y})]\!]=\boldsymbol{0} & \text{on }\partial\mathrm{Y}_c,\,\partial\mathrm{Y}_f\\ [\![\boldsymbol{\sigma}^{j+p}(\boldsymbol{x},\boldsymbol{y})\cdot\boldsymbol{n}]\!]=\boldsymbol{0} & \text{on }\partial\mathrm{Y}_c,\,\partial\mathrm{Y}_f\\ \boldsymbol{U}^p(\boldsymbol{x},\boldsymbol{y})\quad\text{Y-periodic in }\boldsymbol{y} & \\ \boldsymbol{\sigma}^{j+p}(\boldsymbol{x},\boldsymbol{y})\cdot\boldsymbol{n}\quad\text{Y-antiperiodic in }\boldsymbol{y} & \end{cases}\tag{3.7}$$

and $(i,j,p)\in\mathbb{Z}$. More specifically, in equation (3.6), $i\geq-2$ defines the power of $\varepsilon$ considered and terms that are not part of expansions (3.4) are assumed to be equal to zero. In conditions (3.7), the following considerations apply:

- with the superscript $j$ in $\mathbf{E}^j$, we intend to denote the *fixed* scaling adopted for the elastic coefficient $\mathbf{E}$, as $\varepsilon\to0$;
- following the scaling of the stiffness parameters in subsection 3.1.2, $j\leq2$;
- from the expansion of the displacement field in 3.4, $p\geq-1$;
- with $\boldsymbol{n}$, unless specified differently, we intend to denote the unit normal vector that points outward with respect to the part under consideration.

Therefore, the stress field $\boldsymbol{\sigma}^q$ at a generic order $q\geq-1$ in equation (3.6) can be computed from the first of relations (3.7) as $\boldsymbol{\sigma}^{j+p}$, by using the corresponding index $p$ that is found as $p=q-j$, where $j$ is the fixed order of magnitude of the elastic constants.

In what follows, we derive the equation governing the motion of the homogenized body by starting from the lowest power of $\varepsilon$, that might be different for the different parts. For this reason, one should consider each domain separately, as we do in the following.

[1]This is true only for the matrix $\mathrm{Y}_m$ and, possibly, for part $\mathrm{Y}_f$; for the inclusion $\mathrm{Y}_c$, due to the scaling of its material coefficients, the expansion of the stresses starts from order 1.

### 3.1.5 The matrix $\mathrm{Y}_m$

- $i = -2$. Problem (3.6) becomes

$$\begin{cases} \nabla_{\boldsymbol{y}} \cdot \Big( \mathbf{E}_m \,:\, \boldsymbol{\varepsilon}_{\boldsymbol{y}}(\boldsymbol{U}^0) \Big) = \mathbf{0} & \text{in } \mathrm{Y}_m, \\ \boldsymbol{\sigma}^{-1}(\boldsymbol{x},\boldsymbol{y}) \cdot \boldsymbol{n} = \mathbf{0} & \text{on } \partial\mathrm{Y}_c, \\ \boldsymbol{U}^0(\boldsymbol{x},\boldsymbol{y}) \quad \mathrm{Y}\text{-periodic in } \boldsymbol{y}, \\ \boldsymbol{\sigma}^{-1}(\boldsymbol{x},\boldsymbol{y}) \cdot \boldsymbol{n} \quad \mathrm{Y}\text{-antiperiodic in } \boldsymbol{y}, \end{cases} \tag{3.8}$$

  that gives:

$$\boldsymbol{U}^0(\boldsymbol{x},\boldsymbol{y}) = \hat{\boldsymbol{U}}^0_m(\boldsymbol{x}) \quad \text{in } \mathrm{Y}_m. \tag{3.9}$$

- $i = -1$. Problem (3.6) becomes

$$\begin{cases} \nabla_{\boldsymbol{y}} \cdot \Big( \mathbf{E}_m \,:\, \Big( \boldsymbol{\varepsilon}_{\boldsymbol{x}}(\hat{\boldsymbol{U}}^0_m) + \boldsymbol{\varepsilon}_{\boldsymbol{y}}(\boldsymbol{U}^1) \Big) \Big) = \mathbf{0} & \text{in } \mathrm{Y}_m, \\ \boldsymbol{\sigma}^0(\boldsymbol{x},\boldsymbol{y}) \cdot \boldsymbol{n} = \mathbf{0} & \text{on } \partial\mathrm{Y}_c, \\ \boldsymbol{U}^1(\boldsymbol{x},\boldsymbol{y}) \quad \mathrm{Y}\text{-periodic in } \boldsymbol{y}, \\ \boldsymbol{\sigma}^0(\boldsymbol{x},\boldsymbol{y}) \cdot \boldsymbol{n} \quad \mathrm{Y}\text{-antiperiodic in } \boldsymbol{y}. \end{cases} \tag{3.10}$$

  The variable $\boldsymbol{x}$ plays the role of a parameter in the above problem (3.10). Therefore, by linearity, one can express $\boldsymbol{U}^1$ as:

$$\boldsymbol{U}^1(\boldsymbol{x},\boldsymbol{y}) = \sum_{k,h=1}^{n} \mathbf{w}^{kh}(\boldsymbol{y})\, \varepsilon_{\boldsymbol{x}[kh]}(\hat{\boldsymbol{U}}^0_m) + \hat{\boldsymbol{U}}^1(\boldsymbol{x}), \tag{3.11}$$

  where vectors $\mathbf{w}^{kh}$, with $k, h \in \{1, \dots, n\}$, are the solutions of the so-called *cell problem*:

$$\begin{cases} \nabla_{\boldsymbol{y}} \cdot \Big( \mathbf{E}_m \,:\, \boldsymbol{\varepsilon}_{\boldsymbol{y}}(\mathbf{w}^{kh}) \Big) = \mathbf{0} & \text{in } \mathrm{Y}_m, \\ \Big[ \mathbf{E}_m \,:\, \Big( \boldsymbol{e}_k \odot \boldsymbol{e}_h + \boldsymbol{\varepsilon}_{\boldsymbol{y}}(\mathbf{w}^{kh}) \Big) \Big] \cdot \boldsymbol{n} = \mathbf{0} & \text{on } \partial\mathrm{Y}_c, \\ \mathbf{w}^{kh}(\boldsymbol{y}) \quad \mathrm{Y}\text{-periodic in } \boldsymbol{y}, \\ \Big( \mathbf{E}_m \,:\, \boldsymbol{\varepsilon}_{\boldsymbol{y}}(\mathbf{w}^{kh}) \Big) \cdot \boldsymbol{n} \quad \mathrm{Y}\text{-antiperiodic in } \boldsymbol{y}. \end{cases} \tag{3.12}$$

  By applying the *Fredholm's alternative*[1], the above problem (3.12) admits a unique solution in the space $\mathcal{V}(\mathrm{Y})$ defined as:

$$\mathcal{V}(\mathrm{Y}) := \left\{ \boldsymbol{u} \in [H^1_{\#}(\mathrm{Y})]^n, \quad \int_{\mathrm{Y}} \boldsymbol{u}\, d\boldsymbol{y} = \mathbf{0} \right\}.$$

  Problem (3.12) needs to be solved numerically. Note that, up to this order, the problem coincides with the case when the inclusions $\mathrm{Y}_c$ and $\mathrm{Y}_f$ (if present) are substituted by a cavity: this comes from the fact that part $\mathrm{Y}_c$ is assumed to be much softer than part $\mathrm{Y}_m$.

[1] Its definition will be given later in the current section

- $i = 0$. Problem (3.6) becomes

$$\begin{cases} \nabla_{\boldsymbol{y}} \cdot \Big( \mathbf{E}_m \,:\, \Big( \boldsymbol{\varepsilon}_{\boldsymbol{x}}(\boldsymbol{U}^1) + \boldsymbol{\varepsilon}_{\boldsymbol{y}}(\boldsymbol{U}^2) \Big) \Big) + & \\ \quad \nabla_{\boldsymbol{x}} \cdot \Big( \mathbf{E}_m \,:\, \Big( \boldsymbol{\varepsilon}_{\boldsymbol{x}}(\hat{\boldsymbol{U}}^0_m) + \boldsymbol{\varepsilon}_{\boldsymbol{y}}(\boldsymbol{U}^1) \Big) \Big) + \rho_m \, \omega^2 \hat{\boldsymbol{U}}^0_m(\boldsymbol{x}) = \mathbf{0} & \text{in } \mathrm{Y}_m, \\ [\![ \boldsymbol{\sigma}^1(\boldsymbol{x}, \boldsymbol{y}) \cdot \boldsymbol{n} ]\!] = \mathbf{0} & \text{on } \partial \mathrm{Y}_c, \\ \boldsymbol{U}^1(\boldsymbol{x}, \boldsymbol{y}) \quad \mathrm{Y}\text{-periodic in } \boldsymbol{y}, & \\ \boldsymbol{\sigma}^1(\boldsymbol{x}, \boldsymbol{y}) \cdot \boldsymbol{n} \quad \mathrm{Y}\text{-antiperiodic in } \boldsymbol{y}. & \end{cases} \tag{3.13}$$

Problem (3.13) can be averaged over Y to obtain:

$$\underbrace{-\frac{1}{|\mathrm{Y}|} \int_{\partial \mathrm{Y}_c} \Big( \mathbf{E}_c \,:\, \boldsymbol{\varepsilon}_{\boldsymbol{y}}(\boldsymbol{U}^0) \Big) \cdot \boldsymbol{n} \, d\boldsymbol{\Gamma}}_{①} + \underbrace{\frac{1}{|\mathrm{Y}|} \int_{\mathrm{Y}_m} \sum_{k,h=1}^{n} \nabla_{\boldsymbol{x}} \cdot \Big( \mathbf{E}_m \,:\, \Big( \boldsymbol{e}_k \odot \boldsymbol{e}_h + \boldsymbol{\varepsilon}_{\boldsymbol{y}}(\mathbf{w}^{kh}) \Big) \, \varepsilon_{\boldsymbol{x}[kh]}(\hat{\boldsymbol{U}}^0_m) \Big) \, d\boldsymbol{y}}_{②} + \underbrace{\frac{1}{|\mathrm{Y}|} \int_{\mathrm{Y}_m} \rho_m \, \omega^2 \hat{\boldsymbol{U}}^0_m(\boldsymbol{x}) \, d\boldsymbol{y}}_{③} = \mathbf{0}, \tag{3.14}$$

where the divergence theorem, the continuity of stresses over $\partial \mathrm{Y}_c$ and relation (3.11) for $\boldsymbol{U}^1$ have been used.
While terms ② and ③ are "known" since they depend on $\hat{\boldsymbol{U}}^0_m$, term ① depends on the displacement field in the inclusion $\mathrm{Y}_c$ and can be computed after considering the motion of that part. This motion is strictly dependent on the presence of the inner inclusion. Let us thus consider separately the case with part $\mathrm{Y}_f$ (*three-phase LRM*) from the case without that part (*bi-phase LRM*).

### 3.1.6 Three-phase LRM: the inclusion $\mathrm{Y}_c \bigcup \mathrm{Y}_f$

It is convenient to determine first the behavior of the inner inclusion $\mathrm{Y}_f$ and then consider the motion of the outer inclusion $\mathrm{Y}_c$, that is influenced by the presence of the inner part.

#### The inner inclusion $\mathrm{Y}_f$

At the leading order, in the inner inclusion problem (3.6) becomes

$$\begin{cases} \nabla_{\boldsymbol{y}} \cdot \Big( \mathbf{E}_f \,:\, \boldsymbol{\varepsilon}_{\boldsymbol{y}}(\boldsymbol{U}^0) \Big) = \mathbf{0} & \text{in } \mathrm{Y}_f, \\ \boldsymbol{\sigma}^{1-\ell}(\boldsymbol{x}, \boldsymbol{y}) \cdot \boldsymbol{n} = \mathbf{0} & \text{on } \partial \mathrm{Y}_f, \end{cases} \tag{3.15}$$

with the order $\ell \geq 1$ depending on the scaling assumed in subsection 3.1.2. Let us call $\boldsymbol{y}_f$ the center of mass of part $\mathrm{Y}_f$. Solutions of the above problem (3.15) can be searched under the form:

$$\boldsymbol{U}^0(\boldsymbol{x},\boldsymbol{y}) = \hat{\boldsymbol{U}}^0_f(\boldsymbol{x}) + \hat{\mathbf{R}}^0_f(\boldsymbol{x}) \wedge (\boldsymbol{y}-\boldsymbol{y}_f) \quad \text{in } \mathrm{Y}_f, \tag{3.16}$$

where $\hat{\boldsymbol{U}}^0_f$ and $\hat{\mathbf{R}}^0_f$ are respectively the translation of the inner inclusion $\mathrm{Y}_f$ and the rotation of that same part with respect to its center of mass $\boldsymbol{y}_f$.

Note that, due to the scaling adopted, part $\mathrm{Y}_f$ moves as a rigid body for any $\ell \geq 1$. It is thus useful to express the *global* equilibrium equations for that part. According to relation (3.16), the linear momentum balance for part $\mathrm{Y}_f$ at the leading order reads

$$\rho_f\,\omega^2\,|\mathrm{Y}_f|\,\hat{\boldsymbol{U}}^0_f(\boldsymbol{x}) = \int_{\partial \mathrm{Y}_f} \boldsymbol{\sigma}^1(\boldsymbol{x},\boldsymbol{y})\cdot\boldsymbol{n}\,d\boldsymbol{\Gamma}, \tag{3.17}$$

while the angular momentum balance reads

$$\rho_f\,\omega^2\,\mathbf{I}_f\cdot\hat{\mathbf{R}}^0_f(\boldsymbol{x}) = \int_{\partial \mathrm{Y}_f} (\boldsymbol{y}-\boldsymbol{y}_f)\wedge\boldsymbol{\sigma}^1(\boldsymbol{x},\boldsymbol{y})\cdot\boldsymbol{n}\,d\boldsymbol{\Gamma}, \tag{3.18}$$

where $\boldsymbol{n}$ here denotes the inner unit normal to part $\mathrm{Y}_f$, $\mathbf{I}_f$ is the classical second-order tensor of inertia of part $\mathrm{Y}_f$, and $\boldsymbol{\sigma}^1$ is the stress field in part $\mathrm{Y}_c$ at order 1 that reads

$$\boldsymbol{\sigma}^1(\boldsymbol{x},\boldsymbol{y}) = \mathbf{E}_c \,:\, \boldsymbol{\varepsilon}_{\boldsymbol{y}}(\boldsymbol{U}^0).$$

In the above relations, we have used the continuity of the stresses on $\partial\mathrm{Y}_f$ to express the right-hand sides in terms of the stress field in part $\mathrm{Y}_c$.

The motion of the inner inclusion $\mathrm{Y}_f$ is still unknown and can be found only considering the behavior of the outer inclusion $\mathrm{Y}_c$.

### The outer inclusion $\mathrm{Y}_c$

Due to the chosen scaling, part $\mathrm{Y}_c$ enters in the problem only starting from order $i=0$.

We can obtain a problem in part $\mathrm{Y}_c$ by using the *global* equilibrium equations (3.17) and (3.18) for part $\mathrm{Y}_f$. At the leading order, using equation (3.6), the motion problem for the outer inclusion $\mathrm{Y}_c$ becomes: find $\boldsymbol{U}^0$ in part $\mathrm{Y}_c$ such that

$$\begin{cases} \nabla_{\boldsymbol{y}}\cdot\Big(\mathbf{E}_c \,:\, \boldsymbol{\varepsilon}_{\boldsymbol{y}}(\boldsymbol{U}^0)\Big) + \rho_c\,\omega^2\boldsymbol{U}^0(\boldsymbol{x},\boldsymbol{y}) = \mathbf{0} & \text{in } \mathrm{Y}_c, \\ \boldsymbol{U}^0(\boldsymbol{x},\boldsymbol{y}) = \hat{\boldsymbol{U}}^0_m(\boldsymbol{x}) & \text{on } \partial\mathrm{Y}_c, \\ \boldsymbol{U}^0(\boldsymbol{x},\boldsymbol{y}) = \hat{\boldsymbol{U}}^0_f(\boldsymbol{x}) + \hat{\mathbf{R}}^0_f(\boldsymbol{x})\wedge(\boldsymbol{y}-\boldsymbol{y}_f) & \text{on } \partial\mathrm{Y}_f, \\ \rho_f\,\omega^2\,|\mathrm{Y}_f|\,\hat{\boldsymbol{U}}^0_f(\boldsymbol{x}) = \displaystyle\int_{\partial\mathrm{Y}_f}\Big(\mathbf{E}_c \,:\, \boldsymbol{\varepsilon}_{\boldsymbol{y}}(\boldsymbol{U}^0)\Big)\cdot\boldsymbol{n}\,d\boldsymbol{\Gamma}, & \\ \rho_f\,\omega^2\,\mathbf{I}_f\cdot\hat{\mathbf{R}}^0_f(\boldsymbol{x}) = \displaystyle\int_{\partial\mathrm{Y}_f}(\boldsymbol{y}-\boldsymbol{y}_f)\wedge\Big[\Big(\mathbf{E}_c \,:\, \boldsymbol{\varepsilon}_{\boldsymbol{y}}(\boldsymbol{U}^0)\Big)\cdot\boldsymbol{n}\Big]\,d\boldsymbol{\Gamma}. & \end{cases} \tag{3.19}$$

In the above problem, $\hat{\boldsymbol{U}}_m$ is given and the boundary condition on $\partial \mathrm{Y}_f$ must be understood as follows: $\boldsymbol{U}^0$ is a rigid body displacement, but its translation and rotation parts are not known a priori, they will be given by using the two global equilibrium equations.

Solutions to problem (3.19), due to linearity, can be searched under the form:

$$\boldsymbol{U}^0(\boldsymbol{x},\boldsymbol{y}) = \sum_{h=1}^{n} \hat{U}^0_{m[h]}(\boldsymbol{x}) \left(\boldsymbol{e}_h + \mathbf{v}^h(\boldsymbol{y})\right) \quad \text{in } \partial \mathrm{Y}_c. \tag{3.20}$$

Using this transformation, problem (3.19) can be rewritten as: find $\mathbf{v}^h$, for $h \in \{1,\dots,n\}$, such that

$$\begin{cases} \nabla_{\boldsymbol{y}} \cdot \left(\mathbf{E}_c \,:\, \boldsymbol{\varepsilon}_{\boldsymbol{y}}(\mathbf{v}^h)\right) + \rho_c\, \omega^2 \left[\boldsymbol{e}_h + \mathbf{v}^h(\boldsymbol{y})\right] = \mathbf{0} & \text{in } \mathrm{Y}_c, \\ \mathbf{v}^h(\boldsymbol{y}) = \mathbf{0} & \text{on } \partial \mathrm{Y}_c, \\ \rho_f\, \omega^2\, |\mathrm{Y}_f|\, \hat{\boldsymbol{U}}^0_f(\boldsymbol{x}) = \hat{U}^0_{m[h]}(\boldsymbol{x}) \displaystyle\int_{\partial \mathrm{Y}_f} \left(\mathbf{E}_c \,:\, \boldsymbol{\varepsilon}_{\boldsymbol{y}}(\mathbf{v}^h)\right) \cdot \boldsymbol{n}\, d\boldsymbol{\Gamma}, \\ \rho_f\, \omega^2\, \mathbf{I}_f \cdot \hat{\mathbf{R}}^0_f(\boldsymbol{x}) = \hat{U}^0_{m[h]}(\boldsymbol{x}) \displaystyle\int_{\partial \mathrm{Y}_f} (\boldsymbol{y} - \boldsymbol{y}_f) \wedge \left[\left(\mathbf{E}_c \,:\, \boldsymbol{\varepsilon}_{\boldsymbol{y}}(\mathbf{v}^h)\right) \cdot \boldsymbol{n}\right] d\boldsymbol{\Gamma}, \\ \hat{\boldsymbol{U}}^0_f(\boldsymbol{x}) = \displaystyle\sum_{h=1}^{n} \hat{U}^0_{m[h]}(\boldsymbol{x}) \left(\boldsymbol{e}_h + \boldsymbol{U}(\mathbf{v}^h)\right), \quad \hat{\mathbf{R}}^0_f(\boldsymbol{x}) = \sum_{h=1}^{n} \hat{U}^0_{m[h]}(\boldsymbol{x}) \left(\mathbf{R}(\mathbf{v}^h)\right). \end{cases} \tag{3.21}$$

where $\boldsymbol{U}(\mathbf{v}^h)$ and $\mathbf{R}(\mathbf{v}^h)$ denote the translation and rotation of the (rigid) inner inclusion $\mathrm{Y}_f$ with respect to part $\mathrm{Y}_m$, associated with $\mathbf{v}^h$ and respecting the two global equilibrium equations of part $\mathrm{Y}_f$.

Let us now study the eigenvalue problem related to problem (3.21), namely: find $\mathbf{v}^*$ and $\omega$ such that

$$\begin{cases} \nabla_{\boldsymbol{y}} \cdot (\mathbf{E}_c \,:\, \boldsymbol{\varepsilon}_{\boldsymbol{y}}(\mathbf{v}^*)) + \rho_c \omega^2 \mathbf{v}^*(\boldsymbol{y}) = \mathbf{0} & \text{in } \mathrm{Y}_c, \\ \mathbf{v}^*(\boldsymbol{y}) = \mathbf{0} & \text{on } \partial \mathrm{Y}_c, \\ \exists \boldsymbol{U}(\mathbf{v}^*),\, \mathbf{R}(\mathbf{v}^*) \in \mathbb{R}^n \quad \text{such that:} & \\ \quad \mathbf{v}^*(\boldsymbol{y}) = \boldsymbol{U}(\mathbf{v}^*) + \mathbf{R}(\mathbf{v}^*) \wedge (\boldsymbol{y} - \boldsymbol{y}_f) \quad \text{on } \partial \mathrm{Y}_f, & \\ \quad \rho_f\, \omega^2\, |\mathrm{Y}_f|\, \boldsymbol{U}(\mathbf{v}^*) = \displaystyle\int_{\partial \mathrm{Y}_f} (\mathbf{E}_c \,:\, \boldsymbol{\varepsilon}_{\boldsymbol{y}}(\mathbf{v}^*)) \cdot \boldsymbol{n}\, d\boldsymbol{\Gamma}, & \\ \quad \rho_f\, \omega^2\, \mathbf{I}_f \cdot \mathbf{R}(\mathbf{v}^*) = \displaystyle\int_{\partial \mathrm{Y}_f} (\boldsymbol{y} - \boldsymbol{y}_f) \wedge [(\mathbf{E}_c \,:\, \boldsymbol{\varepsilon}_{\boldsymbol{y}}(\mathbf{v}^*)) \cdot \boldsymbol{n}]\, d\boldsymbol{\Gamma}, & \end{cases} \tag{3.22}$$

where the condition at the boundary $\partial \mathrm{Y}_f$ states that the motion there must be that of a rigid body, with $\boldsymbol{U}(\mathbf{v}^*)$ and $\mathbf{R}(\mathbf{v}^*)$ denoting its translational and rotational parts. Accordingly, the solution $\mathbf{v}^*$ of the above problem belongs to the set $\mathcal{V}$ of kinematically admissible displacement fields $\boldsymbol{v}$, such that:

$$\begin{aligned} \mathcal{V} = \{ &\boldsymbol{v}(\boldsymbol{y}) \in [H^1(\mathrm{Y}_c)]^n \,:\, \boldsymbol{v}(\boldsymbol{y}) = \mathbf{0} \text{ on } \partial \mathrm{Y}_c, \\ &\exists \boldsymbol{U}(\boldsymbol{v}),\, \mathbf{R}(\boldsymbol{v}) \in \mathbb{R}^n \,:\, \boldsymbol{v}(\boldsymbol{y}) = \boldsymbol{U}(\boldsymbol{v}) + \mathbf{R}(\boldsymbol{v}) \wedge (\boldsymbol{y} - \boldsymbol{y}_f) \text{ on } \partial \mathrm{Y}_f \}. \end{aligned}$$

So $\mathcal{V}$ is a linear space (close[1] subspace of $[H^1(\mathrm{Y}_c)]^n$ and, as such, Hilbert space with respect to the $H^1$ norm). At each element $\boldsymbol{v}$ of $\mathcal{V}$ is attached a translation $\boldsymbol{U}(\boldsymbol{v})$ and a rotation $\mathbf{R}(\boldsymbol{v})$ of the (rigid) inclusion $\mathrm{Y}_f$. Consequently, the motion $\boldsymbol{v}$ at the boundary $\partial\mathrm{Y}_f$ is a rigid displacement. The dependence of $\boldsymbol{U}(\boldsymbol{v})$ and $\mathbf{R}(\boldsymbol{v})$ on $\boldsymbol{v}$ is linear. Therefore, within the space $\mathcal{V}$ one looks for $\mathbf{v}^*$ and $\omega$ respecting, at the same time, the equation governing the eigenvalue problem and the two global equilibrium equations of the inner inclusion.

Let us look for the solutions of the eigenvalue problem (3.22) by using the *Rayleigh quotient* $J$ defined on $\mathcal{V}$ as follows:

$$\mathcal{V}\backslash 0 \ni \boldsymbol{v} \mapsto J(\boldsymbol{v}) = \frac{\displaystyle\int_{\mathrm{Y}_c} (\mathbf{E}_c \,:\, \boldsymbol{\varepsilon}_{\boldsymbol{y}}(\boldsymbol{v})) \,:\, \boldsymbol{\varepsilon}_{\boldsymbol{y}}(\boldsymbol{v})\, d\boldsymbol{y}}{\displaystyle\int_{\mathrm{Y}_c} \rho_c \boldsymbol{v}(\boldsymbol{y})\cdot\boldsymbol{v}(\boldsymbol{y})\, d\boldsymbol{y} + \rho_f\,|\mathrm{Y}_f|\,\boldsymbol{U}(\boldsymbol{v})\cdot\boldsymbol{U}(\boldsymbol{v}) + \rho_f(\mathbf{I}_f\cdot\mathbf{R}(\boldsymbol{v}))\cdot\mathbf{R}(\boldsymbol{v})}.$$

The following proposition holds true:

**Proposition.** *The eigenmodes* $\mathbf{v}^*$ *solutions of problem* (3.22) *are the stationary points of the Rayleigh quotient* $J$ *and the associated eigenfrequencies* $\omega$ *are given by the Rayleigh quotient of* $\mathbf{v}^*$*:*

$$J'(\mathbf{v}^*)(\boldsymbol{v}) = 0 \quad \forall \boldsymbol{v} \in \mathcal{V}, \qquad \omega^2 = J(\mathbf{v}^*),$$

*where* $J'(\mathbf{v}^*)(\boldsymbol{v})$ *stands for the directional derivative of* $J$ *at* $\mathbf{v}^*$ *in the direction* $\boldsymbol{v}$*.*

The prove is rather classical and is not given here (see *e.g.* Borthwick (2016)).

Exploiting the Rayleigh quotient, we can deduce that the *spectral theorem* applies, such that (see *e.g.* Dautray et al. (1990)):

1. The eigenvalues $\lambda_q = \omega_q^2$ are real and constitute an increasing sequence $(\omega_q)_{q\in\mathbb{N}^*}$ of positive eigenfrequencies that tends to infinity;
2. The eigenmodes $\mathbf{v}_q^*$ associated to an eigenfrequency $\omega_q$ constitute a linear space of finite dimension $\mathcal{E}_{\omega_q}$ (called eigenspace);
3. The family of all the eigenmodes constitutes an orthogonal basis (in the sense of the $[L^2(\mathrm{Y}_c)]^n$ inner product pondered by the mass or the stiffness of part $\mathrm{Y}_c$) of the space $\mathcal{V}$.

### 3.1.7 Bi-phase LRM: the inclusion $\mathrm{Y}_c$

As for the three-phase LRM, due to the chosen scaling, part $\mathrm{Y}_c$ enters in the problem only starting from order $i = 0$. Problem (3.6) can be rewritten as:

$$\begin{cases} \nabla_{\boldsymbol{y}}\cdot\Big(\mathbf{E}_c \,:\, \boldsymbol{\varepsilon}_{\boldsymbol{y}}(\boldsymbol{U}^0)\Big) + \rho_c\,\omega^2\boldsymbol{U}^0(\boldsymbol{x},\boldsymbol{y}) = \mathbf{0} & \text{in } \mathrm{Y}_c, \\ \boldsymbol{U}^0(\boldsymbol{x},\boldsymbol{y}) = \hat{\boldsymbol{U}}^0_m(\boldsymbol{x}) & \text{on } \partial\mathrm{Y}_c. \end{cases} \tag{3.23}$$

[1] It is indeed the closure of the space of infinitely differentiable functions with compact support in $\mathrm{Y}_c$ (functions $[C_0^\infty(\mathrm{Y}_c)]^n$) and respecting the condition on the boundary $\partial\mathrm{Y}_f$ given above.

Solutions to the above problem, due to linearity, can be searched again under the form (3.20), here rewritten for clarity:

$$\boldsymbol{U}^0(\boldsymbol{x},\boldsymbol{y}) = \sum_{h=1}^{n} \hat{U}^0_{m[h]}(\boldsymbol{x}) \left(\boldsymbol{e}_h + \mathbf{v}^h(\boldsymbol{y})\right) \quad \text{in } \partial \mathrm{Y}_c, \tag{3.24}$$

Following this transformation, problem (3.23) becomes: find $\mathbf{v}^h$, for $h \in \{1,\dots,n\}$, such that

$$\begin{cases} \nabla_{\boldsymbol{y}} \cdot \left(\mathbf{E}_c \,:\, \boldsymbol{\varepsilon}_{\boldsymbol{y}}(\mathbf{v}^h)\right) + \rho_c\,\omega^2 \left(\boldsymbol{e}_h + \mathbf{v}^h(\boldsymbol{y})\right) = \mathbf{0} & \text{in } \mathrm{Y}_c, \\ \mathbf{v}^h(\boldsymbol{y}) = \mathbf{0} & \text{on } \partial \mathrm{Y}_c. \end{cases} \tag{3.25}$$

The operator of problem (3.25) is compact and self-adjoint on $[H^1_0(\mathrm{Y}_c)]^n$. It follows that the so-called *spectral theorem*, whose results were listed in subsection 3.1.7 for the three-phase LRM, applies also for the bi-phase LRM, such that:

1. The eigenvalues $\lambda_q = \omega_q^2$ are real and constitute an increasing sequence $(\omega_q)_{q\in\mathbb{N}^*}$ of positive eigenfrequencies that tends to infinity;
2. The eigenmodes $\mathbf{v}^*_q$ associated to an eigenfrequency $\omega_q$ constitute a linear space of finite dimension $\mathcal{E}_{\omega_q}$ (called eigenspace);
3. The family of all the eigenmodes constitutes an orthogonal basis (in the sense of the $[L^2(\mathrm{Y}_c)]^n$ inner product pondered by the mass or the stiffness of part $\mathrm{Y}_c$) of the space $[H^1_0(\mathrm{Y}_c)]^n$.

### 3.1.8 Solution of the problem in part $\mathrm{Y}_c$

We are now in position to discuss about the existence and uniqueness of the solutions to problems (3.21) and (3.25). Specifically, one has the so-called *Fredholm's alternative*:

1. If $\omega$ is not an eigenfrequency ($\omega \neq \omega_q$ for any $q$), the solutions are unique;
2. If $\omega$ is an eigenfrequency whose eigenspace is orthogonal to the field $\boldsymbol{e}_h$ in $\mathrm{Y}_c$, with $h \in \{1,\dots,n\}$, a (non unique) solution defined up to an arbitrary eigenmode is admitted, otherwise no solutions exist.

Let us consider the physical meaning of these results. Problems (3.19) and (3.23) can be interpreted as follows: the motion of the inclusion relative to that of the matrix is activated by slowly varying translations of part $Y_m$, that can be understood as rigid at the microscale (*i.e.* locally). Eigenmodes of part $\mathrm{Y}_c$ alone for the bi-phase LRM and of part $\mathrm{Y}_c \cup \mathrm{Y}_f$ for the three-phase LRM, such that their corresponding displacement fields are perpendicular to (slowly varying) translations of parts $\mathrm{Y}_m$ cannot be "activated" by these (locally rigid) translations. Therefore, the unit cell does not experience internal resonances. These modes will correspond to so-called "*flat bands*" in the dispersion plot, as will be later shown.

A proof of the validity of Fredholm's alternative is here given for the three-phase LRM (a similar derivation applies also to the bi-phase case). For this, let us decompose the field $\mathbf{v}^h$ in problem (3.21) on the countable orthogonal basis given by the eigenmodes

$\mathbf{v}_q^*$ solutions of problem (3.22):

$$\mathbf{v}^h(\boldsymbol{y}) = \sum_{q=1}^{\infty} A_q \mathbf{v}_q^*(\boldsymbol{y}),$$

where $A_q$ denotes the $q$-th component in the mentioned basis.

Multiplying by $\mathbf{v}_q^*$ the equation in (3.21) that governs the motion in part $\mathrm{Y}_c$, integrating over $\boldsymbol{Y_c}$ and integrating by parts gives:

$$\begin{aligned}\int_{\mathrm{Y}_c} (\mathbf{E}_c \,:\, \boldsymbol{\varepsilon_y}(\mathbf{v}^h)) \,:\, \boldsymbol{\varepsilon_y}(\mathbf{v}_q^*)\, d\boldsymbol{y} = \omega^2 \rho_c \int_{\mathrm{Y}_c} \mathbf{v}^h(\boldsymbol{y}) \cdot \mathbf{v}_q^*(\boldsymbol{y})\, d\boldsymbol{y} + \omega^2 \rho_f \left|\mathrm{Y}_f\right| (\boldsymbol{e}_h \\ + \boldsymbol{U}(\mathbf{v}^h)) \cdot \boldsymbol{U}(\mathbf{v}_q^*) + \omega^2 \rho_f (\mathbf{I}_f \cdot \mathbf{R}(\mathbf{v}^h)) \cdot \mathbf{R}(\mathbf{v}_q^*) + \omega^2 \rho_c \boldsymbol{e}_h \cdot \int_{\mathrm{Y}_c} \mathbf{v}_q^*(\boldsymbol{y})\, d\boldsymbol{y}.\end{aligned}$$

From the orthogonality and the variational property of the eigenmodes, one has:

$$\begin{aligned}A_q \left(1 - \frac{\omega^2}{\omega_q^2}\right) \int_{\mathrm{Y}_c} (\mathbf{E}_c \,:\, \boldsymbol{\varepsilon_y}(\mathbf{v}_q^*)) \,:\boldsymbol{\varepsilon_y}(\mathbf{v}_q^*)\, d\boldsymbol{y} \\ = \omega^2 \boldsymbol{e}_h \cdot \left[\rho_f \left|\mathrm{Y}_f\right| \boldsymbol{U}(\mathbf{v}_q^*) + \rho_c \int_{\mathrm{Y}_c} \mathbf{v}_q^*(\boldsymbol{y})\, d\boldsymbol{y}\right].\end{aligned} \tag{3.26}$$

Let us note that the term corresponding to an elastic energy in the above relation is always greater than zero due to the coercivity of this quadratic functional (*cf.* assumptions (2.3)). We are now in position to discuss existence and uniqueness of problem (3.21):

1. $\omega$ is not an eigenfrequency: $A_q$ can be found and the solution is unique;
2. $\omega$ is an eigenfrequnecy (say $\omega = \omega_q$): the left-hand side of the above equation vanishes and thus also the right-hand side must vanish. Two cases can arise:
   - A the right-hand side vanishes: both the eigenmode $\mathrm{v}_q^*$ of part $\mathrm{Y}_c$ corresponding to $\omega_q$ and the rigid translation $\boldsymbol{U}(\mathbf{v}_q^*)$ of part $\mathrm{Y}_f$ due to this eigenmode are orthogonal to the constants, $A_q$ remains undetermined and the solution exists but is not unique,
   - B the right-hand side does not vanish: both the eigenmode $\mathrm{v}_q^*$ of part $\mathrm{Y}_c$ corresponding to $\omega_q$ and the rigid translation $\boldsymbol{U}(\mathbf{v}_q^*)$ of part $\mathrm{Y}_f$ due to this eigenmode are not orthogonal to the constants and the solution does not exist (besides the trivial solution $\hat{\boldsymbol{U}}_m^0 = 0$).

We found exactly the Fredholm's alternative. Let us note that the condition on the rigid translation $\boldsymbol{U}(\mathbf{v}_q^*)$ of part $\mathrm{Y}_f$ is absent when a bi-phase LRM is analyzed (indeed part $\mathrm{Y}_f$ is not present anymore). We thus found that it is "easier" for the three-phase case to fulfill the condition of non-existence of a solution to the problem. We anticipate here that this might correspond to an increase of the number of band gaps for a given frequency range.

A solution to problem (3.21), when it exists and is unique (point 1 above), can finally be written as:

$$\mathbf{v}^h(\boldsymbol{y}) = \sum_{q=1}^{\infty} \frac{\boldsymbol{e}_h \cdot \left[\rho_f \frac{|\mathrm{Y}_f|}{|\mathrm{Y}|}\boldsymbol{U}(\mathbf{v}_q^*) + \rho_c \left\langle \mathbf{v}_q^*(\boldsymbol{y})\right\rangle_c\right]}{\left\langle (\mathbf{E}_c \,:\, \boldsymbol{\varepsilon}_{\boldsymbol{y}}(\mathbf{v}_q^*)) \,:\, \boldsymbol{\varepsilon}_{\boldsymbol{y}}(\mathbf{v}_q^*)\right\rangle_c} \frac{\omega^2}{1-\dfrac{\omega^2}{\omega_q^2}} \mathbf{v}_q^*(\boldsymbol{y}), \tag{3.27}$$

where the series in the above relation converges in the $L^2$ norm, to be understood in the sense specified previously in the third point of the spectral theorem.

From relation (3.20), one obtains the displacement fields in part $\mathrm{Y}_c$ as:

$$\boldsymbol{U}^0(\boldsymbol{x},\boldsymbol{y}) = \hat{\boldsymbol{U}}^0_m(\boldsymbol{x}) \cdot [\boldsymbol{I} + \boldsymbol{\Upsilon}(\boldsymbol{y},\omega)] \quad \text{in } \mathrm{Y}_c, \tag{3.28}$$

with:

$$\boldsymbol{\Upsilon}(\boldsymbol{y},\omega) = \sum_{q=1}^{\infty} \frac{\mathbf{v}_q^*(\boldsymbol{y}) \otimes \left[\rho_f \frac{|\mathrm{Y}_f|}{|\mathrm{Y}|}\boldsymbol{U}(\mathbf{v}_q^*) + \rho_c \left\langle \mathbf{v}_q^*(\boldsymbol{y})\right\rangle_c\right]}{\left\langle (\mathbf{E}_c \,:\, \boldsymbol{\varepsilon}_{\boldsymbol{y}}(\mathbf{v}_q^*)) \,:\, \boldsymbol{\varepsilon}_{\boldsymbol{y}}(\mathbf{v}_q^*)\right\rangle_c} \frac{\omega^2}{1-\dfrac{\omega^2}{\omega_q^2}}. \tag{3.29}$$

Finally, when a solution to problem (3.21) exists and is unique, the global equilibrium equations (3.17) and (3.18) allow us to determine the rigid motion of part $\mathrm{Y}_f$.

As we stated before, a similar derivation applies also for the bi-phase LRM. In particular, one can find a solution $\boldsymbol{U}^0$ of problem (3.25), when it exists, from the solution given by relations (3.28) and (3.29) by considering $|\mathrm{Y}_f| = 0$. Clearly, the eigenvalues $\omega_q$ and the eigenmodes $\mathbf{v}_q^*$ will differ, in general, from those obtained for the three-phase LRM.

### 3.1.9 The effective material properties

#### Three-phase LRM

Let us go back to relation (3.14). Following the results from parts $\mathrm{Y}_c$ and $\mathrm{Y}_f$, term ① is now known. In particular, one obtains:

- *Term* ①.

$$\begin{aligned}
① &= -\left\langle \nabla_{\boldsymbol{y}} \cdot \left(\mathbf{E}_c \,:\, \boldsymbol{\varepsilon}_{\boldsymbol{y}}(\boldsymbol{U}^0)\right)\right\rangle_c + \frac{1}{|\mathrm{Y}|}\int_{\partial \mathrm{Y}_f} \left(\mathbf{E}_c \,:\, \boldsymbol{\varepsilon}_{\boldsymbol{y}}(\boldsymbol{U}^0)\right) \cdot \boldsymbol{n}\, d\boldsymbol{\Gamma} \\
&= \left\langle \rho_c\, \omega^2 \boldsymbol{U}^0(\boldsymbol{x},\boldsymbol{y})\right\rangle_c - \left\langle \nabla_{\boldsymbol{y}} \cdot \boldsymbol{\sigma}^1(\boldsymbol{x},\boldsymbol{y})\right\rangle_f \\
&= \left\langle \rho_c\, \omega^2 \boldsymbol{U}^0(\boldsymbol{x},\boldsymbol{y})\right\rangle_c + \left\langle \rho_f\, \omega^2 \boldsymbol{U}^0(\boldsymbol{x},\boldsymbol{y})\right\rangle_f
\end{aligned}$$

- *Term* ②.

$$② = \nabla_{\boldsymbol{x}} \cdot \left(\boldsymbol{E}^{eff} \,:\, \boldsymbol{\varepsilon}_{\boldsymbol{x}}(\hat{\boldsymbol{U}}^0_m)\right),$$

with $\mathbf{E}^{eff}$ being the *effective stiffness tensor* of the homogenized body, whose components $\mathsf{E}^{eff}_{[khij]}$ are given as

$$\mathsf{E}^{eff}_{[khij]} = \left\langle \left[ \mathbf{E}_m \,:\, \left( \boldsymbol{e}_k \odot \boldsymbol{e}_h + \boldsymbol{\varepsilon}_{\boldsymbol{y}}(\mathbf{w}^{kh}) \right) \right] \,:\, \left[ \boldsymbol{e}_i \odot \boldsymbol{e}_j + \boldsymbol{\varepsilon}_{\boldsymbol{y}}(\mathbf{w}^{ij}) \right] \right\rangle_m \tag{3.30}$$

In general, the homogenized material is not isotropic. Nevertheless, if some invariance hypotheses are assumed at the microscopic level, the homogenized material can present some symmetries, other than the *triclinic* symmetry inherited from the elastic tensor $\mathbf{E}_m$ (see *e.g.* Sanchez-Palencia et al. (1987) for more details).

- *Term* ③.

$$③ = \rho_m \, \omega^2 \, \frac{|\mathrm{Y}_m|}{|\mathrm{Y}|} \, \boldsymbol{I} \cdot \hat{\boldsymbol{U}}^0_m(\boldsymbol{x}).$$

The displacement field $\boldsymbol{U}^0(\boldsymbol{x}, \boldsymbol{y})$ in part $\mathrm{Y}_c$ is not defined for a set of frequencies $\omega$ that fulfills point 2B in the previous subsection. Accordingly, considering the two other cases in Fredholm's alternative, it is convenient here to rewrite the displacement field as

$$\boldsymbol{U}^0(\boldsymbol{x}, \boldsymbol{y}) = \sum_{h=1}^{n} \hat{U}^0_{m[h]}(\boldsymbol{x}) \tilde{\mathbf{v}}^h(\boldsymbol{y}), \tag{3.31}$$

where $\tilde{\mathbf{v}}^h(\boldsymbol{y}) = \boldsymbol{e}_h + \mathbf{v}^h(\boldsymbol{y})$. Problem (3.19) thus becomes:

$$\begin{cases} \nabla_{\boldsymbol{y}} \cdot \left( \mathbf{E}_c \,:\, \boldsymbol{\varepsilon}_{\boldsymbol{y}}(\tilde{\mathbf{v}}^h) \right) + \rho_c \, \omega^2 \tilde{\mathbf{v}}^h(\boldsymbol{y}) = \mathbf{0} & \text{in } \mathrm{Y}_c, \\ \tilde{\mathbf{v}}^h(\boldsymbol{y}) = \boldsymbol{e}_h & \text{on } \partial\mathrm{Y}_c, \\ \tilde{\mathbf{v}}^h(\boldsymbol{x}) = \boldsymbol{U}^h(\boldsymbol{x}) + \mathbf{R}^h(\boldsymbol{x}) \wedge (\boldsymbol{y} - \boldsymbol{y}_f) & \text{on } \partial\mathrm{Y}_f, \\ \rho_f \, \omega^2 \, |\mathrm{Y}_f| \, \boldsymbol{U}^h(\boldsymbol{x}) = \displaystyle\int_{\partial \mathrm{Y}_f} \left( \mathbf{E}_c \,:\, \boldsymbol{\varepsilon}_{\boldsymbol{y}}(\tilde{\mathbf{v}}^h) \right) \cdot \boldsymbol{n} \, d\boldsymbol{\Gamma}, & \\ \rho_f \omega^2 \, \mathbf{I}_{\boldsymbol{f}} \cdot \mathbf{R}^h(\boldsymbol{x}) = \displaystyle\int_{\partial \mathrm{Y}_f} (\boldsymbol{y} - \boldsymbol{y}_f) \wedge \left[ \left( \mathbf{E}_c \cdot \boldsymbol{\varepsilon}_{\boldsymbol{y}}(\tilde{\mathbf{v}}^h) \right) \cdot \boldsymbol{n} \right] \, d\boldsymbol{\Gamma}, & \end{cases} \tag{3.32}$$

where $\boldsymbol{U}^h(\boldsymbol{x})$ and $\mathbf{R}^h(x)$ are the rigid body translation and rotation of part $\mathrm{Y}_f$, such that

$$\hat{\boldsymbol{U}}^0_f(\boldsymbol{x}) = \sum_{h=1}^{n} \hat{U}^0_{m[h]}(\boldsymbol{x}) \boldsymbol{U}^h(\boldsymbol{x}), \quad \hat{\boldsymbol{R}}^0_f(\boldsymbol{x}) = \sum_{h=1}^{n} \hat{U}^0_{m[h]}(\boldsymbol{x}) \mathbf{R}^h(\boldsymbol{x}). \tag{3.33}$$

The problem above admits a unique solution when $\omega$ is not an eigenfrequency and a solution up to an element of the eigenspace when $\omega$ is an eigenfrequency.

The equation governing the motion of the homogenized body can finally be derived. Specifically, from problem (3.14) and considering the results above, one has:

$$\nabla_{\boldsymbol{x}} \cdot \left( \mathbf{E}^{eff}(\boldsymbol{x}) \,:\, \boldsymbol{\varepsilon}_{\boldsymbol{x}}(\hat{\boldsymbol{U}}^0_m) \right) = \omega^2 \boldsymbol{\rho}^{eff}(\omega) \cdot \hat{\boldsymbol{U}}^0_m(\boldsymbol{x}) \quad \text{in } \mathrm{Y}, \tag{3.34}$$

where $\boldsymbol{\rho}^{eff}$ is the *effective mass density tensor*, whose components are given by:

$$\rho^{eff}_{[ij]}(\omega) = \rho_m \frac{|\mathrm{Y}_m|}{|\mathrm{Y}|}\delta_{ij} + \frac{\rho_c}{|\mathrm{Y}|}\int_{\mathrm{Y}_c} \tilde{\mathrm{v}}^i_{[j]}(\boldsymbol{y})\, d\boldsymbol{y} + \rho_f \frac{|\mathrm{Y}_f|}{|\mathrm{Y}|} U^i_{[j]}(\boldsymbol{x}). \tag{3.35}$$

Let us note that the effective mass density is well defined even when $\tilde{\mathbf{v}}^i$ is given up to an eigenmode, due to the orthogonality of that eigenmode with respect to the constants (point 2A in the previous subsection).

#### Bi-phase LRM

When the inner inclusion $\mathrm{Y}_f$ is absent, only term ① of relation (3.14) is modified. In particular this term, for a bi-phase LRM, reads

$$① = \Big\langle \rho_c\, \omega^2 \boldsymbol{U}^0(\boldsymbol{x}, \boldsymbol{y}) \Big\rangle_c$$

Relation (3.34) is then still valid for this case, with the only difference that the effective mass density tensor is now given by

$$\rho^{eff}_{[ij]}(\omega) = \rho_m \frac{|\mathrm{Y}_m|}{|\mathrm{Y}|}\delta_{ij} + \frac{\rho_c}{|\mathrm{Y}|}\int_{\mathrm{Y}_c} \tilde{\mathrm{v}}^i_{[j]}(\boldsymbol{y})\, d\boldsymbol{y}. \tag{3.36}$$

### 3.1.10 Properties of the effective mass density

At this point, we make the choice to go on by studying the three-phase LRM. This latter case is indeed more involved with respect to the bi-phase LRM, whose effective material properties were still given in the previous subsection.

#### Symmetry

Let us prove that the second order tensor $\boldsymbol{\rho}^{eff}$ is symmetric. For this we consider the equation in problem (3.32) governing the motion of part $\mathrm{Y}_c$. Multiplying by $\tilde{\mathbf{v}}^j - \boldsymbol{e}_j$ and integrating over $\mathrm{Y}_c$ leads to:

$$\begin{aligned}\omega^2 \int_{\mathrm{Y}_c} \Big[ \rho_c \tilde{\mathbf{v}}^i(\boldsymbol{y}) \cdot \tilde{\mathbf{v}}^j(\boldsymbol{y}) - \frac{1}{\omega^2} (\mathbf{E}_c \,:\, \boldsymbol{\varepsilon}_{\boldsymbol{y}}(\tilde{\mathbf{v}}^i)) \,:\, \boldsymbol{\varepsilon}_{\boldsymbol{y}}(\tilde{\mathbf{v}}^j) \Big]\, d\boldsymbol{y} \\ + \rho_f \omega^2 |\mathrm{Y}_f|\, \boldsymbol{U}^i(\boldsymbol{x}) \cdot (\boldsymbol{U}^j(\boldsymbol{x}) - \boldsymbol{e}_j) + \rho_f \omega^2 (\mathbf{I}_f \cdot \mathbf{R}^i(\boldsymbol{x})) \cdot \mathbf{R}^j(\boldsymbol{x}) - \omega^2 \rho_c \int_{\mathrm{Y}_c} \tilde{\mathbf{v}}^i_j(\boldsymbol{y}) = 0,\end{aligned}$$

from which we can re-express the following term in relation (3.35)

$$\frac{\rho_c}{|\mathrm{Y}|}\int_{\mathrm{Y}_c} \tilde{\mathrm{v}}^i_{[j]}(\boldsymbol{y})\, d\boldsymbol{y} + \rho_f \frac{|\mathrm{Y}_f|}{|\mathrm{Y}|} U^i_{[j]}(\boldsymbol{x}).$$

The effective mass tensor (3.35) can thus be rewritten as

$$\begin{aligned}\rho^{eff}_{[ij]}(\omega) = \rho_m \frac{|\mathrm{Y}_m|}{|\mathrm{Y}|}\delta_{ij} + \rho_f \frac{|\mathrm{Y}_f|}{|\mathrm{Y}|}\boldsymbol{U}^i(\boldsymbol{x})\cdot\boldsymbol{U}^j(\boldsymbol{x}) + \frac{\rho_f}{|\mathrm{Y}|}(\mathbf{I}_f\cdot\mathbf{R}^i(\boldsymbol{x}))\cdot\mathbf{R}^j(\boldsymbol{x}) \\ + \left\langle\left[\rho_c\tilde{\mathbf{v}}^i(\boldsymbol{y})\cdot\tilde{\mathbf{v}}^j(\boldsymbol{y}) - \frac{1}{\omega^2}(\mathbf{E}_c : \boldsymbol{\varepsilon}(\tilde{\mathbf{v}}^i)) : \boldsymbol{\varepsilon}(\tilde{\mathbf{v}}^j)\right]\right\rangle_c .\end{aligned} \tag{3.37}$$

It follows that $\boldsymbol{\rho}^{eff}_{[ij]} = \boldsymbol{\rho}^{eff}_{[ji]}$. Let us note that the first four terms in the right-hand side of relation (3.37) are positive, the unique negative term comes from the elastic energy of part $\mathrm{Y}_c$.

### Monotony

Let us consider the case when $\omega$ is not an eigenfrequency. Then problem (3.19) admits a unique solution $\boldsymbol{U}^0(\boldsymbol{x},\boldsymbol{y})$ given by relation (3.28). Let us define the following function F of $\omega^2$, that will be useful later on for identifying band gaps:

$$\omega^2 \mapsto \mathrm{F}(\omega^2) = \omega^2 |\mathrm{Y}| \, (\boldsymbol{\rho}^{eff}\cdot\hat{\boldsymbol{U}}^0_m)\cdot\hat{\boldsymbol{U}}^0_m. \tag{3.38}$$

Using relations (3.31), (3.33), and (3.37), function F can be expressed as

$$\begin{aligned}\mathrm{F}(\omega^2) =& \omega^2\rho_m |\mathrm{Y}_m| \, \hat{\boldsymbol{U}}^0_m(\boldsymbol{x})\cdot\hat{\boldsymbol{U}}^0_m(\boldsymbol{x}) \\ &+ \omega^2\rho_f |\mathrm{Y}_f| \, \hat{\boldsymbol{U}}^0_f(\boldsymbol{x})\cdot\hat{\boldsymbol{U}}^0_f(\boldsymbol{x}) + \omega^2\rho_f(\mathbf{I}_f\cdot\hat{\boldsymbol{R}}^0_f(\boldsymbol{x}))\cdot\hat{\boldsymbol{R}}^0_f(\boldsymbol{x}) \\ &+ \int_{\mathrm{Y}_c}\left[\omega^2\rho_c\boldsymbol{U}^0(\boldsymbol{x},\boldsymbol{y})\cdot\boldsymbol{U}^0(\boldsymbol{x},\boldsymbol{y}) - (\mathbf{E}_c : \boldsymbol{\varepsilon}(\boldsymbol{U}^0)) : \boldsymbol{\varepsilon}(\boldsymbol{U}^0)\right] d\boldsymbol{y}.\end{aligned}$$

Let us study the monotony of this function.

For this, let us start by giving the variational problem associated to problem (3.19): find $\boldsymbol{U}^0 \in \mathcal{W}$ such that

$$\begin{aligned}&\int_{\mathrm{Y}_c}\left[(\mathbf{E}_c : \boldsymbol{\varepsilon}_{\boldsymbol{y}}(\boldsymbol{U}^0)) : \boldsymbol{\varepsilon}_{\boldsymbol{y}}(\boldsymbol{v}) - \omega^2\rho_c\boldsymbol{U}^0(\boldsymbol{x},\boldsymbol{y})\cdot\boldsymbol{v}(\boldsymbol{x},\boldsymbol{y})\right] d\boldsymbol{y} \\ &\quad = \omega^2\rho_f |\mathrm{Y}_f| \, \boldsymbol{U}(\boldsymbol{U}^0)\cdot\boldsymbol{U}(\boldsymbol{v}) + \omega^2\rho_f(\mathbf{I}_f\cdot\mathbf{R}(\boldsymbol{U}^0))\cdot\mathbf{R}(\boldsymbol{v}) \quad \forall\boldsymbol{v}(\boldsymbol{x},\boldsymbol{y}) \in \mathcal{W}_0.\end{aligned} \tag{3.39}$$

with

$$\begin{aligned}\mathcal{W} = \{\boldsymbol{v}(\boldsymbol{x},\boldsymbol{y}) \in &[H^1(\mathrm{Y}_c)]^n \, : \, \boldsymbol{v}(\boldsymbol{x},\boldsymbol{y}) = \hat{\boldsymbol{U}}^0_m(\boldsymbol{x}) \text{ on } \partial\mathrm{Y}_c, \\ &\exists\boldsymbol{U}(\boldsymbol{v}),\, \mathbf{R}(\boldsymbol{v}) \in \mathbb{R}^n \, : \, \boldsymbol{v}(\boldsymbol{x},\boldsymbol{y}) = \boldsymbol{U}(\boldsymbol{v}) + \mathbf{R}(\boldsymbol{v}) \wedge (\boldsymbol{y}-\boldsymbol{y}_f) \text{ on } \partial\mathrm{Y}_f\}, \\ \mathcal{W}_0 = \{\boldsymbol{v}(\boldsymbol{x},\boldsymbol{y}) \in &[H^1(\mathrm{Y}_c)]^n \, : \, \boldsymbol{v}(\boldsymbol{x},\boldsymbol{y}) = \mathbf{0} \text{ on } \partial\mathrm{Y}_c, \\ &\exists\boldsymbol{U}(\boldsymbol{v}),\, \mathbf{R}(\boldsymbol{v}) \in \mathbb{R}^n \, : \, \boldsymbol{v}(\boldsymbol{x},\boldsymbol{y}) = \boldsymbol{U}(\boldsymbol{v}) + \mathbf{R}(\boldsymbol{v}) \wedge (\boldsymbol{y}-\boldsymbol{y}_f) \text{ on } \partial\mathrm{Y}_f\}.\end{aligned}$$

The fields $\boldsymbol{U}(\boldsymbol{v})$ and $\mathbf{R}(\boldsymbol{v})$ denote the translation and rotation of the fiber, associated to the admissible field $\boldsymbol{v}$. Accordingly, $\boldsymbol{U}(\boldsymbol{U}^0) = \hat{\boldsymbol{U}}^0_f$ and $\mathbf{R}(\boldsymbol{U}^0) = \hat{\mathbf{R}}^0_f$.

When the displacement field $\hat{\boldsymbol{U}}^0_m$ is given, the quantities $\boldsymbol{U}^0$, $\hat{\boldsymbol{U}}^0_f$, and $\hat{\mathbf{R}}^0_f$ are smooth functions of $\omega^2$ (this can be directly checked for $\boldsymbol{U}^0$ by looking at relation (3.28): $\boldsymbol{U}^0$ is smoothly dependent from $\omega^2$, when it exists and is unique). The derivative $\partial\boldsymbol{U}^0/\partial\omega^2$ is thus the solution of the following variational problem, obtained by differentiating problem (3.39): find $\partial\boldsymbol{U}^0/\partial\omega^2 \in \mathcal{W}_0$ such that

$$\begin{aligned}\int_{\mathrm{Y}_c} \left[ \left( \mathsf{E}_c \,:\, \boldsymbol{\varepsilon}_{\boldsymbol{y}} \left( \frac{d\boldsymbol{U}^0}{d\omega^2} \right) \right) \,:\, \boldsymbol{\varepsilon}_{\boldsymbol{y}}(\boldsymbol{v}) - \omega^2 \rho_c \frac{d\boldsymbol{U}^0}{d\omega^2}(\boldsymbol{x},\boldsymbol{y}) \cdot \boldsymbol{v}(\boldsymbol{x},\boldsymbol{y}) \right] d\boldsymbol{y} \\ = \int_{\mathrm{Y}_c} \boldsymbol{U}^0(\boldsymbol{x},\boldsymbol{y}) \cdot \boldsymbol{v}(\boldsymbol{x},\boldsymbol{y})\, d\boldsymbol{y} + \rho_f \left|\mathrm{Y}_f\right| \boldsymbol{U}(\boldsymbol{U}^0) \cdot \boldsymbol{U}(\boldsymbol{v}) + \rho_f (\mathbf{I}_f \cdot \mathbf{R}(\boldsymbol{U}^0)) \cdot \mathbf{R}(\boldsymbol{v}) \\ + \omega^2 \rho_f \left|Y_f\right| \boldsymbol{U} \left( \frac{d\boldsymbol{U}^0}{d\omega^2} \right) \cdot \boldsymbol{U}(\boldsymbol{v}) + \omega^2 \rho_f \left( \mathbf{R} \left( \frac{d\boldsymbol{U}^0}{d\omega^2} \right) \right) \cdot \mathbf{R}(\boldsymbol{v}) \quad \forall \boldsymbol{v}(\boldsymbol{x},\boldsymbol{y}) \in \mathcal{W}_0.\end{aligned} \tag{3.40}$$

with

$$\frac{d\hat{\boldsymbol{U}}^0_f}{d\omega^2} = \boldsymbol{U}\left( \frac{d\boldsymbol{U}^0}{d\omega^2} \right), \quad \frac{d\hat{\boldsymbol{R}}^0_f}{d\omega^2} = \mathbf{R}\left( \frac{d\boldsymbol{U}^0}{d\omega^2} \right)$$

for linearity.

We are now in position to express the variation of the function $\mathrm{F}(\omega^2)$ as

$$\begin{aligned}\frac{d\mathrm{F}}{d\omega^2} =& \rho_m \left|\mathrm{Y}_m\right| \hat{\boldsymbol{U}}^0_m(\boldsymbol{x}) \cdot \hat{\boldsymbol{U}}^0_m(\boldsymbol{x}) + \rho_f \left|\mathrm{Y}_f\right| \hat{\boldsymbol{U}}^0_f(\boldsymbol{x}) \cdot \hat{\boldsymbol{U}}^0_f(\boldsymbol{x}) \\ &+ \rho_f (\mathbf{I}_f \cdot \hat{\boldsymbol{R}}^0_f(\boldsymbol{x})) \cdot \hat{\boldsymbol{R}}^0_f(\boldsymbol{x}) + \rho_c \int_{\mathrm{Y}_c} \boldsymbol{U}^0(\boldsymbol{x},\boldsymbol{y}) \cdot \boldsymbol{U}^0(\boldsymbol{x},\boldsymbol{y})\, d\boldsymbol{y} \\ &+ 2\rho_f \omega^2 \left|\mathrm{Y}_f\right| \hat{\boldsymbol{U}}^0_f(\boldsymbol{x}) \cdot \frac{d\hat{\boldsymbol{U}}^0_f}{d\omega^2}(\boldsymbol{x}) + 2\rho_f (\mathbf{I}_f \cdot \hat{\boldsymbol{R}}^0_f(\boldsymbol{x})) \cdot \frac{d\hat{\boldsymbol{R}}^0_f}{d\omega^2}(\boldsymbol{x}) \\ &+ 2 \int_{\mathrm{Y}_c} \left[ \omega^2 \rho_c \frac{d\boldsymbol{U}^0}{d\omega^2}(\boldsymbol{x},\boldsymbol{y}) \cdot \boldsymbol{U}^0(\boldsymbol{x},\boldsymbol{y}) - \left( \mathsf{E}_c \,:\, \boldsymbol{\varepsilon}_{\boldsymbol{y}} \left( \frac{d\boldsymbol{U}^0}{d\omega^2} \right) \right) \,:\, \boldsymbol{\varepsilon}_{\boldsymbol{y}}(\boldsymbol{U}^0) \right] d\boldsymbol{y} \end{aligned} \Bigg\} (\star)$$

where the term $(\star)$ vanishes as one can check by taking $\boldsymbol{v} = \partial\boldsymbol{U}^0/\partial\omega^2$ in equation (3.39). Accordingly, one has:

$$\begin{aligned}\frac{d\mathrm{F}}{d\omega^2} =& \rho_m \left|\mathrm{Y}_m\right| \hat{\boldsymbol{U}}^0_m(\boldsymbol{x}) \cdot \hat{\boldsymbol{U}}^0_m(\boldsymbol{x}) + \rho_f \left|\mathrm{Y}_f\right| \hat{\boldsymbol{U}}^0_f(\boldsymbol{x}) \cdot \hat{\boldsymbol{U}}^0_f(\boldsymbol{x}) \\ &+ \rho_f (\mathbf{I}_f \cdot \hat{\boldsymbol{R}}^0_f(\boldsymbol{x})) \cdot \hat{\boldsymbol{R}}^0_f(\boldsymbol{x}) + \rho_c \int_{\mathrm{Y}_c} \boldsymbol{U}^0(\boldsymbol{x},\boldsymbol{y}) \cdot \boldsymbol{U}^0(\boldsymbol{x},\boldsymbol{y})\, d\boldsymbol{y} \end{aligned} \Bigg\} \boxed{> 0}$$

Summing up, we found that F is increasing at each $\omega$ that is not an eigenfrequency. Moreover, F is continuous at the eigenfrequencies whose eigenspace is orthogonal to rigid translations and F is not definite at the other eigenfrequencies. Let us now study $\mathrm{F}(\omega)$ in the neighborhood of one of these eigenfrequencies. For this, let $\mathbf{v}^*_m$ be an eigenmode that is not orthogonal to the translations, such that

$$\left[ \rho_f \left|\mathrm{Y}_f\right| \boldsymbol{U}(\mathbf{v}^*_m) + \rho_c \int_{\mathrm{Y}_c} \mathbf{v}^*_m(\boldsymbol{y})\, d\boldsymbol{y} \right] \neq \mathbf{0}. \tag{3.41}$$

Let $\omega$ be close, but not equal, to $\omega_m$. Then $\boldsymbol{U}^0(\boldsymbol{x},\boldsymbol{y})$ in part $\mathrm{Y}_c$ is uniquely defined and, using the decomposition (3.20) reads:

$$\boldsymbol{U}^0(\boldsymbol{x},\boldsymbol{y}) = \hat{\boldsymbol{U}}^0_m(\boldsymbol{x}) + \sum_{q=1}^{\infty} A_q(\boldsymbol{x})\boldsymbol{v}^*_q(\boldsymbol{y}),$$

where $A_q(\boldsymbol{x})$ can be found by employing relation (3.26) as:

$$A_q(\boldsymbol{x})\left(1-\frac{\omega^2}{\omega_q^2}\right)\int_{\mathrm{Y}_c}(\mathsf{E}_c \,:\, \boldsymbol{\varepsilon}_{\boldsymbol{y}}(\mathbf{v}^*_q)) \,:\boldsymbol{\varepsilon}_{\boldsymbol{y}}(\mathbf{v}^*_q)\,d\boldsymbol{y} \\ = \omega^2\hat{\boldsymbol{U}}^0_m(\boldsymbol{x})\cdot\left[\rho_f\,|\mathrm{Y}_f|\,\boldsymbol{U}(\mathbf{v}^*_q)+\rho_c\int_{\mathrm{Y}_c}\mathbf{v}^*_q(\boldsymbol{y})\,d\boldsymbol{y}\right]. \tag{3.42}$$

Note that the term $\boldsymbol{e}_h$ in relation (3.26) is here substituted with $\hat{\boldsymbol{U}}^0_m(\boldsymbol{x})$. Inserting relation (3.35) for the effective mass in relation (3.38) of the function F, one obtains:

$$\mathrm{F}(\omega) = \rho_m\,|\mathrm{Y}_m|\,\omega^2\hat{\boldsymbol{U}}^0_m(\boldsymbol{x})\cdot\hat{\boldsymbol{U}}^0_m(\boldsymbol{x})+\rho_c\omega^2\int_{\mathrm{Y}_c}\boldsymbol{U}^0(\boldsymbol{x},\boldsymbol{y})\cdot\hat{\boldsymbol{U}}^0_m(\boldsymbol{x})\,d\boldsymbol{y} \\ +\rho_f\omega^2\,|\mathrm{Y}_f|\,\hat{\boldsymbol{U}}^0_f(\boldsymbol{x})\cdot\hat{\boldsymbol{U}}^0_m(\boldsymbol{x}).$$

The term $\hat{\boldsymbol{U}}^0_f(\boldsymbol{x})$ can be expressed by taking the translation part of the motion $\boldsymbol{U}^0(\boldsymbol{x},\boldsymbol{y})$ at the boundary $\partial\mathrm{Y}_f$ such that

$$\hat{\boldsymbol{U}}^0_f(\boldsymbol{x}) = \hat{\boldsymbol{U}}^0_m(\boldsymbol{x}) + \sum_{q=1}^{\infty} A_q(\boldsymbol{x})\boldsymbol{U}(\boldsymbol{v}^*_q).$$

Inserting this in the above relation for $\mathrm{F}(\omega^2)$, one gets:

$$\mathrm{F}(\omega^2) = \omega^2\left(\rho_m\,|\mathrm{Y}_m|+\rho_c\,|\mathrm{Y}_c|+\rho_f\,|\mathrm{Y}_f|\right)\hat{\boldsymbol{U}}^0_m(\boldsymbol{x})\cdot\hat{\boldsymbol{U}}^0_m(\boldsymbol{x}) \\ +\omega^2\sum_{q=1}^{\infty}A_q(\boldsymbol{x})\left[\int_{\mathrm{Y}_c}\rho_c\mathbf{v}^*_q\,d\boldsymbol{y}+\rho_f\,|\mathrm{Y}_f|\,\boldsymbol{U}(\mathbf{v}^*_q)\right]\cdot\hat{\boldsymbol{U}}^0_m(\boldsymbol{x}).$$

All the terms in the above relation have a finite limit when $\omega$ tends to the eigenfrequency $\omega_m$ under consideration, except those terms which involve the eigenmodes not orthogonal to the translations, *i.e.* the $m$-th term in the sum. By using relation (3.42), this term reads

$$\frac{\omega^2}{1-\dfrac{\omega^2}{\omega_m^2}}\left[\int_{\mathrm{Y}_c}\rho_c\mathbf{v}^*_m\,d\boldsymbol{y}+\rho_f\,|\mathrm{Y}_f|\,\boldsymbol{U}(\mathbf{v}^*_m)\cdot\hat{\boldsymbol{U}}^0_m\right]^2\frac{1}{\displaystyle\int_{\mathrm{Y}_c}(\mathsf{E}_c \,:\, \boldsymbol{\varepsilon}(\boldsymbol{v}^*_m)) \,:\boldsymbol{\varepsilon}(\boldsymbol{v}^*_m)},$$

from which we can conclude that $\mathrm{F}(\omega^2)\to+\infty$ when $\omega\to\omega_m^-$ and $\mathrm{F}(\omega^2)\to-\infty$ when $\omega\to\omega_m^+$.

Finally, when $\omega \to 0$, one has $\mathrm{F}(\omega^2) = 0$ and $\mathrm{F}(\omega^2)/\omega^2 = |\mathrm{Y}|\,\rho_{st}\hat{\boldsymbol{U}}^0_m(\boldsymbol{x}) \cdot \hat{\boldsymbol{U}}^0_m(\boldsymbol{x})$, with $\rho_{st}$ being the *equivalent static mass density* of the material, given by

$$\rho_{st} = \rho_m \frac{|\mathrm{Y}_m|}{|\mathrm{Y}|} + \rho_c \frac{|\mathrm{Y}_c|}{|\mathrm{Y}|} + \rho_f \frac{|\mathrm{Y}_f|}{|\mathrm{Y}|}.$$

The graph of F is given in figure 3.2, where the frequencies $\omega_m$ denote the eigenfrequencies whose corresponding eigenspace is not orthogonal to translations. The function F will thus monotonically increase from 0 to $+\infty$ between 0 and $\omega_1$; then it will monotonically increase from $-\infty$ to $+\infty$ between two subsequent eigenfrequencies $\omega_m$. The function will thus be negative in a family of intervals that we can call $I_m$.

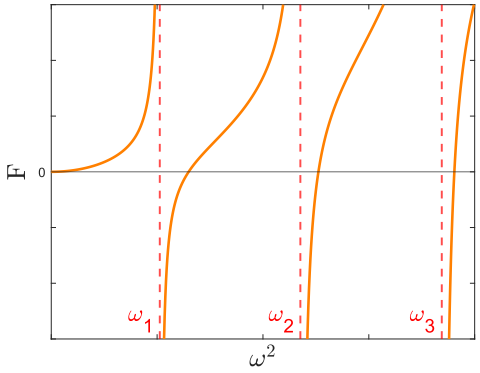


Figure 3.2: *Behavior of the function* $\mathrm{F}(\omega^2)$. *The frequency range is subdivided in intervals by the frequencies* $\omega_m$ *(vertical dashed lines) whose eigenspace is not orthogonal to translations. Inside each one of these intervals,* F *monotonically increases from* $-\infty$ *to* $+\infty$.

### Band gaps

Let us consider the effective equation of motion (3.34) for the homogenized material. As this problem governs the propagation of waves in an infinite homogeneous medium, the theory derived in section 2.1.1 can be applied and solutions are searched in the form of harmonic plane waves, such that:

$$\boldsymbol{u}^0(\boldsymbol{x}, t) = \hat{\mathbf{U}}^0_m \exp\{\mathrm{i}\,(\omega t + k\boldsymbol{p} \cdot \boldsymbol{x})\} \quad \text{in Y}.$$

It follows that

$$\hat{\boldsymbol{U}}^0_m = \hat{\mathbf{U}}^0_m \exp\{\mathrm{i}k\boldsymbol{p} \cdot \boldsymbol{x}\}.$$

Inserting this in equation (3.34) gives

$$k^2 \mathsf{E}^{eff}_{c[ijkh]}\, p_{[i]}\, p_{[k]}\, \hat{\mathrm{U}}^0_{m[h]} = \omega^2 \rho^{eff}_{[jh]}\, \hat{\mathrm{U}}^0_{m[h]}$$

that is the *dispersion relation* of the problem. Multiplying by $\hat{\mathrm{U}}^0_{m[j]}$ leads to

$$k^2 \mathsf{E}^{eff}_{c[ijkh]}\, p_{[i]}\, p_{[k]}\, \hat{\mathrm{U}}^0_{m[h]}\, \hat{\mathrm{U}}^0_{m[j]} = \omega^2 \rho^{eff}_{[jh]}\, \hat{\mathrm{U}}^0_{m[h]}\, \hat{\mathrm{U}}^0_{m[j]}.$$

The term $\boldsymbol{p} \cdot \mathbf{E}^{eff}_c \cdot \boldsymbol{p}$ can be identified with $\boldsymbol{\Gamma}$ given by relation (2.11), with $\mathbf{E}^{eff}_c$ instead of $\mathbf{E}_c$. moreover, the right-hand side of the above relation corresponds to $\mathrm{F}(\omega^2)$ with $\hat{\mathbf{U}}^0_m$ instead of $\hat{\boldsymbol{U}}^0_m(\boldsymbol{x})$. Since the quadratic form $\hat{\mathbf{U}}^0_m \cdot \boldsymbol{\Gamma} \cdot \hat{\mathbf{U}}^0_m$ in the left-hand side is positive definite, choosing a frequency $\omega$ at which the effective mass density tensor is defined, the above relation can be satisfied by a real wavenumber $k$ only if $\mathrm{F}(\omega^2) > 0$. This means that harmonic waves can only propagate for frequencies $\omega$ where $\mathrm{F}(\omega^2)$ is non-negative, *i.e.* not belonging to intervals $I_m$, with $m \in \mathbb{N}^*$. Consequently, these intervals correspond to pass bands.

It is fundamental here to remark that, by virtue of the basic symmetry properties of the elastic and mass density effective tensors, for a fixed frequency and a given direction $\boldsymbol{p}$ the corresponding eigenvectors $\hat{\mathbf{U}}^0_m$, defining the polarization of a wave, are orthogonal with each other. Nevertheless, they are generally neither parallel nor perpendicular to the direction $\boldsymbol{p}$ of propagation.

Note that, when $\mathrm{F}(\omega^2)$ tends to $+\infty$ (*i.e.* when it becomes very large), the homogenization is no more valid, as was shown in chapter 2 for the discrete mass-in-mass chain: the wavelengths at these frequencies become too short and the separation of scales is lost.

## 3.2 Analytic solutions for two cases with simple geometries

We now particularize the general results found in the previous section for a 2D and a 3D LRM, respectively presenting cylindrical and spherical inclusions. The shapes chosen for the inclusions enable for a closed form solution of problem (3.21). The frequency dependent effective mass density (3.35) can thus be analytically obtained. Some of these results will be used in chapter 4.

### 3.2.1 Out-of-plane waves in LRMs with cylindrical inclusions (2D LRMs)

Let us initially consider the LRM characterized by a 2D periodicity in the $x_1 - x_2$ plane (see figure 3.3). The cross-section of the three dimensional domain is denoted by $S$. We study the propagation of waves whose polarization is out-of-plane (*i.e.* along $x_3$) with respect to the plane of the periodicity. The displacement field has only one component in the third direction[1], that depends on coordinates $(x_1, x_2)$ (anti-plane strain condition), such that

$$\boldsymbol{U}^\varepsilon(\boldsymbol{x}) = U^\varepsilon(x_1, x_2)\boldsymbol{e}_3.$$

[1] With respect to the more general framework of subsection 3.1.1, we here consider a dimension for the space of the displacement field that is lower than that of the domain under consideration.

The non vanishing stress components are $\sigma^\varepsilon_{13} = \sigma^\varepsilon_{31}$ and $\sigma^\varepsilon_{23} = \sigma^\varepsilon_{32}$. Hence we will

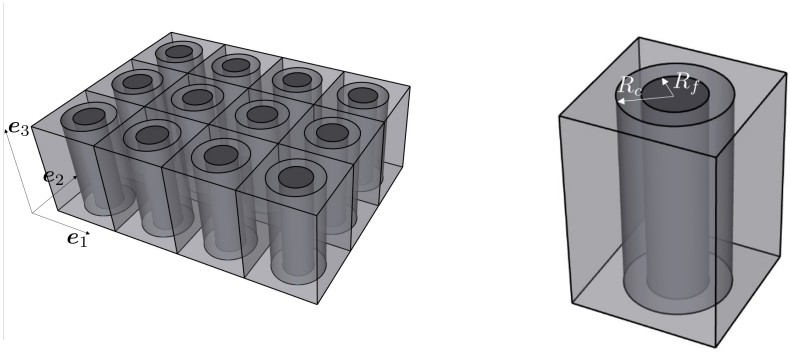


Figure 3.3: *Sketch of a three-phase LRM with cylindrical inclusions, together with its unit cell. The LRM has to be thought of as infinitely extended along direction* $\boldsymbol{e}_3$.

consider that the stress field is the vector field $\boldsymbol{\sigma}^\varepsilon(x_1, x_2) = (\sigma^\varepsilon_{31}(x_1, x_2), \sigma^\varepsilon_{32}(x_1, x_2))$, which is defined on $S$ and related to $U^\varepsilon$ by

$$\boldsymbol{\sigma}^\varepsilon(x_1, x_2) = \mu^\varepsilon \nabla(U^\varepsilon(x_1, x_2)).$$

We here fully derive the effective description for a three-phase LRM, whose unit cells Y are composed of parts $\mathrm{Y}_m$, $\mathrm{Y}_c$ and $\mathrm{Y}_f$. In particular, we consider parts $\mathrm{Y}_c$ and $\mathrm{Y}_f$ to be cylinders whose shared central axis is disposed along direction $x_3$. We call $R_c$ and $R_f$ ($R_c > R_f$) their radii (*cf.* figure 3.3).

In order to simplify the derivation (without loosing the attenuating capabilities of the composite), we consider part $\mathrm{Y}_f$ to be *rigid*. We also give the main results valid for the bi-phase case (see the work of Comi et al. (2020) for a detailed treatment).

To lighten the notation, we will refer to parts $\{\mathrm{Y}_m \times S,\ \mathrm{Y}_c \times S,\ \mathrm{Y}_f \times S\}$ and to boundaries $\{\partial\mathrm{Y}_c \times S,\ \partial\mathrm{Y}_f \times S\}$ respectively simply as $\{\mathrm{Y}_m,\ \mathrm{Y}_c,\ \mathrm{Y}_f\}$ and $\{\partial\mathrm{Y}_c,\ \partial\mathrm{Y}_f\}$.

### Eigenvalues of the inclusion $\mathrm{Y}_c$

Let us consider the eigenvalue problem (3.22), here specialized for out-of-plane waves in three-phase 2D LRMs, such that:

$$\begin{cases} \nabla_{\boldsymbol{y}} \cdot (\mu_c \,:\, \nabla_{\boldsymbol{y}}(\mathrm{v}^*(\boldsymbol{y}))) + \rho_c \omega^2 \mathrm{v}^*(\boldsymbol{y}) = 0 & \text{in } \mathrm{Y}_c, \\ \mathrm{v}^*(\boldsymbol{y}) = 0 & \text{on } \partial\mathrm{Y}_c, \\ \exists U(\mathrm{v}^*) \in \mathbb{R} \quad \text{such that:} & \\ \quad \mathrm{v}^*(\boldsymbol{y}) = U(\mathrm{v}^*) \quad \text{on } \partial\mathrm{Y}_f, & \\ \quad \rho_f\, \omega^2\, |\mathrm{Y}_f|\, U(\mathrm{v}^*) = \displaystyle\int_{\partial\mathrm{Y}_f} (\mu_c \nabla_{\boldsymbol{y}}(\mathrm{v}^*(\boldsymbol{y}))) \cdot \boldsymbol{n}\, d\boldsymbol{\Gamma} & \end{cases} \tag{3.43}$$

Note that the rotational degree of freedom of the inner inclusion $\mathrm{Y}_f$ is no more considered here since only out-of-plane displacements are allowed.

For the 2D cylindrical domain under study, a 2D cylindrical coordinate system is employed, such that:

$$\boldsymbol{y} = r\cos\theta\,\boldsymbol{e}_1 + r\sin\theta\,\boldsymbol{e}_2 \quad r \in [R_f, R_c],\ \theta \in [0, 2\pi].$$

Consequently, solutions to problem (3.43) are searched as

$$\mathbf{v}_n^*(\boldsymbol{y}) = (A_n\,J_n(kr) + B_n\,Y_n(kr))\exp\{\mathsf{i}\,(n\theta)\}, \quad n \in \mathbb{N} \tag{3.44}$$

where

$$k = \omega\sqrt{\rho_c/\mu_c} \tag{3.45}$$

is the (rescaled) wave number of part $\mathrm{Y}_c$, and $J_n$, $Y_n$ are the $n$-th Bessel functions respectively of the first and second kind.

The constants $A_n$ and $B_n$ have to be chosen in such a manner that the boundary conditions on $\partial\mathrm{Y}_c$ and $\partial\mathrm{Y}_f$ be satisfied, and the global equilibrium equation of the inner inclusion $\mathrm{Y}_f$ be respected by the rigid translation $\boldsymbol{U}(\mathbf{v}^*)$. Accordingly, we have:

$$(A_n\,J_n(kR_c) + B_n\,Y_n(kR_c)) = 0 \quad n \in \mathbb{N},\ \forall\theta \tag{3.46}$$

and

$$\begin{aligned}(A_n\,J_n(kR_f) + B_n\,Y_n(kR_f))\exp\{\mathsf{i}\,(n\theta)\} &= U(\mathrm{v}_n^*) \quad n \in \mathbb{N},\ \forall\theta \\ \text{such that: } \rho_f\,\omega^2\,|\mathrm{Y}_f|\,U(\mathrm{v}_n^*) &= \underbrace{\int_{\partial\mathrm{Y}_f} (\mu_c\nabla_{\boldsymbol{y}}(\mathrm{v}_n^*(\boldsymbol{y})))\cdot\boldsymbol{n}\,d\boldsymbol{\Gamma}}_{(\star)}.\end{aligned} \tag{3.47}$$

Let us consider the integral $(\star)$. This term can be computed explicitly for the current case, such that:

$$(\star) = \begin{cases} 0 & \text{when } n \neq 0 \Rightarrow U(\mathrm{v}_n^*) = 0 \\ -2\pi\mu_c R_f k\,[A_0 J_1(kR_f) + B_0 Y_1(kR_f)] & \text{when } n = 0 \end{cases}.$$

We are interested in studying the orthogonality to translations of the modes $\mathrm{v}_n^*$ and of the associated translations $U(\mathrm{v}_n^*)$, *i.e.* condition (3.41). From the previous results, we found that the orthogonality condition is fulfilled only for $n \neq 0$. Specifically, for these cases, from the term $(\star)$ above one has $U(\mathrm{v}_n^*) = 0$. The corresponding eigenvalues can be obtained by imposing the boundary conditions (3.46) and (3.47), such that:

$$J_n(kR_c)Y_n(kR_f) - J_n(kR_f)Y_n(kR_c) = 0 \quad \forall n \neq 0. \tag{3.48}$$

Let us now derive the family of eigenvalues and eigenmodes corresponding to $n = 0$. Note that these eigenvalues correspond to the frequencies at which the effective mass

density is not defined and, consequently, will identify the opening frequencies of the band gaps. We will refer to this family of frequencies as $\{\omega_m\}_{m\in\mathbb{N}^*}$.

Specifically, one finds that the two boundary conditions (3.46) and (3.46) are satisfied for $n = 0$ only at those frequencies that verify

$$\begin{aligned} kR_f\rho_f \left(J_0(kR_c)Y_0(kR_f) - Y_0(kR_c)J_0(kR_f)\right) \\ + 2\rho_c \left(Y_0(kR_c)J_1(kR_f) - J_0(kR_c)Y_1(kR_f)\right) = 0. \end{aligned} \tag{3.49}$$

**Motion problem of part $\mathrm{Y}_c$**

Let us write the displacement field $U^0(\boldsymbol{x}, \boldsymbol{y})$ of the inclusion $\mathrm{Y}_c$ as in relation (3.31), such that

$$U^0(\boldsymbol{x}, \boldsymbol{y}) = \hat{U}^0_m(\boldsymbol{x})\tilde{\mathrm{v}}(\boldsymbol{y})$$

Accordingly, the motion of the outer inclusion can be found by considering problem (3.32), that for the current case reads as:

$$\begin{cases} \nabla_{\boldsymbol{y}} \cdot (\mu_c \,:\, \nabla_{\boldsymbol{y}}(\tilde{\mathrm{v}})) + \rho_c\,\omega^2\tilde{\mathrm{v}}(\boldsymbol{y}) = 0 & \text{in } \mathrm{Y}_c, \\ \tilde{\mathrm{v}}(\boldsymbol{y}) = 1 & \text{on } \partial\mathrm{Y}_c, \\ \tilde{\mathrm{v}}(\boldsymbol{y}) = U(\tilde{\mathrm{v}}) & \text{on } \partial\mathrm{Y}_f, \\ \rho_f\,\omega^2\,|\mathrm{Y}_f|\,U(\tilde{\mathrm{v}}) = \displaystyle\int_{\partial\mathrm{Y}_f} (\mu_c \,:\, \nabla_{\boldsymbol{y}}(\tilde{\mathrm{v}})) \cdot \boldsymbol{n}\, d\boldsymbol{\Gamma}. \end{cases} \tag{3.50}$$

The above problem admits a unique solution whenever $\omega$ is not an eigenfrequency of problem (3.43). In particular, for these cases, one finds

$$\tilde{\mathrm{v}}(\boldsymbol{y}) = \tilde{\mathrm{v}}(r) = \frac{\begin{aligned} kR_f\rho_f \left(J_0(kr)Y_0(kR_f) - Y_0(kr)J_0(kR_f)\right) \\ + 2\rho_c \left(Y_0(kr)J_1(kR_f) - J_0(kr)Y_1(kR_f)\right) \end{aligned}}{\mathrm{den}}. \tag{3.51}$$

The denominator "den" is given by:

$$\begin{aligned} \mathrm{den} = kR_f\rho_f \left(J_0(kR_c)Y_0(kR_f) - Y_0(kR_c)J_0(kR_f)\right) \\ + 2\rho_c \left(Y_0(kR_c)J_1(kR_f) - J_0(kR_c)Y_1(kR_f)\right). \end{aligned} \tag{3.52}$$

Note that "den" is equal to the left-hand side of relation (3.49). This is not by coincidence, indeed whenever $\mathrm{den} = 0$, *i.e.* for frequencies $\omega \in \{\omega_m\}_{m\in\mathbb{N}^*}$ whose eigenspace is not orthogonal to rigid translations, problem (3.50) has no solutions and, as we will later show, the effective mass density is not defined. This results being in accordance with our findings from the general case (*cf.* subsection 3.1.10).

By using the global equilibrium of part $\mathrm{Y}_f$, one also finds the ratio between the displacements of the inner inclusion and the matrix, that reads as

$$\frac{\hat{U}^0_f(\boldsymbol{x})}{\hat{U}^0_m(\boldsymbol{x})} = \tilde{\mathrm{v}}(R_f) = \frac{2\rho_c \left(Y_0(kR_f)J_1(kR_f) - J_0(kR_f)Y_1(kR_f)\right)}{\mathrm{den}}. \tag{3.53}$$

Note that, when $\omega \in \omega_{q(n)}$, with $n \neq 0$ and $q \in \mathbb{N}^*$, then problem (3.50) admits a solution that is defined *up to an eigenmode* belonging to the eigenspace defined by the eigenfrequency under consideration. More specifically, for this case one has to superimpose the solution (3.51) and any vector belonging to the eigenspace $\mathcal{E}_{\omega_{q(n)}}$, associated to $\omega_{q(n)}$.

### The effective elastic tensor

For the case under consideration, the in-plane behavior is decoupled from the anti-plane behavior. Let us now consider the case of a square unit cell with a central circular inclusion[1] The homogenized material results to be orthotropic, the effective elastic tensor given by relation (3.30) being that of a *tetragonal* system (see *e.g.* Royer et al. (1996)). The anti-plane problem here considered is governed by a shear stiffness tensor $\boldsymbol{\mu}^{eff}$ give by

$$\mu_{ij}^{eff} = \left\langle \left[\mu_m \left(\boldsymbol{e}_i + \nabla_{\boldsymbol{y}} \mathrm{w}^i(\boldsymbol{y})\right)\right] \cdot \left(\boldsymbol{e}_j + \nabla_{\boldsymbol{y}} \mathrm{w}^j(\boldsymbol{y})\right) \right\rangle_m \quad i,j \in \{1,2\}, \tag{3.54}$$

where $\mathrm{w}^h$, with $h = \{1,2\}$, are the solutions of cell problems (3.12), that for the current case become: find $\mathrm{w}^h$, with $h = \{1,2\}$, such that

$$\begin{cases} \Delta_{\boldsymbol{y}} \cdot \mathrm{w}^h(\boldsymbol{y}) = 0 & \text{in } \mathrm{Y}_m, \\ \mu_m \left(\boldsymbol{e}_h + \nabla_{\boldsymbol{y}} \mathrm{w}^h(\boldsymbol{y}))\right) \cdot \boldsymbol{n} = 0 & \text{on } \partial \mathrm{Y}_c, \\ \mathrm{w}^h(\boldsymbol{y}) \quad \text{Y-periodic in } \boldsymbol{y}, & \\ \mu_m \left(\nabla_{\boldsymbol{y}} \mathrm{w}^h(\boldsymbol{y}))\right) \cdot \boldsymbol{n} \quad \text{Y-antiperiodic in } \boldsymbol{y}. & \end{cases} \tag{3.55}$$

The two problems above can be solved numerically. Specifically, when the tensor (3.54) is expressed with respect to a reference system whose axes are disposed along the two perpendicular axes of symmetry of part $\mathrm{Y}_m$, the effective mass tensor becomes a scalar tensor and the problem is governed by only one material coefficient $\mu^{eff} = \mu_{[11]}^{eff} = \mu_{[22]}^{eff}$.

### The effective mass density

From relation (3.35) the effective mass density for anti-plane waves is a scalar field $\rho^{eff}$, that can be written as:

$$\rho^{eff}(\omega) = \rho_m \frac{|\mathrm{Y}_m|}{|\mathrm{Y}|} + \rho_f \frac{|\mathrm{Y}_f|}{|\mathrm{Y}|} \frac{\hat{U}_f^0(\boldsymbol{x})}{\hat{U}_m^0(\boldsymbol{x})} + \langle \rho_c \mathrm{v}(r) \rangle_c \,, \tag{3.56}$$

where the last term can be explicitly computed using relation (3.51) as:

$$\langle \rho_c \mathrm{v}(r) \rangle_c = \frac{\rho_c}{|\mathrm{Y}|} (h(R_c) - h(R_f)),$$

[1] Inner and outer inclusions must be centered in the square cell.

with

$$h(r) = \frac{r}{k} \frac{\begin{array}{c} kR_f\rho_f \left(J_1(kr)Y_0(kR_f) - Y_1(kr)J_0(kR_f)\right) \\ + 2\rho_c \left(Y_1(kr)J_1(kR_f) - J_1(kr)Y_1(kR_f)\right) \end{array}}{\text{den}}.$$

As we anticipated earlier, we found that the effective mass is thus not defined for the frequencies $\omega$ which are roots of $\text{den} = 0$, *i.e.* corresponding to the family of eigenfrequencies $\{\omega_m\}_{m\in\mathbb{N}^*}$. It tends to $-\infty$ and $+\infty$ when $\omega$ tends to $\omega_m$ from above and from below, respectively. Therefore, $\rho^{eff}$ is negative in a countable set of frequency intervals $\{I_m\}_{m\in\mathbb{N}^*}$. The values of $\omega_m$, which fix the position of these intervals, depend only on the geometry and material properties of part $\mathrm{Y}_c$ through the non-dimensional groups $kR_f$ and $kR_c$ defined for the rescaled problem in Y. The corresponding real physical quantities in $\mathrm{Y}^\varepsilon$ are defined as

$$k^\varepsilon = \omega\sqrt{\frac{\rho_c}{\varepsilon^2\mu_c}}, \quad R_f^\varepsilon = \varepsilon R_f, \quad R_c^\varepsilon = \varepsilon R_c,$$

that give

$$k^\varepsilon R_f^\varepsilon = kR_f, \quad k^\varepsilon R_c^\varepsilon = kR_c.$$

Therefore, the frequencies intervals determined with the above analysis remain valid for the physical problem.

### Bi-phase 2D LRMs

Let us now consider a bi-phase LRM with cylindrical inclusion $\mathrm{Y}_c$. Part $\mathrm{Y}_f$ will thus be absent for this case.

From problem (3.23), utilizing Fredholm's alternative, unique solutions can be found whenever the frequency $\omega$ is not an eigenfrequency $\omega_q$ for the inclusion $\mathrm{Y}_c$ with fixed boundaries. More specifically, one has:

$$U^0(\boldsymbol{x},\boldsymbol{y}) = \frac{J_0(kr)}{J_0(kR_c)}\,\hat{U}_m^0(\boldsymbol{x}) \quad \text{in } \mathrm{Y}_c. \tag{3.57}$$

When $\omega = \omega_q$, if the associated eigenmode $\mathrm{v}_q^*$ is orthogonal to translations, then solution (3.57) is still valid up to a vector in the eigenspace $\mathcal{E}_{\omega_q}$ associated to $\omega_q$. Otherwise, problem (3.23) have no solutions different than the trivial one. More specifically, one finds that $\omega_q = \{\omega_{q(n)}\}_{q\in\mathbb{N}^*,\,n\in\mathbb{N}}$ are obtained from condition

$$J_n(kR_c) = 0 \quad \text{for } n \in \mathbb{N} \tag{3.58}$$

and that solutions to problem (3.23) exist (although defined up to an eigenmode) for $n \neq 0$.

Considering again the case of a square unit cell with a central circular inclusion, the effective shear modulus is still given by relation (3.54) and can be computed numerically. The frequency dependent effective mass density can be explicitly found, such that:

$$\rho^{eff}(\omega) = \rho_{st} + \rho_c \frac{|\mathrm{Y}_c|}{|\mathrm{Y}|}\frac{J_2(kR_c)}{J_0(kR_c)}, \tag{3.59}$$

where the equivalent static mass density $\rho_{st}$ is defined as:

$$\rho_{st} = \rho_m \frac{|\mathrm{Y}_m|}{|\mathrm{Y}|} + \rho_c \frac{|\mathrm{Y}_c|}{|\mathrm{Y}|}.$$

By studying the behavior of $\rho^{eff}(\omega)$, one finds that it is negative in a countable set of intervals, whose opening frequencies coincide with the eigenfrequencies $\omega_{q(0)}$, such that problem (3.23) have no solutions.

### 3.2.2 Free plane waves in LRMs with spherical inclusions (3D LRMS)

Let us now consider a LRM characterized by a 3D periodicity (see figure 3.4). The domain of the problem is thus V, with dimension $n = 3$, whose three-dimensional unit cells are Y. We here limit ourselves to the study of a bi-phase composite with parts $\mathrm{Y}_m$ and $\mathrm{Y}_c$. In particular, the inclusion $\mathrm{Y}_c$ is a sphere with radius $R_c$. We are interested in the propagation of plane waves. As in the previous section, we proceed

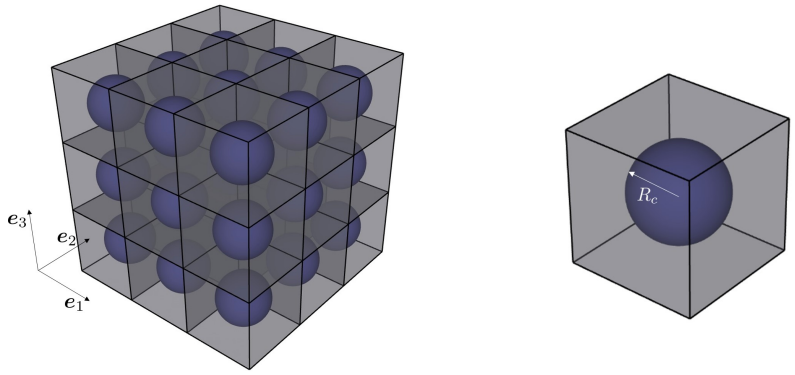


Figure 3.4: *Sketch of a bi-phase LRM with spherical inclusions, together with its unit cell.*

by first looking for the eigenvalues of part $\mathrm{Y}_c$ with fixed boundaries, then we find the solutions of problem (3.25) and finally we define the effective material coefficients of the homogenized LRM.

#### Eigenvalues of the inclusion $\mathrm{Y}_c$

Let us study the eigenvalue problem associated to problem (3.25). For the geometry here considered for part $\mathrm{Y}_c$, this corresponds to finding the eigenvibrations of a sphere with fixed boundaries. The eigenproblem can be rewritten as

$$\begin{cases} \mu_c \Delta \mathbf{v}^*(\boldsymbol{y}) + (\lambda_c + \mu_c) \nabla\nabla \cdot \mathbf{v}^*(\boldsymbol{y}) + \omega^2 \rho_c(\boldsymbol{y}) \mathbf{v}^*(\boldsymbol{y}) = \mathbf{0} & \text{in } \mathrm{Y}_c, \\ \mathbf{v}^* = \mathbf{0} & \text{on } \partial\mathrm{Y}_c \end{cases} \tag{3.60}$$

and, for spherical inclusions, it can be solved explicitly by employing a spherical coordinate system, such that:

$$\boldsymbol{y} = r\sin\theta\cos\varphi\,\boldsymbol{e}_1 + r\sin\theta\sin\varphi\,\boldsymbol{e}_2 + r\cos\theta\,\boldsymbol{e}_3 \quad r\in[0,R_c],\ \theta\in[0,\pi],\ \varphi\in[0,2\pi].$$

Solutions to problem (3.60) can thus be searched as

$$\mathbf{v}^*_{nm}(\boldsymbol{y}) = u_{r(nm)}(r,\theta,\varphi)\boldsymbol{e}_r + u_{\theta(nm)}(r,\theta,\varphi)\boldsymbol{e}_\theta + u_{\varphi(nm)}(r,\theta,\varphi)\boldsymbol{e}_\varphi, \tag{3.61}$$

where $\boldsymbol{e}_r$, $\boldsymbol{e}_\theta$ and $\boldsymbol{e}_\varphi$ are the unit vectors in the spherical coordinates system (see figure 3.4), and $u_{r(nm)}$, $u_{\theta(nm)}$ and $u_{\varphi(nm)}$, with $n\in\mathbb{Z}$ and $m\in\{-|n|,\dots,|n|\}$, are given in Appendix A1. By substitution of relation (3.61) in problem (3.60), a family of eigenvalues $\{\omega_{q(nm)}\}_{q\in\mathbb{N}^*}$ and corresponding eigenvectors $\mathbf{v}^*_{q(nm)}$ are then found by imposing the boundary condition on $\partial\mathrm{Y}_c$.

Following the discussion given in subsection 3.1.8, we are interested in studying the orthogonality of the eigenmodes $\mathbf{v}^*_{q(nm)}$ with respect to the constants. Due to the spherical symmetry of part $\mathrm{Y}_c$, the behavior of the inclusion will be the same whatever the direction of the locally rigid displacement imposed on the boundaries $\partial\mathrm{Y}_c$ will be. Therefore, we can reduce our study to the direction $\boldsymbol{e}_3$ (this choice slightly simplifies the treatment). The orthogonality condition becomes:

$$\int_{\mathrm{Y}_c} \mathbf{v}^*_{q(nm)}(\boldsymbol{y})\cdot\boldsymbol{e}_3 = 0. \tag{3.62}$$

In particular, we are interested in finding which are the eigenfrequencies $\omega_{q(nm)}$ of problem (3.60) whose corresponding eigenspace does not verify condition (3.62). One finds that condition (3.62) is not satisfied when $n=1$ and $m=0$. Details of the calculations are given in Appendix A1. Note that integration over $r$ of the eigenmodes such that $n=1$ and $m=0$ is missing and could make them orthogonal to the constants, as was found for the in-plane problem of 2D LRMs by Comi et al. (2020).

We are now in position to express the relation that determines the eigenfrequencies $\omega_{q(10)}$. The components of the associated eigenmodes $\mathbf{v}^*_{q(10)}$ can be rewritten as

$$\begin{cases} u_{r(10)}(r,\theta,\varphi) = \dfrac{1}{r}\left[\mathsf{A}U_1(k^\ell r) + \mathsf{C}U_3(k^s r)\right]\cos\theta, \\ u_{\theta(10)}(r,\theta,\varphi) = \dfrac{1}{r}\left[\mathsf{A}V_1(k^\ell r) + \mathsf{C}V_3(k^s r)\right](-\sin\theta) \\ u_{\varphi(10)}(r,\theta,\varphi) = \mathsf{B}V_2(k^s r)\sin\theta, \end{cases}$$

where all the terms in the above relations are outlined in the Appendix A1 and we just report here the relations defining the longitudinal wave number $k^\ell$ and the shear wave number $k^s$, such that

$$k^\ell = \sqrt{\frac{\omega}{c_\ell}}, \quad k^s = \sqrt{\frac{\omega}{c_s}},$$

with $c_\ell$ and $c_s$, being the longitudinal and shear wave speeds, given by relations (2.15).

By imposing the Dirichlet boundary condition of problem (3.60), one has to solve the following system of equations:

$$\begin{bmatrix} 1/R_c\, U_1(k^\ell R_c) & 0 & 1/R_c\, U_3(k^s R_c) \\ 1/R_c\, V_1(k^\ell R_c) & 0 & 1/R_c\, V_3(k^s R_c) \\ 0 & V_3(k^s R_c) & 0 \end{bmatrix} \begin{bmatrix} \mathsf{A} \\ \mathsf{B} \\ \mathsf{C} \end{bmatrix} = \mathbf{0}$$

Two classes of solutions exist, namely:

- *Class 1.* Coefficients $\mathsf{A}$ and $\mathsf{B}$ are equal to zero and the displacement field remains solenoidal (torsional eigenmodes). The eigenvalues can be found from:

$$V_2(k^s r) = 0. \tag{3.63}$$

- *Class 2.* Coefficient $\mathsf{B}$ is equal to zero and the irrotational and solenoidal parts of the displacement field are coupled (spheroidal eigenmodes). The eigenvalues can be found from:

$$U_1(k^\ell R_c)V_3(k^s R_c) - V_1(k^\ell R_c)U_3(k^s R_c) = 0. \tag{3.64}$$

When the properties of orthogonality of the eigenmodes with the translations is of concern, the eigenmodes belonging to the first class are perpendicular to the constants, as can be checked by applying relation (3.62). The eigenmodes $\mathbf{v}^*_{q(10)}$ that are not orthogonal to the constants must belong to the second class above. The corresponding eigenfrequencies $\omega_{q(10)}$ are found from relation (3.64) and can be expressed as follows:

$$\omega_{q(10)} = \zeta_q \frac{c_\ell}{R_c},$$

where $\zeta_q$ are dimensionless frequencies. Making this substitution in equation (3.64), one finds that the eigenfrequencies $\zeta_q$ depend only on the ratio $c$ between the longitudinal and shear wave velocities of part $\mathrm{Y}_c$, *i.e.* on its Poisson's coefficient $\nu_c$, such that:

$$c = \frac{c_\ell}{c_s} = \sqrt{\frac{2\,(1-\nu_c)}{1-2\nu_c}}.$$

**Motion problem of the inclusion $\mathrm{Y}_c$**

Let us recall that the motion of the inclusion $\mathrm{Y}_c$, *i.e.* the solution of problem (3.23), can be determined by using relation (3.24), obtaining problem (3.25), for $h \in \{1,2,3\}$. Solutions to this problem, when they exist and are unique, can be expressed as in relation (3.27), by posing $|\mathrm{Y}_f| = 0$, such that

$$\mathbf{v}^h(\boldsymbol{y}) = \sum_{q=1}^{\infty} \frac{\left\langle \boldsymbol{e}_h \cdot \mathbf{v}^*_q(\boldsymbol{y}) \right\rangle_c}{\left\langle \|\mathbf{v}^*_q\|^2 \right\rangle_c} \frac{\mathbf{v}^*_q(\boldsymbol{y})}{\dfrac{\omega_q^2}{\omega^2} - 1}, \tag{3.65}$$

where we have used the following relation

$$\int_{\mathrm{Y}_c} \left(\mathbf{E}_c \,:\, \boldsymbol{\varepsilon}_{\boldsymbol{y}}(\boldsymbol{v}_q^*)\right) \,:\, \boldsymbol{\varepsilon}_{\boldsymbol{y}}(\boldsymbol{v}_q^*)\, d\boldsymbol{y} = \rho_c \omega^2 \int_{\mathrm{Y}_c} \mathbf{v}_q^*(\boldsymbol{y}) \cdot \mathbf{v}_q^*(\boldsymbol{y})\, d\boldsymbol{y},$$

obtained by employing the divergence theorem and by imposing $\mathbf{v}_q^* = \mathbf{0}$ on $\partial \mathrm{Y}_c$. Exploiting the orthogonality to the constants of the eigenmodes previously studied, solutions can be found from relation (3.65) as:

$$\mathbf{v}^h(\boldsymbol{y}) = \sum_{q=1}^{\infty} \frac{\left\langle \boldsymbol{e}_h \cdot \mathbf{v}_{q(10)}^*(\boldsymbol{y}) \right\rangle_c}{\left\langle \|\mathbf{v}_q^{*10}(\boldsymbol{y})\|^2 \right\rangle_c} \frac{\mathbf{v}_{q(10)}^*(\boldsymbol{y})}{\frac{\omega_{q(10)}^2}{\omega^2} - 1}.$$

The tensor $\boldsymbol{\Upsilon}$ in (3.29) thus becomes:

$$\boldsymbol{\Upsilon}(\boldsymbol{y}, \omega) = \sum_{q=1}^{\infty} \frac{\mathbf{v}_{q(10)}^*(\boldsymbol{y}) \otimes \left\langle \mathbf{v}_{q(10)}^*(\boldsymbol{y}) \right\rangle_c}{\left\langle \|\mathbf{v}_{q(10)}^*(\boldsymbol{y})\|^2 \right\rangle_c} \frac{1}{\frac{\omega_{q(10)}^2}{\omega^2} - 1} \tag{3.66}$$

and the displacement field of part $\mathrm{Y}_c$ is known from relation (3.28).

### The effective elastic tensor

Relation (3.30) can be directly used to compute the effective material coefficients. When part $\mathrm{Y}_m$ is characterized by a cubic symmetry (as will be later the case), there will be only three independent components (Royer et al., 1996).

### The effective mass density

The effective mass density tensor (3.36) is finally obtained as:

$$\boldsymbol{\rho}^{eff}(\omega) = \rho_{st} \boldsymbol{I} + \langle \boldsymbol{\Upsilon}(\boldsymbol{y}, \omega) \rangle_c \,, \tag{3.67}$$

with

$$\rho_{st} = \rho_m \frac{|\mathrm{Y}_m|}{|\mathrm{Y}|} + \rho_c \frac{|\mathrm{Y}_c|}{|\mathrm{Y}|}.$$

We state here that the effective mass is a scalar tensor. To prove this, one has to consider the numerator of the term $\langle \boldsymbol{\Upsilon}(\boldsymbol{y}, \omega) \rangle_c$ in relation (3.67), that reads

$$\left\langle \mathbf{v}_{q(10)}^*(\boldsymbol{y}) \right\rangle_c \otimes \left\langle \mathbf{v}_{q(10)}^*(\boldsymbol{y}) \right\rangle_c = \left\langle \mathbf{v}_{q(10)}^*(\boldsymbol{y}) \cdot \boldsymbol{e}_i \right\rangle_c \left\langle \mathbf{v}_{q(10)}^*(\boldsymbol{y}) \cdot \boldsymbol{e}_j \right\rangle_c .$$

Therefore, for $\boldsymbol{\rho}^{eff}$ to be a scalar tensor, we must have that, if $\mathbf{v}_{q(10)}^*(\boldsymbol{y})$ is not orthogonal to a rigid translation along direction $\boldsymbol{e}_i$, then it must be orthogonal to rigid translations along directions $\boldsymbol{e}_j$, with $j \neq i$. This can be readily proved for direction $\boldsymbol{e}_3$: when $\mathbf{v}_{q(10)}^*(\boldsymbol{y})$ is not orthogonal to translations along this direction, then the integration over

$d\varphi$ in Appendix A1 is zero also for $m = 0$. This same consideration is valid for the other two perpendicular directions $\boldsymbol{e}_j$, with $j \neq 3$: we can indeed rotate the Cartesian coordinates so that one between the directions previously along $\boldsymbol{e}_j$, with $j \neq 3$, is now coincident to $\boldsymbol{e}_3$.

The effective mass density tensor $\boldsymbol{\rho}^{eff}$ can thus be expressed as:

$$\boldsymbol{\rho}^{eff}(\omega) = \rho^{eff}(\omega)\boldsymbol{I}.$$

The scalar function $\rho^{eff}$ is given by

$$\rho^{eff}(\omega) = \rho_{st} + \rho_c \frac{|\mathrm{Y}_c|}{|\mathrm{Y}|} \sum_{q=1}^{\infty} \Upsilon_q(\omega) \frac{1}{\frac{\omega_{q(10)}^2}{\omega^2} - 1}, \tag{3.68}$$

where

$$\Upsilon_q(\omega) = \frac{\left( \left\langle \mathbf{v}^*_{q(10)}(\boldsymbol{y}) \right\rangle_c \cdot \boldsymbol{e}_i \right)^2}{\left\langle \|\mathbf{v}^*_{q(10)}(\boldsymbol{y})\|^2 \right\rangle_c} \tag{3.69}$$

can be computed in a closed form (see Appendix A1), with $i$ that can take whatever value in $\{1, 2, 3\}$.

As for the 2D LRM, the effective mass is not defined for a countable set $\{\omega_{q(10)}\}_{q\in\mathbb{N}^*}$ of eigenfrequencies of part $\mathrm{Y}_c$, which are found from relation (3.64). The effective mass density $\rho^{eff}(\omega)$ again becomes negative in a set of frequency intervals $\{I_m\}_{m\in\mathbb{N}^*}$, whose position is fixed by $\omega_{q(10)}$. The width of these intervals depends only on the mass ratio between parts $\mathrm{Y}_m$ and $\mathrm{Y}_c$ and on the Poisson's coefficient $\nu_c$ of part $\mathrm{Y}_c$, as can be checked by noting that the dimensionless eigenfrequencies $\zeta_q$ remain the same also when the real physical quantities are used, since $c_\ell/R_c = c_\ell^\varepsilon/R_c^\varepsilon$.

## 3.3 Results from the homogenization technique

Following the results from the previous sections, we are now in position to study the propagation of mechanical waves by using the concept of *effective mass density tensor*. In particular, relations (3.56), (3.59) and (3.68) can be directly employed to study the dispersion plot of the three cases considered: whenever $\rho^{eff}(\omega)$ becomes negative, a band gap should appear. The prediction of band gaps can thus be compared to the results obtained by exploiting the Bloch-Floquet theory, introduced in chapter 2. Moreover, since a closed form expressions of $\rho^{eff}$ are found, one can easily perform parametric studies to evidence the influence of different geometries and/or materials on the wave propagation properties.

### 3.3.1 Comparison with Bloch-Floquet theory

As shown in chapter 2, the propagation of waves in periodic materials is often studied making use of the Bloch-Floquet theory solving the eigenvalues problem (2.28) for

the elementary cell, parametrized by the wave vector $\boldsymbol{k}$ considered. The continuous spectrum of the problem in the infinite periodic domain is thus obtained by "connecting" the discrete spectrum of these eigenvalues problems, for varying $\boldsymbol{k}$. The dispersion surfaces $\omega = \omega(\boldsymbol{k})$ can be numerically evaluated, *e.g.* by finite elements analyses (Åberg et al., 1997; Comi et al., 2018; Moscatelli et al., 2019).

Due to the periodicity and to the symmetries of the unit cell (if any), the description of the dynamic behavior of the metamaterial for all the possible wave vectors can be obtained by considering only the first "*Irreducible Brillouin Zone*" (IBZ) of the reciprocal lattice, that is a part of the FBZ (see subsection 2.1.3). Furthermore, often only the wave vectors along the boundary of the IBZ are considered (see *e.g.* the works of Kittel (2004) and Phani et al. (2006) for further details). We sketch in figure 3.5 the FBZ for the square and cubic unit cells here treated, together with their corresponding IFBZ path that will be followed to compute the dispersion relation using Bloch-Floquet approach. Band gaps appear in the dispersion diagrams as intervals of frequencies with

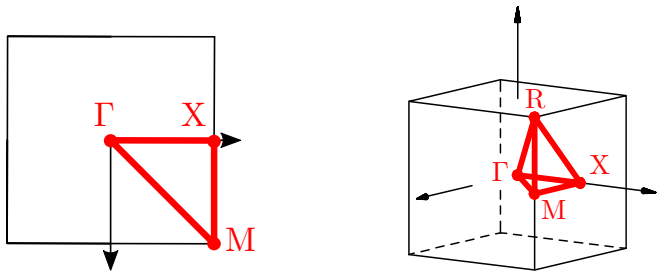


(a) (b)

Figure 3.5: *First Brillouin Zones (FBZs) for a square (a) and a cubic (b) unit cell. The corresponding paths followed along the IBZ are highlighted in red.*

no real solutions, *i.e.* as gaps in the spectrum of the problem under study.

In the work of Comi et al. (2020), it is proved (for the bi-phase case) that the asymptotic analysis of the Bloch-Floquet problem leads (at first order) to the same effective equation of motion obtained through the two scale homogenization methods. The two approaches therefore, in the low frequency range, give the same prediction of the band structure. In the following we illustrate these results for the bi- and three-phase LRM with two dimensional periodicity and for the bi-phase LRM with three dimensional periodicity.

The material parameters chosen are listed in table 3.1. As stated at the very beginning of the current chapter, the homogenization technique is based on the presence of two well-separated length scales, such that the wave length $\lambda_m$ of the wave propagating in part $\mathrm{Y}_m$ is larger than the characteristic size of the unit cell $a$. For this hypothesis to be fulfilled, one must have:

$$\frac{a}{\lambda_m} = a\frac{\omega}{2\pi}\sqrt{\frac{\rho_m}{\mu_m}} \ll 1.$$

Therefore, with the chosen constituents, the homogenization technique is expected to be applicable up to the (reduced) frequency $\omega_{max}\, a/2\pi = \sqrt{\mu_m/\rho_m} = 1.055$ [$10^6$ m/s]. Note, moreover, that the scaling assumptions of section 3.1.2 are here fulfilled (see table 3.1). Consequently, band gaps are expected.

Table 3.1: Material properties.

| Constituents | $E$ [MPa] | $\nu$ [-] | $\rho$ [kg/m$^3$] |
|---|---|---|---|
| part $\mathrm{Y}_m$ (epoxy) | 3600 | 0.370 | 1180 |
| part $\mathrm{Y}_c$ (rubber) | 0.118 | 0.469 | 1300 |
| part $\mathrm{Y}_f$ (lead) | 14000 | 0.420 | 11340 |

While the results of the homogenization theory are general, in the sense that they are independent from the actual shape of the unit cell, the numerical analyses of the Bloch-Floquet approach require to fix the geometry of the unit cell.

For the sequel, we here define the *Filling Fraction* (FF) as the ratio between the measure of the domain occupied by the inclusions with respect to that of the entire unit cell, such that:

$$\mathrm{FF} = \frac{|\mathrm{Y}_c| + |\mathrm{Y}_f|}{|\mathrm{Y}_m|}.$$

### Bi- and three-phase 2D LRMs

We consider that the inclusions are distributed on $S$ following a *square lattice*, characterized by orthogonal primitive base vectors $\boldsymbol{a}_1$ and $\boldsymbol{a}_2$ with the same modulus, so that the unit cell is a square of side $a$.

In figures 3.6 and 3.7, we compare the numerical and the analytic results, for out-of-plane waves respectively in bi- and three-phase 2D LRMs. Specifically, figures 3.6a and 3.7a report the numerically computed dispersion plots, whereas figures 3.6b and 3.7b show the evolution of the normalized effective mass density (analytically derived throughout homogenization) with frequency. The shaded regions correspond to band gaps obtained from the asymptotic technique. In view of property 4 of subsection 2.1.5, the dispersion plot in terms of reduced frequency $\omega\, a/2\pi$, is independent from the cell size $a$.

One can observe an extremely good agreement of the two approaches for the determination of the first two band gaps. This is indeed expected since they appear at frequencies $\omega \ll \omega_{max}$. Note, however, that the second band gap for the three-phase LRM (figures 3.7) is characterized by the presence of two so-called "*flat bands*". These modes correspond to eigenfrequencies $\omega_q$ of problem (3.43) such that the corresponding eigenspace and associated motion on the boundary $\partial\mathrm{Y}_f$ are orthogonal to translations. The effective mass density is still defined at these frequencies (although negative). Modes belonging to this family can also appear outside band gaps, as it is the case for

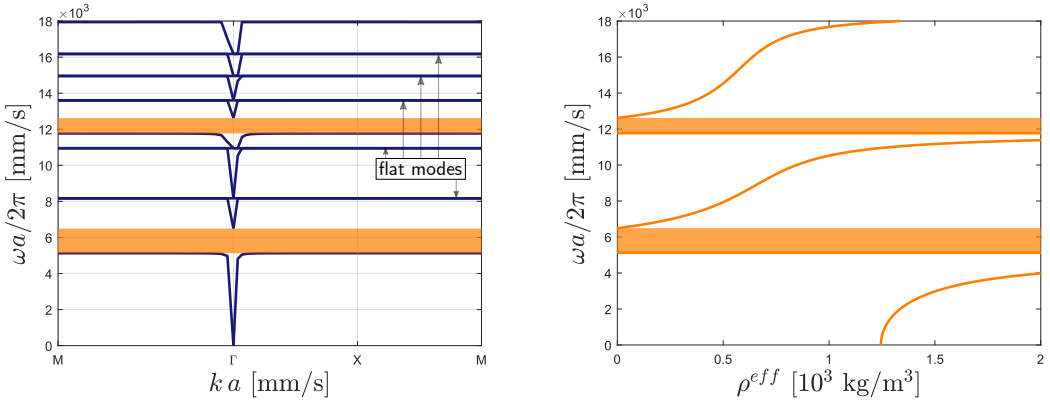


(a) (b)

Figure 3.6: *Propagation of out-of-plane waves in two-phase 2D LRMS, filling fraction* $FF = 0.541$*: (a) dispersion plot computed numerically using the Bloch-Floquet approach (normalized wave number* $ka$ *vs reduced frequency* $\omega a/2\pi$*), (b) effective mass density* $\rho^{eff}$ *vs reduced frequency. Shaded regions denote the band gaps. The path followed along the IBZ are the ones highlighted in red in figure 3.5a.*

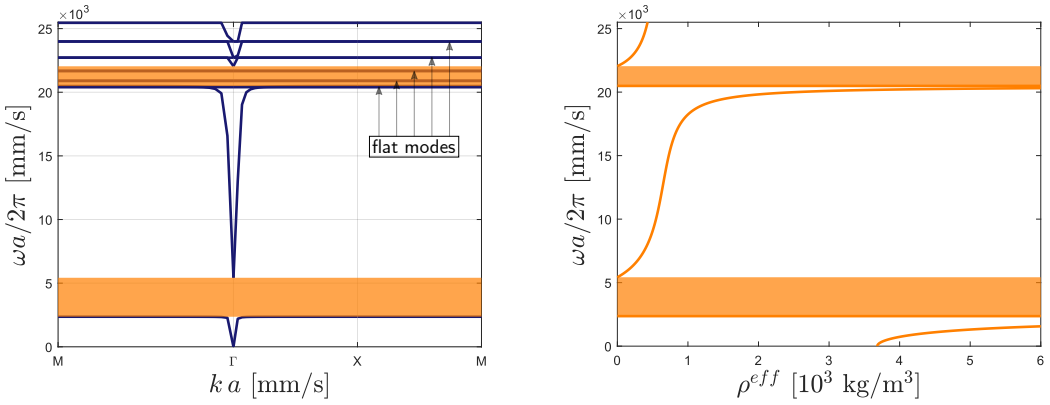


(a) (b)

Figure 3.7: *Propagation of out-of-plane waves in three phase 2D LRMS, filling fraction* $FF = 0.541$ $(R/a = 0.415)$*,* $R_f/R_c = 0.67$*: (a) dispersion plot computed numerically using the Bloch-Floquet approach (normalized wave number* $ka$ *vs reduced frequency* $\omega a/2\pi$*), (b) effective mass density* $\rho^{eff}$ *vs reduced frequency. Shaded regions denote the band gaps. The path followed along the IBZ are the ones highlighted in red in figure 3.5a.*

the bi- and three-phase LRMs here considered (see figures 3.6a and 3.7a). Due to the

mentioned orthogonality, these eigenmodes will not be "activated" when dealing with the problem of wave propagation in an infinite (periodic) domain at low frequencies[1]. Nevertheless, they do appear in the dispersion plot: the latter is indeed obtained from an eigenvalue problem in a finite domain (Bloch-Floquet approach) and the concept of propagation is therefore absent.

Before analyzing the presence of these flat modes, let us initially report in figure 3.8 the contour plots of some eigenmodes from the dispersion analysis of the three-phase case. The opening and the closing modes of the first band gap are shown in figures 3.8a

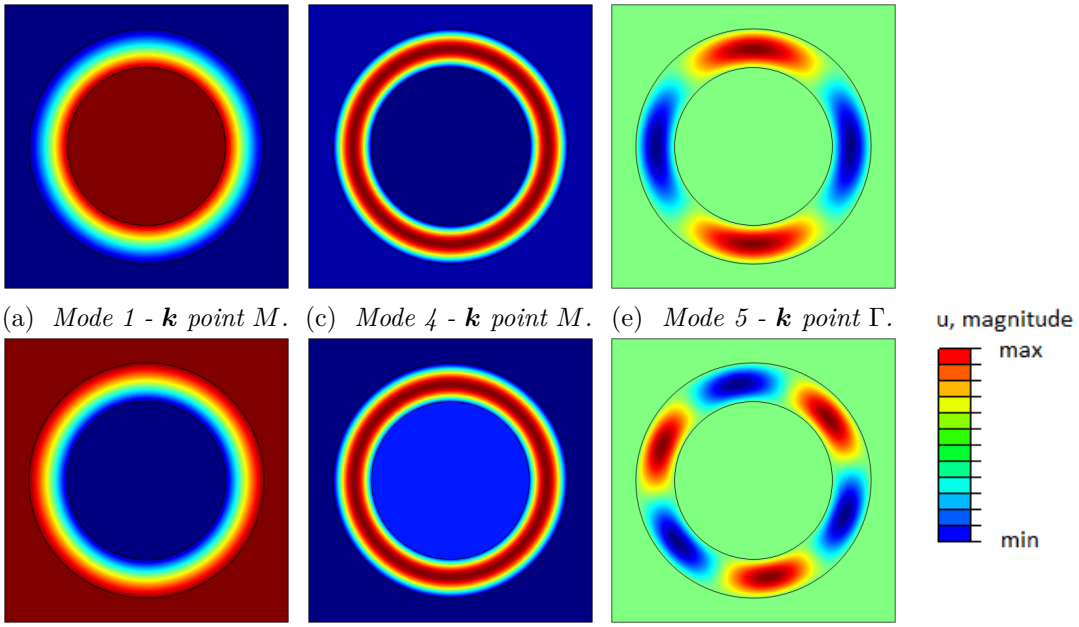


(a) *Mode 1 -* $\boldsymbol{k}$ *point* $M$. (c) *Mode 4 -* $\boldsymbol{k}$ *point* $M$. (e) *Mode 5 -* $\boldsymbol{k}$ *point* $\Gamma$.

(b) *Mode 2 -* $\boldsymbol{k}$ *point* $\Gamma$. (d) *Mode 7 -* $\boldsymbol{k}$ *point* $\Gamma$. (f) *Mode 6 -* $\boldsymbol{k}$ *point* $M$.

Figure 3.8: *Three components metamaterial, filling fraction* $FF = 0.541$, $R_f/R_c = 0.67$*: (a) and (b) opening and closing modes of first band gap, (c) and (d) opening and closing modes of second band gap, (e) and (f) flat modes inside second band gap.*

and 3.8b, they are axial symmetric and correspond to different symmetry points of the IBZ (as common for band-gaps generated by a local resonant mechanism). The opening and closing modes of this second band gap, shown in figures 3.8c and 3.8d, are again axial-symmetric. The two flat modes within the second band gap in the dispersion plot are shown in figures 3.8e and 3.8f. They correspond to local resonances inside the coating characterized by a displacement field depending on both the radial and the angular coordinates. From figure 3.8 one can also observe that the displacement is

[1] At low frequencies waves in part $Y_m$ are characterized by a long wave length. The corresponding displacement field will thus be locally constant. We have found that these modes are perpendicular to the constants and therefore their contribution to the motion must be null.

uniform in the internal lead inclusion (part $\mathrm{Y}_f$) and the simplifying hypothesis of rigid inclusion is therefore justified.

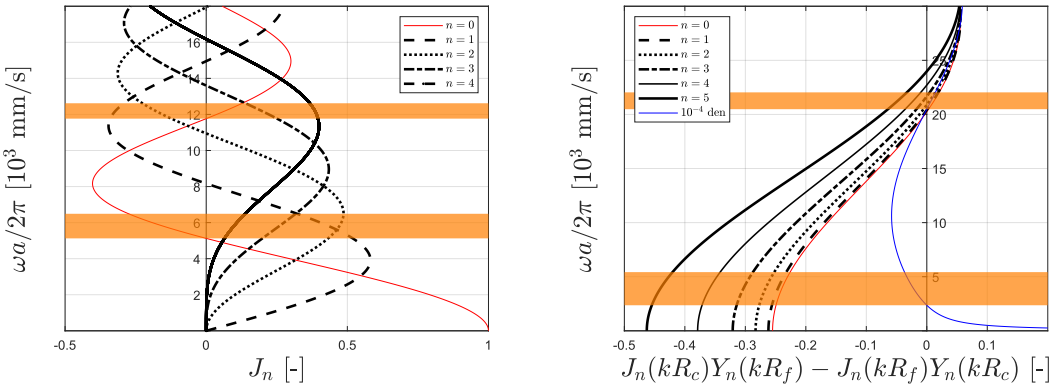


(a) (b)

Figure 3.9: *Left-hand side members of relations* (3.48) *(a) and* (3.58) *(b)) are represented in black with respect to the reduced frequency* $\omega a/2\pi$*, respectively for* $0 < n < 4$ *and* $0 < n < 5$*: their zeros correspond to flat modes in the dispersion plots (a) and (a). Red curves correspond to* $n = 0$*. The blue curve in figure (b) represents the quantity "den" defined by relation* (3.52) *(it is multiplied by* $10^{-4}$ *for a better visualization). The orange shaded regions denote the band gaps obtained with the homogenization.*

Let us now go back to the flat modes. Their prediction is verified in figure 3.9, where the left-hand side members of relations (3.48) and (3.58), for $n \neq 0$, are reported with respect to the reduced frequency, respectively for the bi- and three- phase LRMs. The zeros of these functions (represented as black curves), for $n \neq 0$, indeed correspond to the flat modes present in the dispersion plots of figures 3.6a and 3.7a, indicating a displacement localized in parts $\mathrm{Y}_c$. Moreover, the red curves in the plots of figure 3.9 correspond to those same functions for $n = 0$. Their zeros thus coincide to the opening of a band gap for the bi-phase LRM (figure 3.9a). This would have been also the case for the three-phase LRM, if one had assumed the rigid translation $U(\mathrm{v}_0^*)$ of part $\mathrm{Y}_f$, associated to mode $\mathrm{v}_0^*$, to be null. Nevertheless, this assumption would be unreasonable, preventing the motion of the inner inclusion. By doing this, we would also not be able to correctly predict the band gaps, as one can check by looking at the red curve in figure 3.9b: its zeros do not intersect all the openings of the band gaps.

While the resonant behavior of the bi-phase case entirely depends on the dynamics of part $\mathrm{Y}_c$, this is not the case for the three-phase material, where the presence of part $\mathrm{Y}_f$ can strongly influence the motion of the LRM. In particular, this behavior characterizes the first band gap for the three-phase LRM here analyzed. By looking at the modal shape in figure 3.8a, it is clear that the opening of this band gap is mainly caused by the resonant motion of part $\mathrm{Y}_f$, that moves out-of-phase with respect to

part $\mathrm{Y}_m$. Finally, the blue curve in figure 3.9b represents the function "den" defined by relation (3.52) (it is multiplied by $10^{-4}$ for a better visualization) and becomes null each time a band gap appears. This function indeed contains information on the combined dynamic behavior of both parts $\mathrm{Y}_c$ and $\mathrm{Y}_f$.

### Bi-phase 3D LRMs

We consider that the inclusions are distributed in V following a *cubic lattice*, characterized by orthogonal primitive base vectors $\boldsymbol{a}_1$, $\boldsymbol{a}_2$ and $\boldsymbol{a}_3$ with the same modulus, so that the unit cell is a cube of side $a$.

In figure 3.10, we again compare the numerical results (figure 3.10a) with the analytic ones (figure 3.10b). The agreement is excellent also in this case. Note that, for the cubic unit cell here considered, the IBZ is characterized by a third dimension with respect to the 2D cases previously considered and is represented in figure 3.5b.

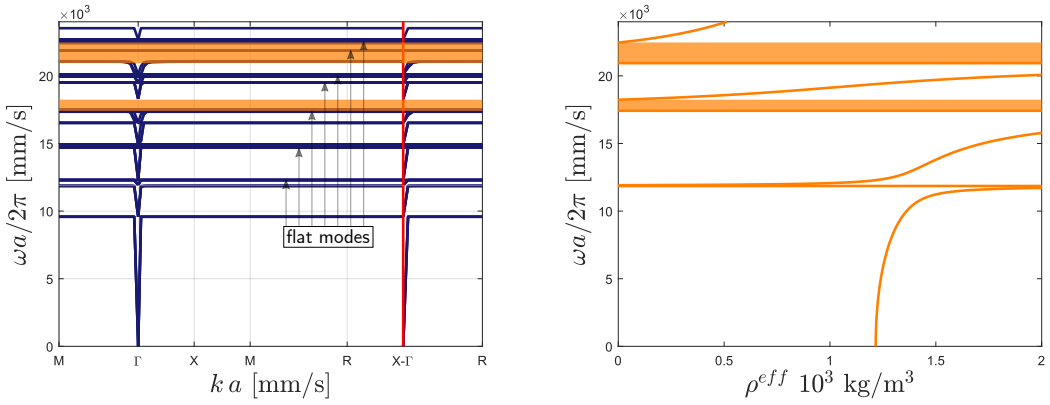


Figure 3.10: *Propagation of waves in bi-phase 3D LRMS, filling fraction* $FF = 0.299$ *(*$R/a = 0.415$*): (a) dispersion plot computed numerically using the Bloch-Floquet approach (normalized wave number* $ka$ *vs reduced frequency* $\omega a/2\pi$*), (b) effective mass density* $\rho^{eff}$ *vs reduced frequency. Shaded regions denote the band gaps. The path followed along the IBZ is highlighted in red in figure 3.5b.*

Flat bands are present in the dispersion plot. Their analytic prediction is not analyzed here as the same procedure valid for the 2D case applies for the 3D LRM. In particular, one has to impose the boundary condition of problem (3.60) using the general solution (3.61); the relations obtained for $n \neq 1$, $m \neq 0$, with $n \in \mathbb{Z}$, $m \in \{-|n|, \ldots, |n|\}$, allow to find the eigenfrequencies $\omega_{q(nm)}$ corresponding to flat modes.

### 3.3.2 Parametric studies

Since closed form solutions are obtained, one can easily perform parametric studies to evidence the influence of different geometries and material coefficients on the wave propagation properties.

Concerning the problem of out-of-plane waves in three-phase 2D LRMs with the constituents given in table 3.1, the influence of the thickness of the coating is highlighted in figure 3.11, where the regions of negative effective mass are shown at varying $R_f/R_c$. The dashed line corresponds to the effective mass evolution shown in figure 3.7b. The amplitude of the first band gap increases as the thickness of the coating decreases since, at fixed filling ratio, this corresponds to an increase of the resonating fiber mass. Figure 3.12 displays the frequency intervals of negative effective mass at varying filling fractions for the case of a thick coating (figure 3.12a) and that of a thin coating (figure 3.12b).

For out-of-plane waves in bi-phase 2D LRM, keeping again the same constituents as before, the only parameters affecting the position and width of the band gaps is the mass ratio between the parts composing each unit cell. Instead, in 3D bi-phase LRM, band gaps depend not only on the mass ratio but also on the Poisson's coefficient of part $\mathrm{Y}_c$ (as shown before). We report in figure 3.13 the variation of the first band gap due to different Poisson's ratios. The frequency is normalized with respect to $\omega_1 = \omega_{1(10)}$, being the first eigenfrequency of part $\mathrm{Y}_c$, found from relation (3.63) for $n = 1$ and $m = 0$.

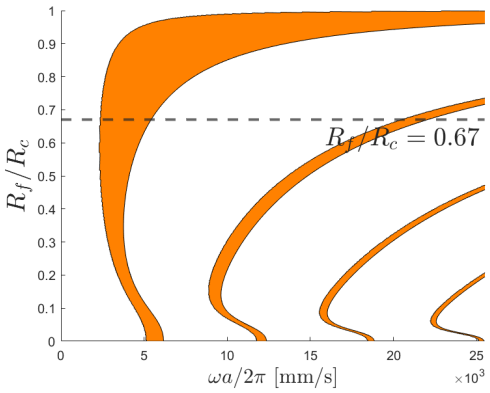


Figure 3.11: *Three-phase 2D LRM with filling fraction* $FF = 0.54$*: intervals of negative effective mass in the plane (reduced frequency* $\omega a/2\pi$ *-* $R_f/R_c$*) for out-of-plane waves, the dashed line corresponds to the case considered in the previous calculations (*$R_f/R_c = 0.67$*).*

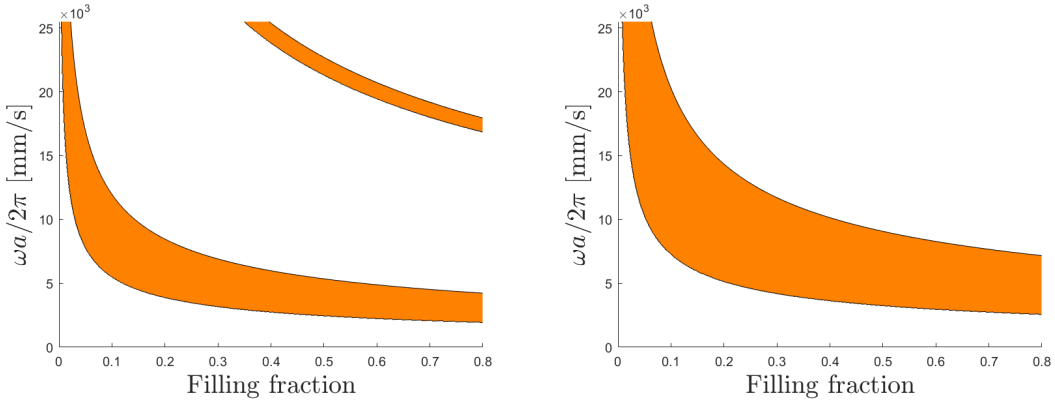


Figure 3.12: *Intervals of negative effective mass in terms of reduced frequency* $\omega a/2\pi$*, for varying filling fraction: (a) thick coating* $R_f/R_c = 0.67$*, (b) thin coating* $R_f/R_c = 0.87$*.*

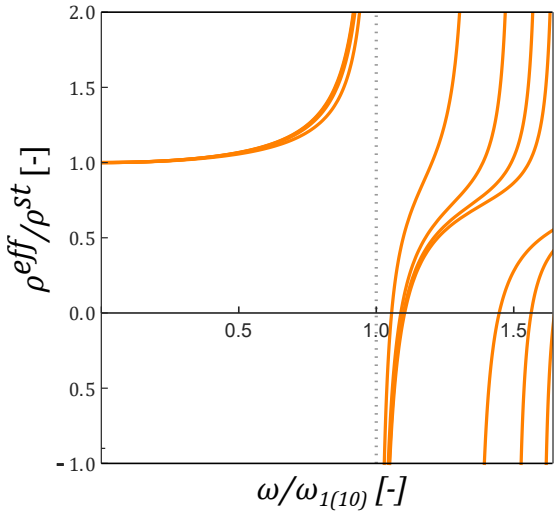


Figure 3.13: *Bi-phase 3D LRM with filling fraction* $FF = 0.299$*: effective mass density for varying Poisson's ratios of part* $\mathrm{Y}_c$ *vs frequency normalized with respect to* $\omega_1 = \omega_{1(10)}$*.*

CHAPTER

# 4

# The localization phenomenon in defective metamaterials

Chapter summary: *The problem of the localization of classical waves is introduced herein. The key point for the occurrence of the aforementioned phenomenon is the presence of band gaps. Metamaterials of the type treated in this thesis have shown good abilities to control the propagation of waves (see chapter 1). The insertion of so-called "defects" (also known as "cavities"), i.e. perturbations of their periodicity, causes the formation of eigenmodes localized in space around the defect. An exhaustive description of the mechanisms governing the problem of wave localization in metamaterials and, more in general, in systems with band gaps presenting defects is given, in parallel with a concise review. A new method for the localization of classical waves, analogous to the resonant tunneling effect in quantum mechanics, is discussed. Proof of its validity is shown by means of a discrete system.*

## Contents

As stated in the introduction of this thesis, our aim is to analyze and idealize possible solutions to be applied in what we had defined as "*Defective Energy Harvesting*" (DEH) devices, *i.e.* systems whose response to an external energy source is localized in a defect of their structure. One of the goals of this chapter is to introduce the localization phenomenon at the basis of the functioning of these systems. Structures presenting band gaps in their spectra and point or line defects in their domains can sustain the formation of local modes, characterized by oscillations that are localized in a compact region. Consequently, the energy injected into the system from spread sources could in principle be confined in the defect.

The focusing and trapping of "*classical waves*"[1], in photonic and phononic crystals by means of defects is well-known in the literature, where theoretical and experimental validations can be found. Evidences of this phenomenon in locally resonant materials also exists (although they have been much less studied). We here intend to present a "new" way for the localization of classical waves, inspired to the quantum-mechanical *resonant tunneling effect*[2]. Our aim in this chapter is that of proving its validity and efficiency in relation to the trapping and focusing of mechanical energy, by employing a simplified model able to work both as a locally resonant material and a phononic crystal.

Part of this chapter was the subject of the following publication: Moscatelli et al., 2021.

## 4.1 The problem of waves localization in defective media

The phenomenon of wave localization first appeared in solid state physics following the seminal paper by Anderson (1958). Solids, at the microscopic scale, are composed of a periodic repetition of elementary units. The wave nature of electrons in such crystalline structures gives rise to allowed energy-bands. Outside these bands, destructive interference of different scattering trajectories inhibits the electrons motion, forming forbidden intervals that are nothing else than what we defined as band gaps for classical waves[3]. By introducing small enough perturbations of periodicity (*i.e.* by considering a slightly disordered crystal), the electronic wave functions are localized in space at some energies in the vicinity of the edges of the gaps, decaying exponentially away from the center of the localization (Figotin et al., 1994b). If the disorder is further increased, the energies corresponding to localized waves can fill up the entire band gap (Figotin et al., 1996c).

The very same phenomenon appeared to be valid also at a macroscopic scale, when classical waves are deemed. It has been demonstrated for lattice models (Figotin et al.,

[1] With "classical" we intend electromagnetic, acoustic and elastic waves, where quantum effects are not of importance.

[2] This is the reason why the word "new" was quoted before in the text: the application is new but the idea is not.

[3] Frequencies have to be interpreted as energy levels: electrons whose energy is inside a band gap will experience "attenuation" in some form.

1994a) and for continuous domains (Figotin et al., 1996c, 1997a).

If instead of distributing the imperfections all over the domain of the problem, one considers a single (or a few) compact defect(s), localization can still be activated, provided that the system sustains the formation of band gaps. Indeed, defects are nothing else than compactly-supported imperfections of an otherwise homogeneous or periodic domain. Note that a slightly disordered media can be thought of as a superposition of local perturbations. The basic physical mechanism responsible for the confined response in disordered media is exactly the same experienced by defective systems. Namely, a compact defect can support a localized state that decays away from it and that oscillates at a frequency inside a band gap for the unperturbed problem. We will call this state "eigenmode" for the moment and we will later on give the reason why we can call it like that. Consequently, we will refer to its corresponding frequency of oscillation as "eigenvalue".

We are interested precisely in analyzing this remarkable behavior, *i.e.* in studying systems presenting band gaps and characterized by the presence of one (or a few) point or line defect(s).

We underline again that the existence of localized eigenmodes is strictly related to the presence of band gaps in the spectrum of the operator governing the problem under consideration and this is valid both for electron and classical waves. Nonetheless, in spite of all the similarities between the two problems, an important difference exists. The reinterpretation of the results concerning the localization phenomenon in terms of classical waves is made possible by the strong analogy between the Schrödinger operator

$$\mathscr{S}(\bullet) := (-\Delta + V(\boldsymbol{x}))(\bullet) \quad \text{on } L^2(\mathbb{R}^n;\mathbb{C})$$

and the operators for classical waves

$$\mathscr{A}(\bullet) := -\nabla \cdot \frac{1}{\chi(\boldsymbol{x})}\nabla(\bullet) \quad \text{on } L^2(\mathbb{R}^n;\mathbb{C}),$$
$$\mathscr{E}(\bullet) := \nabla \times \frac{1}{\chi(\boldsymbol{x})}\nabla \times (\bullet) \quad \text{on } L^2(\mathbb{R}^n;\mathbb{C}^n),$$

with $n$ denoting the dimension of the domain. Let us list here below some comments on the above operators:

- The term $V$ in the operator $\mathscr{S}$ is a position dependent potential.
- $\mathscr{A}$ is the operator for acoustic waves, obtained by considering a position dependent mass density $\chi(\boldsymbol{x})$ and a unit compressibility.
- $\mathscr{E}$ is the operator for electromagnetic waves, obtained by considering a position dependent dielectric constant $\chi(\boldsymbol{x})$ and a unit material permeability.
- The operator for elastic waves (2.23) has exactly the same form as the operator $\mathscr{A}$ when a scalar field is under consideration, with $\chi(\boldsymbol{x})$ being the inverse of the stiffness in that case. Studying higher dimensions for the elastic problem does not bring anything more with respect to the considerations that apply to the scalar

problem and that will later be made. Therefore, we consider here only the scalar operator.

The difference mentioned above stems from the fact that for the electron case it suffices to perturb locally a homogeneous medium, *i.e.* a constant potential $V(\boldsymbol{x}) = v$, in order to generate a localized response. Indeed, the spectrum $\sigma$ for the operator $\mathscr{S}$ is obtained as $\sigma(\mathscr{S}) = [v, \infty)$, with the interval $(-\infty, v)$ being a gap of the spectrum. The closing edge of this gap depends on the potential of the homogeneous medium and, hence, a compact perturbation of the homogeneous medium could move this edge into the gap for positions $\boldsymbol{x}$ within the perturbed domain, causing the formation of eigenmodes localized inside the defect.

For classical waves, a local perturbation of a homogeneous medium (*i.e.* of a constant $\chi$ in the operators defined above) cannot generate a localized eigenmode. One always have $\sigma(\mathscr{A}) = \sigma(\mathscr{E}) = [0, \infty)$ and thus the interval $(-\infty, 0)$ corresponds to a gap in the spectrum of classical waves. Nonetheless, contrary to the previous case, the closing edge of this gap is now independent from the material properties of the homogeneous medium analyzed. Any compact perturbation cannot expand the spectrum into the gap and no localized eigenmodes can appear (Figotin et al., 1997b).

Due to this fundamental difference between electron and classical waves, in order to activate the phenomenon of localization in the latter case, it is necessary to design heterogeneous domains for classical waves that enable for the formation of gaps in the spectrum, whose edges depend on the medium under consideration. This can be achieved in different ways.

The easiest approach to obtain a gap for classical waves is to consider waveguides. Looking at the above operators $\mathscr{A}$ and $\mathscr{E}$, they are both applied to functions defined on $\mathbb{R}^n$. For $n \geq 2$, one can reduce the domain of the medium to form a waveguide. Depending on the conditions imposed at the boundaries[1], it is possible to obtain a spectrum with cut-off frequencies dependent on the geometry of the domain (Nazarov, 2011a). Therefore, by introducing a local modification of the waveguide width, a defect mode can appear in the spectrum of the problem.

The other natural way to generate band gaps is to consider periodic domains, as we have shown in the previous chapters. Photonic crystals, phononic crystals, and locally resonant materials are thus all candidates for the development of systems experiencing the localization phenomenon described herein. A point (or line) defect can be created by locally modifying the properties of one (or more) unit cell that composes the material. Since the position of the edges of the band gaps that appear in their spectra depends on the periodicity, an imperfection of such periodicity could lead to the formation of localized eigenmodes.

Combining the two previous configurations, periodic waveguides can offer the very same phenomenon of localization, when defects of periodicity are introduced (Nazarov, 2011b; Delourme et al., 2017, 2020).

[1] One can choose between Dirichlet and Neumann boundary conditions.

### 4.1.1 Defects in metamaterials

In this thesis we are mainly interested in the behavior of metamaterials for *mechanical waves*, *i.e.* waves that are not capable of transmitting their energy through vacuum. Elastic and acoustic waves belong to this class, whereas electromagnetic waves does not. We will thus focus on the problem of wave localization in this type of materials with defects of periodicity.

We have previously called the localized wave field "*eigenmode*" and its corresponding frequency of oscillation "*eigenvalue*". From a mathematical point of view, when dealing with self-adjoint operators (as it is the case here), the spectrum of the problem can be subdivided in the so-called *discrete* and *essential* spectra, the former being composed of all the eigenvalues of finite multiplicity and the latter being its complement[1]. When dealing with periodic media, such spectrum would only be composed of its *essential part*. By introducing a compact defect, the essential spectrum is stable[2] and thus its band gap structure remains unchanged (Reed et al., 1978; Figotin et al., 1997b). This means also that, if a particular band gap is considered, the spectrum for the defective system in that same band gap can consist at most of the *discrete spectrum* of the perturbed problem, allowing us to refer to localized states as eigenmodes and to corresponding frequencies as eigenvalues (of finite multiplicity).

It is clear that a defect in a periodic structure can be realized in different ways, nevertheless important differences arise when comparing phononic crystals (PnCs) and locally resonant materials (LRMs). Specifically, the mechanism responsible for the formation of a defect mode, *i.e.* an eigenmode localized in the defect, is the same in both cases, however the "working regime" is very different: considering the same characteristic size for the unit cell, the order of magnitude of the frequencies involved in the formation of band gaps are different. We indeed specified since the beginning of this thesis that, while in PnCs band gaps open for wavelengths of the order of one spatial period, LRMs are generally designed to work in a sub-wavelength regime.

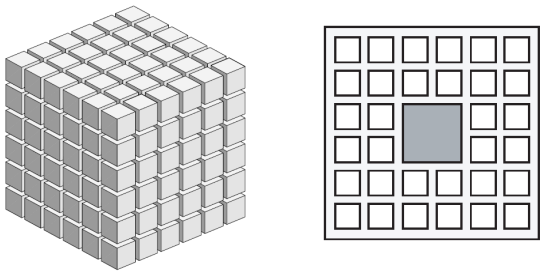

Figure 4.1: *Sketch of 3D periodic system (left) containing a compactly-supported defect, represented by the darker region in its sectioned representation (right). Source: Klein et al. (1998).*

[1] Note that the *residual* spectrum for self-adjoint operators is always empty.
[2] This comes from a corollary of Weyl's theorem.

To list possible defective systems, let us consider the typical geometrical configuration of a metamaterial, with a background medium (the matrix) presenting a periodic lattice of non-connected scatterer elements (the inclusions). The easiest way to create a defect in such periodic material is by removing the inclusion from one (or a few neighboring) unit cell(s) (see figure 4.1). In doing so, the characteristic size of the imperfection is that of one unit cell. Localized eigenmodes can thus appear only if the characteristic wave length of the corresponding resonating motion of the defect is at maximum of the same order of magnitude of the cell size. From what we just said, this perturbed configuration can generate a defect mode only in a PnC. Numerical and experimental proofs of the formation of defect states for elastic and acoustic waves were first given by Sigalas (1997, 1998), Khelif et al. (2003), and Wu et al. (2009b). Similar results for PnCs can be found by modifying the geometry of the inclusion, instead of completely removing it (Sigalas, 1997, 1998; Wu et al., 2001, 2004).

In all the works just cited, the existence of a defect mode was not assured a priori, but had to be verified by treating the problem first and by checking that the choice made was good enough for an eigenvalue of finite multiplicity to be present in a band gap. In Figotin et al. (1997b) and Klein et al. (1998), the authors come up with a necessary and sufficient condition to ensure the rise of at least one eigenvalue in a gap of a perturbed periodic medium obtained by the substitution of one or more unit cells with a homogeneous material. Specifically, they provide a rigorously derived condition for the acoustic and the electromagnetic operators previously defined. For completeness, let us rewrite here this condition:

$$\ell^2\check{\chi} > \frac{4(a+b)}{(b-a)^2} \inf_{\substack{\xi\in C_0^2(\mathrm{D},\mathbb{R}),\|\xi\|=1 \\ \hat{\boldsymbol{\kappa}}\in S^n}} \left\{ \|\hat{\boldsymbol{\kappa}}\cdot\nabla\xi\|^2 \left[ 1+\left( 1+\frac{\|\nabla\xi\|^2}{4\|\hat{\boldsymbol{\kappa}}\cdot\nabla\xi\|^4} \left(\frac{b-a}{a+b}\right)^2 \right)^{1/2} \right] \right\},$$

where: $\ell$ is the characteristic length for the spatial size of the defect; $\check{\chi}$ is the constant coefficient for the material that composes the defect; $a$ and $b$ are respectively the opening and closing frequencies of a band gap; D is a bounded subset of $\mathbb{R}^n$; $C_0^2(\mathrm{D},\mathbb{R})$ is the space $C_0^2(\mathbb{R}^n,\mathbb{R})$ of functions $\xi$ such that $\mathrm{supp}(\xi)$ is contained in the interior of D; $S^n$ is the unit sphere in $\mathbb{R}^n$. In the above relation, the norms have to be understood in the $L^2$ space.

To give an example of application of the above condition, let us consider a 2D metamaterial for out-of-plane elastic waves composed of an array of square unit cells and characterized by a band gap in its spectrum between $a$ and $b$. A defect is created by removing an inclusion from one cell (this example is very similar to the one given by Figotin et al. (1997b)). Let us take

$$\xi(\boldsymbol{x}) = \frac{\prod_{i=1}^2 \upsilon(x_i)}{\|\prod_{i=1}^2 \upsilon(x_i)\|}$$

with

$$\upsilon(t) = \begin{cases} (t-1/2)^2(t+1/2)^2 & \text{for } -1/2 \le t \le 1/2 \\ 0 & \text{otherwise} \end{cases}$$

and $\hat{\boldsymbol{\kappa}} \equiv \boldsymbol{e}_i$, with $i \in \{1, 2\}$, to be the unit vector along one of the directions given by the coordinate axes. For this case, $\check{\chi}$ denotes the inverse of the shear modulus of the material composing the defect. The above condition for the existence of a defect mode becomes:

$$\ell^2 \check{\chi} > \frac{48(a+b)}{(b-a)^2} \left[ 1 + \left( 1 + \frac{11}{8} \left( \frac{b-a}{a+b} \right)^2 \right)^{1/2} \right] \approx \frac{61(a+b)}{(b-a)^2},$$

considering the fact that $(b-a)/(a+b) < 1$ for the approximation.

Therefore, one has that the spatial size and the material coefficient of the defect must be large enough to assure the creation of at least one defect mode inside the band gap $(a, b)$.

To the authors knowledge, no equivalent results exist for elastic waves in 3D (operator (2.23)). Nevertheless, one expects to find similar conditions because of the aforementioned similarities of the operators involved and of the mechanisms responsible for the formation of band gaps and defect modes.

By using the above relation, one finds that the formation of localized eigenstates is less obvious with continuous LRMs due to their sub-wavelength regime. Intuitively, considering the same position in the spectrum[1] and the same size for the defect ($\ell$), the condition above is satisfied depending on the coefficient $\check{\chi}$, being the inverse of the stiffness of the background material (matrix) of the metamaterial under consideration. Accordingly, this coefficient is smaller in LRMs (soft-in-stiff configuration) with respect to PnCs (stiff-in-soft configuration). Therefore, at fixed band gap position (*i.e.* fixing the right-hand side in the above condition), one has either to consider a larger defect (larger $\ell$) or to tune its resonance such that a localized motion can appear in the band gap. The latter solution has been exploited in the work of Ammari et al. (2018), where the authors extensively and rigorously analyzed the localization problem for acoustic waves in bubbly crystals. This same concept has also been used in PnCs for the formation of a defect modes generated by a Helmholtz resonator inserted in the defect (Wu et al., 2010).

Our contribution to the problem of wave localization in LRMs is in the other direction, namely we try to control the formation of localized modes by varying the dimensions of the defect, as will be shown in the next chapter 5. Our objective is not only to generate defect modes, but also to trap propagating waves in the defect, together with the energy they carry with them.

[1] Although, as we said before, the working frequencies in LRMs and PnCs are generally different, the resonant scatterers in a LRM could be tuned to rise in frequency, positioning the band gaps close to the one obtained from a PnCs with the same cell size.

## 4.2 Exploitation of the resonant tunneling phenomenon for the localization of mechanical waves

Let us describe the system we have conceived for the localization of mechanical waves in defective metamaterials.

As we claimed in the previous section, we intend to obtain localized eigenmodes by tuning the dimensions of the defect. The system we are willing to study is sketched in figure 4.2 and is composed of a metamaterial that has been inserted in the unbounded

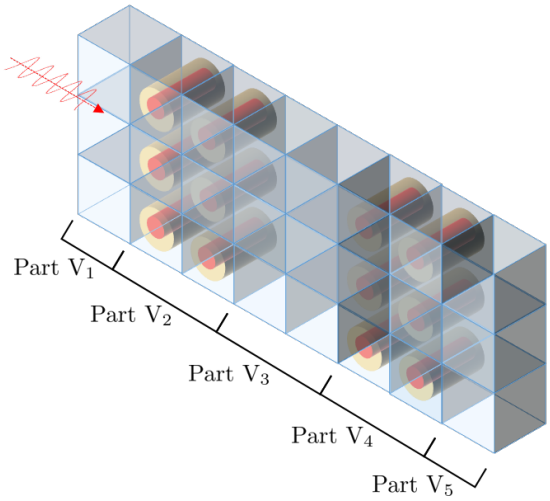


Figure 4.2: *Sketch of the studied system. A defect (part* $V_3$*) splits the metamaterial in parts* $V_2$ *and* $V_4$*. A wave propagating from part* $V_1$ *to part* $V_2$ *travels through the whole system.*

domain V and split into two regions (parts $V_2$ and $V_4$) by the insertion of a defect (part $V_3$), whose role is that of a resonant cavity. The metamaterial used is classically made up of a homogeneous matrix with a periodic array of scatter elements. Our objective is that of trapping in the defect the wave that is traveling from part $V_1$ to part $V_5$. Note that, in figure 4.2, the background material employed for the matrix is the same of that considered for the defect (part $V_3$) and for the medium surrounding the system (parts $V_1$ and $V_5$); this is just a specific configuration, as different materials could be envisaged as well.

As we anticipated earlier in this chapter, the functioning of the above system resembles very much the resonant tunneling phenomenon for electron waves in quantum physics (see *e.g.* Bohm (1989)). An electron wave $\psi$, function of position $x$ and of energy $E > 0$, is sent towards two barriers of potential $P > E$, that are disposed in series and separated by a certain distance. The problem is 1D and outside the barriers $P = 0$. By considering Schrödinger equation

$$\psi''(x) + (E - P(x))\psi = 0,$$

it is clear that, as in the barriers the term $E - P(x)$ is smaller than zero, the electron wave is attenuated. Conversely, outside the barriers the wave can propagate freely. By adjusting the distance between the two barriers, it is found that the transmission coefficient is unity for certain wave lengths, meaning that the two barriers become completely transparent for the electron. This phenomenon is due to the multiple reflections that take place in the resonant cavity within the two barriers, acting as mirrors for the internal wave.

Our idea is that of using a metamaterial to behave as mirrors, exactly as the two potential barriers, and to exploit the multiple reflections to trap and focus inside the cavity the mechanical energy carried by the incoming wave.

We aim to solve the problem in closed form, in order to have a condition that enables us not only to assure the presence of defect modes, but also to place and locate it in the spectrum.

Before studying the behavior of the continuous system depicted in figure 4.2, we first consider in the next section its 1D discrete version, by employing the mass-in-mass chain widely described in chapter 2.

## 4.3 1D discrete metamaterials for energy localization

Let us analyze the system shown in figure 4.3, with five regions equivalent to those in figure 4.2 and made of springs $k_1$ and masses $m_1$ either alone (spring-mass chain) or connected to masses $m_2$ by springs $k_2$ (mass-in-mass chain analyzed in section 2.2). As we did in section 2.2, we call $\ell$ the size of a unit cell, that is the same for the whole system. The regions of the first type, corresponding to the matrix, are indicated as $\mathrm{V_I}$, $\mathrm{V_{III}}$ and $\mathrm{V_V}$; those of the second type, corresponding to the metamaterial (matrix with inclusions), are regions $\mathrm{V_{II}}$ and $\mathrm{V_{IV}}$; region $\mathrm{V_{III}}$ represents the "*cavity*", *i.e.* a defect of periodicity for the metamaterial, inserted between regions $\mathrm{V_{II}}$ and $\mathrm{V_{IV}}$ which can be

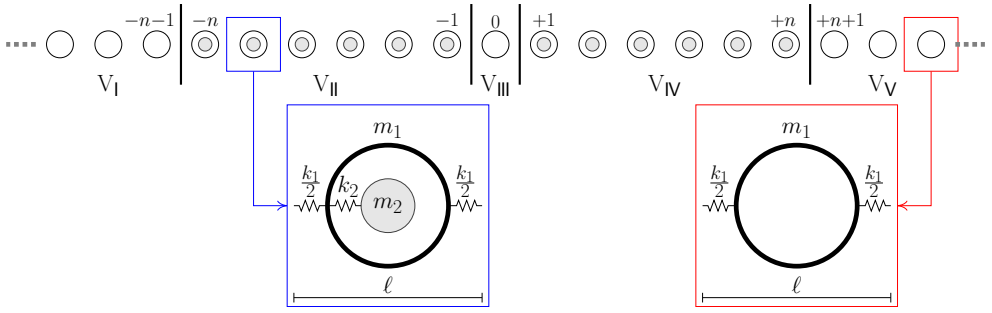


Figure 4.3: *Sketch of the studied system, with unit cells of the metamaterial and of the matrix. In parts* $\mathrm{V_I}$ *and* $\mathrm{V_V}$*, the chain of masses* $m_1$ *and springs* $k_1$ *is infinitely extended for* $j \to \pm\infty$*. Regions* $\mathrm{V_{II}}$ *and* $\mathrm{V_{IV}}$ *are composed of* $n$ *cells each. We call* $\ell$ *the size of a unit cell.*

thought of as the previously defined "barriers". Specifically, in this case we are creating a defect by removing the inclusion from the central unit cell. We assume that each metamaterial region contains $n$ cells and the defect only one. The number above a cell represents its index $j \in \mathbb{Z}$ in the chosen numbering. We consider an incoming wave in the region $\mathrm{V_I}$ which propagates at the angular frequency $\omega$ with an amplitude 1, and we search the response in the five regions.

Before studying the behavior of the system described here-above, it is necessary to analyze the problem of wave propagation in a spring-mass chain, as the one composing parts $\mathrm{V_I}$, $\mathrm{V_{III}}$, and $\mathrm{V_V}$.

### 4.3.1 The spring-mass chain

Let us consider a classical spring-mass chain. This model is usually exploited to represent the discrete counterpart of a homogeneous material. It must be underlined though that this is only partially true: the dynamic behavior of a sprig-mass chain is indeed dispersive and therefore different from that of a homogeneous medium. Nonetheless, we can say that spring-mass chains are for discrete media what homogeneous materials are for continuous media, *i.e.* they are characterized by the most basic among all the possible behaviors. We thus employ mass-spring chains to model the material outside the two barriers for the discrete domain here analyzed[1].

Keeping the notation used in section 2.2, the lattice is obtained by considering only masses $m_1$ connected by springs $k_1$ (see figure 2.2). In this way, we are modeling the discrete counterpart of a continuous system made up of the same material used for the matrix of the metamaterial previously described. In a 1D chain of this type, the motion problem is governed by the following equation:

$$m_1 \ddot{u}_j = k_1 \Delta_j u, \tag{4.1}$$

with $\Delta_j u = u_{j+1} + u_{j-1} - 2u_j$ still defined as in relation (2.33). Considering waves at given frequency $\omega$ and using again the same notation of chapter 2.2, in terms of dimensionless quantities, equation (4.1) can be rewritten as

$$\epsilon^2 \Delta_j U + \theta \Omega U_j = 0. \tag{4.2}$$

This Helmholtz equation has the same form of equation (2.38), with $\mu_\theta(\Omega)$ replaced by $\theta\Omega$, with $\Omega$ being the frequency of the wave under consideration normalized with respect to the eigenfrequency of the internal resonators, $\epsilon$ the square of the ratio between stiffness $k_1$ and $k_2$, and $\theta$ the ratio between masses $m_1$ and $m_2$. The subscripts 1 and 2 as before refer respectively to the outer and the inner mass.

[1] We will see later on that this choice affects the design of the REH. We anticipate that, contrary to what would happen for defective but continuous LRMs, defect modes can appear in the discrete REH here analyzed just by removing the inclusion from one unit cell. This is not possible when continuous LRMs are used, as we stated in the introduction of the chapter.

Using the same procedure described in subsection 2.2.2, when considering the matrix alone the motion corresponds to propagating waves only when

$$0 < \Omega < \frac{4\epsilon^2}{\theta}.$$

In such a case, setting

$$\frac{\theta\Omega}{2\epsilon^2} = 1 - \cos \mathsf{K} \quad \text{with} \quad \mathsf{K} \in (0, \pi), \tag{4.3}$$

the general solution of equation (4.2) is given by

$$U_j = a_1 \cos j\mathsf{K} + a_2 \sin j\mathsf{K} \tag{4.4}$$

where $a_1$ and $a_2$ are arbitrary constants.

### 4.3.2 Necessary conditions for the activation of a localization effect

For localizing the energy carried by an incoming wave inside the defect, the propagation must be inhibited outside it, hence we consider $\Omega$ inside a band gap of the metamaterial and in the pass band of the matrix, *i.e.*

$$\Omega < \frac{4\epsilon^2}{\theta} \quad \text{and} \quad \Omega \in (\Omega_m, \Omega_0) \cup (\Omega_M, +\infty). \tag{4.5}$$

Taking into account relation (2.49) of $\Omega_m$ and $\Omega_M$, one has $4\epsilon^2/\theta = \Omega_m\Omega_M$, and since $\Omega_m < 1 < \Omega_M$, the following inequalities hold:

$$\Omega_m < \frac{4\epsilon^2}{\theta} < \Omega_M. \tag{4.6}$$

Therefore, to comply with conditions (4.5), $\Omega$ must be chosen such that

$$\Omega_m < \Omega < \min\left\{1 + \frac{1}{\theta}, \frac{4\epsilon^2}{\theta}\right\}. \tag{4.7}$$

Condition (4.7) depends on $\epsilon$ and $\theta$: by fixing one of the two parameters, the variation of the interval of frequencies respecting (4.7) can be studied with respect to the other parameter. This is done in figure 4.4a and 4.4b, where we fixed $\theta = 1$ and $\epsilon = 1$ respectively. These two figures are a zoom near the origin of figures 2.6b and 2.7b. The frequencies fulfilling condition (4.7) are those inside the darkest regions in figure 4.4 and, hence, can belong to either part A or B, composing the first band gap. This means that, by properly fixing the parameters $\epsilon$ and $\theta$, one can choose whether to exploit a Bragg mechanism (part A) or a locally resonant mechanism (part B) for trying to activate a localization phenomenon.

In what follows, we consider both cases. Two situations can arise: when $4\epsilon^2 > \theta$, one can work with frequencies belonging either to band gap A or B (although for $\epsilon >> 1$, band gap A disappears since $\Omega_m \to 1$); when $4\epsilon^2 \leq \theta$, one has that $\Omega \leq 4\epsilon^2/\theta \leq 1$ and localization can only be generated by a Bragg mechanism (part A of the band gap).

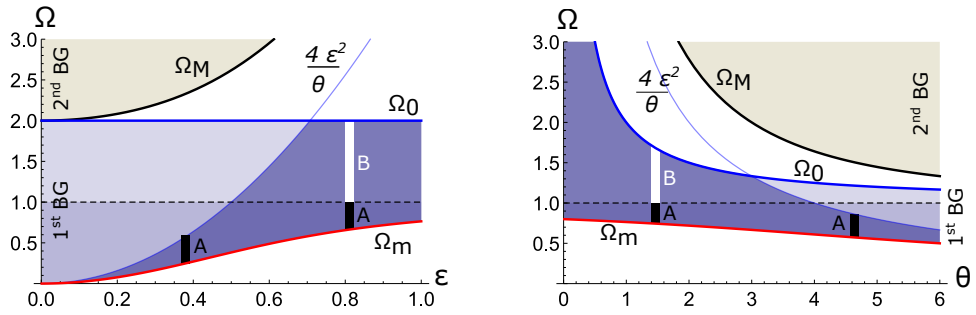


(a) $\theta = 1$. (b) $\epsilon = 1$.

Figure 4.4: *study of condition* (4.7) *with respect to* $\epsilon$ *(a) and* $\theta$ *(b), respectively for* $\theta = 1$ *and* $\epsilon = 1$. *Band gaps are denoted by the filled areas. The darkest regions indicate all the frequencies which fulfill condition* (4.7). *Letters A and B are used for denoting frequencies respecting condition* (4.7) *and belonging to band gaps.*

### 4.3.3 The motion of the system

All the following calculations are carried out in the plane of complex numbers. We recall here that the conjugate of a complex number $u$ is denoted $\overline{u}$, its modulus $|u|$, its real part $\mathcal{R}e(u)$ and its imaginary part $\mathcal{I}m(u)$.

1. In region $\mathrm{V_I}$, using equation (4.2) and the definition (4.3) of $\mathsf{K}$, the displacement $U_j^{\mathsf{I}}$ can be written as

$$U_j^{\mathsf{I}} = \mathsf{A}^{\mathsf{I}} \exp\{-\mathsf{i}\mathsf{K}(j+n+1)\} + \mathsf{B}^{\mathsf{I}} \exp\{\mathsf{i}\mathsf{K}(j+n+1)\}, \quad j < -n, \tag{4.8}$$

   the first term corresponding to the incoming wave with a known amplitude $\mathsf{A}^{\mathsf{I}}$ (propagating from the left to the right, in the direction of the increasing $j$'s), the second one to the reflected wave propagating in the opposite direction and whose amplitude $\mathsf{B}^{\mathsf{I}} = \mathsf{R}$ has to be determined. Without loss of generality, we here consider $\mathsf{A}^{\mathsf{I}} = 1$. Substituting relation (4.8) into equation (4.2) written for $j = -n-1$ and accounting for relation (4.3), one obtains $U_{-n}^{\mathsf{I}} = \exp\{-\mathsf{i}\mathsf{K}\} + \mathsf{R}\exp\{\mathsf{i}\mathsf{K}\}$. Therefore, the expression (4.8) is also valid for $j = -n$ and this can be thought of as a continuity condition for the field $U$. Rewriting relation (4.8) for $j = -n-1$ and for $j = -n$, one gets

$$U_{-n-1}^{\mathsf{I}} = 1 + \mathsf{R}, \qquad U_{-n}^{\mathsf{I}} = \exp\{-\mathsf{i}\mathsf{K}\} + \mathsf{R}\exp\{\mathsf{i}\mathsf{K}\}. \tag{4.9}$$

2. In region $\mathrm{V_{II}}$, the general solution of equation (2.38) is given by relations (2.45) or (2.47) according to whether $\mu_\theta(\Omega) < 0$ or $\mu_\theta(\Omega) > 4\epsilon^2$.

   A When $\Omega < 1$, the general solution is given by relation (2.47). Accordingly, in region $\mathrm{V_{II}}$ the displacement can be written as

$$U_j^{\mathsf{II}} = \mathsf{A}^{\mathsf{II}} (-1)^{j+n+1} \cosh \mathsf{K}^*(j+n+1) + \mathsf{B}^{\mathsf{II}} (-1)^{j+n+1} \sinh \mathsf{K}^*(j+n+1), \tag{4.10}$$

where $\mathsf{A}^{\text{II}}$ and $\mathsf{B}^{\text{II}}$ have to be determined and $-n-1 \leq j \leq 0$. Note that relation (4.10) can still be used for $j=-n-1$ and $j=0$, *i.e.* for the last point in the region $\mathrm{V_I}$ of the matrix and for the point of the defect. This is a continuity condition for $U$ and using it for $j=-n-1$ and $j=-n$ gives $U^{\text{II}}_{-n-1}=\mathsf{A}^{\text{II}}$ and $U^{\text{II}}_{-n}=-\mathsf{A}^{\text{II}}\cosh\mathsf{K}^*-\mathsf{B}^{\text{II}}\sinh\mathsf{K}^*$. Comparing with relations (4.9) one has

$$\mathsf{A}^{\text{II}}=1+\mathsf{R} \qquad \mathsf{B}^{\text{II}}\sinh\mathsf{K}^*=-(1+\mathsf{R})\left(\cosh\mathsf{K}^*+\exp\{\mathsf{iK}\}\right)+2\mathsf{i}\sin\mathsf{K}. \tag{4.11}$$

B When $\Omega>1$, the general solution is given by relation (2.45). In region $\mathrm{V_{II}}$ the displacement reads

$$U^{\text{II}}_j=\mathsf{A}^{\text{II}}\cosh\mathsf{K}^*(j+n+1)+\mathsf{B}^{\text{II}}\sinh\mathsf{K}^*(j+n+1). \tag{4.12}$$

Using relation (4.12) for $j=-n-1$ and $j=-n$ gives $U^{\text{II}}_{-n-1}=\mathsf{A}^{\text{II}}$ and $U^{\text{II}}_{-n}=\mathsf{A}^{\text{II}}\cosh\mathsf{K}^*+\mathsf{B}^{\text{II}}\sinh\mathsf{K}^*$. Comparing with relation (4.9) one has

$$\mathsf{A}^{\text{II}}=1+\mathsf{R} \qquad \mathsf{B}^{\text{II}}\sinh\mathsf{K}^*=-(1+\mathsf{R})\left(\cosh\mathsf{K}^*-\exp\{\mathsf{iK}\}\right)-2\mathsf{i}\sin\mathsf{K}. \tag{4.13}$$

3. In region $\mathrm{V_V}$, assuming that no wave comes from the right, the displacement can be written as

$$U^{\text{V}}_j=\mathsf{A}^{\text{V}}\exp\{-\mathsf{iK}(j-n-1)\}, \quad j\geq+n, \tag{4.14}$$

$\mathsf{A}^{\text{V}}=\mathsf{T}$ denoting the amplitude of the transmitted signal. This expression is also valid for $j=+n$, the last point in the region $\mathrm{V_{IV}}$ of metamaterial. Therefore, one gets

$$U^{\text{V}}_{+n+1}=\mathsf{T} \qquad U^{\text{V}}_{+n}=\mathsf{T}\exp\{\mathsf{iK}\}. \tag{4.15}$$

4. In region $\mathrm{V_{IV}}$, as in region $\mathrm{V_{II}}$, the general solution of equation (2.38) is given by either relation (2.45) or (2.47).

A When $\Omega<1$, the general solution is given by relation (2.47):

$$U^{\text{IV}}_j=\mathsf{A}^{\text{IV}}(-1)^{j-n-1}\cosh\mathsf{K}^*(j-n-1)+\mathsf{B}^{\text{IV}}(-1)^{j-n-1}\sinh\mathsf{K}^*(j-n-1) \tag{4.16}$$

where $\mathsf{A}^{\text{IV}}$ and $\mathsf{B}^{\text{IV}}$ have to be determined and $0\leq j\leq+n+1$. Using relation (4.16) for $j=+n+1$ (which corresponds to the first point in the region $\mathrm{V_V}$) and for $j=+n$, gives $U^{\text{IV}}_{+n+1}=\mathsf{A}^{\text{IV}}$ and $U^{\text{IV}}_{+n}=-\mathsf{A}^{\text{IV}}\cosh\mathsf{K}^*+\mathsf{B}^{\text{IV}}\sinh\mathsf{K}^*$. Comparing with relation (4.15) one has

$$\mathsf{A}^{\text{IV}}=\mathsf{T}, \qquad \mathsf{B}^{\text{IV}}\sinh\mathsf{K}^*=\mathsf{T}\left(\cosh\mathsf{K}^*+\exp\{\mathsf{iK}\}\right). \tag{4.17}$$

B When $\Omega>1$, the general solution is given by (2.45)

$$U^{\text{IV}}_j=\mathsf{A}^{\text{IV}}\cosh\mathsf{K}^*(j-n-1)+\mathsf{B}^{\text{IV}}\sinh\mathsf{K}^*(j-n-1). \tag{4.18}$$

Using relation (4.18) for $j=+n+1$ and for $j=+n$, gives $U^{\text{IV}}_{+n+1}=\mathsf{A}^{\text{IV}}$ and $U^{\text{IV}}_{+n}=\mathsf{A}^{\text{IV}}\cosh\mathsf{K}^*-\mathsf{B}^{\text{IV}}\sinh\mathsf{K}^*$. Comparing with relation (4.15) one has

$$\mathsf{A}^{\text{IV}}=\mathsf{T}, \qquad \mathsf{B}^{\text{IV}}\sinh\mathsf{K}^*=\mathsf{T}\left(\cosh\mathsf{K}^*-\exp\{\mathsf{iK}\}\right). \tag{4.19}$$

5. In region $\mathrm{V}_{\mathsf{III}}$, the displacement can be written as

$$U_j^{\mathsf{III}} = \mathsf{A}^{\mathsf{III}} \exp\{-\mathsf{i}\mathsf{K}j\} + \mathsf{B}^{\mathsf{III}} \exp\{\mathsf{i}\mathsf{K}j\}, \quad -1 \leq j \leq +1, \tag{4.20}$$

where $\mathsf{A}^{\mathsf{III}}$ and $\mathsf{B}^{\mathsf{III}}$ have to be determined. Applying this expression for $j = -1$ and $j = +1$, one obtains $U_{-1}^{\mathsf{III}} = \mathsf{A}^{\mathsf{III}} \exp\{\mathsf{i}\mathsf{K}\} + \mathsf{B}^{\mathsf{III}} \exp\{-\mathsf{i}\mathsf{K}\}$ and $U_{+1}^{\mathsf{III}} = \mathsf{A}^{\mathsf{III}} \exp\{-\mathsf{i}\mathsf{K}\} + \mathsf{B}^{\mathsf{III}} \exp\{\mathsf{i}\mathsf{K}\}$.

We are now able to calculate the displacement of the mass in the defect. In what follows, we only show in detail the calculations for frequencies belonging to band gap A. The same procedure can be also applied for frequencies inside band gap B, with small differences that will result in a slightly changed expression for the displacement of the mass inside the defect (see the final relations (4.27) and (4.28)).

The continuity of displacement and stress fields at the interface between parts $\mathsf{II}$, $\mathsf{III}$ and between parts $\mathsf{III}$, $\mathsf{IV}$ entails:

$$\begin{cases} U_{-1}^{\mathsf{II}} = U_{-1}^{\mathsf{III}} \\ U_0^{\mathsf{II}} = U_0^{\mathsf{III}} \end{cases}, \quad \begin{cases} U_{+1}^{\mathsf{IV}} = U_{+1}^{\mathsf{III}} \\ U_0^{\mathsf{IV}} = U_0^{\mathsf{III}} \end{cases}.$$

From relations (4.10), (4.16), and (4.20), by using relations (4.11) and (4.17), these two systems of equations can be rewritten as

$$\begin{bmatrix} \exp\{\mathsf{i}\mathsf{K}\} & \exp\{-\mathsf{i}\mathsf{K}\} \\ 1 & 1 \end{bmatrix} \begin{bmatrix} \mathsf{A}^{\mathsf{III}} \\ \mathsf{B}^{\mathsf{III}} \end{bmatrix} = \frac{(-1)^n}{\sinh \mathsf{K}^*} \begin{bmatrix} -(\mathsf{R}\,\alpha + \overline{\alpha}) \\ \mathsf{R}\,\beta + \overline{\beta} \end{bmatrix} \tag{4.21}$$

$$\begin{bmatrix} \exp\{-\mathsf{i}\mathsf{K}\} & \exp\{\mathsf{i}\mathsf{K}\} \\ 1 & 1 \end{bmatrix} \begin{bmatrix} \mathsf{A}^{\mathsf{III}} \\ \mathsf{B}^{\mathsf{III}} \end{bmatrix} = \frac{\mathsf{T}\,(-1)^n}{\sinh \mathsf{K}^*} \begin{bmatrix} -\alpha \\ \beta \end{bmatrix} \tag{4.22}$$

with $\alpha$ and $\beta$ defined as

$$\alpha = \sinh \mathsf{K}^*(n-1) + \exp\{\mathsf{i}\mathsf{K}\} \sinh \mathsf{K}^* n, \quad \beta = \sinh \mathsf{K}^* n + \exp\{\mathsf{i}\mathsf{K}\} \sinh \mathsf{K}^*(n+1).$$

From systems (4.21) and (4.22) one finds:

$$\begin{cases} \mathsf{A}^{\mathsf{III}} = \dfrac{(-1)^{n+1}}{2\mathsf{i} \sin \mathsf{K} \sinh \mathsf{K}^*} \{\overline{c} + \mathsf{R}\, d\} \\ \mathsf{B}^{\mathsf{III}} = \dfrac{(-1)^n}{2\mathsf{i} \sin \mathsf{K} \sinh \mathsf{K}^*} \left\{\overline{d} + \mathsf{R}\, c\right\} \end{cases} \tag{4.23}$$

$$\begin{cases} \mathsf{A}^{\mathsf{III}} = \dfrac{\mathsf{T}\,(-1)^n}{2\mathsf{i} \sin \mathsf{K} \sinh \mathsf{K}^*} \{c\} \\ \mathsf{B}^{\mathsf{III}} = \dfrac{\mathsf{T}\,(-1)^{n+1}}{2\mathsf{i} \sin \mathsf{K} \sinh \mathsf{K}^*} \{d\} \end{cases} \tag{4.24}$$

with $c$ and $d$ given by:

$$c = \alpha + \beta \exp\{\mathsf{i}\mathsf{K}\}, \quad d = \alpha + \beta \exp\{-\mathsf{i}\mathsf{K}\}.$$

By imposing the equality between the amplitudes $\mathsf{A}^{\text{III}}$ and $\mathsf{B}^{\text{III}}$ in (4.23) and the corresponding ones in (4.24), $\mathsf{R}$ and $\mathsf{T}$ can be found from:

$$\begin{bmatrix} d & c \\ c & d \end{bmatrix} \begin{bmatrix} \mathsf{R} \\ \mathsf{T} \end{bmatrix} = - \begin{bmatrix} \overline{c} \\ \overline{d} \end{bmatrix}.$$

Hence, the coefficient $\mathsf{R}$ of the reflected wave and $\mathsf{T}$ of the transmitted wave read

$$\mathsf{R} = \frac{-\overline{c}d + c\overline{d}}{d^2 - c^2}, \qquad \mathsf{T} = \frac{-d\overline{d} + c\overline{c}}{d^2 - c^2}. \tag{4.25}$$

Finally, the displacement of the point inside the defect takes the form

$$U_0^{\text{III}} = \mathsf{A}^{\text{III}} + \mathsf{B}^{\text{III}}, \tag{4.26}$$

that, with relations (4.24) and the second of relations (4.25), gives

$$U_0^{\text{III}} = \frac{(-1)^n \mathsf{i} \sin \mathsf{K} \ \sinh \mathsf{K}^*}{\sinh(n-1)\mathsf{K}^* + (\exp\{\mathsf{i}\mathsf{K}\} + \cos \mathsf{K}) \ \sinh n\mathsf{K}^* + \exp\{\mathsf{i}\mathsf{K}\} \cos \mathsf{K} \ \sinh(n+1)\mathsf{K}^*}. \tag{4.27}$$

Relation (4.27), as stated before, is valid for frequencies belonging to band gap A. When band gap B is considered, $U_0^{\text{III}}$ slightly changes and is given by

$$U_0^{\text{III}} = \frac{\mathsf{i} \sin \mathsf{K} \ \sinh \mathsf{K}^*}{\sinh(n-1)\mathsf{K}^* - (\exp\{\mathsf{i}\mathsf{K}\} + \cos \mathsf{K}) \ \sinh n\mathsf{K}^* + \exp\{\mathsf{i}\mathsf{K}\} \cos \mathsf{K} \ \sinh(n+1)\mathsf{K}^*}. \tag{4.28}$$

## 4.4 The mechanical energy involved in the system

Let us now study the localization phenomenon in terms of the mechanical energy that is traveling through the system. Specifically, our aim is that of comparing the case where attenuation is predominantly due to a Bragg scattering phenomenon, with the case mainly characterized by local resonances.

In the subsequent calculations, we will often use the average of quantities over a period of time

$$\langle \bullet \rangle_t := \frac{1}{T} \int_0^T (\bullet) dt$$

and we will generally omit the subscript since no confusion with the spatial average can arise. We also make use of the following relation for the time average of a harmonically varying quantity $u = U \exp \mathsf{i}\omega t$:

$$\langle (\mathcal{R}e(u))^2 \rangle = \frac{1}{2} \, U \, \overline{U} = \frac{1}{2} \ |U|^2 . \tag{4.29}$$

### 4.4.1 Mechanical energy of the barriers

The mechanical energy density of the barriers $e_j^i$, with $i = \mathsf{II}, \mathsf{IV}$ and $j$ denoting the $j$-th mass $m_1$, is the sum of the potential energy density $p_j^i$ and the kinetic energy density $c_j^i$, that are given by:

$$\begin{cases} p_j^i = \dfrac{1}{2\ell}\left\{\dfrac{k_1}{2}\left[\mathcal{R}e(u_{j+1}^i - u_j^i)\right]^2 + \dfrac{k_1}{2}\left[\mathcal{R}e(u_j^i - u_{j-1}^i)\right]^2 + k_2\left[\mathcal{R}e(v_j^i - u_j^i)\right]^2\right\} \\ c_j^i = \dfrac{1}{2\ell}\left\{m_1\left[\mathcal{R}e(\dot{u}_j^i)\right]^2 + m_2\left[\mathcal{R}e(\dot{v}_j^i)\right]^2\right\} \end{cases}. \tag{4.30}$$

Normalizing relations (4.30) with $k_2\ell$, the dimensionless mechanical energy density $\gamma_j^i = e_j^i/(k_2\ell)$ can be found. Using relation (4.29) for averaging with respect to time relations (4.30) and then substituting equation (2.37), the dimensionless averaged mechanical energy density $\langle\gamma_j^i\rangle$ can be written as

$$\langle\gamma_j^i\rangle = \frac{1}{4\ell^2}\left\{\frac{\epsilon^2}{2}\left[\left|U_{j+1}^i - U_j^i\right|^2 + \left|U_j^i - U_{j-1}^i\right|^2\right] + \left[\mu_\theta + \frac{2\Omega^2}{(1-\Omega)^2}\right]\left|U_j^i\right|^2\right\}, \tag{4.31}$$

with $i = \mathsf{II}, \mathsf{IV}$ and $j$ denoting the $j$-th mass $m_1$. We recall that terms $\epsilon$ and $\mu_\theta$ are respectively the stiffness ratio and the effective mass for the mass-in-mass chain (*cf.* relations (2.35) and (2.38)).

As shown previously, the motion $U_j^i$ of the $j$-th mass $m_1$ belonging to the $i$-th part depends on whether the frequency of the incoming wave belongs to band gap A or B. Therefore, inserting either relations (4.10) and (4.16) or (4.12) and (4.18) in relation (4.31), the averaged mechanical energy density in the two cases can be expressed as follows:

- Band gap A.

$$\begin{aligned} \langle\gamma_j^i\rangle = &\frac{1}{4\ell^2}\left\{\left(\mu_\theta + \frac{\Omega^2}{(1-\Omega)^2}\right)\left[\left|\mathsf{A}^i\right|^2 - \left|\mathsf{B}^i\right|^2\right]\right. \\ &+ \left(\frac{1+\cosh\mathsf{K}^*}{2} + \frac{\Omega^2}{(1-\Omega)^2}\right)\left[\left(\left|\mathsf{A}^i\right|^2 + \left|\mathsf{B}^i\right|^2\right)\cosh 2\mathsf{K}^* s\right. \\ &\left.\left. + 2\left(\mathcal{R}e(\mathsf{A}^i)\mathcal{R}e(\mathsf{B}^i) + \mathcal{I}m(\mathsf{A}^i)\mathcal{I}m(\mathsf{B}^i)\right)\sinh 2\mathsf{K}^* s\right]\right\} \end{aligned} \tag{4.32}$$

- Band gap B.

$$\begin{aligned}\langle\gamma_j^i\rangle =& \frac{1}{4\ell^2}\Bigg\{\left(\mu_\theta + \frac{\Omega^2}{(1-\Omega)^2}\right)\left[\left|\mathsf{A}^i\right|^2 - \left|\mathsf{B}^i\right|^2\right] \\ &+ \left(\frac{1-\cosh\mathsf{K}^*}{2} + \frac{\Omega^2}{(1-\Omega)^2}\right)\Bigg[\left(\left|\mathsf{A}^i\right|^2 + \left|\mathsf{B}^i\right|^2\right)\cosh 2\mathsf{K}^* s \\ &+ 2\left(\mathcal{R}e(\mathsf{A}^i)\mathcal{R}e(\mathsf{B}^i) + \mathcal{I}m(\mathsf{A}^i)\mathcal{I}m(\mathsf{B}^i)\right)\sinh 2\mathsf{K}^* s\Bigg]\Bigg\}\end{aligned} \tag{4.33}$$

with

$$\begin{cases} i = \mathsf{II} \text{ and } s = j + n + 1 \\ i = \mathsf{IV} \text{ and } s = j - n - 1 \end{cases}.$$

### 4.4.2 Mechanical energy of the mass-spring chain

The dimensionless averaged mechanical energy density $\langle\gamma_j\rangle$ of the $j$-th unit cell for a mass-spring chain (regions $\mathrm{V}_\mathsf{I}$, $\mathrm{V}_\mathsf{III}$ and $\mathrm{V}_\mathsf{IV}$ of the system) is given by:

$$\langle\gamma_j^i\rangle = \frac{1}{4\ell^2}\left\{\frac{\epsilon^2}{2}\left|U_{j+1}^i - U_j^i\right|^2 + \frac{\epsilon^2}{2}\left|U_j^i - U_{j-1}^i\right|^2 + \Omega\theta\left|U_j^i\right|^2\right\}, \tag{4.34}$$

with $i = \mathsf{I}, \mathsf{III}, \mathsf{V}$. The motion $U_j^i$ of the $j$-th mass $m_1$ is obtained either from relation (4.8), (4.14) or (4.20). Inserting these latter relations into (4.34), one obtains:

$$\begin{aligned}\langle\gamma_j^i\rangle =& \frac{2\epsilon^2}{\ell^2}\sin^2\frac{\mathsf{K}}{2}\Bigg\{\left[\left|\mathsf{A}^i\right|^2 + \left|\mathsf{B}^i\right|^2\right] \\ &+ (1-\cos\mathsf{K})\Big[\left(\mathcal{R}e(\mathsf{A}^i)\mathcal{R}e(\mathsf{B}^i) + \mathcal{I}m(\mathsf{A}^i)\mathcal{I}m(\mathsf{B}^i)\right)\cos 2\mathsf{K}j \\ &+ \left(\mathcal{I}m(\mathsf{A}^i)\mathcal{R}e(\mathsf{B}^i) - \mathcal{R}e(\mathsf{A}^i)\mathcal{I}m(\mathsf{B}^i)\right)\sin 2\mathsf{K}j\Big]\Bigg\},\end{aligned} \tag{4.35}$$

with $\mathsf{A}^i$ and $\mathsf{B}^i$ denoting the wave amplitudes for the $i$-th part, with $i = \mathsf{I}, \mathsf{III}, \mathsf{V}$, and where we have used relation (4.3). Note that the defect (region $\mathrm{V}_\mathsf{III}$) is composed by a single cell, therefore only $j = 0$ is considered.

### 4.4.3 The localization phenomenon

Let us now consider the localization phenomenon. By tuning the parameters governing the problem, it is possible to exploit either a Bragg or a locally resonant behavior for focusing inside the defect the energy carried by an incoming wave. Specifically, as shown in figures 2.6 and 2.7, the two attenuating mechanisms can be activated depending on the values chosen for $\theta$ and $\epsilon$. The number $n$ of unit cells composing each barrier only

modifies the efficacy of the attenuation generated by the barriers and, hence, it can be fixed without varying the width of band gaps A and B.

In what follows, we fix $n = 2$ and discuss several systems characterized by different $\theta$ and $\epsilon$. Selecting *e.g.* $\theta = 1$ and looking at figure 4.4a, depending on $\epsilon$ the system can work either with $\Omega$ belonging only to band gap A, to band gap A and B, or only to band gap B. Specifically, one has:

$$\begin{cases} \epsilon^2 \leq \theta/4 & \text{only band gap A} \\ \theta/4 < \epsilon^2 < \mathcal{O}(1) & \text{band gaps A and B} \\ \epsilon^2 >> 1 & \text{only band gap B} \end{cases}$$

Therefore, the following three cases are analyzed: $\epsilon = 0.4$, $\epsilon = 1$ and $\epsilon = 3$ (this latter value is high enough to consider the problem governed only by band gap B).

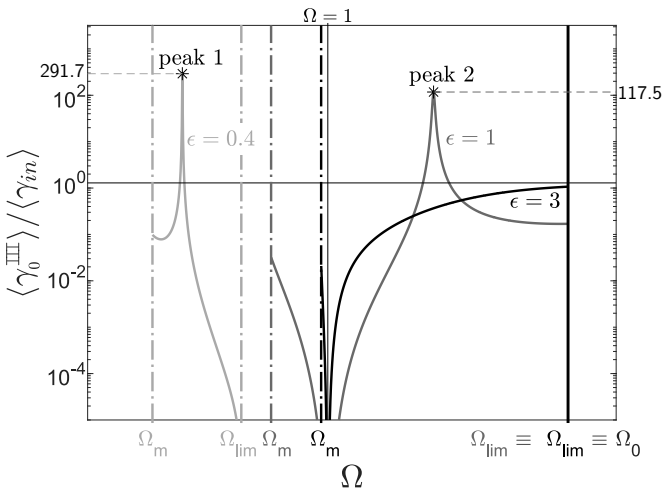


Figure 4.5: *averaged mechanical energy density of the defect* $\langle \gamma_0^{III} \rangle$*, normalized with respect to* $\langle \gamma_{in} \rangle$ *(i.e. the energy carried by the incoming wave) versus frequency* $\Omega$ *for:* $\epsilon = 0.4$ *(light gray),* $\epsilon = 1$ *(gray) and* $\epsilon = 3$ *(black). A logarithmic scale is used for the vertical axis. The vertical dashed-dotted lines delimit the intervals of frequencies* $\Omega$ *respecting condition* (4.7) *for each of the three considered* $\epsilon$*. The vertical line at* $\Omega = 1$ *separates band gap A from band gap B. When* $\epsilon = 3$*, the normalized energy density is not experiencing any peak and is smaller than* 1 $\forall\Omega$ *respecting condition* (4.7)*.*

By employing relations (4.35) and (4.3), the averaged mechanical energy density of the unit cell composing the defect $\langle \gamma_0^{III} \rangle$, normalized with respect to the incoming energy $\langle \gamma_{in} \rangle$, can be plotted as a function of the frequency $\Omega$, as shown in figure 4.5, where a logarithmic scale is used for the vertical axis. More specifically, the energy has been computed only for those frequencies respecting condition (4.7), which itself depends on $\epsilon$; for this reason, the intervals of frequencies between $\Omega_m$ and $\Omega_{lim}$ vary for the three cases.

From figure 4.5, for $\epsilon = 0.4$ and $\epsilon = 1$ a peak appears ("peak 1" and "peak 2" respectively) that corresponds to a maximum localization of the incoming energy and, more in general, to a defect mode in the spectrum of the problem. Normally, for $\Omega$ belonging to a band gap, the presence of the first barrier generates a reflected wave and, as a consequence, the energy transmitted to the defect should be less than the incoming one ($\langle\gamma_0^{\text{III}}\rangle/\langle\gamma_{in}\rangle \leq 1$). The presence of a peak greater than 1 confirms that the introduction of a defect gives rise to a peculiar behavior, causing an accumulation of the energy traveling along the system. Nevertheless, the localization doesn't always take place, as one can verify by looking at the behavior of $\langle\gamma_0^{\text{III}}\rangle/\langle\gamma_{in}\rangle$ for $\epsilon = 3$ (see figure 4.5): for this particular value, no peaks are present.

Note that, up to now, we are not modifying the cavity width. Our aim here is indeed not that of designing and optimizing the REH (as we will do in the next chapter), but it is simply that of checking that the system, as we have imagined it, is capable of effectively localizing some mechanical energy. For this, we analyze the discrete REH with a fixed width for the defect, corresponding to that of one unit cell for the chain, without knowing *a priori* if a defect mode appears in the band gap of the mass-in-mass chain. In general, as we stated in the introduction of the current chapter, a defect generated by removing the inclusion from one cell (as it is the case here) is not enough for continuous LRMs to assure the presence of defect modes. This is possible here because of the dispersive behavior of the mass-spring chain that composes the defect and that enables for the presence of waves in the cavity with wave lengths of the order of one unit cell, already at frequencies that are sub-wavelengths for the two barriers.

"Peak 1" and "peak 2" appear respectively at $\Omega = 0.394$ and $\Omega = 1.440$. Considering these two frequencies, the normalized energy $\langle\gamma_j\rangle/\langle\gamma_{in}\rangle$ along the entire system is shown in figure 4.6 ($j \in \mathbb{Z}$ indicates the $j$-th unit cell). The behavior of the system is very similar for the two cases, although the level of concentration for $\epsilon = 0.4$ (figure 4.6a) is higher than that of $\epsilon = 1$ (figure 4.6b). This aspect can also be quantified by introducing what we have indicated as *Index of Concentration* (IC), defined as follows:

$$IC = \frac{\langle E^{\text{III}}\rangle}{\langle E^{\text{II}}\rangle + \langle E^{\text{III}}\rangle + \langle E^{\text{IV}}\rangle}, \tag{4.36}$$

with $E^i$ denoting the total mechanical energy of the $i$-th part, simply given by $E^i = \ell \sum_j \gamma_j \, k_2 \ell$, for $j \in$ part $i$-th (this means that the sum considers all the unit cells $j$ composing the $i$-th part). Using this index for peaks 1 and 2, one obtains respectively $IC_1 = 0.57$ and $IC_2 = 0.33$, thus confirming a larger localization for $\epsilon = 0.4$.

Since "peak 1" belongs to band gap A and "peak 2" to band gap B, the above analysis shows that both Bragg scattering and local resonance can generate a localization phenomenon.

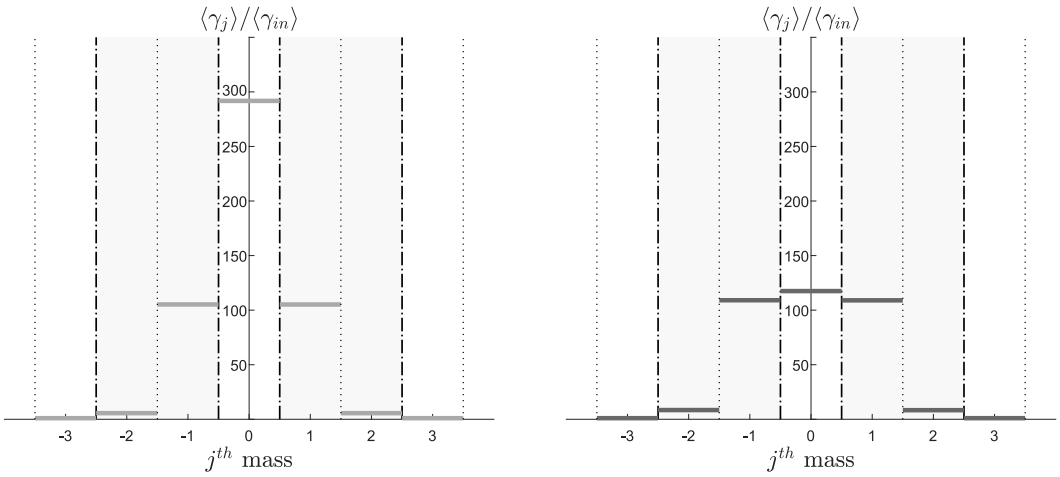


(a) (b)

Figure 4.6: *mechanical energy density $\gamma^j$ of each unit cell $j$ composing the system, averaged over a time period and normalized with respect to the incoming one, for $\Omega$ corresponding to "peak 1" (figure 4.6a) and "peak 2" (figure 4.6b). The vertical dotted lines are used to separate the different unit cells; moreover, the dashed-dotted vertical lines delimit the two barriers in both figures.*

## 4.5 Motion of the mass in the defect

Let us now go back to the study of the motion $U_0^{\text{III}}$ of the mass inside the defect and how its presence affects the transmission coefficient $\mathsf{T}$. In particular, as we had stated before, a maximum of energy coincides with a maximum localization of the motion of the defective unit cell. By using the second of relations (4.25) and (4.26), both quantities can be expressed for varying frequencies. This is shown in figures 4.7a and 4.7b, where we plot respectively $\left|U_0^{\text{III}}(\Omega)\right| / |U_{in}|$ ($U_{in}$ is the motion imposed in part $\text{V}_\text{I}$ by the incoming wave) and $|\mathsf{T}(\Omega)|$, again only for those frequencies verifying condition (4.7), for each $\epsilon$. In figure 4.7a, a logarithmic scale is used for the vertical axis. When $\epsilon = 0.4$ and $\epsilon = 1$, both plots in figure 4.7 present one peak, exactly at the same frequency where $\langle\gamma_0^{\text{III}}(\Omega)\rangle/\langle\gamma_{in}\rangle$ is maximum. These frequencies also correspond to perfect transmission (*i.e.* $|\mathsf{T}| = 1$): this is another peculiar behavior activated by the presence of a defect. Note also that this result coincides with the one coming from the resonant tunneling phenomenon, that was described earlier on in this chapter.

### 4.5.1 Localization in the time domain

Up to now, we have only considered the behavior of the system at its steady state for a given frequency. Here we also analyze numerically the problem in the time domain, by means of a centered finite difference scheme and we check that, for $\epsilon = 0.4$ and $\epsilon = 1$

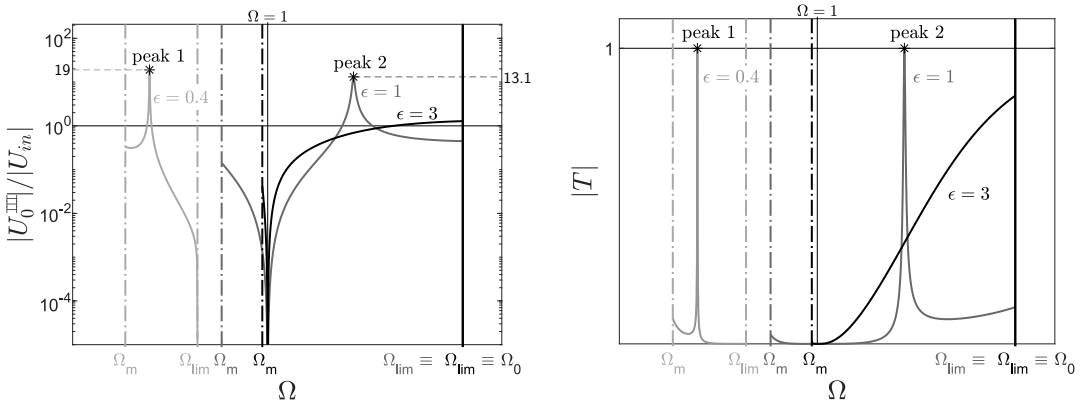


Figure 4.7: *(a) Displacement magnitude* $\left|U_0^{\text{III}}\right|$ *of the mass inside the defect normalized with the amplitude* $|U_{in}|$ *of the incoming wave, as a function of* $\Omega$*. A logarithmic scale is used for the vertical axis. (b) Modulus* $|\mathsf{T}|$ *of the transmission coefficient versus* $\Omega$*. The different colors refer to the three different* $\epsilon$ *(light gray:* $\epsilon = 0.4$*, gray:* $\epsilon = 1$*, black:* $\epsilon = 3$*).*

and for a time $t$ large enough, $\left|U_0^{\text{III}}(t)\right| / |U_{in}|$ tends to the peak values shown in figure 4.7a and $|\mathsf{T}(t)| \approx 1$ ($|U_{in}|$ is not a function of $t$ because it is imposed to be constant).

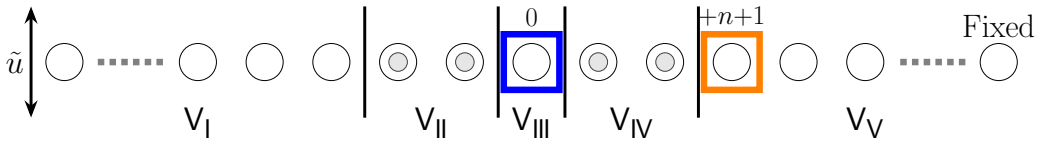


Figure 4.8: *sketch of the system used for the time domain analysis. Parts* $\mathrm{V_I}$ *and* $\mathrm{V_V}$ *are now of finite thickness. The first mass on the left is subjected to an imposed displacement* $\tilde{u} = \sin \omega t$*, with* $\omega = \sqrt{\overline{\Omega}}\,\omega_2$ *and* $\overline{\Omega}$ *denoting the peak frequency under consideration. The last mass on the right is fixed. Masses* $j = 0$ *(blue) and* $j = +n+1$ *(orange) are evidenced for later use.*

Figure 4.8 schematically represents the system used for the time domain analysis. In order to carry out a numerical solution of the problem, we considered finite dimensions for parts $\mathrm{V_I}$ and $\mathrm{V_V}$ and we imposed boundary conditions on the first and final mass respectively of parts $\mathrm{V_I}$ and $\mathrm{V_V}$. In particular, the motion of the first mass on the left is constrained to be $\tilde{u} = \sin \omega t$ (the amplitude of the generated incoming wave is hence equal to 1, $|U_{in}| = 1$), with $\omega = \sqrt{\overline{\Omega}}\,\omega_2$, where $\overline{\Omega}$ is the frequency of the peaks computed in the previous section; the last mass on the right instead is fixed. By choosing the properties of the resonator (mass $m_2$ and spring $k_2$), $\omega_2$ is defined and thus also $\omega$. The two quantities of interest, namely $\left|U_0^{\text{III}}(t)\right|$ and $|\mathsf{T}(t)|$, are the amplitudes, for large $t$,

of the displacements $|u_0(t)|$ and $|u_{+n+1}(t)|$ of the masses highlighted respectively in orange and blue in figure 4.8. They can be derived by analyzing the motion of the two masses with respect to time, as shown in figures 4.9a ($\epsilon = 0.4$) and 4.10a ($\epsilon = 1$). In particular, the amplitude $|u_0(t)|$ at large $t$ almost coincides with the corresponding

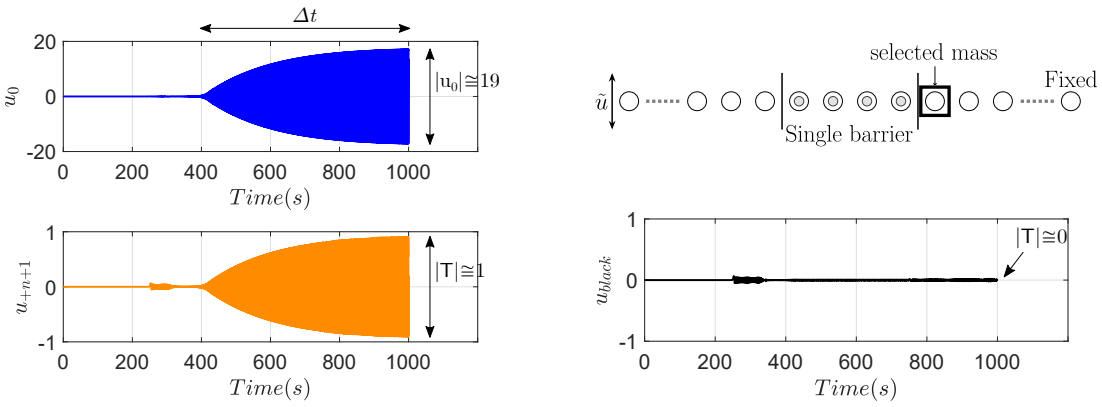


Figure 4.9: *(a) Oscillations in time of displacements $u_0$ and $u_{+n+1}$ of the masses evidenced respectively in blue and orange in figure 4.8. (b) Oscillation in time of the displacement of the first cell after a barrier without defect (sketch above). Material parameters: $\theta = 1$, $\epsilon = 0.4$, $m_2 = 0.01$ kg, $k_2 = 1$ N $m^{-1}$.*

value $\left|U_0^{\text{III}}(\Omega)\right|$ shown in figure 4.7a, for both peaks; moreover, again for large $t$, the amplitude $|u_{+n+1}(t)|$ of the transmitted wave tends to 1. This verifies the localization phenomenon and quantifies the time frame $\Delta t$, which is necessary for the system to reach the maximum level of concentration. More in details, the transitory time $\Delta t$ depends on the final level of energy concentration inside the cavity, when a stationary condition is reached. The higher is the energy peak in figure 4.5, the larger will be the time needed for reaching the final regime. This is shown in figures 4.9a and 4.10a: the transitory time for "peak 1" is larger with respect to that related to "peak 2". As the level of concentration depends on the level of attenuation provided by the barriers at the frequency corresponding to a peak of energy, the transitory time is indirectly influenced by both the stiffness and mass ratios.

An important remark is here necessary: the presence of boundaries could affect the result by generating reflected waves that, nevertheless, need some time to reach the two masses of interest. Therefore, by tuning the total time of the analysis in relation to the speed of the traveling waves and the number of unit cells used in parts $\text{V}_\text{I}$ and $\text{V}_\text{V}$, it is possible to neglect the presence of these reflected waves.

The influence of the defect can be finally evidenced by considering the system schematically depicted in figures 4.9b, 4.10b (above) and analyzing the amplitude $|u_{black}(t)|$ of the transmitted wave, *i.e.* the amplitude of the motion of the mass

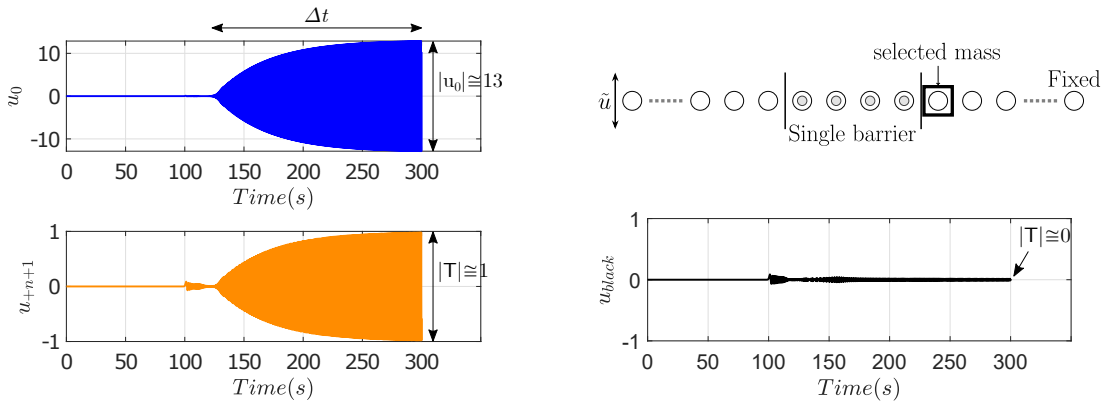


Figure 4.10: *(a) Oscillations in time of displacements $u_0$ and $u_{+n+1}$ of the masses evidenced respectively in blue and orange in figure 4.8. (b) Oscillation in time of the displacement of the first cell after a barrier without defect (sketch above). Material parameters: $\theta = 1$, $\epsilon = 1$, $m_2 = 0.01$ kg, $k_2 = 1$ N $m^{-1}$.*

evidenced in black in the figures. The system is composed by a mass-spring chain with a single barrier of 4 cells without defect. For both $\epsilon$ the transmitted wave amplitude is almost zero, as shown in figures 4.9b and 4.10b (below). This final result confirms the substantial change of behavior with respect to the case with the defect.

Chapter 5

# Design of a 2D continuous resonant energy harvester

Chapter summary: *A defective continuous Locally Resonant Material (LRM) is analyzed. The system is treated by applying the homogenization technique previously described (see chapter 3). An analytic derivation of the problem is possible and the creation of defect modes in a band gap can be governed by modifying the width of the cavity. We thus find that the system can be designed to trap and to focus external energy that is traveling through it, i.e. that can behave as a Resonant Energy Harvester.*

## Contents



In the previous chapter we studied a discrete version of a defective metamaterial based on the mechanical counterpart of the resonant tunneling phenomenon. Following the results obtained for that case, we can argue that the same behavior could also characterize a continuous defective Locally Resonant Material (LRM) of the type analyzed in chapter 3.

Our aim here is that of designing a defective mematamaterial for sub-wavelength energy localization, with a structure that resembles very much that of the system depicted in figure 4.2. In this chapter, we thus combine the results from the homogenization technique treated in chapter 3 and the ideas presented in chapter 4 to conduct an analytic derivation of the problem of energy localization in our Resonant Energy Harvester (REH). More specifically, we will come up with a condition that enables to place and locate one defect mode in a band gap of the LRM under consideration.

The fundamental difference with respect to the discrete problem tackled in chapter 4 is that the homogeneous materials employed for the defect and the domain external to the LRM is characterized by a non-dispersive behavior. We have thus no such limitations on the frequencies as those indicated in subsection 4.3.2. This enables us to potentially dealing with any frequency from 0 to $+\infty$, by correctly placing a band gap at the frequencies of interest, *i.e.* by properly designing the LRM. Moreover, in general, we expect that removing just one row of inclusions from the LRM will not be sufficient for activating a localization phenomenon, unless one modifies the material used for the defect.

This chapter was the subject of the following publications: Moscatelli et al., 2020a,b.

## 5.1 Problem formulation

Let us consider the system represented in figure 5.1. The domain V is composed of five regions: parts $V_1$, $V_3$ and $V_5$ are constituted by an isotropic homogeneous medium (defined as $V_h$ in the following), whereas parts $V_2$ and $V_4$, which will be denoted as "barriers" ($V_b$), are made of the same LRM. This system coincides with the one described in the previous chapter and represented in figure 4.2, with a defect splitting the metamaterial in two regions. We will refer to the current system as Resonant Energy Harvester (REH).

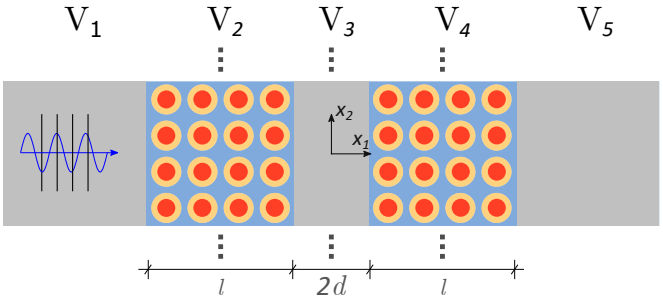


Figure 5.1: *Top-view of the studied system. The wave shown in the figure represents an out-of-plane wave propagating across all the five domains. The dots denote the fact that the system must be extended along the $x_2$ direction towards $\pm\infty$.*

The LRM employed is built from a 2D periodic repetition of a typical unit cell as the one represented in figure 5.2, with a stiff matrix $Y_m$ containing a very compliant

part denoted as $\mathrm{Y}_c$, that can possibly itself embed an almost rigid circular fiber $\mathrm{Y}_f$. The LRMs considered are thus of the same type as those described in chapter 3, as can be checked by looking at figure 3.1.

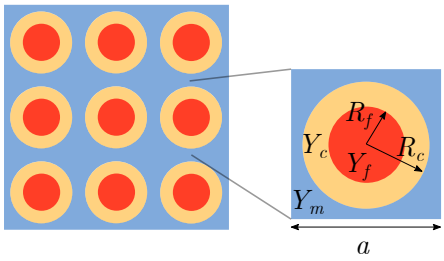


Figure 5.2: *Periodic structure of the LRM and zoom over a unit cell composing it. $R_f$ and $R_c$ are respectively the fiber and coating external radii.*

The system analyzed herein is thought of to possess a thickness in the out-of-plane direction and along the axis $x_2$ which is much larger than the characteristic size $a$ of the unit cell; parts $\mathrm{V}_1$ and $\mathrm{V}_5$ are considered as infinitely extended towards $-\infty$ and $+\infty$ along the axis $x_1$.

We analyze the propagation of anti-plane elastic waves along the $x_1$ direction, allowing for the decoupling from the in-plane wave propagation problem. Let us consider an harmonic regime (see section 2.1.1), such that

$$u(x,t) = U(x)\exp\{\mathrm{i}\omega t\},$$

resulting in the following problem:

$$\begin{cases} \nabla\cdot\boldsymbol{\sigma}(\boldsymbol{x}) + \rho(\boldsymbol{x})\omega^2 U(\boldsymbol{x}) = 0 & \text{in V} \\ \boldsymbol{\sigma}(\boldsymbol{x}) = \mu(\boldsymbol{x})\ \nabla(U(\boldsymbol{x})) & \text{in V} \\ U(\boldsymbol{x}) \text{ and } \boldsymbol{\sigma}(\boldsymbol{x})\cdot\boldsymbol{n} \text{ continuous at each interface,} \end{cases} \tag{5.1}$$

where $\boldsymbol{\sigma}$ collects the non vanishing stress components $\sigma_{[31]}$ and $\sigma_{[32]}$. The mass density $\rho$ and the shear elastic modulus $\mu$ are spatially varying parameters, depending on the position $\boldsymbol{x}$ in the system, as specified in the following:

$$\mu(\boldsymbol{x}) = \begin{cases} \mu_m & \text{in } \mathrm{Y}_m \\ \mu_f & \text{in } \mathrm{Y}_f \\ \mu_c & \text{in } \mathrm{Y}_c \\ \mu_h & \text{in } \mathrm{V}_h \end{cases}, \qquad \rho(\boldsymbol{x}) = \begin{cases} \rho_m & \text{in } \mathrm{Y}_m \\ \rho_f & \text{in } \mathrm{Y}_f \\ \rho_c & \text{in } \mathrm{Y}_c \\ \rho_h & \text{in } \mathrm{V}_h \end{cases}. \tag{5.2}$$

Denoting by $k_m = \omega\sqrt{\rho_m/\mu_m}$ the wavenumber in the matrix, we limit our study by considering a low frequency regime such that the dimensionless parameter $\varepsilon = k_m a$, defined in chapter 3, be very small ($\varepsilon \ll 1$). This assumption can be equivalently

set by requiring that the characteristic size $a$ of the cell be much smaller than the wave length, in the matrix, of the considered wave. As we showed in chapter 3, this hypothesis enables the application of a two-scale asymptotic homogenization technique for the description of the motion of the barriers. Specifically, since we are interested in resonances happening inside the inclusions, the product between the wavenumber $k_c$ in part $\mathrm{Y}_c$ and the characteristic size of the cell $a$ must be of order 1, namely $k_c a = \mathcal{O}(1)$. By assuming $\rho_m/\rho_c = \mathcal{O}(1)$, the ratio $\mu_c/\mu_m$ must be of order $\mathcal{O}(\varepsilon^2)$: this means that we shall consider a soft inclusion $\mathrm{Y}_c$ with a high contrast in the shear modulus with respect to part $\mathrm{Y}_f$.

### 5.1.1 Solution of the homogenized system

By virtue of the homogenization results, the barriers can be described by an equivalent material characterized by an effective mass density $\rho^{eff}$ and by an effective shear modulus $\mu^{eff}$. Consequently, for anti-plane waves, the REH is finally treated as an equivalent system composed of five *homogeneous* and isotropic parts. Since we are interested in the propagation of waves whose wave front is perpendicular to the $x_1$ direction, there is no dependency on the $x_2$ direction, $\sigma_{[32]} = 0$ and the problem becomes one-dimensional, obtaining the simplified system sketched in figure 5.3 (thick lines here and in the following figures always represent a LRM).

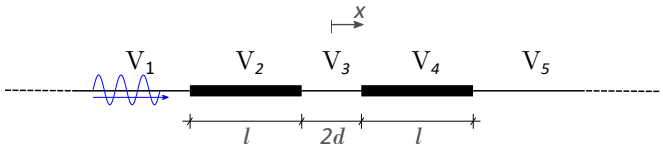


Figure 5.3: *One-dimensional scheme for the two-dimensional homogenized problem. The system is simplified by fixing a position along the $x_2$ axis and by considering $x_1 = x$. The dashed ends are used to indicate that the domain is infinitely extended towards $-\infty$ and $+\infty$.*

Let us report here below the homogenized problem for the motion inside each of the five parts composing the system:

$$\begin{cases} \partial\sigma(x)/\partial x + \rho_h \omega^2 U(x) = 0 & \text{in } \mathrm{V}_h \\ \sigma = \mu_h \, \partial U(x)/\partial x & \text{in } \mathrm{V}_h \\ \partial\sigma(x)/\partial x + \rho^{eff}(\omega)\, \omega^2 & \text{in } \mathrm{V}_b \\ U(x) = 0, \quad \sigma = \mu^{eff} \, \partial U(x)/\partial x & \text{in } \mathrm{V}_b \\ U(x) \text{ and } \sigma(x) \text{ continuous at each interface} & \end{cases} \tag{5.3}$$

where $U$ in parts $\mathrm{V}_b$ stands for the leading order approximation $U^0$ coming from the homogenization technique and $\sigma = \sigma_{[31]}$ denotes the only non-zero stress component.

As discussed in chapter 3, the sign of the effective mass density $\rho^{eff}$ depends on whether the frequency $\omega$ is inside or outside a band gap; this means that within the barriers $V_2$ and $V_4$ problem (5.3) has a general solution whose form varies depending on the frequency, as follows:

$$\begin{cases} U_j(x) = \mathsf{A}_j \, \exp\{-\mathsf{i}sx\} + \mathsf{B}_j \, \exp\{\mathsf{i}sx\} & \text{when } \rho^{eff} \geq 0 \\ U_j(x) = \mathsf{A}_j \, \cosh sx + \mathsf{B}_j \, \sinh sx & \text{when } \rho^{eff} < 0 \end{cases} \tag{5.4}$$

where

$$s = \omega \sqrt{\frac{\left|\rho^{eff}\right|}{\mu^{eff}}}$$

and $\mathsf{A}_j$, $\mathsf{B}_j$ (with $j = 2, 4$) are complex integration constants.

The general solution of the motion problem inside regions $V_h$ is instead always given by:

$$U_j(x) = \mathsf{A}_j \, \exp\{-\mathsf{i}kx\} + \mathsf{B}_j \, \exp\{\mathsf{i}kx\}, \tag{5.5}$$

with $j = 1$,3 or 5 and

$$k = k_h = \omega \sqrt{\frac{\rho_h}{\mu_h}}.$$

Considering a propagating incoming wave, the integration constants are obtained imposing the continuity of the displacement and of the stresses between the various regions and the conditions at $\pm\infty$. In particular, when considering a wave which travels from the left towards the right (see figure 5.3) of amplitude 1, the displacement in the different parts $V_i$ reads:

$$\begin{cases} U_1(x) = \exp\{-\mathsf{i}k(x+d+l)\} + \mathsf{R} \, \exp\{\mathsf{i}k(x+d+l)\} \\ U_2(x) = (1+\mathsf{R}) \, \cosh s(x+d+l) + \mathsf{i}\, a \, (\mathsf{R}-1) \, \sinh s(x+d+l) \\ U_3(x) = \dfrac{\mathsf{T}}{2} \, \beta \, \exp\{-\mathsf{i}k(x-d)\} + \dfrac{\mathsf{T}}{2} \, \alpha \, \exp\{\mathsf{i}k(x-d)\} \\ U_3(x) = \mathsf{T} \, \cosh s(x-d-l) - \mathsf{i}\, a \, \mathsf{T} \, \sinh s(x-d-l) \\ U_5(x) = \mathsf{T} \, \exp\{-\mathsf{i}k(x-d-l)\}, \end{cases} \tag{5.6}$$

where $\mathsf{R}$ and $\mathsf{T}$ are respectively the amplitudes of the reflected and transmitted wave:

$$\mathsf{T} = \frac{4}{\alpha^2 \, \exp\{2\mathsf{i}kd\} - \beta^2 \, \exp\{-2\mathsf{i}kd\}}, \tag{5.7}$$

$$\mathsf{R} = \frac{\alpha\beta \exp\{2\mathsf{i}kd\} - \bar{\alpha}\bar{\beta} \exp\{-2\mathsf{i}kd\}}{\alpha^2 \, \exp\{2\mathsf{i}kd\} - \beta^2 \, \exp\{-2\mathsf{i}kd\}}. \tag{5.8}$$

with

$$\mathsf{a} = \frac{\mu_m k}{\mu^{eff} s}, \quad \alpha = 2 \, \cosh sl + \mathsf{i} \left(\mathsf{a} - \frac{1}{\mathsf{a}}\right) \, \sinh sl, \quad \beta = \mathsf{i} \left(\mathsf{a} + \frac{1}{\mathsf{a}}\right) \, \sinh sl. \tag{5.9}$$

## 5.2 Transmission analyses: preliminary studies

Before dealing directly with the REH, let us first consider two cases: the transmission of a wave approaching towards an half-plane constituted by the LRM previously described (figure 5.4) and the transmission of a wave crossing a LRM of finite thickness (figure 5.5). In the figures, we have used the same conventions already described in figure 5.3.

### 5.2.1 Infinitely long barrier

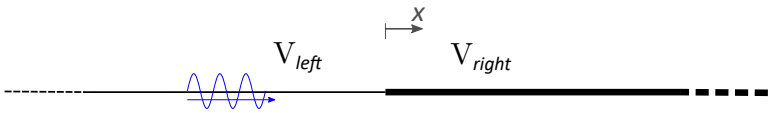


Figure 5.4: *Sketch of the system with an infinitely long barrier along direction $x$.*

Let us consider the system reported in Figure 5.4, the two domains indicated as $\mathrm{V}_{left}$ and $\mathrm{V}_{right}$ are of the same type respectively as $\mathrm{V}_h$ and $\mathrm{V}_b$, defined before. Consequently, the motion of the system can be written as[1]

$$\begin{cases} U_l(x) = \exp\{-\mathsf{i}kx\} + R\exp\{\mathsf{i}kx\} & \text{in } \mathrm{V}_{left} \\ U_r(x) = A_2\cosh sx + B_2\sinh sx & \text{in } \mathrm{V}_{right} \end{cases} \tag{5.10}$$

By imposing the condition that the solution does not diverge for $x \to +\infty$, the following relation must hold true $A_2 = -B_2$. Applying the continuity of displacements and stresses at the interface, all the coefficients can be found. The complex amplitude of the reflected wave is:

$$R = \frac{\mathsf{ia}-1}{\mathsf{ia}+1}, \tag{5.11}$$

where the parameter $\mathsf{a}$ was defined in (5.9).

Note that $|R| = 1$ as expected, since otherwise some energy would pile up somewhere between $x = 0$ and $x \to +\infty$; as the metamaterial is not defective, this cannot happen. In part $\mathrm{V}_{right}$ the displacement finally reads as

$$U_r(x) = \frac{2\mathsf{ia}}{\mathsf{ia}+1}\exp(-sx)$$

and hence is exponentially decreasing with $x$.

[1]Note that in relations (5.10) the constants are not *sans serif*, to distinguish them from those used for the problem in the REH. The same comment is valid also for the next subsection.

### 5.2.2 Penetration across a single finite barrier

Let us look at the system depicted in figure 5.5. Now the general solutions inside each domain are given by

$$\begin{cases} U_l(x) = \exp\{-\mathsf{i}k(x+l)\} + R\exp\{\mathsf{i}k(x+l)\} & \text{in } \mathrm{V}_{left} \\ U_c(x) = A_2\cosh sx + B_2\sinh sx & \text{in } \mathrm{V}_{central} \\ U_r(x) = T\exp\{\mathsf{i}k(x-l)\} & \text{in } \mathrm{V}_{right} \end{cases} \tag{5.12}$$

Again the continuity of the displacement and stress fields allows to compute all the

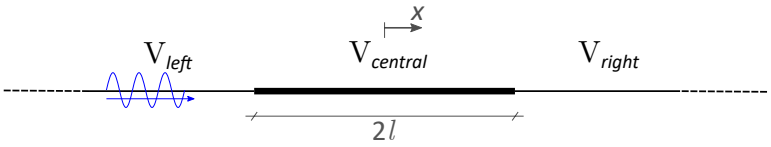


Figure 5.5: *Sketch of tunneling through a single barrier of finite thickness.*

unknowns; the amplitude of the transmitted wave results:

$$T = \frac{1}{\sinh^2 sl + \cosh^2 sl + \mathsf{i}\left(\mathsf{a} - \dfrac{1}{\mathsf{a}}\right)\cosh sl\,\sinh sl}. \tag{5.13}$$

Note that $T$ is exponentially decreasing from 1 to 0 when the length $l$ of the barrier goes from 0 to infinity, which is in agreement with the results of the previous subsection. Moreover, inserting $d = 0$ in relation (5.7), *i.e.* removing the defect from the REH, one finds again the above relation (5.13).

## 5.3 Energy localization in the cavity

We now go back to the REH. Our aim is that of evaluating the energy in the whole system and to obtain a relation in closed form that allows us to design the optimal cavity, *i.e.* to find the solution that offers the highest concentration of energy inside the defect.

In this chapter, as in the previous one, we will write $\langle(\bullet)\rangle$ for the average over a period of time of the quantity $(\bullet)$.

### 5.3.1 Energy in the homogeneous parts

Let us consider the homogeneous parts first. We are interested in finding the mechanical energy density $e(x,t)$ and the total energy $E(t)$ in parts $\mathrm{V}_2$, $\mathrm{V}_3$ and $\mathrm{V}_4$, both averaged over a time period.

The mechanical energy in regions $\mathrm{V}_j$ with $j = 1$, 3 or 5 of homogeneous material, given by the sum of the elastic potential energy $p$ and the kinetic energy $c$, reads:

$$e_j(x,t) = p_j(x,t) + c_j(x,t) = \frac{1}{2}\mu_h u_j'^2(x,t) + \frac{1}{2}\rho_h \dot{u}_j^2(x,t) \tag{5.14}$$

where a superimposed dot is used to denote the time derivative and a prime for the space derivative; the displacement field $u_j$ is given by:

$$u_j(x,t) = \mathcal{R}e(U_j(x)\,\exp\{\mathsf{i}\omega t\}).$$

Averaging relation (5.14) over time gives:

$$\langle e_j\rangle(x) = \frac{\mu_h\, k^2}{2}\,\left[|\mathsf{A}_j|^2 + |\mathsf{B}_j|^2\right]. \tag{5.15}$$

Let us note that $\langle e_j\rangle$ is independent from the position $x$. Finally, the total mechanical energy $\langle E(t)\rangle$ inside part $\mathrm{V}_3$ reads:

$$\langle E(t)\rangle = 2d\,\langle e_3\rangle \tag{5.16}$$

### 5.3.2 Energy inside the LRM: homogenization approach

While the energy inside regions $\mathrm{V}_h$ can be easily obtained, a particular treatment must be devoted to the calculation of the energy inside the two barriers $\mathrm{V}_j$, with $j = 2, 4$. Specifically, we will derive its expression for the bi- and three-phase 2D LRMs with circular inclusions, that were treated in chapter 3. We proceed by considering the two cases in parallel, indicating at each step the differences. Accordingly, quantities defined on part $\mathrm{Y}_f$ have to be retained only for the three-phase cell.

We specified before that each unit cell is composed of parts $\mathrm{Y}_m$, $\mathrm{Y}_c$, and, possibly, part $\mathrm{Y}_f$. As such, the mechanical energy density of one cell reads:

$$e_j(x,t) = p_j^m(x,t) + c_j^m(x,t) + p_j^c(x,t) + c_j^c(x,t) + c_j^f(x,t), \tag{5.17}$$

where $p$ stands for an (elastic) *potential* energy, $c$ for a *kinetic* energy, while the apex $m$, $c$, and $f$ denote the *matrix*, the *coating*, and the *fiber*, indicating respectively parts $\mathrm{Y}_m$, $\mathrm{Y}_c$, and $\mathrm{Y}_f$. Note that, since part $\mathrm{Y}_f$ is rigid, its elastic energy is null. Clearly, for the bi-phase cell, $c_j^f = 0$ as part $\mathrm{Y}_f$ is absent.

The homogenization technique enables to find the displacement field and the stress over a cell composing the metamaterial. It should be noted that, while at the macroscale the problem is one-dimensional so that only the variable $x_{[1]} = x$ must be retained, at the microscale, *i.e.* inside each cell, the problem remains 2D and the coordinates $\mathbf{y} = \{y_{[1]}, y_{[2]}\}$ or the polar coordinates $\{r, \vartheta\}$ must be preserved. Similarly, the stress

$\sigma_{[32]}$ is non-zero and a stress vector should be considered at microscale. Following these considerations, at the leading order one has:

$$u(x,t) \approx u^0(x,t) = \begin{cases} U(x)\exp\{\mathrm{i}\omega t\} & \text{in } \mathrm{Y}_m \\ U(x)\tilde{\mathrm{v}}(r)\exp\{\mathrm{i}\omega t\} & \text{in } \mathrm{Y}_c \\ U(x)\tilde{\mathrm{v}}(R_f)\exp\{\mathrm{i}\omega t\} & \text{in } \mathrm{Y}_f \text{ if present} \end{cases}, \tag{5.18}$$

and

$$\boldsymbol{\sigma}(x,t) \approx \boldsymbol{\sigma}^0(x,t) = \begin{cases} \mu_m \left(\nabla_{\mathbf{y}} \mathrm{w}^1(\boldsymbol{y}) + \boldsymbol{e}_1\right) \dfrac{\partial U(x)}{\partial x} \exp\{\mathrm{i}\omega t\} & \text{in } \mathrm{Y}_m \\ \mathbf{0} & \text{in } \mathrm{Y}_c \end{cases}, \tag{5.19}$$

where we have not written the stress field in part $\mathrm{Y}_f$ because, being this part rigid, we do not need it for deriving the mechanical energy of the cell. The term $\mathrm{w}^1$ is the solution of the cell problem (3.55), written for $h = 1$. We recall that $\boldsymbol{e}_1$ is the unit vector along direction $x \equiv x_1$.

Relations (5.18) and (5.19) for parts $\mathrm{Y}_m$ and $\mathrm{Y}_c$ can be written in the same way for the bi- and three-phase cell, nevertheless the term $\tilde{\mathrm{v}}(r) \equiv \tilde{\mathrm{v}}(\boldsymbol{y}(r))$ is different for the two cases. More specifically, for the three-phase unit cell $\tilde{\mathrm{v}}(r)$ is given by relation (3.51), while in a bi-phase unit cell $\tilde{\mathrm{v}}(r)$ can be obtained from relation (3.57) as $\tilde{\mathrm{v}}(r) = J_0(kr)/J_0(kR_c)$.

Let us denote the real part of the displacement $u(x,t)$ in the matrix (defined in relation (5.18)) by

$$\mathsf{u}_j(x,t) = \mathcal{R}e(U_j(x)\ \exp\{\mathrm{i}\omega t\}).$$

From relations (5.4), the above expression gives:

$$\mathsf{u}_j(x,t) = \begin{cases} [a_1\ \cosh sx + b_1\ \sinh sx]\cos\omega t & \\ \qquad + [a_1\ \cosh sx + b_1\ \sinh sx]\sin\omega t & \text{for } \omega \in \text{ band gap} \\ [(a_1{+}b_1)\cos sx + (b_2 - a_2)\sin sx]\cos\omega t & \\ \qquad + [(a_2 + b_2)\cos sx + (a_1 - b_1)\sin sx]\sin\omega t & \text{for } \omega \notin \text{ band gap} \end{cases} \tag{5.20}$$

where $a_1$, $b_1$ and $a_2$, $b_2$ denote respectively the real and imaginary parts of the constants $A_j$ and $B_j$, with $j = 2, 4$. Accordingly, both for frequencies inside and outside a band gap, the displacement field $\mathsf{u}_j(x,t)$ can be written as

$$\mathsf{u}_j(x,t) = \mathsf{V}(x)\cos\omega t + \mathsf{W}(x)\sin\omega t, \tag{5.21}$$

where $\mathsf{V}(x)$ and $\mathsf{W}(x)$ can be derived by comparing relations (5.20) and (5.21).

The contributions to the energy density in (5.17) read

$$p_j^m(x,t) = \frac{1}{2}\,\mu^{eff}\,\mathsf{u}_j'^2(x,t), \tag{5.22}$$

$$c_j^m(x,t) = \frac{|\mathrm{Y}_m|}{|\mathrm{Y}|}\frac{\rho_m}{2}\,\dot{\mathsf{u}}_j^2(x,t), \tag{5.23}$$

$$p_j^c(x,t) = \frac{\mu_c}{2}\int_{\mathrm{Y}_c} \nabla_{\mathbf{y}}\tilde{\mathrm{v}}(\boldsymbol{y})\cdot\nabla_{\mathbf{y}}\tilde{\mathrm{v}}(\boldsymbol{y})\,d\mathbf{y}\,\frac{\mathsf{u}_j^2(x,t)}{|\mathrm{Y}|}, \tag{5.24}$$

$$c_j^c(x,t) = \frac{\rho_c}{2}\int_{\mathrm{Y}_c} \tilde{\mathrm{v}}^2(\boldsymbol{y})\,d\mathbf{y}\,\frac{\dot{\mathsf{u}}_j^2(x,t)}{|\mathrm{Y}|}, \tag{5.25}$$

$$c_j^f(x,t) = \frac{|\mathrm{Y}_f|}{|\mathrm{Y}|}\frac{\rho_f}{2}\tilde{\mathrm{v}}^2(R_f)\,\dot{\mathsf{u}}_j^2(x,t), \tag{5.26}$$

where the term $\tilde{\mathrm{v}}$ must again be interpreted differently for the bi- and three-phase cases, as specified above.

From relations (5.22) to (5.26) and (5.21), after some manipulations (see Appendix A2), the energy $\langle e_j\rangle$, with $j = 2$ or 4, can be written as:

$$\langle e_j\rangle(x) = \frac{1}{4}\left\{\mu^{eff}s^2(\mathsf{V}'^2(x) + \mathsf{W}'^2(x)) + \omega^2\,\gamma(\omega)\,(\mathsf{V}^2(x) + \mathsf{W}^2(x))\right\}, \tag{5.27}$$

where $\mu^{eff}$ is obtained from relation (3.54)[1] and $\gamma(\omega)$ is given by:

$$\gamma(\omega) = \begin{cases} \rho^{eff}(\omega) + \dfrac{2}{|\mathrm{Y}|}\left[\rho_c\displaystyle\int_{\mathrm{Y}_c}\left(\tilde{\mathrm{v}}^2(\boldsymbol{y}) - \tilde{\mathrm{v}}(\boldsymbol{y})\right)d\mathbf{y}\right. & \\ \qquad\qquad \left. + \rho_f\,|\mathrm{Y}_f|\,\tilde{\mathrm{v}}(R_f)\,(\tilde{\mathrm{v}}(R_f) - 1)\right] & \text{three phases,} \\ \rho^{eff}(\omega) + \dfrac{2}{|\mathrm{Y}|}\left[\rho_c\displaystyle\int_{\mathrm{Y}_c}\left(\tilde{\mathrm{v}}^2(\boldsymbol{y}) - \tilde{\mathrm{v}}(\boldsymbol{y})\right)d\mathbf{y}\right] & \text{two phases.} \end{cases} \tag{5.28}$$

Note that $\gamma$ for the two-phase LRM can be obtained from that of the three-phase problem by considering $|\mathrm{Y}_f| = 0$, *i.e.* by assuming that part $\mathrm{Y}_f$ has zero area, and by considering the "correct" effective mass density $\rho^{eff}$, that is given by relation (3.56) for three phases and by relation (3.59) for two phases.

From the expressions above, for frequencies inside a band gap, the average energy

[1] We recall that, for the square unit cell and the anti-plane shear problem here treated, the tensor of effective shear becomes a scalar tensor with diagonal terms $\mu^{eff}$.

density (5.27) of the two barriers becomes:

$$\langle e_2\rangle(x) = \frac{1}{4}\Big\{\mu^{eff}\, s^2\, |(1+\mathsf{R})\ \sinh sl + \mathsf{a}\,\mathsf{i}\,(\mathsf{R}-1)\ \cosh sl| + \omega^2\,\gamma(\omega)\ |(1+\mathsf{R})\ \cosh sl + \mathsf{a}\,\mathsf{i}\,(\mathsf{R}-1)\ \sinh sl|\ \Big\}, \tag{5.29}$$

$$\langle e_4\rangle(x) = \frac{1}{4}\Big\{\mu^{eff}\, s^2\, |\mathsf{T}\ \sinh sl - \mathsf{a}\,\mathsf{i}\mathsf{T}\ \cosh sl| + \omega^2\,\gamma(\omega)\ |\mathsf{T}\ \cosh sl - \mathsf{a}\,\mathsf{i}\mathsf{T}\ \sinh sl|\ \Big\}, \tag{5.30}$$

and, upon integrating over their thickness $l$, one can derive the averaged total mechanical energies $\langle E_2\rangle$ and $\langle E_4\rangle$ as:

$$\begin{aligned}\langle E_2\rangle = \frac{1}{4}\Big\{ &\left[\frac{l}{2}(\mathsf{a}^2-1)(\mu^{eff}s^2-\omega^2\gamma(\omega)) + \frac{\sinh 2sl}{4s}(\mathsf{a}^2+1)(\mu^{eff}s^2+\omega^2)\right] + \\ &- 2\,\mathcal{R}e(\mathsf{R})\left[\frac{l}{2}(\mathsf{a}^2+1)(\mu^{eff}s^2-\omega^2\gamma(\omega)) + \frac{\sinh 2sl}{4s}(\mathsf{a}^2-1)(\mu^{eff}s^2+\omega^2\gamma(\omega))\right] + \\ &+ \mathsf{a}\,\mathcal{I}m(\mathsf{R})(1-\cosh 2sl)(\mu^{eff}s^2+\omega^2\gamma(\omega))\Big\}\end{aligned} \tag{5.31}$$

$$\langle E_4\rangle = \frac{1}{4}\,|\mathsf{T}|^2\left[\frac{l}{2}(\mathsf{a}^2-1)(\mu^{eff}s^2-\omega^2\gamma(\omega)) + \frac{\sinh 2sl}{4s}(\mathsf{a}^2+1)(\mu^{eff}s^2+\omega^2\gamma(\omega))\right] \tag{5.32}$$

### 5.3.3 Optimal cavity width

The attenuation capabilities of the LRMs can be exploited for obtaining a concentration of mechanical energy inside the defect. For this, let us consider frequencies inside a band gap for the analyzed LRM.

From relation (5.15), the averaged energy in part $\mathrm{V}_3$ is obtained as follows:

$$\langle e_3\rangle(x) = \frac{\mu_h\, k^2}{8}\ |\mathsf{T}|^2\ \Big\{|\alpha|^2\ +\ |\beta|^2\Big\}. \tag{5.33}$$

For given material properties of parts $\mathrm{V}_h$ and $\mathrm{V}_b$, the geometry of the REH can be optimized to increase the energy inside the cavity. Considering a fixed frequency $\omega$ for the traveling wave and a given width $l$ for the barriers, the only variable left is the half-width $d$ of the internal cavity that appears at the denominator $\mathsf{denT}$ of the transmitted complex wave amplitude $\mathsf{T}$ (see relation (5.7)). Accordingly, $\mathsf{denT}$ must be minimized with respect to the product $kd$:

$$\min_{kd}\Big\{|\mathsf{denT}|^2\Big\} = |\alpha|^4\ +\ |\beta|^4\ +\ |\beta|^2\ \underbrace{\min_{kd}\Big\{\bar{\alpha}^2\ \exp\{-4\mathsf{i}kd\} + \alpha^2\exp\{4\mathsf{i}kd\}\Big\}}_{\circledast}. \tag{5.34}$$

Using the definition of $\alpha$, the term indicated as $\circledast$ above can be rewritten as

$$\circledast = \min_{kd} \left\{ 2\left(p^2 - q^2\right) \cos 4kd \; - \; 4pq \sin 4kd \right\}, \tag{5.35}$$

where $p$ and $q$ are given by

$$p = 2 \cosh sl \qquad q = \left(\mathsf{a} - \frac{1}{\mathsf{a}}\right) \sinh sl. \tag{5.36}$$

The optimal solution of relation (5.35), and hence of (5.34), is obtained from

$$\tan 4kd \; = \; \frac{2pq}{q^2 \; - \; p^2}. \tag{5.37}$$

From relation (5.37), the following result is found:

**Result.** *The average mechanical energy density in the defect is maximum for an increasing sequence of optimal half-widths, depending on $l$ and $\omega$, that will be denoted as $d_i^*$, with $i \in \mathbb{N}^*$.*

Moreover, from condition (5.37), one has

$$\sin 4kd = \frac{2pq}{q^2 + p^2}, \qquad \cos 4kd = \frac{q^2 - p^2}{q^2 + p^2}. \tag{5.38}$$

Substituting relation (5.38) into (5.34), one obtains

$$\min_{kd} |\mathsf{den}\mathsf{T}|^2 = \left[\left(p^2 + q^2\right) - |\beta|^2\right]^2 = 4. \tag{5.39}$$

Considering relation (5.7), a second result is thus found:

**Result.** *When the average mechanical energy density in the defect is maximum, the modulus of the transmission wave amplitude $\mathsf{T}$ is maximum as well and equal to 1, whereas the reflected wave amplitude vanishes, $\mathsf{R} = 0$, meaning that the system is "invisible" for the incoming wave.*

Let us note that (5.35) gives also the set of $d$ that minimizes $\mathsf{T}$.

As stated in chapter 3, by decreasing the frequency $\omega$ from the closure of a band gap towards the frequency of resonance $\omega_m$ of the LRM internal inclusions corresponding to the opening frequency of that same band gap, the effective mass density $\rho^{eff}$ decreases monotonically, approaching $-\infty$. By considering this latter condition, *i.e.* $\omega \to \omega_m^+$, then $\cosh sl \sim \sinh sl$, but since $\mathsf{a} \to 0$, then $p^2 = o\left(q^2\right)$ and

$$\lim_{\omega \to \omega_m^+} \cos 4kd = 1 \tag{5.40}$$

In this case the optimal half-widths read

$$d_i^* = \frac{i\pi}{2k} \quad \forall l, \quad \text{with } i \in \mathbb{N}^*. \tag{5.41}$$

This means that, whenever $\omega \to \omega_m^+$, the condition of maximum average energy density becomes independent from the width $l$ of the barriers and thus, in principle, one unit cell would be enough for obtaining the optimal energy localization. The above relation (5.41) can be understood as the condition of resonance of a cavity inserted between two "walls" characterized by perfect reflection.

Let us note that, when the bi-phase LRM is employed, the first frequency of resonance $\omega_1^*$ for part $Y_c$ is found from relation (3.58) that is here rewritten for clarity as

$$J_0(k_c R_c) = 0, \tag{5.42}$$

with $k_c = \omega\sqrt{\rho_c/\mu_c}$ representing the wavenumber inside part $\mathrm{Y}_c$. From equation (5.42), one finds $k_c = \frac{2.4048}{R_c}$. Considering $\omega \to \omega_1^+$, from relation (5.41) the wavenumber in the cavity is $k = \frac{1.5708}{d_1^*}$. If the material in the defect coincided with the material of the soft inclusion, one would have $k \equiv k_c$. Therefore, we would obtain that $d_1^*$ is of the same order of magnitude of $R_c$ for this specific case.

Eventually, when $d = d_i^*$, the total energies in regions $\mathrm{V}_2$, $\mathrm{V}_3$ and $\mathrm{V}_4$ read:

$$\begin{cases} \langle E_2 \rangle & = \langle E_4 \rangle = \dfrac{1}{4}\left[\dfrac{l}{2}(\mathsf{a}^2-1)(\mu^{eff}s^2-\omega^2\gamma) + \dfrac{\sinh 2sl}{4s}(\mathsf{a}^2+1)(\mu^{eff}s^2+\omega^2\gamma)\right] \\ \langle E_3 \rangle & = d\,\dfrac{\mu_m\,k^2}{2}\left[2\,\cosh^2 sl + \left(\mathsf{a}^2+\dfrac{1}{\mathsf{a}^2}\right)\,\sinh^2 sl\right] \end{cases} \tag{5.43}$$

## 5.4 Example

Let us now validate our previous results by analyzing an example case and by comparing them with numerical analyses. For these, we used the commercial software COMSOL Multiphysics 5.4. For clarity, we summarize here below which are the initial assumptions on the materials of the considered system:

- Parts $\mathrm{V}_1$, $\mathrm{V}_3$ and $\mathrm{V}_5$ are constituted by the same material employed for the matrix composing the LRM[1];
- Part $\mathrm{Y}_c$ is very compliant with respect to part $\mathrm{Y}_m$;
- Part $\mathrm{Y}_f$ (if present) is very stiff so that it can be treated as rigid in the homogenization procedure.

We thus first fix the material properties by respecting the three conditions just specified. We choose to use the same materials for parts $\mathrm{Y}_m$, $\mathrm{Y}_c$, and $\mathrm{Y}_f$ as the ones indicated in table 3.1. Following the first point of the list above, parts $\mathrm{V}_1$, $\mathrm{V}_3$, and $\mathrm{V}_5$ are fixed as well. Let us recall in table 5.1 the material properties.

[1]We make this assumption for practical purposes: it is indeed easier to think of a REH obtained by deposing the inclusions in a background homogeneous material. The previous derivation remains valid also when this assumption is not made.

Table 5.1: Material properties.

| Constituents | $E$ [MPa] | $\nu$ [-] | $\rho$ [kg/m$^3$] |
|---|---|---|---|
| part $Y_m$ (epoxy) | 3600 | 0.370 | 1180 |
| part $Y_c$ (rubber) | 0.118 | 0.469 | 1300 |
| part $Y_f$ (lead) | 14000 | 0.420 | 11340 |

We show the results for both a bi- and three-phase LRM. We consider the same square lattice as the one analyzed in the examples treated in chapter 3, with unit cells of side $a = 1$ mm, parts $Y_c$ of radius $R_c = 0.415a$, and parts $Y_f$ (if present) of radius $R_f = 0.7R_c$. We have already underlined in chapter 3 that a scaling of the cell would simply scale the effective mass density when plotted with respect to the frequency, without changing the band gap structure. Different filling fractions ($\pi R_c^2/a^2$) or thicknesses of the coating ($R_c - R_f$) would instead modify it.

### 5.4.1 Analytic and numerical computation of the energy in the system

From the results of chapter 3, the LRM is characterized by the presence of band gaps, as one can check by looking at figures 3.6 and 3.7 respectively for the bi- and three-phase case. The first band gap occurs at frequencies between 5.1 and 6.5 KHz for the bi-phase LRM, and between 2.4 and 5.7 KHz for the three-phase LRM.

We fix to 40 the number of cells employed across the thickness of parts $V_2$ and $V_4$ (hence we choose a value for $l$).

Our choice is to optimize the REH to work at a mid-band gap frequency $\tilde{\omega}$. Accordingly, we have $\tilde{\omega} = 5.8$ KHz for two phases and $\tilde{\omega} = 4.05$ KHz for three phases. From relation (5.37), we thus obtain an ordered set $\{d_i^*\}_{i\in\mathbb{N}^*}$ of increasing optimal cavity half-widths $d_i^*$, for which the energy $\langle e_3\rangle$ in the defect is maximum.

Let us call $\langle e_{in}\rangle$ the energy carried by the incoming wave in part $V_1$, averaged in time. By using relation (5.15) we can express the incoming energy as

$$\langle e_{in}\rangle = \frac{\mu_m\, k^2}{2}. \tag{5.44}$$

Picking up the smallest optimal cavity $d_1^* := d$ for both LRMs, the plots in figures 5.6 show the behavior of the ratio $\langle e_j\rangle/\langle e_{in}\rangle$ (with $j$ from 1 to 5) along the whole system $\bigcup_{j=1}^{5} V_j$ for $d = 12.9$ mm (two phases) and $d = 19.9$ mm (three phases). The orange lines represent the energy density computed by the analytic formulas (5.15) and (5.29), while the results of the numerical analysis are shown in blue. The oscillations of the numerical response are due to the intrinsic heterogeneity of the LRM composing the barriers; the analytic results, based on an homogenized material, give a behavior in good agreement with the numerical curve.

By looking at both plots in figure 5.6, one can observe that not only the energy in the cavity is larger than the incoming energy, but also that the energy exponentially

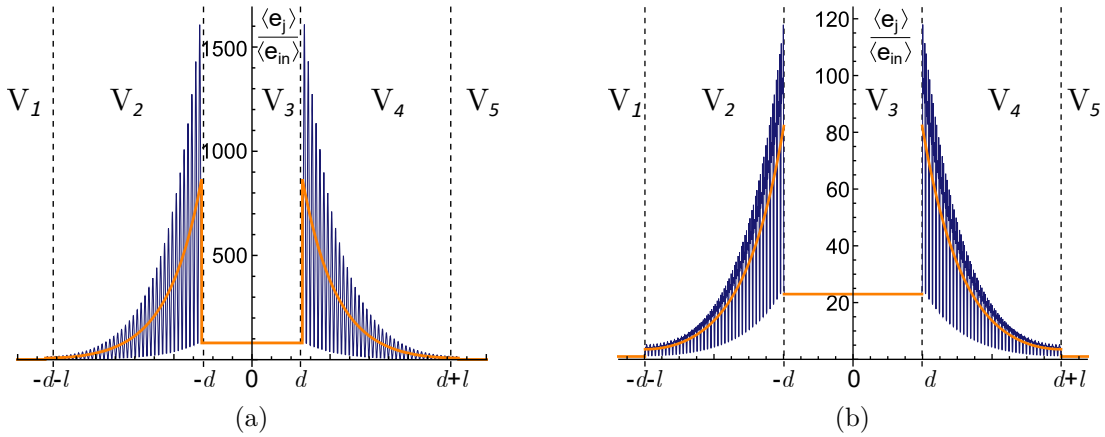


Figure 5.6: *Ratio of the averaged mechanical energy density along the whole system with respect to the incoming one for (a) a bi-phase ($d = 12.9$ mm) and (b) a three-phase LRM ($d = 19.9$ mm). Orange: analytic results, and blue: numerical results. Each part composing the REH is separated by the vertical dashed lines.*

decay outside the defect across the barriers. This feature is fundamental and proves that the incoming wave is localized in the defect.

This allows us to finally compute the ratio $\langle e_3 \rangle / \langle e_{in} \rangle$ between the localized and the incoming energy. In particular, we have that $\langle e_3 \rangle / \langle e_{in} \rangle = 81$ for the bi-phase problem, while $\langle e_3 \rangle / \langle e_{in} \rangle = 23$ for the three-phase one. Therefore, we have that in both cases the incoming energy is smaller than the energy inside the defect. This verifies the first result in subsection 5.3.3.

### 5.4.2 Analytic and numerical computation of the transmission coefficient

Let us now verify our second result in subsection 5.3.3, namely the fact that transmission is maximum and equal to 1 when an optimal cavity half-width is used.

For this, we report in figure 5.7a the transmission coefficient modulus $|\mathsf{T}|$ vs frequency, from a transmission analysis of our REH (bi-phase above and three-phase below). First of all, the results coming from the asymptotic technique agrees very well with those of the real case study. The expected peak of transmission at the frequency $\tilde{\omega}$ inside the band gap is well captured both by the analytic and numerical results. It is thus clear from the figure that also the second result in subsection 5.3.3 is verified.

To show how the presence of a cavity modifies the behavior of an unperturbed LRM, we have plotted in figure 5.7b (bi-phase above and three-phase below) the results coming from a transmission analysis in absence of the cavity, *i.e.* for a simple layer of LRM with a thickness equal to $2l$ (obtained by getting rid of the cavity in the middle of the two barriers and attaching them together): the peak inside the band gap disappears

when no cavity is present.

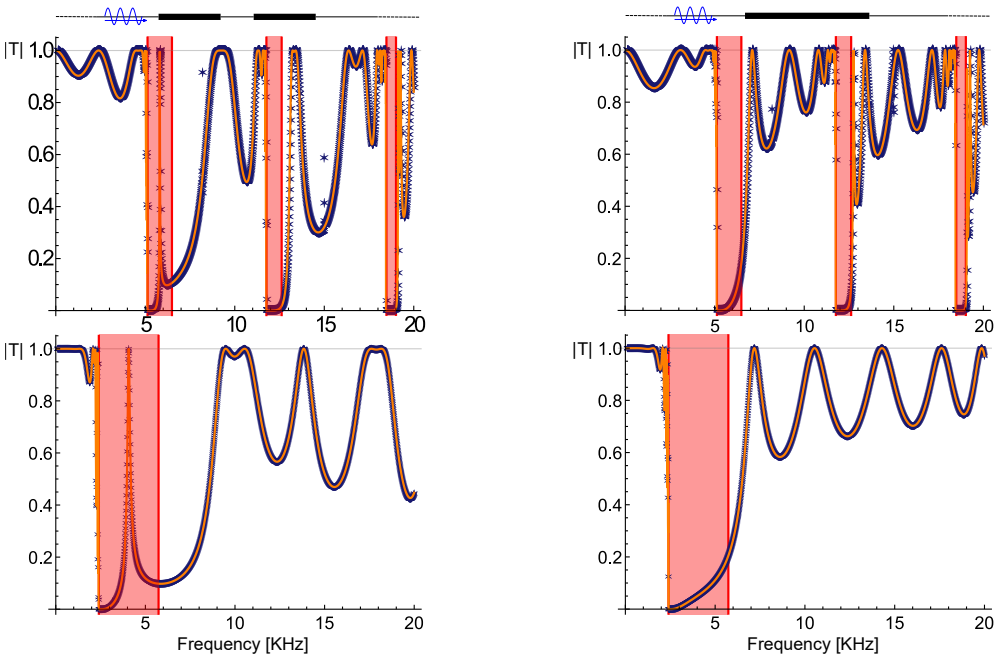


(a) (b)

Figure 5.7: *Transmission coefficient modulus* $|\mathsf{T}|$ *as a function of the frequency* $\omega$ *(a) in presence of the cavity and (b) without any cavity. Bi-phase above and three-phase below. The shaded regions define the band gaps. Orange: analytic results and blue: numerical results.*

### 5.4.3 Towards the optimization of the harvester: parametric study

The results of the previous subsections refer to a particular case, with all the parameters involved in the problem fixed. Let us now consider the effect of different possible configurations of the system with a three-phase LRM. This becomes rather fast thanks to our analytic treatment of the problem.

With the aim of comparing the different solutions, we introduce two indexes as a "measure" of the harvesting capabilities of the REH. One of them is the "*Index of Concentration*" (IC) that was already defined by relation (4.36) for the problem analyzed in chapter 4. The second measure is the "*Averaged Index of Concentration*"

(AIC). We report their expressions here:

$$\begin{aligned} \mathrm{IC} &= \frac{\langle E_3 \rangle}{\langle E_2 \rangle + \langle E_3 \rangle + \langle E_4 \rangle}, \\ \mathrm{AIC} &= \frac{\langle E_3 \rangle / (d_i^*)}{(\langle E_2 \rangle + \langle E_3 \rangle + \langle E_4 \rangle)/(d_i^* + l)}. \end{aligned} \tag{5.45}$$

From the above relations, IC represents a measure of the energy level of concentration reached by the system (as before), whereas AIC gives a ratio between values of energy averaged over the dimensions of the corresponding REH parts, *i.e.* between densities of energy. This is important because a good energy harvester should not be too much "spread" in space and should provide a high energy density around the defect.

By keeping the same geometric dimensions employed in the previous subsection for the unit cell, there are three parameters which can be left free to vary, namely the barrier width $l$, the optimal cavity width $d_i^*$ and the frequency $\omega$.

As stated previously, relation (5.37) gives a set $\{2d_i^*\}_{i\in\mathbb{N}^*}$ of optimal cavity widths, that maximize the energy localized for a given frequency inside the band gap. In figure 5.8, we show the contour plots of the two smallest elements of this set, $d_1^*$ and $d_2^*$, in the plane of the frequency $\omega$ inside the first band gap and the width $l$ of the barriers. One can observe that the optimal cavity widths are almost independent from the thickness of the barriers $l$ while are strongly conditioned by the frequency. This dependence is slightly attenuated when considering thin barriers.

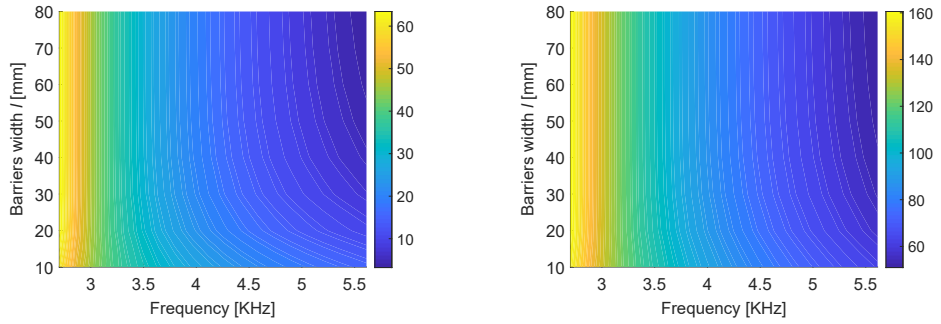


(a) (b)

Figure 5.8: *First (a) and second (b) optimal cavity half-width plotted with respect to the the frequency $\omega$ inside the first band gap and the width $l$ of the barriers.*

Keeping the frequency inside the band gap and the barrier width as variables, the two indexes IC and AIC are plotted in figure 5.9 using the first two optimal cavity widths $2d_1^*$ and $2d_2^*$. The index IC (panels 5.9a and 5.9c) is higher when considering the largest cavity ($2d_2^*$). The dependence on the width of the barriers $l$ is very limited when considering a frequency close to the band gap opening, while IC decreases with $l$ when considering a higher frequency, close to the band gap closing. A different pattern

is exhibited by the index AIC (figure 5.9b and 5.9d). Values of AIC greater than one correspond to systems efficiently concentrating energy in the cavity. High levels of energy density in the defect are obtained, for both cavity dimensions, considering higher frequencies and larger barriers. This can be explained by the fact that, far from the opening frequency of a band gap, the inclusions resonate less and less, meaning that less and less energy is captured by the resonance; moreover, as the barriers are larger, the energy is more spread and the density is smaller. The smaller cavity gives a better solution in terms of AIC.

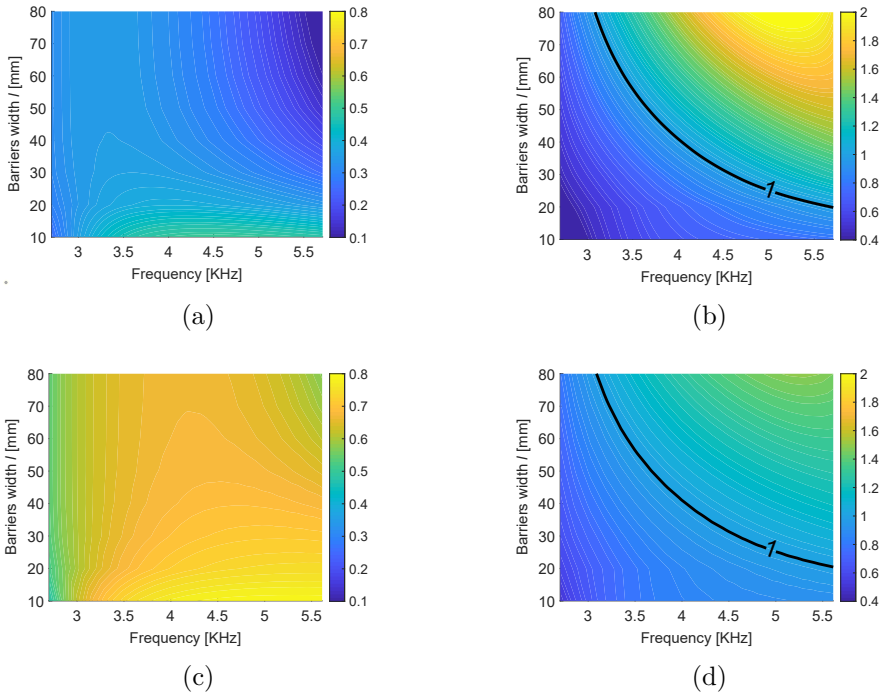


Figure 5.9: *Indexes IC (a) and AIC (b) for the first optimal cavity widths $2d_1^*$; indexes IC (c) and AIC (d) for the second optimal cavity widths $2d_2^*$. The plots are obtained using analytic expressions.*

As shown in chapter 3, a change of the geometry of the unit cell, in terms of both filling fraction and coating thickness, would change the expression of the effective mass density (hence the frequencies of the band gap). Moreover, a change in the filling fraction (or equivalently of the ratio between the radius $R_c$ and the cell size $a$) would also modify the value of the effective stiffness of the barriers. To explore the effect of these variations on the energy localization of the system we study, in particular, the four cases specified in table 5.2.

Figure 5.10 shows the effect of the geometric modifications of the cell on the indexes IC and AIC; the cavity width is fixed to $2d_1^*$ in all cases. As we stated before, the

Table 5.2: Chosen geometry for the unit cell

| **case** | $R_c/a$ | $R_f/R_c$ |
|---|---|---|
| a | 0.475 | 0.9 |
| b | 0.475 | 0.4 |
| c | 0.355 | 0.9 |
| d | 0.355 | 0.4 |

change of the cell also affects the band gap frequencies. Specifically, the frequency ranges represented in figure 5.10 always correspond to the first band gap of the different LRMs. By comparing panels 5.10a and 5.10b with panels 5.10c and 5.10d, one can observe that the concentration of energy is improved by increasing the filling fraction of the LRM. At equal filling fraction, a smaller thickness of part $Y_c$ (panels 5.10a and 5.10c) leads to a higher concentration with respect to the case with a large thickness (panels 5.10b and 5.10d, respectively).

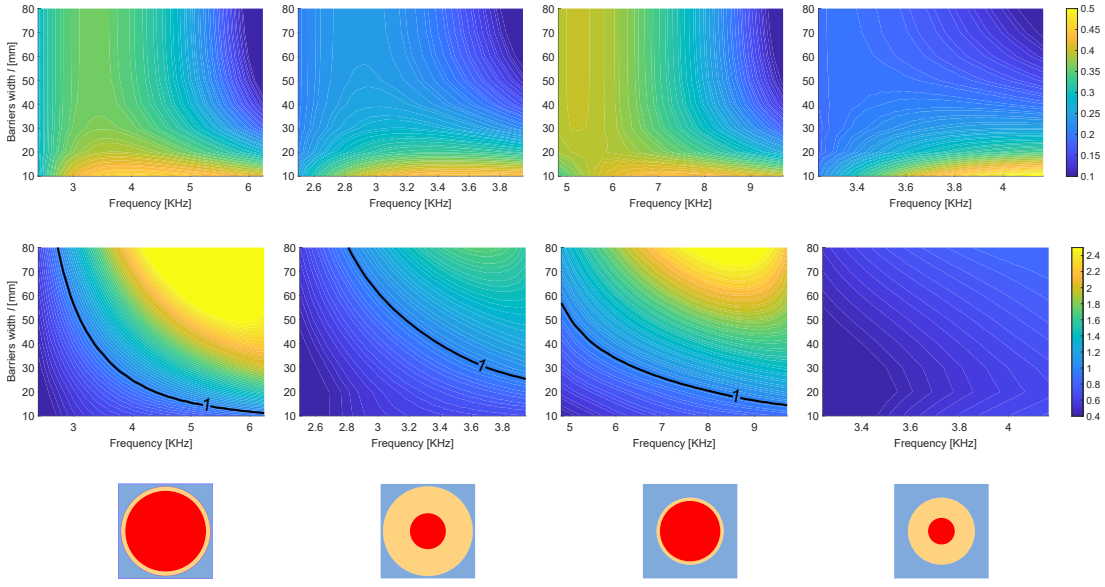


(a) (b) (c) (d)

Figure 5.10: *Each panel (a) - (d) shows the index IC on the first row and AIC on the second row, for the first optimal cavity widths* $2d_1^*$. *The following geometrical dimensions are used: (a)* $R_c = 0.475a$, $R_f = 0.9R_c$, *(b)* $R_c = 0.475a$, $R_f = 0.4R_c$, *(c)* $R_c = 0.355a$, $R_f = 0.9R_c$ *and (d)* $R_c = 0.355a$, $R_f = 0.4R_c$.

CHAPTER

# 6

# Dynamic behavior of cables with scatter elements

Chapter summary: *The motion of cables with and without a family of attached scatter elements periodically distributed along it is considered. A detailed description about the validity of some approximations concerning the static behavior of the system is given. We show that the dynamic behavior of a taut string with attached masses is characterized by the presence of band gaps in the spectrum. By considering a bounded domain for the system, the associated eigenfrequencies respect the banded structure of the spectrum from the unbounded problem. By introducing a defect of periodicity, defect modes appear inside some band gaps. The theoretical results are experimentally tested.*

## Contents

The focus of the present chapter is on the problem of wave propagation in cables presenting a periodic array of scatter elements, consisting in a discrete set of masses that are hanging by means of elastic or rigid connections.

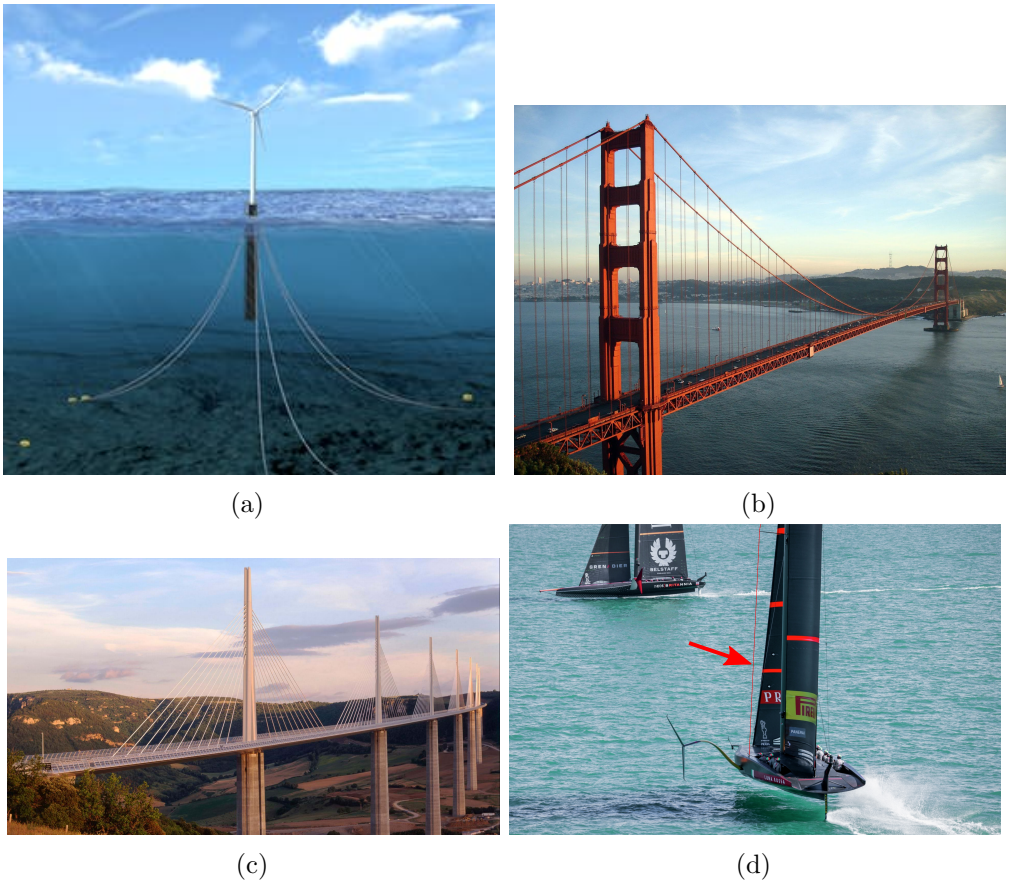

(a) (b)

(c) (d)

Figure 6.1: *Some examples of engineering applications with cable systems: (a) mooring of floating wind turbines, (b) suspension bridge (Golden Gate bridge, USA), (c) cable-stayed bridge (Millau viaduct, France), (d) guy-wire for ship masts (Luna Rossa sailboat).*

The dynamics of cables has attracted large attentions in the scientific community due to the complexity of their behavior. Since engineering cables are usually lengthy and flexible, their vibrations, in general, involve large displacements and are dominated by geometric non-linearities. This can lead to the activation of different interesting phenomena, such as hardening or softening at a primary resonance response, secondary and internal resonances, parametrically excited responses, to name but a few. For an exhaustive literature review of the problem, we refer to the works of Nayfeh et al. (1995a)

and Nayfeh et al. (2008). Beyond the academic interest, cables are used as structural solutions in many applications, such as for the mooring and towing of marine vehicles or platforms, for overhead lines, for roofing systems, for cable-stayed or suspension bridges, or again as guy-wires to add stability to a free-standing structure (see figure 6.1 for some of these examples).

Often an engineering cable presents a family of objects, such as weights, instruments or buoyancy elements (all of them to be considered as punctual masses), attached along it. Systems of this type can model for instance overhead lines presenting Stockbridge dampers, hydrophones arrays, or cableways (figure 6.2). Likewise, the main cable in suspension bridges supports the deck by means of a set of hangers distributed along it (*cf.* figure 6.1b). The motivation for the present work emerged, partially, from the will of studying the dynamics of these cable systems.

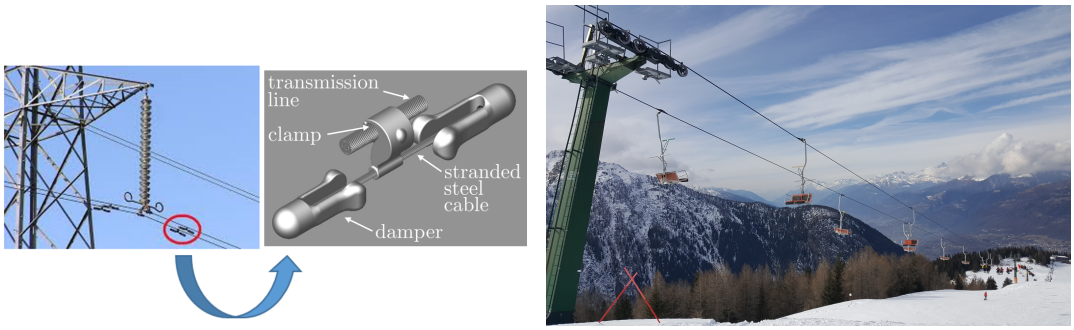


(a) (b)

Figure 6.2: *Examples of engineering cables with a family of attached elements: (a) Stockbridge damper for overhead power lines and (b) cableway (Aprica, Italy).*

We begin this chapter by deriving the exact equations of motion governing the dynamics of cables with and without a discrete arrangement of scatter elements. The first step in the studying of these systems is the derivation of their static equilibrium configurations. This is a well-understood problem. Analytic and numerical tools which provide reliable estimates of the static behavior of the system are already available (see for instance the work of Desai et al. (1988) and citations therein).

The analysis of the dynamic response of cables is much more complex than the static analysis. Different numerical schemes have been proposed (see for instance Henohold et al. (1976) and Gattulli et al. (2004)) and have been used to give important quantitative solutions to the problem, especially in relation to non-linear phenomena. Nevertheless, they provide relatively little information about the effect of the parameters which govern the dynamics of the system. In this context, analytic approaches can be useful. Clearly, in order to derive analytic results, some simplifications must be introduced. However, several interesting phenomena can still be understood in a reliable way. This chapter shall be read using this point of view. From the strongly non-linear equations that govern the problem of cables dynamics, we make subsequent approximations that enable

to treat a simplified version of the problem. This, in turn, allows us to present some known peculiar results that concern the dynamics of bare cables and some new results on the linearized dynamics of cables with scatter elements.

More specifically, we will show that the behavior of these latter systems resembles very much that of the metamaterials described in the previous chapters, being characterized by gaps of frequencies at which propagating waves are attenuated. Their behavior can be viewed halfway between that of a discrete lattice and a continuous metamaterial. Moreover, they can be easily realized, offering the possibility of (inexpensive) experimental validations: our objective, at this point, is that of obtaining some experimental evidences of the phenomena treated before in this work. Accordingly, this chapter is concluded by presenting some experimental results on the linearized dynamics of taut cables with attached masses, that prove both the presence of band gaps in the spectrum of the problem and the occurrence of defects-induced wave localization phenomena.

## 6.1 Exact equations of motion

In this section we aim to derive the equations that govern the motion problem associated to the mechanical system depicted in figure 6.3, constituted of a cable whose *natural configuration* is the curve $S \to \boldsymbol{x}_{\mathrm{R}}(S)$, with $\boldsymbol{x}_{\mathrm{R}} \in \mathbb{R}^3$, being parametrized by its *curvilinear abscissa* $S$. More specifically, we have $S \in \mathcal{C}_{\mathrm{R}}$, where $\mathcal{C}_{\mathrm{R}}$ can be finite

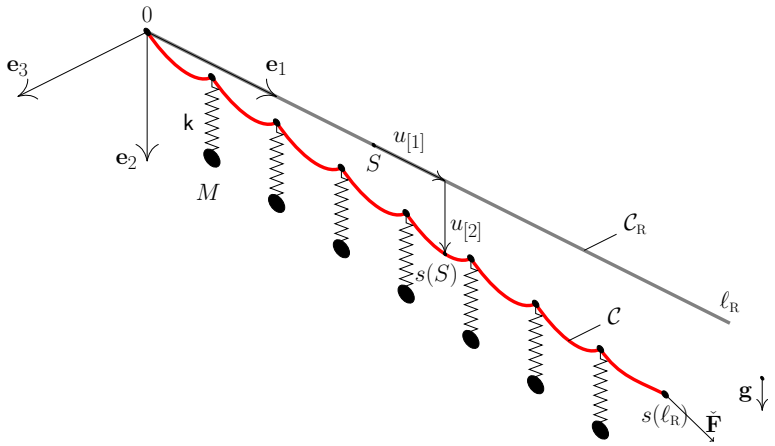


Figure 6.3: *Sketch of the cable system.*

$\mathcal{C}_{\mathrm{R}} = (0, \ell_R)$ or infinite $\mathcal{C}_{\mathrm{R}} = (-\infty, +\infty)$, since we also envisage to study propagation problems (*i.e.* problems where the propagating waves have not reached the boundaries yet). We will often write $\forall S$ for $\forall S \in \mathcal{C}_{\mathrm{R}}$. The coordinate system used is represented in the figure 6.3. Note that, in what follows, we use the subscript "R" to indicate a quantity in the reference configuration, that is taken to be coincident with the natural configuration. A hat $(\hat{\bullet})$ will be used for non-dimensional quantities.

A cable is defined to be a set of elements called *material points* (or particles) with the geometric property that they occupy a curve in $\mathbb{R}^3$ and with the mechanical property that they are perfectly flexible, *i.e.* they do not support any flexural moment. An elegant way of describing this pure cable behavior can be found in the work of Irvine (1981), who himself attributed it to James Bernoulli: "The action of any part of the line upon its neighbor is purely tangential". Accordingly, we assume that couples are not present; shear forces are thus necessarily null for the equilibrium to be satisfied, as we will show later on by considering the balance of the angular momentum.

Let us make the following assumptions:

- In the literature, sometimes the words "string" and "cable" have not the same meaning, with "string" denoting a cable with no static sag when fixed at the two extremities. In this manuscript we will not make this differentiation and we will use the two words indistinctly.
- The cable is of linear mass density $\rho_{\mathrm{R}}$ and area $A_{\mathrm{R}}$ in the reference configuration. In what follows we are going to neglect the Poisson's effect, meaning that the area $A$ at any time $t$ will remain equal to $A_{\mathrm{R}}$[1].
- The end at $S = 0$ (if exists) is fixed, whereas the boundary condition on the opposite end is not defined at the moment.
- Possibly, all along the cable a family of punctual masses $M$ is attached either with the help of linear springs of stiffness $\mathsf{k}$ (the mass of the springs is neglected) or without them, *i.e.* placing the masses directly on the cable. The set containing the points where a punctual mass can be found is called $\mathcal{P} \subset \mathcal{C}_{\mathrm{R}}$, it can be either empty ($\mathcal{P} = \{0\}$), or it can possess a finite cardinality $N$ ($\mathcal{P} = \{s_1, \dots, s_N\}$).
- If $\mathcal{P} \neq \{0\}$, the masses are equally spaced, the distance between two masses being $d = \ell_{\mathrm{R}}/(N+1)$ (accordingly the $i$-th mass is attached to the cable at the point $S_i = id$).
- The cable and the masses are placed in the gravity field $g\boldsymbol{e}_2$.
- We will call the movement that takes place in the plane $x_1 - x_2$ as "*in-plane motion*", whereas that along direction $x_3$ as "*out-of-plane*".

Let us denote $\boldsymbol{x}_{\mathrm{eq}}(S)$ the position of the material point $S$ in the static equilibrium configuration $\mathcal{C}_{\mathrm{eq}}$ and $\boldsymbol{x}(S,t)$ that in the configuration $\mathcal{C}$ of the cable in motion at time $t \in [0, +\infty)$. We consider $\boldsymbol{x}(S,t)$ and its derivative in time $\dot{\boldsymbol{x}}(S,t)$ to be continuous on $\{\overline{\mathcal{C}}_{\mathrm{R}} \times [0, +\infty)\}$, with null values for $(S,t) = \{\overline{\mathcal{C}}_{\mathrm{R}} \times 0\}$. We will use a subscript "eq" any time we are referring to a quantity of the configuration $\mathcal{C}_{\mathrm{eq}}$. Note that we are here not using the *normal parametrization*, *i.e.* the curves $\boldsymbol{x}_{\mathrm{eq}}$ and $\boldsymbol{x}$ are not parametrized with their arclengths. If needed, we will use $p$ to denote the arclength along $\mathcal{C}_{\mathrm{eq}}$ (statically deformed arclength) and $s$ for the same quantity in $\mathcal{C}$ (dinamically deformed arclength). If not specified, $s$ will denote the arclength in any configuration different than $\mathcal{C}_{\mathrm{R}}$.

[1] This corresponds to a Poisson's coefficient $\nu = 0$. In general this is not true, nevertheless the material considered in this manuscript are stiff and thus small axial deformations are often present. For this reason we can neglect the Poisson's effect.

For a string undergoing some motion, we define the displacement $\boldsymbol{u}(S,t)$ at time $t$ from the equilibrium such that:

$$\boldsymbol{x}(S,t) = \boldsymbol{x}_{\text{eq}}(S) + \boldsymbol{u}(S,t), \tag{6.1}$$

with $\boldsymbol{u}(S,t) = u_1(S,t)\boldsymbol{e}_1 + u_2(S,t)\boldsymbol{e}_2 + u_3(S,t)\boldsymbol{e}_3$.

Accordingly, assuming that the function $\boldsymbol{x}(S,t)$ is differentiable in the spatial variable at $(S,t)$, the unit vector tangent to the curve at point $S$ and at time $t$ is

$$\boldsymbol{t}(S,t) := \frac{\boldsymbol{x}'(S,t)}{\|\boldsymbol{x}'(S,t)\|}, \tag{6.2}$$

where we recall that $(\bullet)'(x) := \partial(\bullet)/\partial x$, with $x$ representing a generic spatial coordinate, and with $\| \bullet \|$ being here the usual Euclidean norm. In writing the above relation, we have assumed

$$\|\boldsymbol{x}'(S,t)\| > 0, \quad \forall S,t \tag{6.3}$$

that has to be understood as a condition of non-degeneracy. We will come back on this point in a few moments.

Denoting as $\phi(S,t)$ the tangent angle at position $S$ and time $t$ between vector $\boldsymbol{t}$ and the axis along $\boldsymbol{e}_1$, we are finally able to define the curvature as:

$$C(S,t) := \frac{\phi'(S,t)}{s'(S,t)}. \tag{6.4}$$

We make here an important statement:

**Remark.** *Since the flexural moment is null, and thus already fixed, we cannot control the orientation of the cable. As a consequence, its motion is not necessarily "regular" and its space of definition must be enlarged*[1]*. In particular, the configuration $S \to \boldsymbol{x}(S)$ will always be continuous, but only piecewise differentiable. The vector tangent to the cable can be discontinuous at the points where masses are attached.*

The length of a material segment $dS$ in a configuration different than $\mathcal{C}_{\text{R}}$ can be computed by integrating over space the following relation:

$$s'(S,t) = \|\boldsymbol{x}'(S,t)\|. \tag{6.5}$$

It follows that we can use as measure of axial strain the quantity

$$\varepsilon(S,t) := \|\boldsymbol{x}'(S,t)\| - 1. \tag{6.6}$$

Relation (6.5) allows us to give the physical interpretation of condition (6.3): at any time, any segment of the cable cannot degenerate into a point during motion (and its orientation is note reversed).

We have to make here a fundamental assumption:

[1] They must belong to the space of Lipschitz continuous functions (Sobolev space $W^{1,\infty}(\mathcal{C}_{\text{R}})$).

**Assumption.** *Whenever $\mathcal{P}$ is not empty, the attached masses are assumed to transmit only a vertical force to the cable.*

In practice, we are stating that the masses do not behave like a pendulum when they are hanging to the cable (so their motion is always parallel to direction $x_2$) and do not possess inertia in the plane $x_1 - x_3$ (so their masses do not contribute to the linear momentum balance along directions $x_1$ and $x_3$). This assumption is based on the following considerations (some of them will be clarified in the rest of the chapter):

- we will be interested to restrict the movement of the cable in the plane $x_1 - x_2$;
- at low enough frequencies, the behavior of a bare cable in the axial (longitudinal) direction can be approximated as quasi-static;
- in a linearized framework with small oscillations around an almost flat equilibrium configuration, the in-plane motion of a bare cable is decoupled from the out-of-plane motion.

We can now study the equilibrium of the cable. Let us first define the contact forces acting on any section $S$ of a generic elongated medium ($\ell_\mathrm{R} \gg \sqrt{A_\mathrm{R}}$), avoiding for now any assumption on the transverse stiffness of the body. In particular, we postulate the existence of the internal force $\boldsymbol{R}(S,t)$ and of the couple $\boldsymbol{M}(S,t)$. Let us start with the balance of the angular momentum that can be expressed as:

$$\boldsymbol{M}'(S,t) + \|\boldsymbol{x}'(S,t)\|\boldsymbol{t}(S,t) \wedge \boldsymbol{R}(S,t) + \boldsymbol{m}_\mathrm{R}(S,t) = \boldsymbol{0}, \quad \forall S \in \mathcal{C}_\mathrm{R},\ t \tag{6.7}$$

where

- The equation is valid at any point $S$ of $\mathcal{C}_\mathrm{R}$ because the attached masses (if present) do not transmit any moment;
- The term $\boldsymbol{t}(S,t) \wedge \boldsymbol{R}(S,t)$ represents the shear force exerted on the part $(0,S)$ (or $(-\infty,S)$) of the cable by the part $(S,\ell_\mathrm{R})$ (or $(S,+\infty)$);
- The term $\boldsymbol{m}_\mathrm{R}(S,t)$ denotes distributed moments;
- We have assumed that the inertial term is small and can be neglected (small cross-section $A_\mathrm{R}$).

Since, as we stated before, the cable cannot sustain bending moments, then $\boldsymbol{M}(S,t) = \boldsymbol{m}_\mathrm{R}(S,t) = \boldsymbol{0}$ above. Therefore the angular momentum balance gives

$$\boldsymbol{t}(S,t) \wedge \boldsymbol{R}(S,t) = 0,$$

meaning that the shear force is null and thus that

$$\boldsymbol{R}(S) = N(S,t)\boldsymbol{t}(S,t), \tag{6.8}$$

where $N(S,t)$ is the amplitude of the axial force. Consequently, at a generic point $S$ where no punctual mass is attached, the balance of the linear momentum gives:

$$(N\boldsymbol{t})'(S,t) + \rho_\mathrm{R} g \boldsymbol{e}_2 - \rho_\mathrm{R}\ddot{\boldsymbol{x}}(S,t) = \boldsymbol{0}, \quad \forall S \in \mathcal{C}_\mathrm{R}\backslash\mathcal{P},\ \forall t, \tag{6.9}$$

where we recall that $\ddot{(\bullet)} = \partial^2(\bullet)/\partial t^2$.

The constitutive model can now be chosen[1]. In what follows we will consider two types of cables: one inextensible and the other one extensible, with a linear-elastic behavior. Let us give more details on the equations needed for the two models:

- *Inextensibility*: it can be imposed by requiring that the cable cannot stretch, such that
$$\|\boldsymbol{x}'(S,t)\| = 1. \tag{6.10}$$
It follows from (6.5) that the curvilinear abscissa $s$ of the deformed configuration coincides with the curvilinear abscissa $S$ of the reference configuration. Note that the strain measure (6.6) is thus well-suited for the characterization of deformations. Indeed, when the cable is *inextensible*, then relation (6.10) is valid and thus $\varepsilon = 0$ $\forall S, t$.

- *Linear-elastic behavior*: valid for the extensible cable, it is imposed by requiring that:
$$N(S,t) = EA_{\mathrm{R}}\varepsilon(S,t), \tag{6.11}$$
with $E$ denoting the Young's modulus of the material used for the cable.

If $\mathcal{P}$ is non-empty, at a point $S_i \in \mathcal{P}$ with $1 \leq i \leq N$, where a mass is attached, the cable is submitted to a concentrated vertical force whose intensity $F_i$ is given by

$$F_i(t) = \mathsf{k}(v_i(t) - x_{[2]}(S_i,t)) \tag{6.12}$$

corresponding to the tension in the spring, with $v_i(t)$ denoting the vertical displacement of the end point of the spring where the $i$-th mass is attached (by hypothesis, since the springs remain vertical, the displacement of the $i$-th mass is $x_{[1]}(S_i,t)\boldsymbol{e}_1 + v_i(t)\boldsymbol{e}_2 + x_{[3]}(S_i,t)\boldsymbol{e}_3$). When the masses are directly attached to the cable, one can consider the stiffness $\mathsf{k} \to +\infty$ and thus $v_i(t) = x_{[2]}(S_i,t)$ for the force $F_i$ to be bounded.

At a point $S_i$ the internal force defined by relation (6.8) must satisfy the following jump condition:

$$[\![N\boldsymbol{t}]\!](S_i,t) + F_i(t)\boldsymbol{e}_2 = \boldsymbol{0}. \tag{6.13}$$

Since the mass of the spring is neglected, the balance of linear momentum of the $i$-th mass along the vertical direction $\boldsymbol{e}_2$ reads as

$$M\ddot{v}_i(t) = Mg - F_i(t). \tag{6.14}$$

The system of equations (6.9), (6.12) to (6.14), together with relations (6.1), (6.2), and either (6.10) or (6.11), governs the motion of the cable and of the masses. When $\mathcal{C}_{\mathrm{R}}$ is a bounded set in $\mathbb{R}$, the complete initial-boundary value problem can be attained

[1]Note that, with the assumption that the string cannot sustain any moment, we had already made some hypotheses on the constitutive behavior of the cable.

with the help of the missing boundary condition at point $S = \ell_{\mathrm{R}}$, that, in our case, can be chosen as: specify

$$\boldsymbol{x}(S,t) \quad \text{or} \quad (N\boldsymbol{t})(S,t) \quad \text{at } S = \ell_{\mathrm{R}},\ \forall t.$$

In particular, we name the position of the right end point of the cable and the external force applied there as:

$$\boldsymbol{x}(\ell_{\mathrm{R}},t) = \check{\boldsymbol{x}}_{\mathrm{eq}} + \check{\boldsymbol{u}}(t) \quad \text{and} \quad (N\boldsymbol{t})(\ell_{\mathrm{R}},t) = \check{\boldsymbol{F}}_{\mathrm{eq}} + \check{\boldsymbol{F}}(t). \tag{6.15}$$

In order to guarantee the uniqueness of the solution, it is necessary to add to the equations governing the problem a so-called *stability condition*, such that

$$N(S,t) \geq 0 \quad \forall S,t, \tag{6.16}$$

meaning that the string can never sustain compression forces.

## 6.2 Static equilibrium configuration

In this section we derive in closed form the equilibrium configuration for bounded cables and we point out some limit behaviors that lead to important results concerning the validity of our subsequent approximations in dynamics.

Let us write here-below the boundary value problem for the equilibrium configuration of a cable with masses (non-empty $\mathcal{P}$), derived from the initial-boundary value problem described in the previous section:

$$\begin{cases} \boldsymbol{t}_{\mathrm{eq}}(S) = \dfrac{\boldsymbol{x}'_{\mathrm{eq}}(S)}{\|\boldsymbol{x}'_{\mathrm{eq}}(S)\|}, \quad \|\boldsymbol{x}'_{\mathrm{eq}}(S)\| = 1 + \varepsilon_{\mathrm{eq}}(S) & \forall S \notin \mathcal{P} \\ (N\boldsymbol{t})'_{\mathrm{eq}}(S) + \rho_{\mathrm{R}} g \boldsymbol{e}_2 = \boldsymbol{0} & \forall S \notin \mathcal{P} \\ [\![(N\boldsymbol{t})_{\mathrm{eq}}]\!](S_i) + F_{i(\mathrm{eq})}\boldsymbol{e}_2 = \boldsymbol{0}, \quad F_{i(\mathrm{eq})} = Mg & \forall S \in \mathcal{P},\ 1 \leq i \leq N \\ \boldsymbol{x}_{\mathrm{eq}}(0) = \boldsymbol{0}, \quad x_{[3]\mathrm{eq}}(\ell_{\mathrm{R}}) = 0 \end{cases} \tag{6.17}$$

where, $\varepsilon_{\mathrm{eq}}(S)$ is such that

$$\begin{cases} \varepsilon_{\mathrm{eq}}(S) = 0 \quad \forall S & \text{if the material is inextensible} \\ \varepsilon_{\mathrm{eq}}(S) = \dfrac{N_{\mathrm{eq}}(S)}{EA_{\mathrm{R}}} > -1 \quad \forall S & \text{if the material is extensible} \end{cases} \tag{6.18}$$

Note that, for now, we have only fixed the position of the extremity $S = \ell_{\mathrm{R}}$ to be on the $x_1 - x_2$ plane. Since also gravity acts on the $x_1 - x_2$ plane, the equilibrium configuration $\boldsymbol{x}_{\mathrm{eq}}(S)$ will lie on the same plane[1].

[1] Along direction $x_3$, the linear momentum equation for the cable states that the component $R_{[3]\mathrm{eq}}(S)$ of the internal force must be constant. One has two options:

1. $(N\boldsymbol{t})_{[3]\mathrm{eq}}(S) = 0$, then either $N_{\mathrm{eq}}$ or $t_{[3]\mathrm{eq}}$ must be zero, but $N_{\mathrm{eq}} = 0$ is not possible from the problem in the other 2 directions, thus $t_{[3]\mathrm{eq}} = 0$;
2. $(N\boldsymbol{t})_{[3]\mathrm{eq}}(S) \neq 0$, then both $N_{\mathrm{eq}}$ and $t_{[3]\mathrm{eq}}$ are different from zero and constant, but $t_{[3]\mathrm{eq}}$ cannot be constant otherwise $x_{[3]\mathrm{eq}}(0)$ and $x_{[3]\mathrm{eq}}(\ell_{\mathrm{R}})$ cannot lay on the $x_1 - x_2$ plane.

Therefore, the only possibility is $t_{[3]\mathrm{eq}} = 0\ \forall S$, as we said in the text.

One can retrieve the problem associated to a bare cable, *i.e.* with no masses, simply by remembering that $\mathcal{P}$ is empty in that case and by using the following condition

$$[\![(N\boldsymbol{t})_{\text{eq}}]\!](S) = \mathbf{0} \quad \forall S,$$

to be substituted to the jump conditions in problem (6.17). The relation here-above states the continuity of the internal force $\boldsymbol{R}$ along the whole cable.

We can now proceed by integrating the equilibrium equation of the cable, written as in (6.17). At this point, it is better to distinguish the case without the masses ($\mathcal{P} = \{0\}$) from that with the masses ($\mathcal{P} \neq \{0\}$).

### 6.2.1 Equilibrium of a bare cable

The equilibrium equation of the cable in (6.17) can be expressed $\forall S$ and, by integration, one obtains

$$(N\boldsymbol{t})_{\text{eq}}(S) = \check{F}_{[1]\text{eq}}\boldsymbol{e}_1 + (\check{F}_{[2]\text{eq}} + \rho_{\text{R}} g(\ell_{\text{R}} - S))\boldsymbol{e}_2,$$

where $\check{F}_{[i]\text{eq}}$, with $i = \{1, 2\}$, are the components of the force $\check{\boldsymbol{F}}_{\text{eq}}$ acting at $S = \ell_{\text{R}}$ and defined in (6.15). With the stability condition (6.16), one has

$$\begin{cases} N_{\text{eq}}(S) = \sqrt{\check{F}^2_{[1]\text{eq}} + (\check{F}_{[2]\text{eq}} + \rho_{\text{R}} g(\ell_{\text{R}} - S))^2} \\ \boldsymbol{x}'_{\text{eq}}(S) = \dfrac{1 + \varepsilon_{\text{eq}}(S)}{N_{\text{eq}}(S)} (\check{F}_{[1]\text{eq}}\boldsymbol{e}_1 + (\check{F}_{[2]\text{eq}} + \rho_{\text{R}} g(\ell_{\text{R}} - S))\boldsymbol{e}_2) \end{cases}. \tag{6.19}$$

Here, depending on the constitutive behavior envisaged, one can choose between the two relations (6.18). Let us derive the solution for the extensible case first. Integrating the second of relations (6.19), using the boundary conditions at $S = 0$, one finds the equilibrium configuration for the cable with no masses, in terms of the force acting at $S = \ell_{\text{R}}$, such that

$$\begin{cases} x_{[1]\text{eq}} = \dfrac{\check{F}_{[1]\text{eq}}}{\rho_{\text{R}} g} \left[ \operatorname{arsinh}\left( \dfrac{\check{F}_{[2]\text{eq}} + \rho_{\text{R}} g \ell_{\text{R}}}{\check{F}_{[1]\text{eq}}} \right) - \operatorname{arsinh}\left( \dfrac{\check{F}_{[2]\text{eq}} + \rho_{\text{R}} g(\ell_{\text{R}} - S)}{\check{F}_{[1]\text{eq}}} \right) \right] \\ \qquad + \dfrac{\check{F}_{[1]\text{eq}} S}{E A_{\text{R}}} \\ x_{[2]\text{eq}} = \dfrac{\check{F}_{[1]\text{eq}}}{\rho_{\text{R}} g} \left[ \sqrt{1 + \dfrac{(\check{F}_{[2]\text{eq}} + \rho_{\text{R}} g \ell_{\text{R}})^2}{\check{F}^2_{[1]\text{eq}}}} - \sqrt{1 + \dfrac{(\check{F}_{[2]\text{eq}} + \rho_{\text{R}} g(\ell_{\text{R}} - S))^2}{\check{F}^2_{[1]\text{eq}}}} \right] \\ \qquad + \dfrac{\check{F}_{[2]\text{eq}} S}{E A_{\text{R}}} + \dfrac{\rho_{\text{R}} g}{2 E A_{\text{R}}} S(2\ell_{\text{R}} - S) \end{cases}. \tag{6.20}$$

The solution for the inextensible cable is obtained from the above relations without the boxed terms ($EA_{\mathrm{R}} \to +\infty$).

The configuration of equilibrium is finally determined by imposing the remaining boundary conditions at $S = \ell_{\mathrm{R}}$. Let us note that, by taking $\check{F}_{[1]\mathrm{eq}} > 0$ and $\check{F}_{[2]\mathrm{eq}} = -\rho_{\mathrm{R}} g \ell_{\mathrm{R}}/2$, one finds that the right end of the cable is at height $x_{[2]\mathrm{eq}}(\ell_{\mathrm{R}}) = 0$ and thus at the same height of the left support.

The problem just solved is generally known as *catenary problem*, from the Latin word "*catena*" meaning *chain*.

### 6.2.2 Equilibrium of a cable with discrete hanging masses

This time, the equilibrium equation of the cable in problem (6.17) is valid $\forall S \notin \mathcal{P}$ and $\mathcal{P}$ is non-empty. Its integration thus gives:

$$(N\boldsymbol{t})_{\mathrm{eq}}(S) = \check{\boldsymbol{F}}_{\mathrm{eq}} + \rho_{\mathrm{R}} g(\ell_{\mathrm{R}} - S)\boldsymbol{e}_2 - \sum_{S \in \mathcal{P}_i} [\![(N\boldsymbol{t})_{\mathrm{eq}}]\!](S), \qquad \forall S \in ((i-1)d, id),\ 1 \le i \le N+1,$$

where the sets $\mathcal{P}_i$ are defined as follows:

$$\mathcal{P}_i := \begin{cases} \{0\} & \text{for } i = N+1 \\ \{S_j\}_{i \le j \le N} & \text{for } 1 \le j \le N \end{cases}.$$

If $[\![(N\boldsymbol{t})_{\mathrm{eq}}]\!](S) = \boldsymbol{0}\ \forall S$, one retrieves the solution valid for a bare cable.

Using the jump conditions of problem (6.17), we find

$$(N\boldsymbol{t})_{\mathrm{eq}}(S) = \check{F}_{[1]\mathrm{eq}}\boldsymbol{e}_1 + (\check{F}_{[2]\mathrm{eq}} + \rho_{\mathrm{R}} g(\ell_{\mathrm{R}} - S) - (N+1-i)Mg)\boldsymbol{e}_2, \qquad \forall S \in ((i-1)d, id),\ 1 \le i \le N+1.$$

With the stability condition (6.16), one has

$$N_{\mathrm{eq}}(S) = \sqrt{\check{F}^2_{[1]\mathrm{eq}} + (\check{F}_{[2]\mathrm{eq}} + \rho_{\mathrm{R}} g(\ell_{\mathrm{R}} - S) + (N+1-i)Mg)^2}, \tag{6.21}$$

valid for $S \in ((i-1)d, id),\ 1 \le i \le N+1$. The components of the tangent vector $\boldsymbol{t}_{\mathrm{eq}}$ can be found from

$$\boldsymbol{x}'_{\mathrm{eq}}(S) = \frac{1 + \varepsilon_{\mathrm{eq}}(S)}{N_{\mathrm{eq}}(S)}(\check{F}_{[1]\mathrm{eq}}\boldsymbol{e}_1 + (\check{F}_{[2]\mathrm{eq}} + \rho_{\mathrm{R}} g(\ell_{\mathrm{R}} - S) + (N+1-i)Mg)\boldsymbol{e}_2), \qquad \forall S \in ((i-1)d, id),\ 1 \le i \le N+1, \tag{6.22}$$

where again we can make use of the constitutive behavior (6.18), treating the inextensible problem as a particular case of the extensible one.

From the above ordinary differential equation, completed with the continuity condition $[\![\boldsymbol{x}_{\mathrm{eq}}]\!] = \boldsymbol{0}$ and the boundary conditions at $S = 0$, the equilibrium configuration

can be obtained in closed form and can be found in Appendix A3. The equilibrium configuration corresponds to $N+1$ arches of catenary connected with discontinuous tangent.

With the aim of studying some asymptotic behaviors of the cable, it is interesting here to rewrite the problem in dimensionless form. For this, let us take the length $\ell_{\mathrm{R}}$ of the cable as the reference length[1] and the component $\check{F}_{[1]\mathrm{eq}}$ of the applied force $\check{\boldsymbol{F}}_{\mathrm{eq}}$ as the reference force. Consequently, the equilibrium configuration depends on the following parameters: the number $N$ of attached masses, the ratio $\theta$ between the total mass of the hanging masses and the mass of the cable, the ratio $\eta$ between the own weight of the cable and the intensity of the applied force, the ratio $\zeta$ between the components of the applied force $\check{\boldsymbol{F}}_{\mathrm{eq}}$, and the ratio $\beta$ between the applied horizontal force and the axial stiffness of the cable

$$\theta := \frac{NM}{\rho_{\mathrm{R}}\ell_{\mathrm{R}}}, \quad \eta := \frac{\rho_{\mathrm{R}}\ell_{\mathrm{R}}g}{\check{F}_{[1]\mathrm{eq}}}, \quad \zeta = \check{F}_{[2]\mathrm{eq}}/\check{F}_{[1]\mathrm{eq}}, \quad \beta := \frac{\check{F}_{[1]\mathrm{eq}}}{EA_{\mathrm{R}}}. \tag{6.23}$$

Let us note that the spring stiffness $\mathsf{k}$ does not play any role in statics as far as the equilibrium configuration of the cable is concerned. It enters in the equilibrium position of the hanging masses only, such that

$$v_{i(\mathrm{eq})} = x_{[2]\mathrm{eq}}(S_i) + \frac{Mg}{\mathsf{k}}.$$

Let us further introduce the dimensionless coordinate $\hat{S}$ and the dimensionless fields $\hat{N}_{\mathrm{eq}}$, $\hat{\boldsymbol{x}}_{\mathrm{eq}}$ as

$$\hat{S} = S/\ell_{\mathrm{R}}, \quad \hat{N}_{\mathrm{eq}} = N_{\mathrm{eq}}/\check{F}_{[1]\mathrm{eq}}, \quad \hat{\boldsymbol{x}}_{\mathrm{eq}} = \boldsymbol{x}_{\mathrm{eq}}/\ell_{\mathrm{R}}. \tag{6.24}$$

### 6.2.3 Some asymptotic behaviors of the stable equilibrium configuration

By using the dimensionless quantities defined in (6.23) and (6.24), relations (6.21) and (6.22) can be rewritten in dimensionless form as follows: for $\hat{S} \in (\frac{i-1}{N+1}, \frac{i}{N+1})$ and $1 \leq i \leq N+1$,

$$\hat{N}_{\mathrm{eq}}(\hat{S}) = \sqrt{1 + \left[\zeta + \eta\left(1 - \hat{S} + \left(1 - \frac{i-1}{N}\right)\theta\right)\right]^2} \tag{6.25}$$

and

$$\hat{\boldsymbol{x}}'_{\mathrm{eq}}(\hat{S}) = \frac{1 + \varepsilon_{\mathrm{eq}}(\hat{S})}{\hat{N}_{\mathrm{eq}}(\hat{S})}\left\{\boldsymbol{e}_1 + \left[\zeta + \eta\left(1 - \hat{S} + \left(1 - \frac{i-1}{N}\right)\theta\right)\right]\boldsymbol{e}_2\right\}, \tag{6.26}$$

[1] If $\mathcal{C}_{\mathrm{R}}$ is unbounded, then a propagation problem is under investigation and one can take $\ell_{\mathrm{R}}$ to be a reference wave length.

where the strain $\varepsilon_{\text{eq}}(\hat{S})$ is given by

$$\begin{cases} \varepsilon_{\text{eq}}(\hat{S}) = 0 \quad \forall \hat{S} \backslash \hat{\mathcal{P}} & \text{if the material is inextensible} \\ \varepsilon_{\text{eq}}(\hat{S}) = \hat{N}_{\text{eq}}(\hat{S})\beta > -1 \quad \forall \hat{S} \backslash \hat{\mathcal{P}} & \text{if the material is extensible} \end{cases} . \tag{6.27}$$

The set $\hat{\mathcal{P}}$ can be obtained from $\mathcal{P}$ by multiplying its elements by $1/\ell_{\text{R}}$ to obtain dimensionless coordinates.

We can re-obtain the dimensionless relations valid for a bare cable by making relations (6.25) to (6.27) valid $\forall \hat{S}$ and by considering $\theta = 0$.

### Small sag approximation

Let us start from the bare cable. Accordingly, $\theta = 0$. When the component $\check{F}_{[1]\text{eq}}$ of the force applied at $\hat{S} = 1$ is much larger than the total weight of the cable and than the other component $\check{F}_{[2]\text{eq}}$, then $\eta$ and $\zeta$ are small. From relation (6.25), one obtains

$$\hat{N}_{\text{eq}}(\hat{S}) \approx 1 \quad \forall \hat{S}.$$

Then, from relation (6.26) we have that $\hat{x}'_{[1]\text{eq}} \gg \hat{x}'_{[2]\text{eq}}$. Therefore, for an extensible cable, using relation (6.6) we find that

$$\varepsilon_{\text{eq}}(\hat{S}) \approx \hat{x}'_{[1]\text{eq}}(\hat{S}) - 1.$$

Since $\hat{N}_{\text{eq}}(\hat{S})$ is a constant, inserting the second of relations (6.27) in the above relation, we find that also $\hat{x}'_{[1]\text{eq}}(\hat{S})$ must be a constant, such that:

$$\hat{x}'_{[1]\text{eq}}(\hat{S}) = 1 + \beta. \tag{6.28}$$

Consequently, using the cable equilibrium equation in problem (6.17) along the $x_2$ direction, rewritten in dimensionless form, we find:

$$\hat{x}''_{[2]\text{eq}}(\hat{S}) = -\eta(1 + \beta). \tag{6.29}$$

If the right end of the cable is such that $\hat{x}_{[2]\text{eq}}(1) = 0$, then equation (6.29) gives:

$$\hat{x}_{[2]\text{eq}}(\hat{S}) = \frac{\eta}{2}(1 + \beta)\hat{S}(1 - \hat{S}). \tag{6.30}$$

Hence, the equilibrium configuration of a cable hanging between two supports at the same heights is approximated by a *parabola*. Considering the mid-point of the cable ($\hat{S} = 1/2$), the dimensionless sag $\hat{\mathsf{b}}$ is given by

$$\hat{\mathsf{b}} = \frac{\eta}{8}(1 + \beta). \tag{6.31}$$

The same derivation is also valid for an inextensible cable, by making $\beta \to 0$. From relation (6.28), by assuming $\hat{x}_{[1]\text{eq}}(1) = \ell_{\text{span}}/\ell_{\text{R}}$, we also find:

$$\hat{x}_{[1]\text{eq}}(\hat{S}) = \ell_{\text{span}}/\ell_{\text{R}} + (1+\beta)(\hat{S}-1),$$

where $\ell_{\text{span}}$ is thus the position of the cable right end.

This approximation is commonly made especially in civil engineering applications (see *e.g.* Gazzola (2015)). Note that the equations governing the problem of the static equilibrium of a bare cable hanging between two supports at the same height could be rewritten in terms of a spatial variable $\hat{x}$ along direction $x_1$, such that

$$\begin{cases} \hat{N}_{\text{eq}}(\hat{x})\cos(\phi(\hat{x})) = 1 \\ (\hat{N}_{\text{eq}}(\hat{x})\sin(\phi(\hat{x})))' = -f(\hat{x})\sqrt{1+\hat{x}'^2_{[2]\text{eq}}(\hat{x})} \end{cases}, \tag{6.32}$$

where $\phi(\hat{x})$ is the curvature defined in relation (6.4), here given in terms of $\hat{x}$, and $f(\hat{x})\sqrt{1+\hat{x}'^2_{[2]\text{eq}}(\hat{x})}$ is a generic source term acting along the cable (it can represent its weight per unit of cable length for instance). Problem (6.32) can be rewritten as

$$\hat{x}''_{[2]\text{eq}}(\hat{x}) = -f(\hat{x})\sqrt{1+\hat{x}'^2_{[2]\text{eq}}(\hat{x})}, \tag{6.33}$$

by using the fact that the tangent $\hat{x}'_{[2]\text{eq}}(\hat{x})$ to the cable is obtained as

$$\hat{x}'_{[2]\text{eq}}(\hat{x}) = \tan(\phi(\hat{x})).$$

Note that the constitutive behavior of the cable seems to play no role in these considerations. Nevertheless, it is "hidden" in the term $\hat{N}_{\text{eq}}(\hat{x})$.

The form of the solution to the equation (6.33) depends on $f(\hat{x})$: it is in general a catenary, but it becomes a parabola when $\hat{x}'_{[2]\text{eq}}(\hat{x}) \approx 0$, *i.e.* when $\hat{x}'_{[1]\text{eq}}(\hat{S}) \gg \hat{x}'_{[2]\text{eq}}(\hat{S})$ that is exactly the condition valid for the small sag approximation. In this case, the source term in equation (6.33) is a load per unit of horizontal length. This is indeed the situation which occurs when a beam is suspended to a cable by means of a family of hangers. If we assume that spacing between hangers is small relative to the span, then the hangers can be considered as a continuous sheet or a membrane uniformly connecting the cable and the beam (this case will be treated later on). By neglecting the mass of the cable, then the load is distributed per horizontal unit. This is a simplified sketch of what occurs in a suspension bridge.

When $\mathcal{P}$ is not empty (masses are present), similar results can be derived when $\eta$, $\zeta$ and $\eta\theta$ are small. Accordingly, we added to the assumptions made before for the bare cable the additional request that the component $\check{F}_{[1]\text{eq}}$ of the force applied at $\hat{S} = 1$ must be much larger than the total weight of the attached masses. In particular, for a cable hanging between two supports at the same heights with a set of $N$ masses attached to it, one obtains that the equilibrium configuration corresponds to $N+1$ arches of parabola with continuity of the graph but not of the tangent. Indeed, one finds that the same considerations valid for the bare cable are applicable also here, piecewise in each interval. The final configuration of the cable can then be obtained by using the jump conditions from problem (6.17) at each one of the positions $\hat{S}_i \in \mathcal{P}$.

### Great intensity of the horizontal applied force

Let us now consider the asymptotic behavior of the equilibrium configuration when the intensity $\check{F}_{[1]\text{eq}}$ of the external force applied in direction $x_1$ tends to infinite, the number $N$ and the mass of the hanging masses being fixed, and the axial stiffness $EA_\text{R}$ being $\mathcal{O}(\check{F}_{[1]\text{eq}})$. In other words, $N$, $\theta$ and $\beta$ are fixed and finite, whereas $\eta$ goes to 0. Using (6.26), one immediately gets the following asymptotic behaviors for the tension in the cable and its displacement:

$$\hat{N}_\text{eq}(\hat{S}) = 1 + \mathcal{O}(\eta^2), \quad \hat{x}_{[1]\text{eq}}(\hat{S}) = 1 + \mathcal{O}(\eta^2), \quad \hat{x}_{[2]\text{eq}}(\hat{S}) = \mathcal{O}(\eta). \tag{6.34}$$

Hence, the tension in the cable tends to be uniform and equal to the applied force whereas the equilibrium configuration of the cable tends to be horizontal, the weight of the cable and of the hanging masses being too small to bend the cable.

One can check the validity of this asymptotic behavior, that is strongly dependent on the material considered for the cable (Marigo, 2014). For this, let us give the total cable weight per unit area $w$ and the external force per unit area $p$, such that:

$$w = \rho_\text{R} g \ell_\text{R} / A_\text{R}, \quad p = \check{F}_{[1]\text{eq}} / A_\text{R}.$$

Let us consider the case of a cable hanging between two supports positioned at the same heights. This implies a specific value for the component $\check{F}_{[2]\text{eq}}$ of the external force, such that

$$\begin{cases} \check{F}_{[2]\text{eq}} = -\rho_\text{R} g \ell_\text{R}/2 & \mathcal{P} = \{0\} \\ \check{F}_{[2]\text{eq}} = -(\rho_\text{R}\ell_\text{R} + MN)g/2 & \mathcal{P} \neq \{0\} \end{cases}.$$

Let us look to the bare cable case. Accordingly, from relation (6.20), the positions of the left end and of the central material point of the cable read respectively:

$$\frac{x_{[1]\text{eq}}(\ell_\text{R})}{\ell_\text{R}} = \frac{2p}{w}\ell_\text{R}\,\text{arsinh}\left(\frac{w}{2p}\right) + \frac{p}{E}, \quad \frac{x_{[2]\text{eq}}(\ell_\text{R}/2)}{\ell_\text{R}} = \sqrt{\frac{p^2}{w^2} + \frac{1}{4}} - \frac{p}{w} + \frac{w}{8E} \tag{6.35}$$

With a metallic cable, such as the one that we are going to use later on, the Young's modulus is of the order of $\mathcal{O}(10^{11})$ Pa. The ratio $w/E$ is actually always small and can be neglected. Since we are here considering an elastic regime, the deformation must not overtake that at the yielding limit. Therefore, the ratio $p/E$ is at maximum of the order of $\mathcal{O}(10^{-3})$ and can be neglected in the above relations (6.35). This means that, in statics, the increasing of axial deformation due to extensibility can be neglected. Eventually, $p$ can be as large as $\mathcal{O}(10^8)$ Pa and the cable is still in elastic regime. Consequently, the ratio $p/w \equiv \eta$ can be very small. This considerations justify the assumptions (6.34).

For the metallic cable with attached masses, one has to consider an additional parameter representing the weight of one mass per unit of cable area, namely $Mg/A_\text{R}$. If this term is of the same order of magnitude of $w$ (*i.e.* if cable and masses have comparable weights), then observations similar to those applicable to the bare cable are also valid piecewise for the case with masses and the assumptions (6.34) can be used.

### Small self-weight of the cable

Let us assume that the own weight of the cable is small by comparison with the total mass of the hanging masses and the intensity of the horizontal applied force, these two quantities being of the same order. So, at fixed number of hanging masses, one assumes that $\eta$ is small and $\theta$ is of the order of $1/\eta$, such that

$$\eta\theta = \frac{Mg}{\check{F}_{[1]\mathrm{eq}}}$$

remains finite. Neglecting the term $1 - \hat{S}$ everywhere in (6.25) and (6.26), one gets that $\hat{N}_{\mathrm{eq}}$, $\hat{x}_{[1]\mathrm{eq}}$ and $\hat{x}_{[1]\mathrm{eq}}$ are constant in each interval $(\hat{S}_{i-1}, \hat{S}_i)$ between two attached masses. Accordingly, the equilibrium configuration of the cable is practically piecewise linear, the tangent being discontinuous with a jump depending both on $i$ and $\eta\theta$. Figure

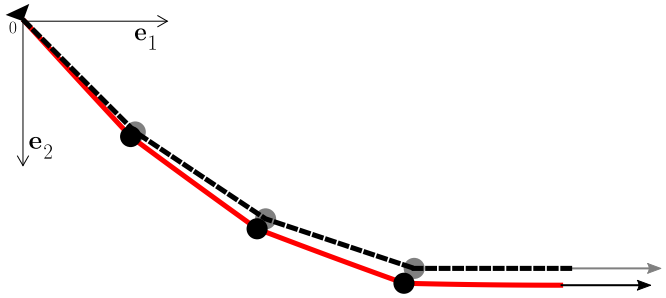


Figure 6.4: *Equilibrium configurations of the cable with 3 hanging masses: in plain line when $\theta = 10$ and $\eta = 0.1$ (so $\eta\theta = 1$), in dashed line when the own weight of the cable is neglected and $\eta\theta = 1$. The left end is fixed while a force is applied on the right end. Circles denote the presence of a mass.*

6.4 compares the equilibrium configuration of the inextensible cable in the case of three hanging masses when $\theta = 10$, $\eta = 0.1$ (hence $\eta\theta = 1$) and $\zeta = 0$ ($\check{F}_{2(\mathrm{eq})} = 0$), with the one when the own weight is neglected (but still with $\eta\theta = 1$). Let us remark that in the approximate configuration the last segment line of the cable is necessarily horizontal and the tension is equal to the applied force by virtue of the force applied at $\hat{S} = \ell$. In the case where $\theta = 100$ and $\eta = 0.01$, the exact equilibrium configuration and the approximate one are practically identical.

### Large number of attached masses

Let us consider the asymptotic behavior of the equilibrium configuration when the number $N$ of attached masses goes to infinity at fixed total mass $M_{tot}$ (and fixed applied horizontal force $\check{F}_{[1]\mathrm{eq}}$). As we anticipated in the case of small sag, the approximation currently studied is very often used for modeling the cable system in suspension bridges. For a given total mass $M_{tot}$ (or equivalently a given ratio $\theta$), we consider the case of $N$ attached masses whose individual mass is $M = M_{tot}/N$ and whose spacing is $d$.

Accordingly, one obtains again the solution (6.20), with $\rho_{\mathrm{R}}$ substituted by the increased mass density $\rho_{\mathrm{R}} + M_{tot}/\ell_{\mathrm{R}}$. Figure 6.5 shows the exact equilibrium configuration

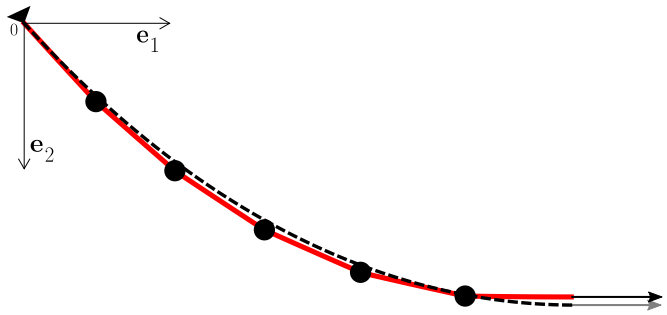


Figure 6.5: *In plain red equilibrium configuration of the cable with 5 hanging masses and in dashed black its configuration in the limit case of an infinite number of hanging masses, in the case where $\theta = 1$ and $\eta = 1/2$. The left end is fixed while a force is applied on the right end. Circles denote the presence of a mass.*

of an inextensible cable when $N = 5$ and the limit configuration (when $N$ goes to infinity), for $\theta = 1$ and $\eta = 1/2$. One sees that the two curves are already close although $N$ is not large.

If $\rho_{\mathrm{R}} \ll M_{tot}/\ell_{\mathrm{R}}$, then the effective mass density of the cable can be approximated with $M_{tot}/\ell_{\mathrm{R}}$. This is generally the assumption used for suspension bridges. If, moreover, the tension in the cable is high enough so that the sag is small, then the cable finds its equilibrium in a parabolic configuration, as we showed before in the small sag approximations.

One can verify that the distance[1] between the exact solution $\hat{\boldsymbol{x}}_{\mathrm{eq}}$ and the approximated solution $\hat{\boldsymbol{x}}_{\infty(\mathrm{eq})}$ is of the order of $1/N$. Additionally, the jump discontinuity of the tangent vector tends to 0 like $1/N$. This asymptotic result remains true even if a few hanging masses are missing all along the cable (in fact, the result still holds provided that the number of missing masses is small with respect to the total number of masses). So such defects have no influence on the equilibrium configuration of the cable, at least at the first order (in fact, the defects induce boundary layer effects in their neighborhood, but their amplitude is small and tends to 0 when $N$ tends to infinity).

In other words, we have found the following result:

**Result.** *When the number of hanging masses goes to infinity (at given total mass $M_{tot}$), the cable behaves like a bare cable with linear mass density increased by $M_{tot}/\ell_R$. There is no more discontinuity of the tangent at the limit, the discrete points of attach are no more visible.*

This intuitive result has been established in a static context. We will later show that the introduction of a defect has instead a significant effect in dynamics.

[1] in the sense of the $W^{1,\infty}$ norm.

## 6.3 Motion of the cable

We now go back to the time dependent motion of a bounded cable. Let us thus first rewrite the initial-boundary value problem valid $\forall t$:

$$\begin{cases} \boldsymbol{t}(S,t) = \dfrac{\boldsymbol{x}'(S,t)}{\|\boldsymbol{x}'(S,t)\|}, \quad \|\boldsymbol{x}'(S,t)\| = 1 + \varepsilon(S,t) & \forall S \notin \mathcal{P} \\ (N\boldsymbol{t})'(S,t) + \rho_{\mathrm{R}} g \boldsymbol{e}_2 - \rho_{\mathrm{R}} \ddot{\boldsymbol{x}}(S,t) = \boldsymbol{0} & \forall S \notin \mathcal{P} \\ [\![(N\boldsymbol{t})]\!](S_i,t) + F_i \boldsymbol{e}_2 = \boldsymbol{0}, \quad F_i = M\left(g - \ddot{v}_i(t)\right) & \forall S \in \mathcal{P},\ 1 \leq i \leq N \\ \boldsymbol{x}(0,t) = \boldsymbol{0}, \quad x_{[3]}(\ell_{\mathrm{R}},t) = 0 & \end{cases} \tag{6.36}$$

where, the vertical displacement $v_i(t)$ of the attached mass can be obtained using relation (6.12) and $\varepsilon(S,t)$ is such that

$$\begin{cases} \varepsilon(S,t) = 0 \quad \forall S & \text{if the material is inextensible} \\ \varepsilon(S,t) = \dfrac{N(S,t)}{EA_{\mathrm{R}}} > -1 \quad \forall S & \text{if the material is extensible} \end{cases}. \tag{6.37}$$

Note that the two boundary conditions at $S = \ell_{\mathrm{R}}$ are not specified at the moment. As for the static case, we will choose between an imposed position or an imposed force for the right end of the cable, along directions $x_1$ and $x_2$.

The problem associated to a bare cable, *i.e.* with no masses, corresponds to the case when $\mathcal{P}$ is empty and can be derived by using the following condition

$$[\![(N\boldsymbol{t})]\!](S,t) = \boldsymbol{0} \quad \forall S, t,$$

to be substituted to the jump conditions in problem (6.36). The above relation states the continuity of the internal force $\boldsymbol{R}$ along the whole cable, for any time.

The position and force at the right end of the cable are given by relations (6.15) and their time dependent parts can be rewritten by using

$$\check{\boldsymbol{u}}(t) = \ell_{\mathrm{R}} \check{\mathbf{u}}(t), \quad \check{\boldsymbol{F}}(t) = \check{F}_{[1]\mathrm{eq}} \check{\mathbf{F}}(t), \tag{6.38}$$

such that the moduli of $\check{\mathbf{u}}(t)$ and $\check{\mathbf{F}}(t)$ remain always small and of the same order of magnitude. Clearly, for any direction, one has to choose between an imposed displacement and an imposed force. We thus seek formal solutions of the initial-boundary value problem specified here-above by assuming that the motion of the cable and the masses remains close to their stable equilibrium configurations, such that

$$\begin{cases} N(S,t) = N_{\mathrm{eq}}(S) + \check{F}_{[1]\mathrm{eq}} \hat{N}(\hat{S},t), \\ \boldsymbol{x}(S,t) = \boldsymbol{x}_{\mathrm{eq}}(S) + \ell_{\mathrm{R}} \hat{\boldsymbol{u}}(\hat{S},t), \\ v_i(t) = v_{i(\mathrm{eq})} + \ell_{\mathrm{R}} \hat{v}_i(\hat{S},t), \end{cases} \tag{6.39}$$

with $\hat{N}(\hat{S},t)$, $\hat{\boldsymbol{u}}(\hat{S},t)$ and $\hat{v}_i(\hat{S},t)$ being small and of the same order of magnitude of the prescribed time dependent data.

In this section we study the first order approximation of the motion of a cable, assuming a *harmonic time variation* for the data (6.38). In particular, we initially study the eigenvalue problem associated to problem (6.36) for bare cables. This allows us to present a fundamental result, first derived by Irvine et al. (1976), concerning the validity of inextensibility in the dynamics of "shallow" cables, *i.e.* in systems where the sag-to-span ratio of the static equilibrium configuration is small (parabolic approximation). This considerations will be useful for our subsequent derivation. Then we present the results from the cable with attached masses, by showing how its behavior resembles very much that of the metamaterials treated in this manuscript.

### 6.3.1 Linearized dynamics for a bare cable with fixed supports

Let us here consider the eigenvalue problem for a bare cable hanging between two supports positioned at the same height. The vertical position of the cable left and right ends is thus fixed. Concerning the boundary condition at $S = \ell_{\mathrm{R}}$ along direction $x_1$, we envisage either an imposed fixed position or an applied horizontal force that can vary with time.

The following considerations are necessary due to the failure of models that approximate the behavior of the cable as inextensible to reproduce, as a limit case, the classical results valid for a *taut cable* (*i.e.* for cables with no initial sag) when the horizontal position of the right support is imposed. More specifically, this theory applies to cables subjected to a tension much larger than their total weight, still remaining in an elastic regime. As we showed previously, metallic cables constitute a typical example. For these cases, the static equilibrium configuration is very close to be aligned with the axis $x_1$ and can be approximated with a parabola. We thus have the following assumptions:

- $N_{\mathrm{eq}}(S) \approx \check{F}_{[1]\mathrm{eq}}$ and thus constant;
- $\check{F}_{[1]\mathrm{eq}}/EA_{\mathrm{R}} \ll 1$;
- $x'_{[1]\mathrm{eq}}(S) \approx 1$ and thus $dS \approx dx_{[1]\mathrm{eq}}$;
- $\mathsf{b} = x_{[1]\mathrm{eq}}(\ell_{\mathrm{R}}/2) \approx \dfrac{\rho_{\mathrm{R}} g \ell_{\mathrm{R}}^2}{8F_{[1]\mathrm{eq}}}$,

where $\mathsf{b}$ is the cable sag (*cf.* relation (6.31)).

It is interesting to initially treat the strongest approximation previously defined as "great intensity of the horizontal applied force", such that the cable static equilibrium configuration can be approximated to be straight and horizontal. At first order, this is the classical problem of a vibrating string and is governed by the following relations:

$$\begin{cases} \ddot{\hat{u}}_{[1]}(\hat{S},t) - c_l^2 \hat{u}''_{[1]}(\hat{S},t) = 0 \\ \ddot{\hat{u}}_{[2]}(\hat{S},t) - c_t^2 \hat{u}''_{[2]}(\hat{S},t) = 0 \\ \ddot{\hat{u}}_{[3]}(\hat{S},t) - c_t^2 \hat{u}''_{[3]}(\hat{S},t) = 0 \end{cases}, \tag{6.40}$$

with

$$c_l = \frac{EA_{\mathrm{R}}(1+\beta)^2}{\rho_{\mathrm{R}}}, \quad c_t = \frac{\check{F}_{[1]\mathrm{eq}}(1+\beta)}{\rho_{\mathrm{R}}}$$

being the wave speeds respectively in the longitudinal and transverse directions, with $(1+\beta)$ standing for the initial deformation due to the static loading phase. The three equations are uncoupled. In particular, from the last two of them, it seems that the role played by elasticity is null for the transverse motion. This is clearly wrong because an inextensible taut cable between two fixed supports could not vibrate without undergoing some deformations: its motion would be geometrically impossible. This is a first evidence on why inextensibility must be considered with care when dealing with the motion problem.

Problem (6.40), together with the boundary conditions that both ends are fixed, represents an eigenvalue problem. One typically finds the following eigenfrequencies for the three uncoupled directions[1]

$$\begin{cases} \omega_q = q\pi c_l/\ell_{\mathrm{R}} & q \in \mathbb{N}^* \quad \text{longitudinal problem} \\ \omega_j = j\pi c_t/\ell_{\mathrm{R}} & j \in \mathbb{N}^* \quad \text{transverse problems} \end{cases}. \tag{6.41}$$

Looking at the ratio between the wave speeds, one has the following relation:

$$\frac{c_l}{c_t} = \sqrt{\frac{1+\beta}{\beta}}.$$

For a metallic cable, the above ratio is very large. Consequently, for $q = j$, we have $\omega_q \gg \omega_j$. We have thus obtained that the longitudinal propagation is much faster than the transverse one, in the sense that, if an external excitation is at the first frequencies of primary resonance for the transverse direction (low index $j$), then such excitation is too slow for the longitudinal modes to be activated and the longitudinal inertia can be neglected (*static condensation*).

Let us now "relax" our assumptions by considering a parabolic cable equilibrium configuration (small sag approximation), that can be written from relation (6.30) as:

$$\hat{x}_{[2]\mathrm{eq}}(\hat{S}) \approx 4\hat{\mathfrak{b}}\hat{S}\left(1-\hat{S}\right). \tag{6.42}$$

After some manipulations of the equation governing the motion of the cable in problem (6.36) (this part of the derivation is not given here and can be found in the Appendix A4), one can again exploit a static condensation: at sufficiently low frequencies of excitation, the longitudinal inertia of the cable can be neglected. With this additional assumption (which is rather feasible for cables with high stiffness), the equation of motion at the first order along the horizontal direction $x_1$ in problem (6.36) can be written as:

$$\left[\hat{u}'_{[1]}(\hat{S},\hat{t}) + \hat{x}'_{[2]\mathrm{eq}}(\hat{S})\hat{u}'_{[2]}(\hat{S},\hat{t}) + \frac{1}{2}\hat{u}'^2_{[2]}(\hat{S},\hat{t}) + \frac{1}{2}\hat{u}'^2_{[3]}(\hat{S},\hat{t})\right]' = 0, \tag{6.43}$$

[1] The trivial solution $\hat{u}_{[i]} = 0$ is discarded for all $i = \{1,2,3\}$.

with

$$\hat{t} = \frac{c_t}{\ell_{\mathrm{R}}}\, t$$

being the non-dimensional time variable. Note that, according to equation (6.43), the longitudinal component $\hat{u}_{[1]}$ of the vibrations must be second order with respect to the small transverse components ($\hat{x}_{[2]\mathrm{eq}}$ is indeed considered $\mathcal{O}(\|\hat{\boldsymbol{u}}\|)$). Let us call $f$ the quantity within the squared brackets on the left-hand side of relation (6.43), such that:

$$f(\hat{t}) = \hat{u}'_{[1]}(\hat{S},\hat{t}) + \hat{x}'_{[2]\mathrm{eq}}(\hat{S})\hat{u}'_{[2]}(\hat{S},\hat{t}) + \frac{1}{2}\hat{u}'^2_{[2]}(\hat{S},\hat{t}) + \frac{1}{2}\hat{u}'^2_{[3]}(\hat{S},\hat{t}). \tag{6.44}$$

This function, if multiplied by the axial stiffness $EA_{\mathrm{R}}$, gives the horizontal component of the axial force due to the motion of the cable and is constant in space, according to relation (6.43). The resulting motion is strongly affected by the boundary condition at $S = \ell_{\mathrm{R}}$, that has not been fixed yet, to be chosen from relations (6.38).

Let us start from the case when the horizontal position of the right end of the cable is fixed to be $x_{[1]}(\ell_{\mathrm{R}}, t) = \ell_{\mathrm{span}}$. Note that $\ell_{\mathrm{span}}$ is the cable span and must be sufficiently large compared to the sag $\mathsf{b}$, such that the parabolic approximation for the static equilibrium configuration is respected (typically, $\ell_{\mathrm{span}} \geq 8\mathsf{b}$ is enough). By integration over space of equation (6.43), using the boundary conditions, we have:

$$\int_0^1 \hat{x}'_{[2]\mathrm{eq}}(\hat{S})\hat{u}'_{[2]}(\hat{S},\hat{t}) + \frac{1}{2}\hat{u}'^2_{[2]}(\hat{S},\hat{t}) + \frac{1}{2}\hat{u}'^2_{[3]}(\hat{S},\hat{t})\, d\hat{S} = f(\hat{t}),$$

where $\hat{x}'_{[2]\mathrm{eq}}$ is obtained by derivation with respect to $\hat{S}$ of relation (6.42). The function $f(\hat{t})$, defined by relation (6.44), can be substituted in the equations of motion written for the other two direction and, upon linearization, one obtains the following problem[1]:

$$\begin{cases} \ddot{\hat{u}}_{[2]}(\hat{S},\hat{t}) - \hat{u}''_{[2]}(\hat{S},\hat{t}) + 32\,\psi\, f(\hat{t}) = 0 \\ \ddot{\hat{u}}_{[3]}(\hat{S},\hat{t}) - \hat{u}''_{[3]}(\hat{S},\hat{t}) = 0 \end{cases}, \tag{6.45}$$

with

$$\psi = \frac{8bEA_{\mathrm{R}}}{\rho_{\mathrm{R}} g \ell_{\mathrm{R}}^2}\left(\frac{\mathsf{b}}{\ell_{\mathrm{R}}}\right)^2. \tag{6.46}$$

Solutions to problem (6.45) completed with the boundary conditions considered in this subsection can be found in closed form. Let us specify here some properties of the solutions:

- the in-plane and the out-of-plane problems are decoupled, as in the case of a taut string;
- for the out-of-plane vibrations, one finds exactly the same results valid for the taut string;

[1] Some steps are skipped here for brevity sake. They can be retrieved by looking in Appendix A4.

- for the in-plane vibrations, one has to distinguish between anti-symmetric and symmetric modes:

  A for the anti-symmetric modes one finds the classical result valid for a taut string, obtaining the eigenfrequencies $\omega_j$ as in (6.41) for $j$ even;

  B the eigenfrequencies corresponding to symmetric modes are instead obtained from

$$\tan\frac{\hat{\omega}}{2} = \frac{\hat{\omega}}{2} - \frac{\hat{\omega}^3}{128\psi}, \quad \text{with } \hat{\omega} = \omega\ell_{\mathrm{R}}/c_t \tag{6.47}$$

  and depend on the parameter $\psi$.

The above results can be visualized in figure 6.6, where equation (6.47) is graphically resolved. In particular, the left- and the right-hand sides of that relation are plotted

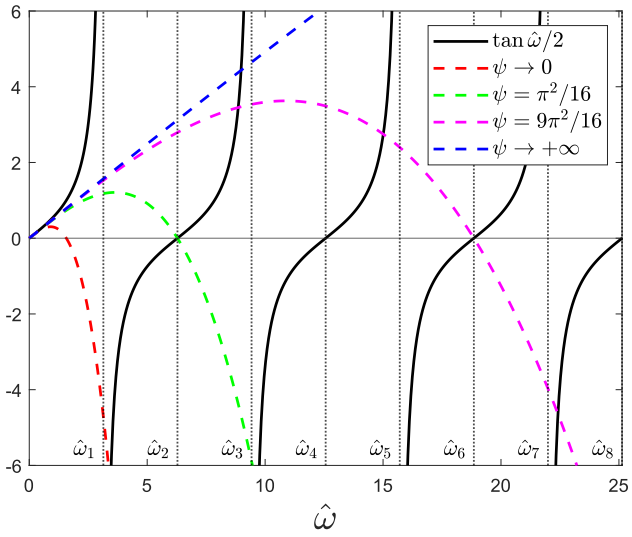


Figure 6.6: *Eigenfrequencies of a cable with a parabolic equilibrium configuration.*

with continuous and dashed curves respectively. The vertical lines correspond instead to all the eigenfrequencies $\omega_j$ coming from the problem of the taut cable, normalized as in (6.47). Accordingly, when $j$ is an even number, $\omega_j$ gives the eigenfrequency of an anti-symmetric eigenmode also when the cable equilibrium configuration is not perfectly straight but has an initial (small) sag. Instead, when $j$ is odd, one has to consider equation (6.47) to find the eigenfrequencies. In the limit of very small sag, one should be able to retrieve the classical results valid for a taut string also for the symmetric in-plane modes.

From figure 6.6, the eigenfrequencies are given as the intersections between the dashed curves and the plain curve representing the plot of $\tan\hat{\omega}/2$. Let us analyze the two extreme cases, namely $\psi \to +\infty$ (blue line) and $\psi \to 0$ (red line). From relation

(6.46) one has:

$$\begin{cases} \psi \to +\infty : & EA_{\mathrm{R}} \to +\infty \\ \psi \to 0 : & b/\ell_{\mathrm{R}} \to 0 \end{cases}$$

The failure of inextensible models to predict the correct behavior of a cable hanging between two fixed supports in the limit of small sag-to-span ratio (*i.e.* when the cable initial configuration is almost horizontal) is thus explained: by stating that $EA_{\mathrm{R}} \to +\infty$, the first eigenfrequency $\omega_1 = \pi c_t/\ell_{\mathrm{R}}$ is lost, as one can see from figure 6.6, where the first intersection of the blue curve (corresponding to $\psi \to +\infty$) with the plot of $\tan \hat{\omega}/2$ takes place at $\hat{\omega}_3$, *i.e.* at the eigenfrequency corresponding to the second symmetric eigenmode of a taut string. The physical reason for this is that the first symmetric eigenmode is geometrically impossible without undergoing some stretch. Consequently, the classical results of a taut string cannot be obtained. To correctly recover the taut string results, one has to consider $EA_{\mathrm{R}}$ as large as it is, but finite. Taking $b/\ell_{\mathrm{R}} \to 0$ will then give the correct result. These results suggest that one has to use with care the inextensibility assumption.

Let us comment on the other two cases (green and violet lines) reported in figure 6.6. For these values of $\psi$, the two curves intersect the graph of $\tan \hat{\omega}/2$ exactly at two eigenfrequencies of the anti-symmetric modes ($\hat{\omega}_2$ and $\hat{\omega}_6$). These particular condition is known as *crossover* and can generate internal resonances (Rega et al., 1999; Nayfeh et al., 2002) when the non-linearities of the problem are taken into account (*i.e.* when the vibrations of the cable are not sufficiently small).

Let us now consider the case when the horizontal position of the right end of the cable is free, while an external horizontal force $\check{F}_{[1]}(t)$ is imposed, with time variation sufficiently slow to avoid the activation of longitudinal inertia. We recall that $f(t)$, given by relation (6.44) expressed in function of the time variable $t$, when multiplied by the axial stiffness $EA_{\mathrm{R}}$ gives the horizontal component of the axial force due to the motion of the cable. Consequently, to fulfill the boundary condition at $S = \ell_{\mathrm{R}}$, one must have:

$$f(t) = \frac{\check{F}_{[1]}(t)}{EA_{\mathrm{R}}}.$$

Substituting the function $f(t)$ in the equations of motion written for the directions $x_2$ and $x_3$ (*cf.*Appendix A4) one obtains:

$$\begin{cases} \rho_{\mathrm{R}} \ddot{u}_{[2]}(S,t) = (\check{F}_{[1]\mathrm{eq}} + \check{F}_{[1]}(t)) u''_{[2]}(S,t) + \check{F}_{[1]}(t) x''_{[2]\mathrm{eq}}(S) \\ \rho_{\mathrm{R}} \ddot{u}_{[3]}(S,t) = (\check{F}_{[1]\mathrm{eq}} + \check{F}_{[1]}(t)) u''_{[3]}(S,t) \end{cases}.$$

If the imposed external force is constant in time ($\check{F}_{[1]}(t) = 0$), then the problem of a taut string is completely restored. The inextensibility assumption can be employed for this case.

Note that, with the results in the present subsection, we have also finally justified the assumption that the masses transmit only a vertical force to the cable (*cf.* section 6.1).

### 6.3.2 Linearized dynamics for a cable with attached masses

Let us now analyze the problem of small harmonic oscillations of a cable with attached masses. We consider a metallic cable that is hanging between two supports at the same

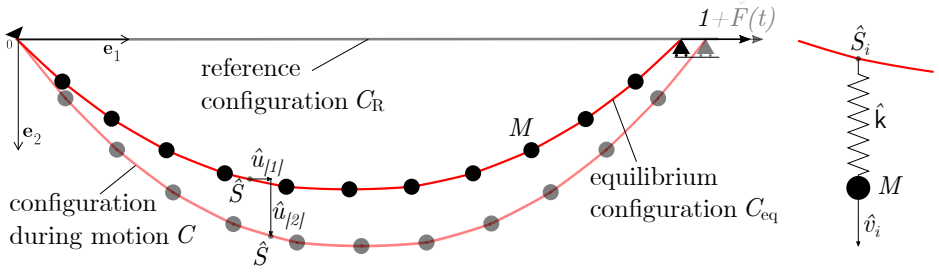


Figure 6.7: *Sketch of the cable system in motion in its plane (left). The circles represent a point mass that can be either directly attached on the cable or hanging to it through an elastic spring (right).*

height, with the left end fixed and the right end free to move horizontally and subjected to an external horizontal force. Let us thus rewrite here relations (6.38) and (6.39), by making explicit their harmonic time dependence:

$$\check{\mathsf{u}}_{[2]}(t) = 0, \quad \check{\mathsf{F}}_{[1]}(t) = \check{\mathsf{F}}_{[1]} \exp\{\mathrm{i}\omega t\}, \tag{6.48}$$

and

$$\begin{cases} N(S,t) = N_{\mathrm{eq}}(S) + \check{F}_{[1]\mathrm{eq}} \hat{N}(\hat{S}) \exp\{\mathrm{i}\omega t\}, \\ \boldsymbol{x}(S,t) = \boldsymbol{x}_{\mathrm{eq}}(S) + \ell_{\mathrm{R}} \hat{\boldsymbol{u}}(\hat{S}) \exp\{\mathrm{i}\omega t\}, \\ v_i(t) = v_{i(\mathrm{eq})} + \ell_{\mathrm{R}} \hat{v}_i(\hat{S}) \exp\{\mathrm{i}\omega t\}. \end{cases} \tag{6.49}$$

From the results of the previous subsection concerning the influence of the inextensibility assumption on the problem, we can now use this approximation to treat the present case study. Moreover, as we showed before, for sufficiently high cable tension we can decouple the in-plane problem from the out-of-plane one at first order. Here we study the in-plane motion of the cable. Accordingly, all the vectorial quantities that appear in this subsection are intended to possess components only along directions $x_1$ and $x_2$. Substituting relations (6.49) in problem (6.36) for $\mathcal{P} \neq \{0\}$, keeping only first order terms, leads to the following simplified equations of motions:

- *Inextensibility at every point* $\hat{S}$

$$\frac{d\hat{x}_{[1]}}{d\hat{S}}(\hat{S}) \frac{d\hat{u}_{[1]}}{d\hat{S}}(\hat{S}) + \frac{d\hat{x}_{[2]\mathrm{eq}}}{d\hat{S}}(\hat{S}) \frac{d\hat{u}_{[2]}}{d\hat{S}}(\hat{S}) = 0; \tag{6.50}$$

- *Horizontal motion equation of the cable at a point* $\hat{S}$ *where no mass is attached*

$$\begin{aligned} \frac{d}{d\hat{S}} \left( \hat{N}_{\mathrm{eq}}(\hat{S}) \frac{du_{[1]}}{d\hat{S}}(\hat{S}) \right) + \frac{d}{d\hat{S}} \left( \hat{N}(\hat{S}) \Big( 1 + \frac{d\hat{x}_{[1]\mathrm{eq}}}{d\hat{S}}(\hat{S}) \Big) \right) \\ + (N+1)^2 \Omega^2 \hat{u}_{[1]}(\hat{S}) = 0; \end{aligned} \tag{6.51}$$

- *Vertical motion equation of the cable at a point $\hat{S}$ where no mass is attached*

$$\frac{d}{d\hat{S}}\left(\hat{N}_{\text{eq}}(\hat{S})\frac{du_{[2]}}{d\hat{S}}(\hat{S})\right)+\frac{d}{d\hat{S}}\left(\hat{N}(\hat{S},t)\frac{d\hat{x}_{[2]}}{d\hat{S}}(\hat{S})\right)+(N+1)^2\Omega^2\hat{u}_{[2]}(\hat{S})=0; \quad (6.52)$$

- *Horizontal jump condition at $\hat{S}_i=i/(N+1), 1\leq i\leq N$, where a mass is attached*

$$\left[\!\left[\hat{N}_{\text{eq}}\frac{d\hat{u}_{[1]}}{d\hat{S}}\right]\!\right](\hat{S}_i)+\left[\!\left[\hat{N}(\hat{S})\Big(1+\frac{d\hat{x}_{[1]\text{eq}}}{d\hat{S}}\Big)\right]\!\right](\hat{S}_i)=0; \quad (6.53)$$

- *Vertical jump condition at $\hat{S}_i=i/(N+1)), 1\leq i\leq N$, where a mass is attached*

$$\left[\!\left[\hat{N}_{\text{eq}}\frac{d\hat{u}_{[2]}}{d\hat{S}}\right]\!\right](\hat{S}_i)+\left[\!\left[\hat{N}(\hat{S})\frac{d\hat{x}_{[2]\text{eq}}}{d\hat{S}}\right]\!\right](\hat{S}_i)-\hat{F}_i(t)=0, \quad (6.54)$$

with

$$\hat{F}_i(t)=\begin{cases}-\theta\dfrac{(N+1)^2}{N}\Omega^2\hat{v}_i(\hat{S}_i) & \text{masses directly on the cable}\\ -\hat{\mathsf{k}}(N+1)(\hat{v}_i-\hat{u}_{[2]}(\hat{S}_i)) & \text{masses hanging with springs}\end{cases}; \quad (6.55)$$

- *Vertical motion equation of the $i^{th}$ hanging mass (from relation (6.14))*

$$\begin{cases}\hat{v}_i=\hat{u}_{[2]}(\hat{S}_i) & \text{masses directly on the cable}\\ \hat{\mathsf{k}}(\hat{v}_i-\hat{u}_{[2]}(\hat{S}_i))=\dfrac{N+1}{N}\theta\Omega^2\hat{v}_i & \text{masses hanging with springs}\end{cases}. \quad (6.56)$$

In the above relations, we have used $\Omega$ and $\hat{\mathsf{k}}$ as the dimensionless parameters associated with the given frequency and the stiffness of the springs, such that:

$$\Omega=\omega\sqrt{\frac{\rho_{\text{R}}d^2}{\check{F}_{[1]\text{eq}}}}, \quad \hat{\mathsf{k}}=\frac{\mathsf{k}d}{\check{F}_{[1]\text{eq}}}. \quad (6.57)$$

The system of equations (6.50) to (6.56) is then completed by the set of boundary conditions

$$\begin{cases}\hat{\boldsymbol{u}}(0)=\mathbf{0}\\ \hat{\mathrm{u}}_{[2]}(1)=0, \quad \hat{N}(1)\dfrac{1}{\hat{N}_{\text{eq}}(1)}+\sqrt{1+\zeta^2}\hat{u}_{[1]}(1)=\check{\mathsf{F}}_{[1]},\end{cases} \quad (6.58)$$

where, for the conditions at the right end of the cable, we have used relations (6.21) and (6.22) written for an inextensible cable at $\hat{S}=1$. Therefore relations (6.50) to (6.56) together with boundary conditions (6.58) constitute a linear differential system for $\hat{S}\mapsto(\hat{\boldsymbol{u}}(\hat{S}),\hat{N}(\hat{S}))$. It can be reduced to a discrete system of equations for the displacements $\hat{\boldsymbol{u}}(\hat{S})$ of the points where a mass is attached after one has solved the differential equations in each interval between two hanging masses. However the solution of the differential equations cannot be obtained in a closed form in the general case. So, we will consider an additional approximation, by making the external static horizontal force large.

### 6.3.3 Dynamics of a cable with hanging masses subjected to a large static horizontal force

We showed in subsection (6.2.3) that, by making the intensity of the horizontal force $\check{F}_{[1]\text{eq}}$ much larger than the total weights of cable and attached masses, the cable equilibrium configuration can be approximated to be horizontal. Let us make this assumption here. Accordingly, relations (6.34) are valid and one has:

$$\hat{N}_{\text{eq}}(\hat{S}) = 1, \quad \hat{x}_{[1]\text{eq}}(\hat{S}) = 1, \quad \hat{x}_{[2]\text{eq}}(\hat{S}) = 0, \quad \forall \hat{S}.$$

Inserting the above relations into equation (6.50) and using the boundary condition at $\hat{S} = 0$ from (6.58) gives

$$\hat{u}_{[1]}(\hat{S}) = 0, \quad \forall \hat{S}.$$

Then relations (6.51) with (6.53) and (6.58) at $\hat{S} = 1$ give

$$\hat{N}(\hat{S}) = \hat{N}_{\text{eq}}(1)\check{\mathsf{F}}_{[1]},$$

and equation (6.52) becomes

$$\hat{u}''_{[2]}(\hat{S}) + (N+1)^2\Omega^2\hat{u}_{[2]}(\hat{S}) = 0, \quad \forall \hat{S} \in \left(\frac{i-1}{N+1}, \frac{i}{N+1}\right), \ 1 \le i \le N+1. \tag{6.59}$$

Integrating the equation (6.59) inside the $i$-th interval leads to:

$$\begin{aligned}\hat{u}_{[2]}(\hat{S}) =& \hat{u}_{[2](i-1)}\cos\Omega((N+1)\hat{S} - i + 1) \\ &+ \frac{\hat{u}_{[2]i} - \hat{u}_{[2](i-1)}\cos\Omega}{\sin\Omega}\sin\Omega((N+1)\hat{S} - i + 1)\end{aligned}, \quad \forall \hat{S} \in \left(\frac{i-1}{N+1}, \frac{i}{N+1}\right) \tag{6.60}$$

where

$$\hat{u}_{[2]i} = \hat{u}_{[2]}(\hat{S}_i), \quad 1 \le i \le N.$$

Relation (6.56) gives $\hat{v}_i$ in terms of $\hat{u}_{[2]i}$. When the masses are directly attached on the cable, one has simply that the motion of the mass $i$-th is equal to the motion of the cable point $\hat{S}_i$, *i.e.*

$$\hat{v}_i = \hat{u}_{[2]}(\hat{S}_i). \tag{6.61}$$

When the masses are hanging on the cable with springs, the motion of the $i$-th mass reads

$$\hat{v}_i = \frac{\hat{\mathsf{k}}}{\hat{\mathsf{k}} - (1 + 1/N)\theta\Omega^2}\hat{u}_{[2]i} \quad \text{for} \quad 1 \le i \le N, \tag{6.62}$$

provided that the following condition is fulfilled

$$\theta(N+1)\Omega^2 \neq N\hat{\mathsf{k}}. \tag{6.63}$$

Condition (6.63) is not fulfilled at the frequency of resonance of the mass-spring system attached to the cable.

Finally (6.54) gives the *discrete* linear system of equations governing the displacements $\hat{u}_{[2]i}$. Specifically, inserting relations (6.60) and (6.61) or (6.62) into equation (6.54) leads to

$$\Delta_i \hat{u}_{[2]} + \mu(\Omega)\hat{u}_{[2]i} = 0 \quad \text{for} \quad 1 \leq i \leq N, \tag{6.64}$$

where $\Delta_i$ denotes the discrete differential operator

$$\Delta_i \hat{u}_{[2]} = \hat{u}_{[2](i+1)} + \hat{u}_{[2](i-1)} - 2\hat{u}_{[2]i} \quad \text{for} \quad 1 \leq i \leq N, \tag{6.65}$$

already used for the dynamics of discrete systems (*cf.* relation (2.33)). The frequency dependent equivalent mass $\mu(\Omega)$ is defined as

$$\mu(\Omega) := \begin{cases} 2(1-\cos\Omega) + \Theta\Omega\sin\Omega & \text{masses directly on the cable} \\ 2(1-\cos\Omega) + \dfrac{\hat{\mathsf{k}}\Theta\Omega\sin\Omega}{\hat{\mathsf{k}} - \Theta\Omega^2} & \text{masses hanging with springs} \end{cases}, \tag{6.66}$$

where the parameter $\Theta$ denotes the ratio between the mass of one hanging mass and the mass of the part of cable between two successive hanging masses, *i.e.*

$$\Theta = \frac{M}{\rho_{\mathrm{R}} d} = \frac{N+1}{N}\theta.$$

Equation (6.64), governing the transverse motion of the cable, has the same form of equation (2.38), that governs the dynamics of a mass-in-mass chain.

The other boundary conditions (6.58) at $\hat{S} = 0$ and at $\hat{S} = 1$ fix the value of the vertical displacement at the two ends:

$$\hat{u}_{[2]0} = 0, \tag{6.67}$$

$$\hat{u}_{[2](N+1)} = 2\hat{u}_{[2]N}\cos\Omega. \tag{6.68}$$

Let us remark that the gravity no longer plays a role after this approximation. On the other hand, the stiffness of the springs (when present) becomes an important parameter (through $\hat{\mathsf{k}}$) in dynamics, at difference to what we observed in statics where it does not play any role.

### 6.3.4 Metamaterials-like behavior

From the results of the previous subsection, we thus have found that the current problem of a cable with attached masses undergoing small oscillations around a flat equilibrium configuration can be led back to the study of equation (2.38) governing the dynamic behavior of a 1D mass-in-mass chain. The results valid for that case can be applied in a similar way also to the current problem. Let us study equation (6.64), without considering the boundary conditions for the moment. We can proceed as we did for the mass-in-mass problem. Accordingly, the solutions to equation (6.64) depend on the values assumed by the effective mass density $\mu(\Omega)$, such that:

- $0 \leq \mu(\Omega) \leq 4$. The general solution reads:

$$\hat{u}_{[2]i} = a_1 \exp\{-\mathsf{i}\mathsf{K}^* i\} + a_2 \exp\{\mathsf{i}\mathsf{K}^* i\} \quad \text{with} \quad \mathsf{K}^* \in [0, \pi] \tag{6.69}$$

  and corresponds to a superposition of a right- and left-propagating waves;

- $\mu(\Omega) < 0$. The general solution reads:

$$\hat{u}_{[2]i} = a_1 \exp\{-\mathsf{K}^* i\} + a_2 \exp\{\mathsf{K}^* i\}. \tag{6.70}$$

  $\mu(\Omega) > 4$. The general solution reads:

$$\hat{u}_{[2]i} = a_1 (-1)^i \exp\{-\mathsf{K}^* i\} + a_2 (-1)^i \exp\{\mathsf{K}^* i\}. \tag{6.71}$$

  In both cases, the solutions correspond to a superposition of attenuated waves.

In the above relations, the term $\mathsf{K}^*$ denotes a wave number normalized with respect to the distance $d$ between two neighboring masses (*cf.* section 2.2.2) and can be obtained from

$$b = \begin{cases} \cos \mathsf{K}^* & \text{for } 0 \leq \mu(\Omega) \leq 4 \\ \cosh \mathsf{K}^* & \text{for } \mu(\Omega) < 0 \\ -\cosh \mathsf{K}^* & \text{for } \mu(\Omega) > 4 \end{cases}, \tag{6.72}$$

where $b$ is given as

$$b = 1 - \frac{\mu(\Omega)}{2}. \tag{6.73}$$

Thus, the dynamic behavior of the system under consideration is characterized by intervals of frequencies where waves are attenuated in space, *i.e.* by band gaps. This can be predicted by looking at the effective mass density $\mu(\Omega)$: when this function is either negative or larger than 4, a band gap is present. In particular, a phenomenon similar to Bragg scattering takes place when masses are directly attached on the cable, while the behavior of the cable with hanging masses is also characterized by local resonances due to the relative motion of the masses with respect to the cable. The physical phenomena originating band gaps are again very similar to those that we encountered in the mass-in-mass chain.

Figure 6.8 represents the graph of $\mu$ as a function of the normalized frequency $\Omega$ for the two cases, obtained using the following values for the parameters of the motion problem[1]

$$\hat{\mathsf{k}} = 4.74, \quad \Theta = 1.18. \tag{6.74}$$

In the plot, the red bands denote regions where the effective mass density $\mu$ is larger than 4, while blue bands indicate band gaps corresponding to a negative effective mass.

[1] We picked these specific values since they are those obtained from the physical quantities that we will use for the experimental test.

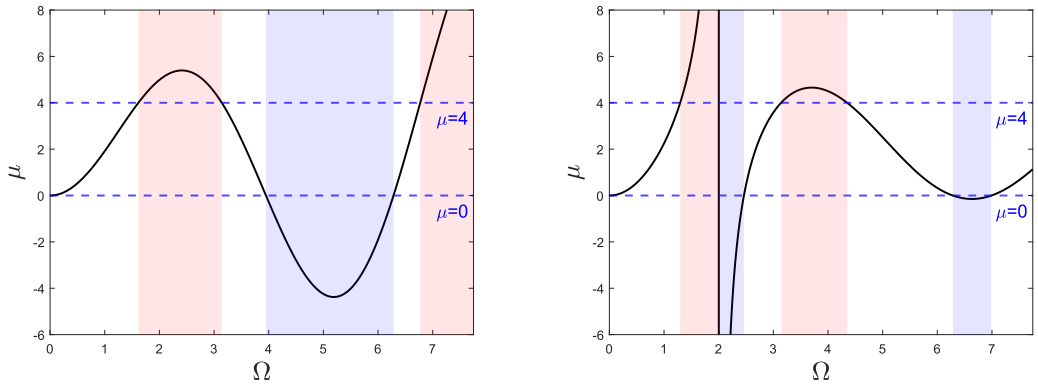


(a) (b)

Figure 6.8: *Graph of the effective mass $\mu(\Omega)$ defined by relation (6.66), for a cable with (a) masses directly attached on it and (b) masses hanging on it.*

### 6.3.5 On the continuous and discrete spectra of the discrete Laplacian operator

In the previous subsection we found the continuous spectrum of the discrete Laplacian operator defined on the (discrete) Lebesgue space $\ell^2(\mathbb{Z})$. It is known from the literature (see *e.g.* Borthwick (2020)) that this problem possess a real continuous spectrum $\sigma_c = [0, 4]$, that coincides with its essential spectrum $\sigma_{ess}$. Therefore, from our results, the effective mass density can be interpreted as the spectrum $\sigma_{ess}$ of the problem. Indeed, we find that, when $\mu$ is such that $0 \leq \mu \leq 4$, then solutions belonging to the space $\ell^2(\mathbb{Z})$ exist and can be represented as superposition of propagating waves (*cf.* solution (6.64)). Outside this range, solutions are no more in that space.

These considerations are only valid when we extend the domain $\mathcal{C}_R$ of the curvilinear abscissa $S$ to be $\mathcal{C}_R = (-\infty, +\infty)$, therefore when we consider a wave propagation problem. As soon as the domain is made bounded and boundary conditions are taken into account, the problem becomes an eigenvalue problem in the space $\ell^2(\mathbb{I})$, with $\mathbb{I} \subset \mathbb{Z}$ being the index set of $\mathcal{P}$, that for the current case is always non-empty and of finite cardinality. Note that these considerations would also apply to the mass-in-mass chain, if boundary conditions were present.

Let us show here how the eigenvalues of problem (6.64), with boundary conditions (6.58) for $\hat{u}_{[2]}(0)$ and $\hat{u}_{[2]}(1)$, are distributed in the spectrum. For this, we use the solution (6.69) that is valid when $0 \leq \mu \leq 4$. By imposing the boundary condition at $\hat{S} = 0$, we find

$$a_1 = -a_2. \tag{6.75}$$

While the boundary condition at $\hat{S} = 1$ gives

$$\sin \mathsf{K}^*(N+1) = 0. \tag{6.76}$$

From this latter relation, we finally have

$$\mathsf{K}^* = \frac{q\pi}{N+1}, \quad q \in \mathbb{N}, \tag{6.77}$$

but since $\mathsf{K}^* \in [0, \pi]$, then we find the preliminary result that, in each interval where $0 \leq \mu \leq 4$, a maximum number of $N+2$ eigenvalues $\mu^*$ can be found using relation (6.73). This is an intermediate result.

To find the correct number, one must consider what happens in each interval when $\mathsf{K}^* = 0$ ($q = 0$) and $\mathsf{K}^* = \pi$ ($q = N+1$), *i.e.* respectively at the eigenvalues $\mu^* = 0$ and $\mu^* = 4$. The dimensionless frequencies corresponding to these two cases can be found combining relations (6.66), (6.72) and (6.73). We will refer to these frequencies as $\hat{\Omega}$. Using condition (6.75) and relation (6.69), when either $\mathsf{K}^* = 0$ or $\mathsf{K}^* = \pi$ all the points $\hat{S}_i$ corresponding to the extremities of each interval $((i-1)/d, i/d)$ do not move. Accordingly, to be eigenfrequencies of the whole system, the frequencies $\hat{\Omega}$ must be equal to the (dimensionless) eigenfrequencies of a taut string with a length equal to one interval $d$, in tension between two fixed supports. Using the second of relations (6.41), the frequencies $\hat{\Omega}$ corresponding to $\mu = 0$ and to $\mu = 4$ are eigenfrequencies only when they are equal to $j\pi$, with $j \in \mathbb{N}$[1]. We find that, in each pass band, this can happen only for one between $\mu^* = 0$ and $\mu^* = 4$ (this can be demonstrated by studying the behavior of $\mu$ using its definition (6.66) for $\mu = 0$ and $\mu = 4$).

We have thus obtained the following result:

**Result.** *In each interval where $0 \leq \mu \leq 4$, a maximum number of $N+1$ eigenvalues $\mu^*$ can be found.*

In figure 6.9 we verify the above result by comparing the continuous and discrete spectra of a cable with attached masses. The continuous spectrum is given by the $y$-coordinates between 0 and 4. The black curve represents the effective mass density $\mu$, for the two cases shown in figure 6.8. From the previous results, the $x$-coordinates of the function $\mu$, when it is between 0 and 4, give the values of (dimensionless) frequencies corresponding to propagating waves. The continuous spectrum of the discrete Laplacian operator is thus associated to a family of pass bands for the system. The discrete spectrum is instead obtained by solving the eigenvalue problem in a bounded domain, here composed of $N = 5$ masses. Using relation (6.77), $N+1$ values of $\mathsf{K}^*$ are found and relation (6.73) with $b = \cos \mathsf{K}^*$ can be used to determine the corresponding values of $\mu^*$, represented in the figure with the horizontal red dotted lines. The allowed eigenfrequencies, *i.e.* those corresponding to a solution of the problem, are identified with asterisks as the $x$-coordinates of the points where the eigenvalues (red dotted lines) intersect the function $\mu$ (black curve).

Note that all the eigenfrequencies are grouped within the pass bands of the problem in the unbounded domain. This can also be explained by looking at the solutions (6.70)

[1] We here consider $j = 0$, although the corresponding eigenfrequency is not part of the spectrum. Since we are looking for solutions to the problem, we also take into account this case corresponding to $\hat{u}_{[2]}(\hat{S}) = 0$ everywhere.

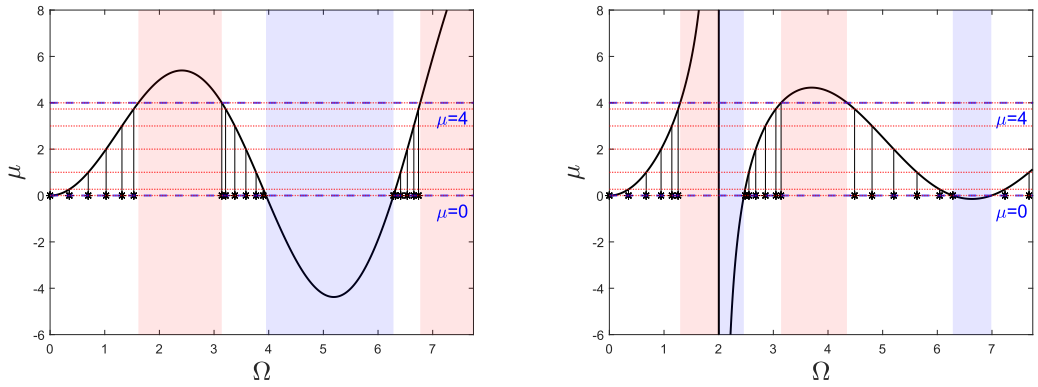


(a) (b)

Figure 6.9: *The intersections of the eigenvalues $\mu^*$ (red dotted lines) with the graph of $\mu$ (black curve) give the eigenfrequencies of the problem (asterisks along the $x$-axis), for $N = 5$ masses along a cable when (a) they are directly attached and when (b) they are hanging.*

and (6.71) valid for frequencies within a band gap: corresponding to superpositions of exponentials, these solutions cannot fulfill the boundary conditions of the problem.

### 6.3.6 Wave and energy localization with a defect of periodicity

We can exploit again the similarity between the discrete equation governing the transverse motion of the current system and that of the discrete system analyzed in section 2.2, to show the localization phenomenon due to an alteration of the periodic arrangement of the masses. Contrary to what we did in previous chapters, here we consider a bounded domain for the problem.

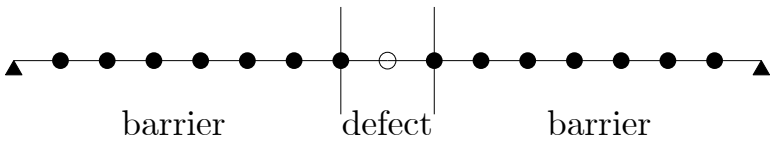


Figure 6.10: *Taut string with a periodic arrangement of attached masses, represented as black dots. The empty circle denotes a removed mass.*

More specifically, we aim to analyze the system reported in figure 6.10, where the cable is shown in its horizontal static equilibrium configuration with a family of masses (directly attached on the cable or hanging on it) represented by filled black dots. An empty circle indicates a mass that has been removed from the system. Accordingly, we are dealing with a domain presenting a periodic array of scatter elements, where a defect is generated by removing one of these scatterers from a unit cell.

We are thus here considering again the case of a compact perturbation. The discrete Laplacian operator on $\ell^2(\mathbb{Z})$, being self-adjoint, conserves its essential spectrum when locally perturbed (from a corollary of Weyl's theorem). It follows that, if an eigevalue exists in the spectrum of the perturbed operator, it will be of finite multiplicity and its corresponding eigenmode will decay exponentially outside the defect, where it will be localized (*cf.* section 4.1).

This localization phenomenon remains valid also when the domain is bounded. From a physical point of view, the system can be decomposed in three regions as in figure 6.10, with two barriers composed of a periodic domain and one defective region where a mass element is removed. We thus have two possible situations:

1. within the two barriers, solutions of the form (6.69) can still exist and can be matched with a standing wave within the defect. From the results of the previous subsection, eigenmodes of this form must belong to a pass band in the continuous spectrum of the unperturbed operator;
2. within the two barriers, solutions of the form (6.70) and (6.71) can exist as well. A standing wave in the defect could be generated at a frequency within a band gap for the unperturbed operator and match the solutions in the barriers, that can exponentially decay towards the two ends of the domain to fulfill the boundary conditions.

These results are verified in figures 6.11 and 6.12. Specifically, as we described before,

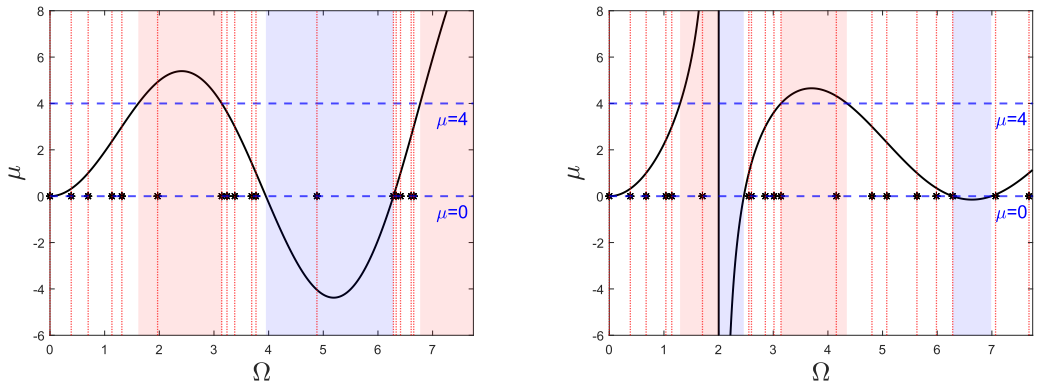


Figure 6.11: *The spectrum of a cable with $N = 5$ masses is studied when (a) they are directly attached and when (b) they are hanging. Black curves represent the effective mass density $\mu$. Red dashed vertical lines, in correspondence of the asterisk along the $x$-axis, gives the (dimensionless) eigenfrequencies when the cable has a central defect (central mass removed).*

the essential spectrum of the discrete Laplacian operator here considered ($0 \leq \mu \leq 4$) corresponds to pass bands for the system, indicated as red and blue shaded regions in

figure 6.11. These regions identify the essential spectrum in terms of frequencies and they are thus conserved when dealing with the perturbed operator. The red dotted vertical lines in the figure identify the eigenvalues of the bounded problem with a defect (indicated with an asterisk). One can check from the figure that, although the majority of the eigenvalues are still grouped inside pass bands for the unbounded problem (situation 1 above), some of them are inside a band gap (situation 2 above). This behavior is different with respect to the case studied in figure 6.9, where no defect was present in the system. In particular, the eigenmodes inside a band gap correspond to a motion of the cable that is localized within the defect, as can be checked in figure 6.12 where we plot the modal shapes of the first localized eigenmode for the two cases analyzed. These results are even more marked when the number of masses is increased,

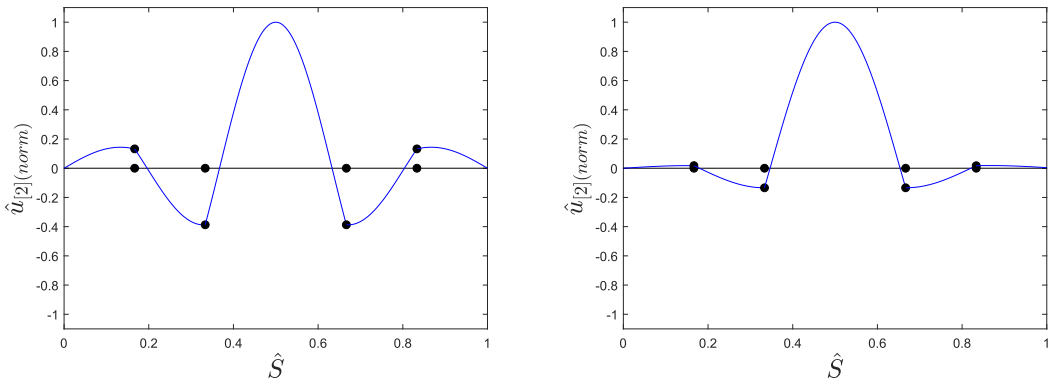


Figure 6.12: *Eigenmodes corresponding to the eigenvalues within the first band gaps of a cable with $N = 5\,(-1)$ masses (from a system of 5 masses, one is removed), when (a) they are directly attached and when (b) they are hanging. The black dots indicate the position of the masses.*

as can be checked in figure 6.13a, where the case of a cable with $N = 11(-1)$ (from a system with 11 masses, one is removed) directly attached masses is considered. The eigenvalues fill more and more the pass bands (*cf.* figure 6.13a) and the eigenmode in the first band gap is characterized by a stronger localization of the motion in the cavity (*cf.* figure 6.13b).

For the harmonic regime, the spatial variation of the elastic energy density of the cable is a non-negative quadratic form on the space of kinematically admissible solutions here envisaged and is given by

$$\int_0^{\ell_R} \frac{1}{2} EA_R (u'_{[2]}(S) - 1)^2 \, dS$$

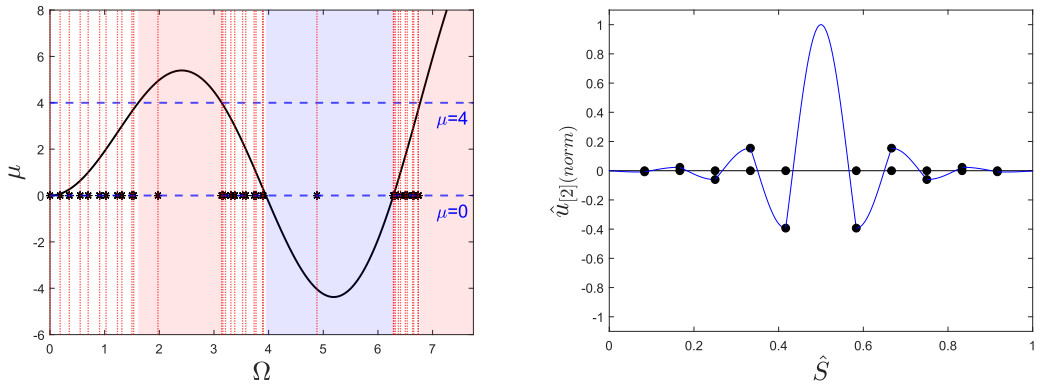


(a) (b)

Figure 6.13: *(a) Spectrum of a cable with $N = 11\,(-1)$ masses directly attached and (b) modal shape of the eigenvalue inside the first band gap. The black dots indicate the position of the masses.*

The spatial variation of the kinetic energy density of the cable is defined as

$$\int_0^{\ell_R} \rho_R \omega^2 u_{[2]}^2(S)\, dS \quad \forall u_{[2]} \text{ kinematically admissible}$$

and is also non-negative. As the motion of the cable is localized within a defect and decaying exponentially outside it, the corresponding mechanical energy density along the system will be localized as well. Results similar to those obtained in previous chapters concerning the concentration of energy can thus be found also for the current problem.

## 6.4 Experimental validation

In this section we aim to verify the theoretical results previously described by means of an experimental test. We consider here the case of a cable with a family of masses that are directly attached on it. Quantitative measurements of the response of the cable/mass suspensions are determined using modal techniques. After presenting the experimental setup developed for the test, an analysis of the linear response of the system is performed on the basis of amplitude-frequency measurements obtained for the system without and with a defect, at different loading conditions.

### 6.4.1 Setup of the test

The experimental setup is shown in figure 6.14. The mechanical system is made up of a taut steel string with an array of lead spheres of mass $M$, *i.e.* of scatter elements,

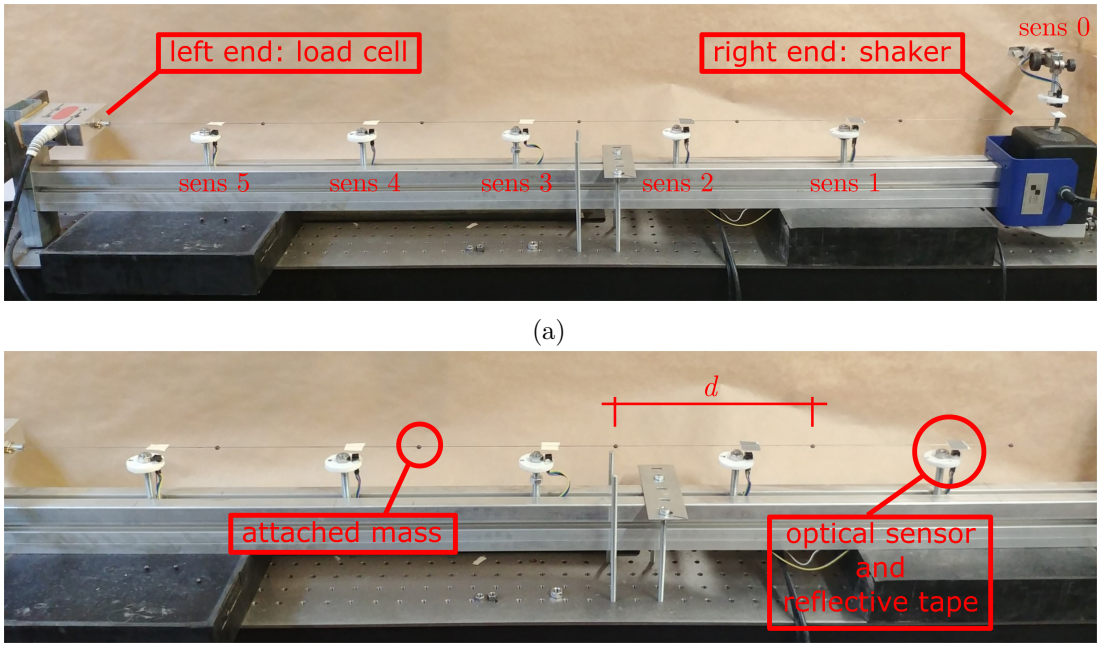


(a)

(b)

Figure 6.14: *The experimental setup. (a) the whole system composed of the cable with attached masses, in tension between a load cell at the left boundary and a shaker at the right boundary, that is adjusted to impose a vertical motion. Five optical sensors are distributed below the cable. The cable points above these sensors are equipped with a square white piece of tape to enable the measurement of the vertical displacement of the cable with the optical sensors. (b) zoom over a part of the cable.*

periodically inserted on the cable and glued to it by means of beeswax. The cable is in tension between two supports. In particular, the left end is fixed to a *load cell* for measuring the tension applied to the cable. The right boundary is instead fixed along the horizontal direction and supported by the head of a *K2007E01 shaker* in the vertical direction, to provide a vertical motion at the support. The shaker is carefully adjusted so that the imposed motion has no horizontal components. This point is critical as the imposition of a horizontal motion at one end could cause a parametric excitation that would modify the motion of the cable (Nayfeh et al., 1995b). The voltage signal that is then converted into motion of the shaker head at the support is given by an *Agilent 33500 series 30 MHz function/arbitrary wave form generator*.

We chose a one-strand metallic cable to reduce at the minimum the influence of the viscous damping and, more importantly, the initial sag. As we showed in subsection 6.2.3, a metallic cable allows the equilibrium configuration to be approximated as horizontal remaining in an elastic regime, thanks to its low weight and its high axial stiffness. The flip-side is that, as we are confined to deal with small scale systems both

for practical reasons and to comply with the theme of this thesis, we are obliged to use very small sections for the cable to comply the need of no flexural stiffness. This results in relatively high frequencies measurements that can be difficult to execute.

Due the lightness of the model, we envisaged to use a contact-less measurement device to study the motion of the cable. To this end, we have employed a *CNY70 reflective optical sensor with transistor output*. This instrument includes an infrared emitter and a photo-transistor in a leaded package which blocks visible light (*cf.* figure 6.15). The device, roughly speaking, continuously emits a light wave that is reflected

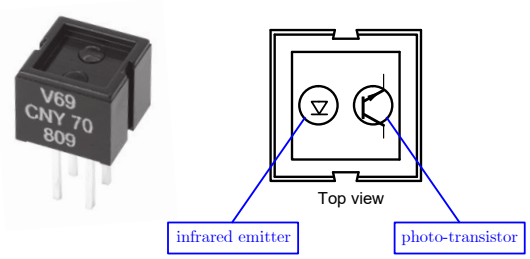


Figure 6.15: *The optical sensor employed for the measurement of the cable motion, together with a sketch of its top view.*

by a target object and comes back to the sensor, interacting with its encapsulated transistor. When the target moves, the voltage output from the optical sensor can be recorded and, after a calibration of the sensor, one can read a variation of the position of the target object. Therefore, placing these optical devices below the cable, we are able to read the vertical displacement of the cable points above these sensors and to study the cable response to the imposed motion at the right support. Figure 6.14b shows the central part of the system, with the sensors distributed below the cable. To enhance the reflection, small pieces of white tape are glued at the cable points above the sensors, constituting the target objects for the measures taken by each sensor (see figure 6.16b).

A total of 5 sensors of this type are employed along the system. To measure the actual imposed motion at the right support, we employ one more sensor above the head of the shaker. Accordingly, we number them starting from the sensor 0 on top of the shaker, in increasing order from the right to the left.

We point out that these optical devices allow for a low-budget test, that, considering the smallness of the target (*i.e.* the cable section) and the frequencies under study, makes this method a very attractive solution.

Let us finally show in figure 6.16 some detailed views of the system under study. In particular, we report in figure 6.16a a zoom view of the right boundary of the system, where the cable is supported by a shaker and the optical sensor 0 is placed over it to read the motion of the support. Figure 6.16b shows an optical device with the target applied to the system.

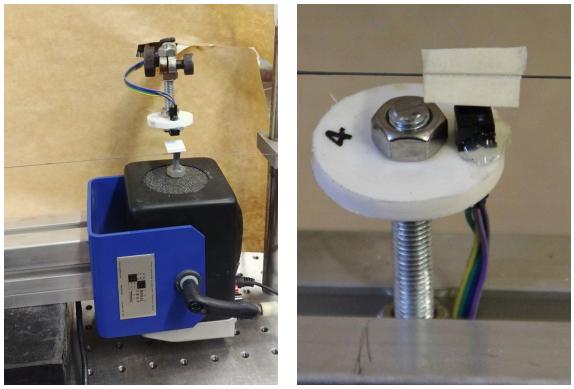

(a) (b)

Figure 6.16: *Zoom over (a) the right boundary and (b) the sensor number* 4 *used in the system.*

### 6.4.2 Experimental results and discussion

For the test we consider both the case when $N$ masses are periodically arranged along the cable and the case when a defect of periodicity is introduced by removing one mass from the system. Our aim is to locate the natural frequencies, corresponding to a primary resonance condition for the cable under study, and to compare them with those obtained from the prior theoretical considerations. Note that we keep the amplitude of the imposed displacement small enough, in order to avoid as much as possible the (inevitable) activation of phenomena typically due to the intrinsic non-linearities of the problem. We give in table 6.1 the material and geometrical characteristics of the system studied[1].

Table 6.1: Material and geometrical parameters used for the experimental test.

| $\rho_{\mathrm{R}}$ [kg/m] | $E$ [Pa] | $A_{\mathrm{R}}$ [m$^2$] | $\ell_{\mathrm{R}}$ [m] | $N$ | $F$ [N] | $M$ [kg] |
|---|---|---|---|---|---|---|
| $1.53 \times 10^{-3}$ | $2.3 \times 10^{11}$ | $1.96 \times 10^{-7}$ | 1.21 | 5 | $\approx 10$ | $3.6 \times 10^{-4}$ |

Figures 6.17a and 6.17b represent the variation of the effective mass with the frequency: they exactly correspond respectively to the plots reported in figure 6.9a and 6.11a, this time displayed using physical quantities. The vertical lines in the plots indicate the eigenfrequencies of the bounded system.

To identify the eigenvalues experimentally, we initially excite the cable with a *white Gaussian noise* directly created using the wave form generator. Its time variation is reported in figure 6.18 and measured by using the "*sensor* 0" positioned above the shaker. The corresponding frequency content is computed by using the *Matlab FFT*

[1] One can check that these values correspond to the dimensionless parameter $\Theta$ given in (6.74).

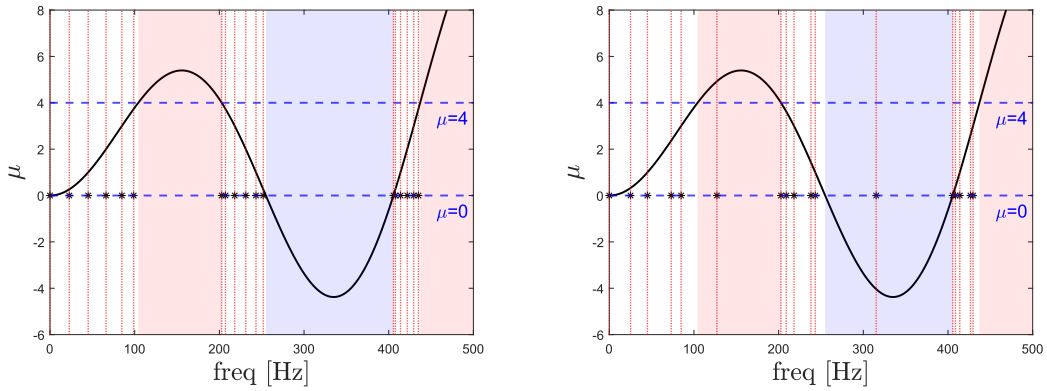


Figure 6.17: *Effective mass density $\mu$ vs frequency. Shaded regions denote band gaps for the unbounded problem. Vertical lines identify the eigenfrequencies of the bounded system.*

*algorithm* and given in figure 6.18 in terms of *Power Spectral Density* (PSD) normalized with respect to its maximum, in a logarithmic scale. In the following, the results in terms of frequency content will be always shown in this way: whenever the content at a specific frequency is higher than 0, the signal measured has a content higher than the maximum value of the PSD obtained from the input signal. Specifically, we will give the results in terms of *Trasmission (T)*, defined as

$$T := 10 \text{ Log} \left( \frac{|PSD_j|}{\max |PSD_0|} \right)^2 ,$$

where $PSD_j$, with $j$ from 0 to 5, denotes the PSD of the signal measured by the $j$-th sensor.

Note that, when a random input signal is created with the wave form generator and sent to the shaker, the actual imposed motion is characterized by a decreasing frequency content. This is because, at equal displacement amplitude, the shaker needs more voltage for a higher frequency than a lower one. Consequently, using a random signal, we are not able to sufficiently activate the higher natural frequencies of the system.

We thus excite the cable using a Gaussian-modulated sinusoidal wave, that we can manipulate to vary both its central frequency (*i.e.* the one with the highest frequency content) and its deviation (*i.e.* the width of the interval of frequencies around the central one whose content is sufficiently relevant to be taken into account). Contrary to the random noise, this type of excitation makes it easier to enhance the activation of high-frequency modes, reducing the energy given to the lower modes.

Let us report in figure 6.19a the time variation of the Gaussian-modulated sinusoidal signal created using the wave form generator and in figure 6.19b its corresponding

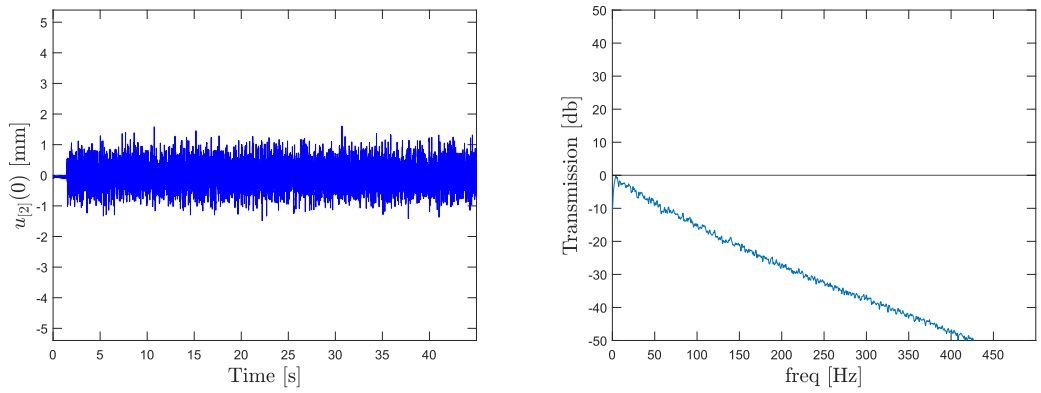


(a) (b)

Figure 6.18: *Time series (a) and corresponding frequency content (b) of the white random noise input signal, created with the waveform generator. The time variation of the signal is measured using the "sensor 0" above the shaker.*

frequency content (blue curves), with the shaded regions representing band gaps for the propagation problem. Note that the signal is given in Volts (V). In figure 6.19a, we also report the actual displacement imposed to the cable (red curve). Note that there is a difference between the signal and the generated displacement. This is mainly due to the fact that the shaker is influenced by the response of the cable and is not able to perfectly reproduce the generated signal.

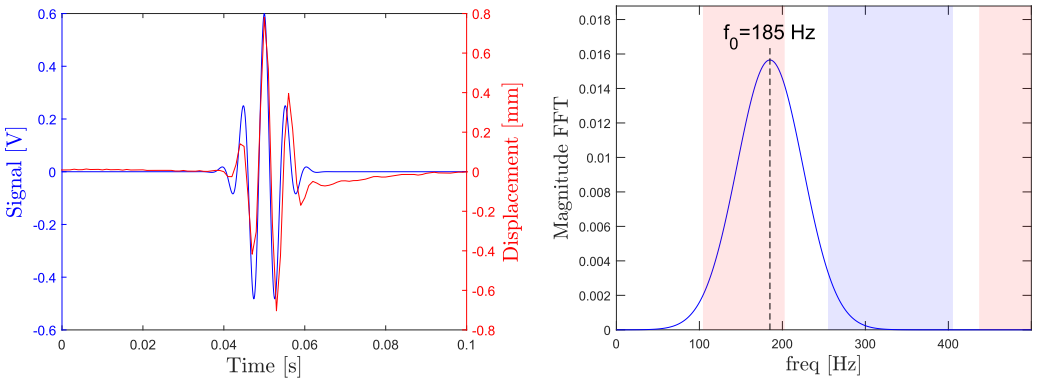


(a) (b)

Figure 6.19: *(a) Time series of the Gaussian-modulated sinusoidal signal used as input for the waveform generator (in blue) and the corresponding imposed displacement (in red). "V" stands for Volts. (b) Frequency content of the signal. Shaded regions denote band gaps for the unbounded problem.*

To study the attenuation properties of the ideal unbounded periodic system, one should input a wave and measure the spatial decay along the system, which is expected for frequencies inside a band gap. However, as the experimental setup has boundaries, we must use the results obtained for a finite system. In particular, we have shown in section 6.3.5 that, although with boundaries the concept of continuous spectrum and thus of band gaps is lost, its effect is still valid in the sense that the eigenfrequencies of the problem are only grouped in the pass bands of the unbounded domain. This is true when no defects are present. If this was not the case, then we expect to find some eigenvalues inside a band gap, corresponding to localized eigenmodes.

With the input signal shown in figure 6.18, the response is entirely transitory. The motion of the cable contains all the frequencies that compose the random signal. At the natural frequencies of the system, the motion of the cable is enhanced due to a resonance condition and peaks appear in the Fourier transform of the signals measured by the sensors along the cable, as can be checked in figure 6.20. Specifically, only the lower modes are activated (corresponding to peaks of PSD), since the frequency content of the input signal gets lower and lower at increasing frequencies (*cf.* figure 6.18). A good agreement between the PSD peaks and the theoretical eigenfrequencies indicated by the vertical dashed red lines is obtained. Note that, for these input, we have varied the axial force in the cable to be of $\approx 16$ N. Band gaps and eigenfrequencies are thus slightly different with respect to the other cases treated in this section. This was done simply as a check of the validity of our test. Nevertheless, by comparing figure 6.20a with the other, one can already note that the banded structure of the spectrum is visible. To facilitate the comparison, we have indicated with a black line in figures 6.20 the linear interpolation of the input PSD in figure 6.20a. Within the first band gap (red shaded region), the corresponding displacement measured along the cable is attenuated in amplitude with respect to that imposed by the shaker.

Let us now consider the input signal shown in figure 6.19. The response is composed of a short transitory phase needed for the activation of the eigenmodes of the bounded problem, followed by a free motion phase during which the input pulse is already ended and the excited eigenmodes decay, at different rates, due to damping. In particular, we report in figure 6.21 the Fourier transforms of the signals measured by the 5 sensors along the cable for the imposed motion given in figure 6.19a, when no masses are removed (case without a defect).

This time, the banded structure of the spectrum is more clear. The normalized PSD of the Gaussian-modulated imposed displacement is given in figure 6.21a. Its graph is also reported in each one of the other figures in 6.21 (black curve), that show the PSD from the signals measured by the sensors from 1 to 5. In particular, one can check from the figures that the modes within the second pass band are now activated, together with some low-frequency modes in the first pass band and some eigenfrequencies belonging to the third pass band. This is mainly due to two reasons. On one hand, the imposed motion at the boundary can be transformed into initial conditions to the problem[1] and

[1] This is possible by a change of variables in the linearized problem.

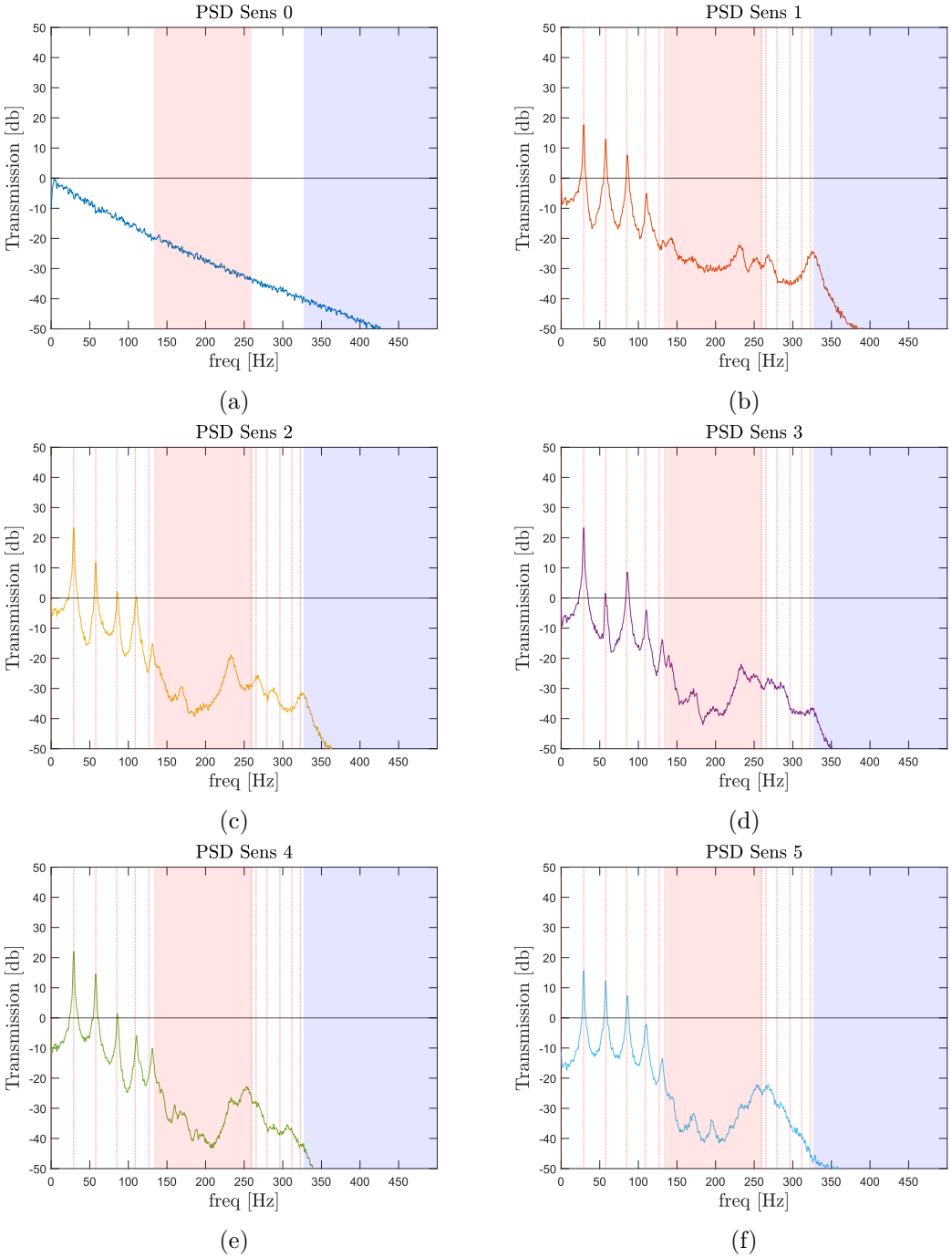


Figure 6.20: *Results from a white random noise signal. From (a) to (f) PSD of the signals from sensors* 0 *to* 5*, normalized with respect to the maximum value of the PSD from sensor* 0 *in subfigure (a). Logarithmic scale is used. The axial force in the cable is increased to* $F \approx 16$ *N. Vertical lines denote theoretical eigenfrequencies.*

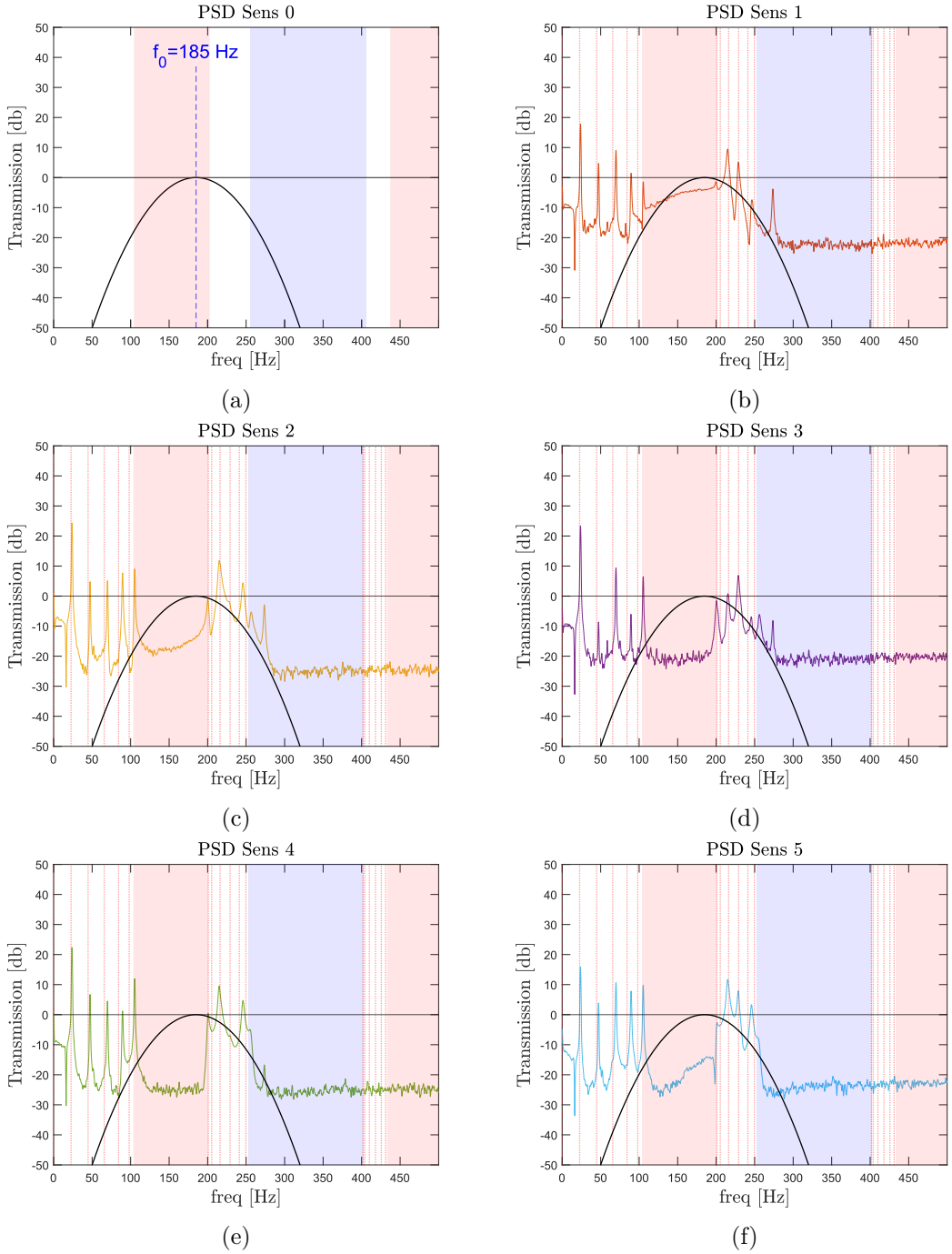


Figure 6.21: *Results from a Gaussian-modulated sinusoidal wave. From (b) to (f) PSD of the signals from sensors* 1 *to* 5*, normalized with respect to the maximum value of the PSD from sensor* 0 *shown in subfigure (a) and reported with a black curve in each plot. Logarithmic scale is used.*

the presence of eigenmodes not directly excited by the imposed motion is thus due to the transient phase associated to the initial conditions, that does not have enough time to be completely attenuated by damping. On the other hand, as we highlighted before, the actual imposed displacement is not precisely equal to the voltage signal triggered by the wave form generator (*cf.* figure 6.19a); in particular, its frequency content is more spread than the one of the signal, that was depicted in figure 6.19b.

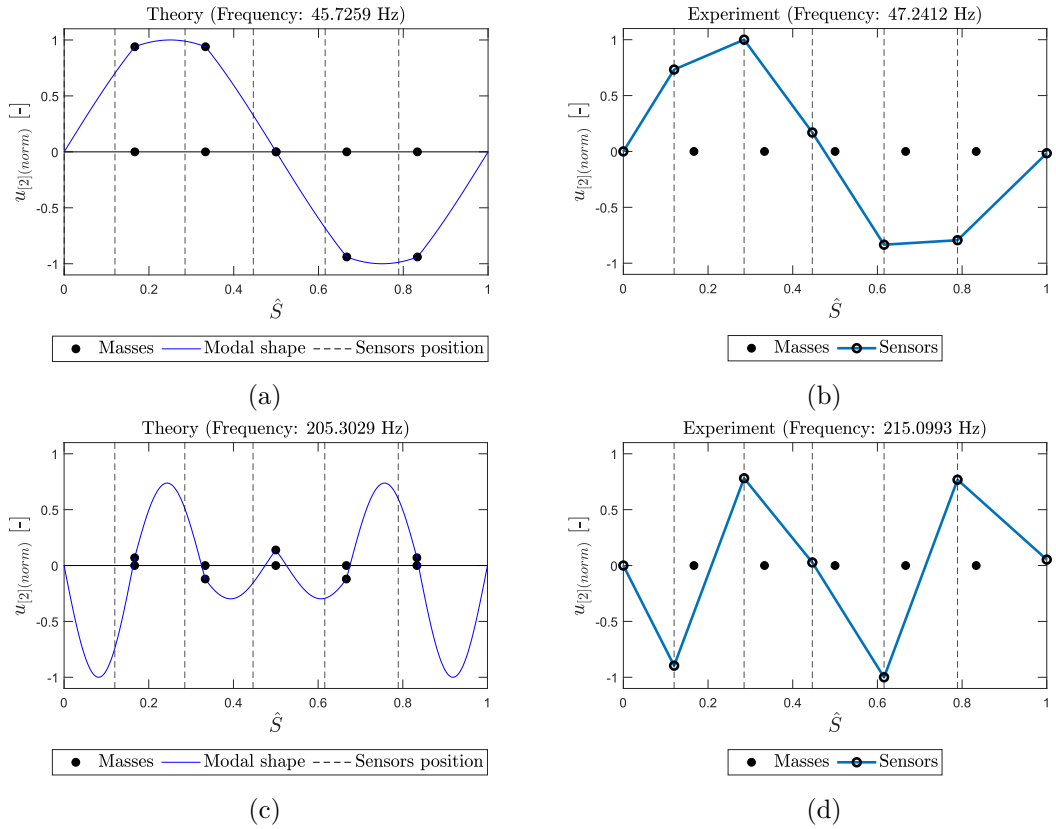


Figure 6.22: *Comparison between modal shapes (a) and (c), and motion of the tested system (b) and (d), for the third eigenmode at $f \approx 46$ Hz (first row) and the eighth eigenmode at $f \approx 205$ Hz (second row). Black dots stand for masses, black circles and vertical dashed lines for points above the optical sensors.*

Contrary to what happens for the lower modes in the first pass band, the agreement between the PSD peaks and the theoretical eigenfrequencies (indicated by the vertical dashed red lines) is not perfect for higher modes. In particular the experimentally obtained eigenfrequencies are slightly moved at higher frequencies with respect to the theoretical ones. This is mainly due to the presence of the tape used as target object for the measurements of the cable motion, that influences the dynamics of the cable. We have checked this by removing all the tapes but one: repeating the analysis, all the

peaks move closer to their theoretical positions. The system is indeed more affected by experimental imperfections at higher frequencies.

### Motion of the system

We can further check the validity of our results by reconstructing the motion of the system from the cable points positioned above the 5 optical sensors. In particular, at an eigenfrequency of the bounded problem, the system should move proportionally to the corresponding modal shape.

We have verified this for the third and the eighth mode in figure 6.22, where the analytically derived modal shapes (figures 6.22a and 6.22c) are compared with the behavior of the tested system (figures 6.22b and 6.22d). Black dots stand for masses, whereas black circles denote the material points above the sensors. The results are in good agreement for the modes under consideration. It must be said that, due to aliasing, we cannot reconstruct modes with a too fast variation in space. For this, more optical sensors should be used along the cable.

Note that, when the frequency content experiences a peak (*i.e.* when a mode is activated), the height of that peak measured by different sensors depends on their positions and on the shape of the eigenmode: when a peak is lower, it means that the corresponding sensor is near a node; viceversa, when is larger, it is closer to an anti-node. For instance, all the sensors in figure 6.21 share a peak at the frequency corresponding to the third eigenmode ($\approx 46$ Hz). Sensors 1, 2, 4 and 5 give the highest peak being positioned far from the central node of the corresponding modal shape (*cf.* figure 6.22a).

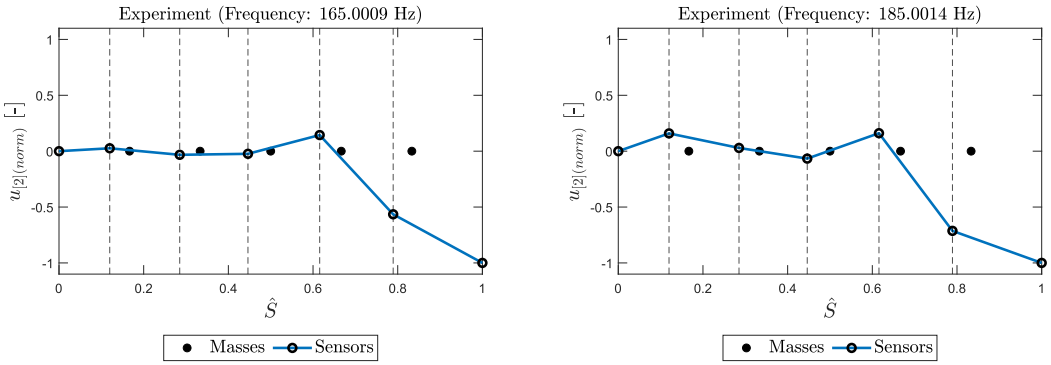


(a) (b)

Figure 6.23: *Motion of the tested cable at (a) $f = 165$ Hz and (b) $f = 185$ Hz. Black dots stand for masses, black circles and vertical dashed lines for points above the optical sensors.*

From the test, we can also check the behavior of the system for frequencies belonging to a band gap. In figure 6.23, we report the motion of the tested cable at the frequencies

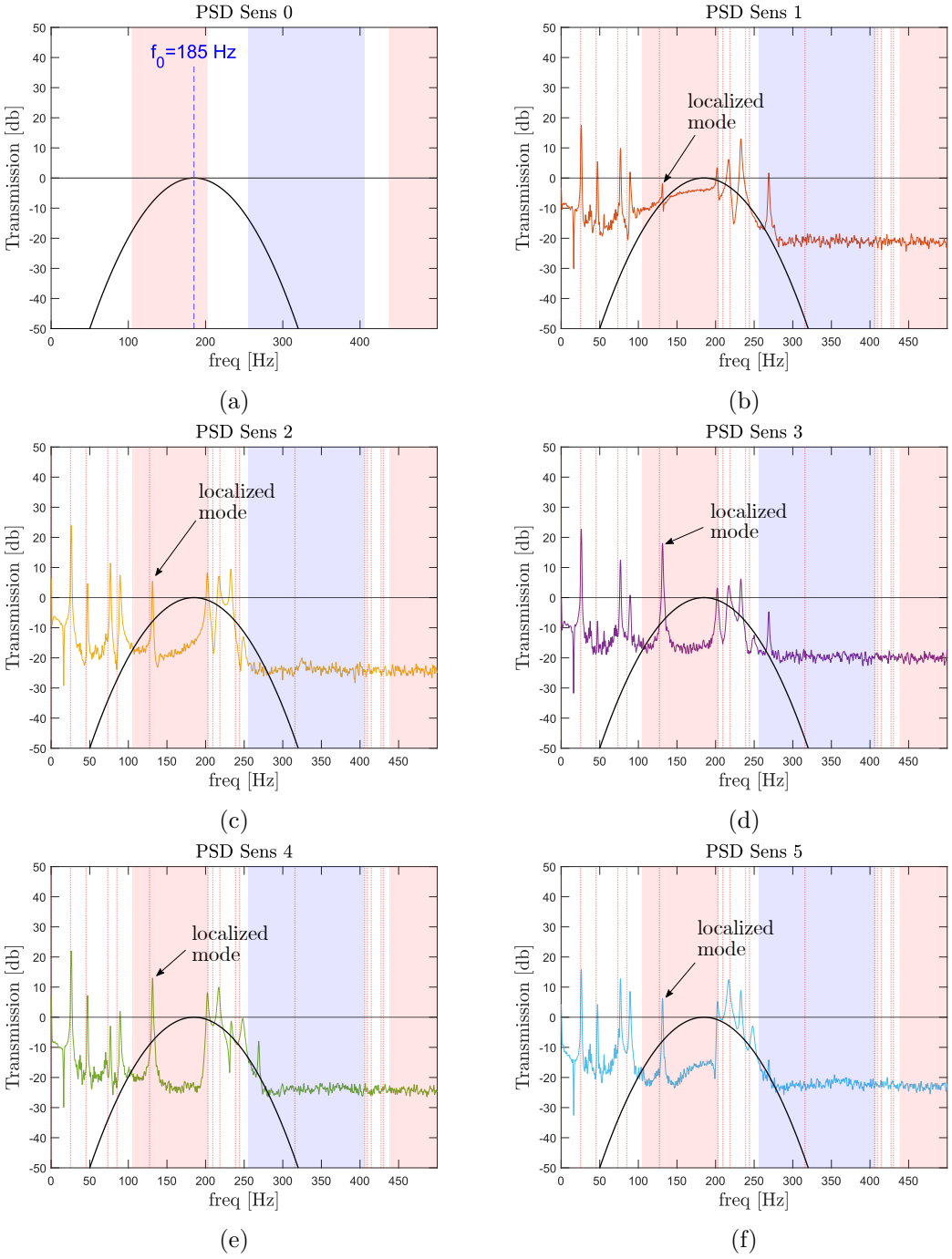


Figure 6.24: *Results from a Gaussian-modulated sinusoidal wave in a defective system. From (b) to (f) PSD of the signals from sensors* 1 *to* 5*, normalized with respect to the maximum value of the PSD from sensor* 0 *shown in subfigure (a) and reported with a black curve in each plot. Logarithmic scale is used.*

$f = 165$ Hz (left) and $f = 185$ Hz (right). Specifically, we find that the wave in the system is characterized by an amplitude that is attenuated from the moving support (right end) to the fixed support (left end), verifying the presence of a band gap in the spectrum. Moreover, at $f = 165$ Hz (figure 6.23a) the attenuation is stronger then at $f = 185$ (figure 6.23b). This latter frequency is indeed positioned closer to the edge of the first band gap and, accordingly, one expects less attenuation.

### 6.4.3 Measurements with a defect

Let us finally test the system by removing the central mass. For this, we use again the Gaussian-modulated sinusoidal input signal depicted in figure 6.19, centered at a frequency of 185 Hz. As it can be checked from the figure, the content in frequency of this signal is sufficiently high both inside the first band gap and the second pass band. Accordingly, from the theoretical results presented in subsection 6.4.2, we expect to activate both the defect mode at the frequency $f \approx 127$ Hz, corresponding to the localized modal shape reported in figure 6.13a, and the eigenfrequencies belonging to the second pass band.

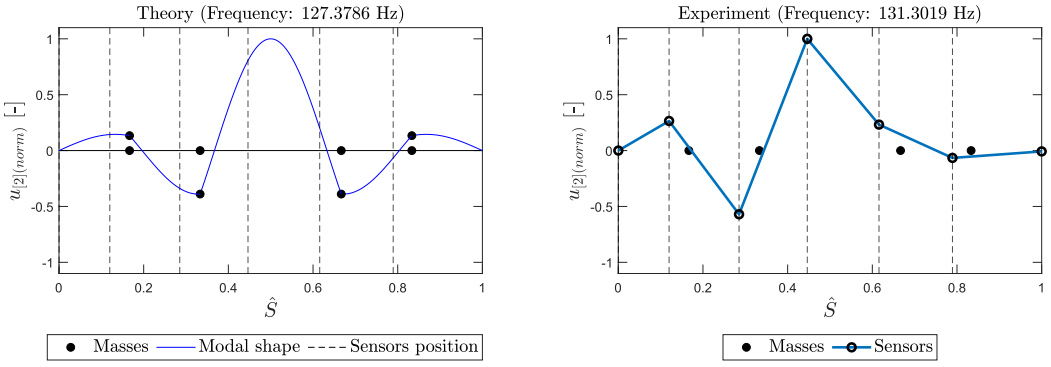


(a) (b)

Figure 6.25: *Comparison between modal shapes (a), and motion of the tested system (b), for a theoretical defect mode at $f \approx 127$ Hz, in the system with $5(-1)$ masses. Black dots stand for masses, black circles and vertical dashed lines for points above the optical sensors.*

This is indeed verified in figure 6.24, where we report the Fourier transform of the signals acquired by the optical sensors. Note also that from figure 6.24b to 6.24f, the content at the frequencies belonging to the first band gap is decreasing, except at the frequency where a localized mode is expected. This confirms the attenuating behavior due to the presence of the scatter elements and the localization capabilities of the system caused by the removal of one mass from the periodic arrangement.

The modal shape of the defect mode is compared in figure 6.25 with the behavior of the tested cable at the corresponding frequency. A good agreement between the two

results is obtained, with the motion being maximum within the defect.

Eventually, we report in figure 6.26 the response of the same cable when the number of masses in the perfectly periodic system is increased to 11 and the central mass is removed. Note that, for this case, the force imposed to the system was reduced to $F = 3.4$ N to lower the frequencies of the second pass band. From the theoretical results, a peak is expected inside the first band gap at a frequency $f_{th} \approx 134$ Hz. The corresponding modal shape, reported in figure 6.13b, is represented again here in figure 6.26a. By looking at the results from the experimental test, from the Fourier transform of the signal measured by sensor 3 (placed within the defect), we found a peak at a frequency of $f_{ex} \approx 147$ Hz. The corresponding motion is reported in figure 6.26b. At the frequency $f_{ex}$, the response of the system resembles very much the modal shape represented in figure 6.26a, meaning that we are indeed activating the defect mode. The difference between $f_{th}$ and $f_{ex}$ is mainly due to experimental imperfections. As we specified before in subsection 6.3.5, since the number of masses is larger, the motion is more concentrated in the defect.

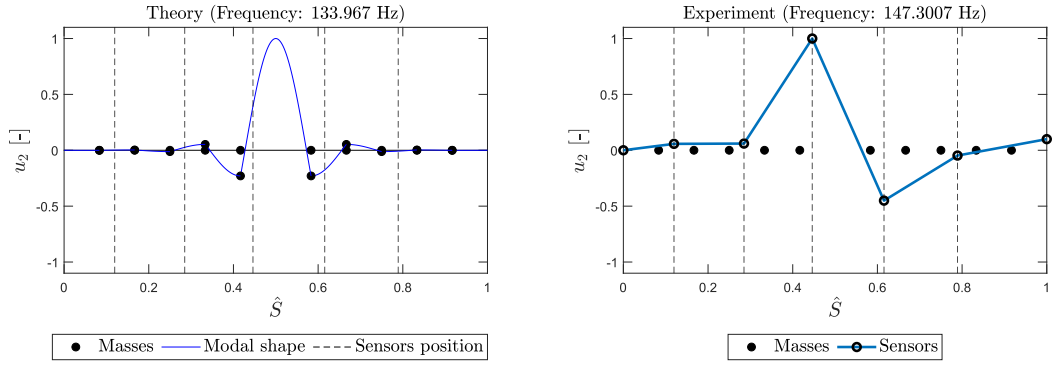


(a) (b)

Figure 6.26: *Comparison between modal shapes (a), and motion of the tested system (b), for a theoretical defect mode at $f \approx 134$ Hz, in the system with $11(-1)$ masses. Black dots stand for masses, black circles and vertical dashed lines for points above the optical sensors.*

CHAPTER

# 7

# Conclusions and perspectives

## 7.1 General conclusions

In this thesis, we have addressed the problem of wave propagation in periodic media that can be classified as "metamaterials", characterized by a non-conventional behavior. The research has focused on the development of systems able to localize and trap mechanical waves in a confined region, to be used for the harvesting of mechanical energy. In particular, phononic crystals and locally resonant materials with a compact defect of periodicity were the subject of this work.

In the initial part, we have studied the dynamics of a mass-in-mass 1D lattice and shown that it can be tuned to behave as either a PnC, or a LRM, or in a hybrid way. This has given us the possibility to introduce the concept of effective material properties, that we have then further elaborated in the context of the two-scale homogenization technique. In particular, we have exploited this method for deriving in a quite general framework the effective behavior of continuous LRMs, whose unit cells were composed of one or two non-connected resonating inclusions. We have proven that the effective mass density is a symmetric tensor and that the spectrum of the problem is characterized by the presence of band gaps and flat bands, corresponding to resonating modes for the inclusions that are not activated by the macroscopic phenomenon. This has allowed us to study the dispersive properties typical of LRMs of this type. The analysis of the aforementioned discrete and continuous systems has proved to be relevant for our subsequent results and, more in general, for the treatment of metamaterials with a defect.

We have thus applied the outcomes from the initial part of this manuscript to study the behavior of a system for the localization of mechanical energy, whose functioning is based on the resonant tunneling phenomenon, well-known from quantum-mechanics. The system has been obtained from the creation of a cavity inside the periodic structures of the metamaterials under consideration. We have verified the occurrence of a localized

behavior by using the previously characterized mass-in-mass 1D lattice and we have then demonstrated its efficiency in terms of energy localization in the sub-wavelength regime. For this second point, we have employed the LRMs of the type previously described and derived a formula for the optimal design of the system. This was possible thanks to the available effective description of the heterogeneous components forming the domain of the problem.

In the last part, by looking at existing engineering solutions involving cable systems with periodic arrangements of suspended objects (such as suspension bridges, overhead lines, and cableways to cite but a few), we started with the conjecture that these structures could possibly behave as metamaterials, offering a spectrum with a banded structure. We have thus given a preliminary proof that this interpretation of the problem can be applied for cable systems of that type. For this, we have considered the small oscillations of a taut string with a family of masses periodically attached to it, either directly or by means of elastic springs. We found that the problem is governed by the same equation valid for a discrete 1D lattice. The spectrum of the unbounded problem being thus characterized by the same observations that were valid for the mass-in-mass chain.

When dealing with the bounded domain for the cable, the spectrum of the problem becomes discrete. We have shown that the eigenfrequencies can only be positioned inside a pass band of the continuous spectrum associated to the same problem expressed for the unbounded domain. This is no more true when a defect is introduced, by removing one mass from the periodic array. The localization phenomenon occurring also for these systems.

All these theoretical results have been compared with those obtained from an experimental test. A good agreement between the two has been observed.

## 7.2 Future perspectives

We conclude with an overview of some possible future developments of the research presented in this theses.

### 7.2.1 Perspectives from the problem related to sub-wavelength waves in defective metamaterials

Concerning the problem of sub-wavelength energy localization, we have proposed a system obtained by creating a cavity inside a locally resonant metamaterial. The problem has been formulated with respect to a scalar field (anti-plane waves in our case) in a 2D domain. We have assumed that the metamaterial was characterized by a 2D periodicity and placed in a region confined in direction $x_1$ and infinitely extended in direction $x_2$. We have then considered only waves with a wave vector aligned with direction $x_1$. This has allowed us to further reduce the dimensions of the problem.

A natural extension of the work could thus be that of relaxing some of these assumptions to consider a more general framework, with the aim of finding a relation between geometrical parameters and material properties of the constituents, for an optimal wave localization. Accordingly, we list here some possible future developments:

- we could consider in-plane waves directed as $x_1$;
- the problem of inclined out-of-plane or in-plane waves in $x_1 - x_2$ could be analyzed. The waves would thus experience both a localization in direction $x_1$ and would be instead guided along direction $x_2$. A wave guide of the type shown in figure 7.1 could then be studied, to convey the waves traveling through the system towards the region denoted as $D$ in the figure;
- a more challenging problem would be that of extending these results in three-dimensions.

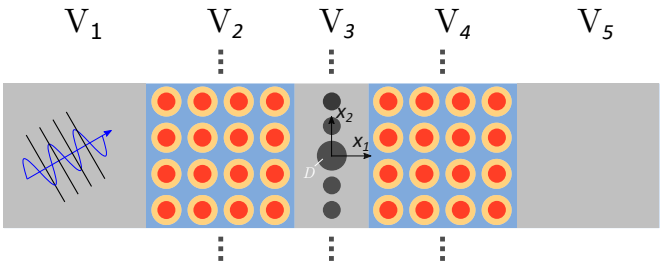


Figure 7.1: *Top-view of a system with a wave guide composed of a row of resonating elements along direction $x_2$ and placed between two barriers made up of a LRM. Region $D$ corresponds to a defect along this wave guide.*

Clearly all these cases will be strongly dependent on the symmetries of the unit cells envisaged for the LRM, which affect the reflection and refraction problem at each interface.

### 7.2.2 Perspectives from the problem related to the dynamics of cables

In the last part of the manuscript, we have studied the dynamics of cables presenting a periodic arrangement of suspended masses, hanging with elastic springs or directly attached to it. In particular, we have verified that the system behaves as a metamaterial, possessing band gaps in its harmonic response. A fundamental hypothesis in our findings was that of considering the cable equilibrium configuration to be horizontal. An interesting extension of our results would be that of understanding how the band gaps change when the equilibrium configuration of the cable is no more horizontal. We have shown that, in the case of a bare cable suspended between two fixed supports, the eigenfrequencies of the associated problem are strongly affected by the actual static equilibrium configuration (*cf.* figure 6.6). When dealing with the wave propagation

problem associated to the cable with a family of scatter elements, we thus expect a similar dependence for the band gaps that we found for a horizontal initial configuration.

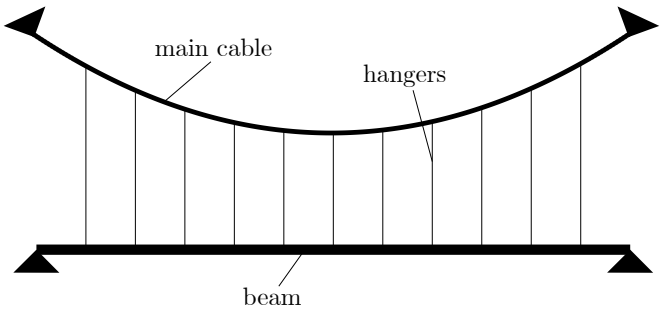


Figure 7.2: *A sketch of a typical suspension bridge.*

Finally, a more long-term extension would be that of considering a model closer to the "true" structure of a suspension bridge (*cf.* figure 7.2), with a beam (representing the deck) that is hanging on a cable, in tension between two fixed supports, by means of a periodic array of elastic springs (representing the hangers). Very likely, the coupling between the dynamics of the cable and that of the beam could result in interesting dynamic phenomena.

# Appendix

## A1 Eigenmodes of a sphere with fixed boundaries

The components of relation (3.61) can be written as:

$$\begin{cases} u_{r(nm)}(r,\theta,\varphi) = \dfrac{1}{r}\left[\mathsf{A}U_1(k^\ell r) + \mathsf{C}U_3(k^s r)\right] P_n^m(\cos\theta)\exp\{\mathsf{i}(m\varphi)\}, \\ u_{\theta(nm)}(r,\theta,\varphi) = \dfrac{1}{r}\Bigg\{ \left[\mathsf{A}V_1(k^\ell r) + \mathsf{C}V_3(k^s r)\right]\left[n\cot\theta P_n^m(\cos\theta) - \dfrac{n+m}{\sin\theta}P_{n-1}^m(\cos\theta)\right] \\ \qquad\qquad + \mathsf{B}V_2(k^s r)\dfrac{\mathsf{i}\,m}{\sin\theta}P_n^m(\cos\theta)\Bigg\}\exp\{\mathsf{i}(m\varphi)\}, \\ u_{\varphi(nm)}(r,\theta,\varphi) = \dfrac{1}{r}\Bigg\{ \left[\mathsf{A}V_1(k^\ell r) + \mathsf{C}V_3(k^s r)\right]\dfrac{\mathsf{i}\,m}{\sin\theta}P_n^m(\cos\theta) \\ \qquad\qquad - r\mathsf{B}V_2(k^s r)\left[n\cot\theta P_n^m(\cos\theta) - \dfrac{n+m}{\sin\theta}P_{n-1}^m(\cos\theta)\right]\Bigg\}\exp\{\mathsf{i}(m\varphi)\}, \end{cases} \tag{A.1}$$

where $\mathsf{A}$, $\mathsf{B}$ and $\mathsf{C}$ are arbitrary constants , $P_n^m(x)$, with $n \in \mathbb{Z}$ and $m \in \{-|n|, \ldots, |n|\}$, are *associated Legendre functions* and $k^\ell$, $k^s$ are respectively the longitudinal and shear wave numbers defined as

$$k^\ell = \sqrt{\frac{\omega}{c_\ell}}, \quad k^s = \sqrt{\frac{\omega}{c_s}},$$

with $c_\ell$ and $c_s$ given by relations (2.15).
In each one of the above components (A.1), the first, the second and the third terms (subscript 1, 2 and 3 above) are respectively the contributions from the three Helmholtz potentials (generally denoted as $\phi$, $\psi$ and $\chi$ in the literature) and can be expressed as:

$$\begin{cases} U_1(k^\ell r) = n j_n(k^\ell r) - k^\ell r j_{n+1}(k^\ell r), \\ U_3(k^s r) = n(n+1) j_n(k^s r), \\ V_1(k^\ell r) = j_n(k^\ell r), \\ V_2(k^s r) = j_n(k^s r), \\ V_3(k^s r) = (n+1) j_n(k^s r) - k^s r j_{n+1}(k^s r), \end{cases} \tag{A.2}$$

where $j_n(x)$, with $n \in \mathbb{Z}$, being *spherical Bessel functions* of the first kind.

We here do not give the expressions for the Helmholtz potentials. We limit ourselves to say that $\phi$, $\psi$ and $\chi$ are solutions of three Helmholtz equations, obtained by breaking down the displacement field in an irrotational and a solenoidal part. For a more satisfactory explanation, the interested reader is referred to the works of Lamb (1881), Eringen et al. (1974), and Dahlen et al. (1998).

Let us now study the orthogonality of the eigenmodes $\boldsymbol{\eta}^*_{nm}$ of problem (3.60). First we rewrite in spherical coordinates the integral of condition (3.62), such that:

$$\int_{\mathrm{Y}_c} \boldsymbol{\eta}^*_{p(nm)}(\boldsymbol{y}) \cdot \boldsymbol{e}_3 = \int_0^{R_c} \int_0^{\pi} \int_0^{2\pi} \left( u_{r(nm)^*} \cos\theta - u^*_{\theta(nm)} \sin\theta \right) r^2 \sin\theta \, dr \, d\theta \, d\varphi.$$

We are interested in finding those eigenvalues $\omega_{q(nm)}$ whose corresponding eigenmodes $\boldsymbol{\eta}^*_{q(nm)}$ are not orthogonal to the constants, *i.e.* for which condition (3.62) is not fulfilled. By substituting relations (A.1) in the above integral, one has:

- *Integration over $d\varphi$.*

$$\int_0^{2\pi} \exp\{\mathrm{i}m\varphi\} \, d\varphi = \begin{cases} 2\pi & \text{if } m = 0 \\ 0 & \text{otherwise} \end{cases}.$$

  Therefore, the integral is not zero only for $\boxed{m = 0}$.

- *Integration over $d\theta$.*

  Considering $m = 0$, two integrations must be checked, namely:

$$\int_0^{\pi} P_n^0(\cos\theta) \cos\theta \sin\theta \, d\theta = \begin{cases} 2/3 & \text{if } n = 1 \\ 0 & \text{otherwise} \end{cases},$$

$$\int_0^{\pi} \left[ n \cot\theta P_n^0(\cos\theta) - \frac{n}{\sin\theta} P_{n-1}^0(\cos\theta) \right] \sin^2\theta \, d\theta = \begin{cases} -4/3 & \text{if } n = 1 \\ 0 & \text{otherwise} \end{cases}.$$

  We have thus found that both the integrals above are different from zero only for $\boxed{n = 1}$.

Note that the integration over $dr$ could still make the eigenmodes orthogonal to the constants even when $m = 0$ and $n = 1$, as it happens for the in-plane problem of 2D LRMs (see Comi et al. (2020)).

The function $\Upsilon_q(\omega)$ defined by relation (3.69) can be computed explicitly as follows:

$$\Upsilon_q(\omega) = \frac{2k^s k^\ell j_2(k^\ell R_c) j_2(k^s R_c)}{\left\{ \begin{array}{r} k^s k^\ell R_c \left( k^s j_1(k^s R_c) j_2(k^\ell R_c) + k^\ell j_1(k^\ell R_c) j_2(k^s R_c) \right) \\ - j_1(k^\ell R_c) j_1(k^s R_c) \left( 2k^{\ell^2} + k^{s^2} \right) \end{array} \right\}}.$$

## A2 The average mechanical energy density in homogenized LRMs

Let us derive the expression (5.27) for the average mechanical energy density in a LRM, by exploiting the results coming from the homogenization technique (chapter 3).

By summing all the terms (5.22) to (5.26) in (5.17), one obtains:

$$\langle e \rangle (x) = \frac{1}{4}\Bigg\{\mu^{eff} s^2 \Big[\mathsf{V}'^2(x) + \mathsf{W}'^2(x)\Big] + \Bigg[\rho_m \frac{|\mathrm{Y}_m|}{|\mathrm{Y}|}\omega^2 + \underbrace{\frac{\rho_c \omega^2}{|\mathrm{Y}|}\int_{\mathrm{Y}_c} \tilde{\mathrm{v}}^2(\boldsymbol{y}) d\mathbf{y}}_{\star} + \frac{\mu_c}{|\mathrm{Y}|}\int_{\mathrm{Y}_c} \nabla_{\mathbf{y}}\tilde{\mathrm{v}}(\boldsymbol{y}) \cdot \nabla_{\mathbf{y}}\tilde{\mathrm{v}}(\boldsymbol{y})\, d\mathbf{y} + \underbrace{\rho_f \tilde{\mathrm{v}}(R_f)^2 \frac{|\mathrm{Y}_f|}{|\mathrm{Y}|}\omega^2}_{\text{Present if } |\mathrm{Y}_f| \neq 0}\Bigg] \big(\mathsf{V}^2(x) + \mathsf{W}^2(x)\big)\Bigg\}. \tag{A.3}$$

Let us consider the term $\star$. For this, we make use of the eigenvalue problem for part $\mathrm{Y}_c$, that corresponds to problems (3.19) and (3.23), respectively for the bi- and three-phase unit cell depicted in figure 3.3. Specifically, for the current case, these problems can be rewritten by considering

$$\hat{U}^0(\boldsymbol{x}, \boldsymbol{y}) = \hat{U}^0_m(\boldsymbol{x})\tilde{\mathrm{v}}(\mathbf{y})$$

as

$$\begin{cases} \mu_c \Delta_{\boldsymbol{y}} \tilde{\mathrm{v}}(\boldsymbol{y}) + \rho_c \omega^2 \tilde{\mathrm{v}}(\boldsymbol{y}) = 0 & \text{in } \mathrm{Y}_c \\ \tilde{\mathrm{v}}(\boldsymbol{y}) = 1 & \text{on } \partial\mathrm{Y}_c \\ \tilde{\mathrm{v}}(\boldsymbol{y}) = \dfrac{\hat{U}^0_f(\boldsymbol{x})}{\hat{U}^0_m(\boldsymbol{x})} & \text{on } \partial\mathrm{Y}_f \end{cases} \tag{A.4}$$

where the condition on $\partial\mathrm{Y}_f$ is there only when $|\mathrm{Y}_f| \neq 0$. The two-phase case can be understood as a particular case of the more general three-phase case. We will thus consider this latter one, being aware that all the quantities and integrals applied to part $\mathrm{Y}_f$ vanish when a two-phase unit cell is analyzed.

Let us rewrite the above problem by using

$$\tilde{\mathrm{v}}(\mathbf{y}) = \mathrm{v}(\mathbf{y}) + 1.$$

This gives

$$\begin{cases} \mu_c \Delta_{\boldsymbol{y}} \mathrm{v}(\boldsymbol{y}) + \rho_c \omega^2 (\mathrm{v}(\boldsymbol{y}) + 1) = 0 & \text{in } \mathrm{Y}_c \\ \mathrm{v}(\boldsymbol{y}) = 0 & \text{on } \partial\mathrm{Y}_c \\ \mathrm{v}(\boldsymbol{y}) = \dfrac{\hat{U}^0_f(\boldsymbol{x})}{\hat{U}^0_m(\boldsymbol{x})} - 1 & \text{on } \partial\mathrm{Y}_f \end{cases}. \tag{A.5}$$

Integrating over $\mathrm{Y}_c$ the governing equation of the original problem (A.4) and multiplying each term by $(\tilde{\mathrm{v}} - 1)$, one finds

$$\int_{\mathrm{Y}_c} \mu_c \Delta_{\boldsymbol{y}} \tilde{\mathrm{v}}(\boldsymbol{y})(\tilde{\mathrm{v}}(\boldsymbol{y}) - 1) + \rho_c \omega^2 \tilde{\mathrm{v}}(\mathbf{y})(\tilde{\mathrm{v}}(\boldsymbol{y}) - 1) d\mathbf{y} = 0.$$

From the equation here-above, applying the divergence theorem and using the boundary condition on $\partial \mathrm{Y}_c$ of problem (A.5), one has

$$\begin{aligned}\star = \frac{\rho_c \omega^2}{|\mathrm{Y}|}\int_{\mathrm{Y}_c} \tilde{\mathrm{v}}(\mathbf{y})^2 d\mathbf{y} = \frac{\rho_c \omega^2}{|\mathrm{Y}|}\int_{\mathrm{Y}_c} \tilde{\mathrm{v}}(\mathbf{y}) d\mathbf{y} \\ + \frac{\mu_c}{|\mathrm{Y}|}\int_{\mathrm{Y}_c} \nabla_{\mathbf{y}}\tilde{\mathrm{v}}(\mathbf{y})\cdot\nabla_{\mathbf{y}}\tilde{\mathrm{v}}(\mathbf{y}) d\mathbf{y} - \rho_f \frac{|\mathrm{Y}_f|}{|\mathrm{Y}|}\omega^2 \tilde{\mathrm{v}}(R_f)(\tilde{\mathrm{v}}(R_f)-1),\end{aligned} \tag{A.6}$$

where we made also use of the linear momentum balance for part $\mathrm{Y}_f$, given by equation (3.17).

We can now rewrite expression (A.3) as follows:

$$\langle e\rangle(x) = \frac{1}{4}\Big\{\mu^{eff} s^2\Big[\mathsf{V}'^2(x)+\mathsf{W}'^2(x)\Big] + \Big[2\frac{\mu_c}{|\mathrm{Y}|}\int_{\mathrm{Y}_c}\nabla_{\mathbf{y}}\tilde{\mathrm{v}}(\boldsymbol{y})\cdot\nabla_{\mathbf{y}}\tilde{\mathrm{v}}(\boldsymbol{y})\,d\mathbf{y} \underbrace{\rho_m\frac{|\mathrm{Y}_m|}{|\mathrm{Y}|}\omega^2 + \frac{\rho_c\omega^2}{|\mathrm{Y}|}\int_{\mathrm{Y}_c}\tilde{\mathrm{v}}(\boldsymbol{y})d\mathbf{y} + \rho_f\frac{|\mathrm{Y}_f|}{|\mathrm{Y}|}\omega^2\tilde{\mathrm{v}}(R_f)^2}_{\rho^{eff}\omega^2}\Big](\mathsf{V}^2(x)+\mathsf{W}^2(x))\Big\}.$$

Denoting $\gamma$ as

$$\gamma(\omega) := \rho^{eff} + 2\frac{\mu_c}{|\mathrm{Y}|}\int_{\mathrm{Y}_c}\nabla_{\mathbf{y}}\tilde{\mathrm{v}}(\boldsymbol{y})\cdot\nabla_{\mathbf{y}}\tilde{\mathrm{v}}(\boldsymbol{y})\,d\mathbf{y}$$

and making use again of relation (A.6), one is left with expressions (5.28), from which the mechanical energy density in a LRM as expressed in (5.27) is found.

## A3 Static equilibrium configuration of a cable with a discrete set of attached masses

The equilibrium configuration for a cable with $N$ equally spaced masses attached is given as follows:

$$\begin{cases} x_{[1](\mathrm{eq})}(S) = \dfrac{F_{[1](\mathrm{eq})}}{\rho_{\mathrm{R}} g}\left[\displaystyle\sum_{j=1}^{i}(A_j+B_j) - \operatorname{arsinh}\left(\frac{\check{F}_{[2](\mathrm{eq})}+\rho_{\mathrm{R}} g(\ell_{\mathrm{R}}-S)+(N+1-i)Mg}{\check{F}_{[1](\mathrm{eq})}}\right)\right] \\ \qquad\qquad \boxed{+\dfrac{F_{[1](\mathrm{eq})}S}{EA_{\mathrm{R}}}} \\ x_{[2](\mathrm{eq})}(S) = \dfrac{1}{\rho_{\mathrm{R}} g}\left[\displaystyle\sum_{j=1}^{i}(C_j+D_j) - \sqrt{\check{F}^2_{[1](\mathrm{eq})}+(\check{F}_{[2](\mathrm{eq})}+\rho_{\mathrm{R}} g(\ell_{\mathrm{R}}-S)+(N+1-i)Mg)^2}\right] \\ \qquad\qquad \boxed{\dfrac{1}{EA_{\mathrm{R}}}\left[(\check{F}_{[2](\mathrm{eq})}+(N+1-i)Mg)S + \rho_{\mathrm{R}} g\frac{S(2\ell_{\mathrm{R}}-S)}{2} + Mg\textstyle\sum_{j=1}^{i}S_{j-1}\right]} \end{cases}$$

valid $\forall S \in ((i-1)d, id)$ with $1 \leq i \leq N+1$, $d$ being the distance between two masses, and with $S_i = id$. The boxed terms disappear when the cable is inextensible ($EA_{\mathrm{R}} \to +\infty$). One can retrieve the relations (6.20) valid for a bare cable (no masses) by assuming $M = 0$ in the above relations. The scalars $A_j$, $B_j$, $C_j$, $D_j$ read

$$A_j = \operatorname{arsinh}\left(\frac{\check{F}_{[2](\mathrm{eq})} + \rho_{\mathrm{R}} g(\ell_{\mathrm{R}} - S_{j-1}) + (N+1-j)Mg}{\check{F}_{[1](\mathrm{eq})}}\right),$$

$$B_j = \begin{cases} 0 & \text{if } j = 1 \\ -\operatorname{arsinh}\left(\dfrac{\check{F}_{[2](\mathrm{eq})} + \rho_{\mathrm{R}} g(\ell_{\mathrm{R}} - S_{j-1}) + (N+1-(j-1))Mg}{\check{F}_{[1](\mathrm{eq})}}\right) & \text{otherwise} \end{cases},$$

$$C_j = \sqrt{\check{F}^2_{[1](\mathrm{eq})} + (\check{F}_{[2](\mathrm{eq})} + \rho_{\mathrm{R}} g(\ell_{\mathrm{R}} - S_{j-1}) + (N+1-j)Mg)^2},$$

$$D_j = \begin{cases} 0 & \text{if } j = 1 \\ -\sqrt{\check{F}^2_{[1](\mathrm{eq})} + (\check{F}_{[2](\mathrm{eq})} + \rho_{\mathrm{R}} g(\ell_{\mathrm{R}} - S_{j-1}) + (N+1-(j-1))Mg)^2} & \text{otherwise} \end{cases}.$$

Similarly to the bare cable, by taking $\check{F}_{[1](\mathrm{eq})} > 0$ and $\check{F}_{[2](\mathrm{eq})} = -(\rho_{\mathrm{R}}\ell_{\mathrm{R}} + MN)g/2$, one finds that the right end of the cable is at height $x_{[2](\mathrm{eq})}(\ell_{\mathrm{R}}) = 0$ and thus at the same height of the left end.

## A4 Linearization of the motion problem of a bare cable

Let us rewrite here from problem (6.36) the equation governing the motion of an elastic bare cable

$$(N\boldsymbol{t})'(S,t) + \rho_{\mathrm{R}} g \boldsymbol{e}_2 - \rho_{\mathrm{R}} \ddot{\boldsymbol{x}}(S,t) = \boldsymbol{0} \quad \forall S. \tag{A.7}$$

The axial force $(N\boldsymbol{t})$ can be written as

$$(N\boldsymbol{t})(S,t) = EA_{\mathrm{R}} \underbrace{\frac{\varepsilon(S,t)}{1+\varepsilon(S,t)}}_{\star\star} \boldsymbol{x}'(S,t), \tag{A.8}$$

with

$$\varepsilon(S,t) = \sqrt{{x_{[1]}}'^2(S,t) + {x_{[2]}}'^2(S,t) + {x_{[3]}}'^2(S,t)} - 1.$$

and $\boldsymbol{x}$ given as in relation (6.1):

$$\boldsymbol{x}(S,t) = \boldsymbol{x}_{\mathrm{eq}}(S) + \boldsymbol{u}(S,t).$$

Considering as small the displacements $\boldsymbol{u}(S,t)$, the strain can be rewritten as

$$\varepsilon(S,t) = \sqrt{\varepsilon_0 + 2\varepsilon_1 + \varepsilon_2} - 1,$$

where the subscripts denote the orders of the infinitesimals, such that:

$$\begin{aligned}
\varepsilon_0 &= x'^2_{[1]\mathrm{eq}}(S) + x'^2_{[2]\mathrm{eq}}(S),\\
\varepsilon_1 &= x'_{[1]\mathrm{eq}}(S)u'_{[1]}(S,t) + x'_{[2]\mathrm{eq}}(S)u'_{[2]}(S,t),\\
\varepsilon_2 &= {u'_{[1]}}^2(S,t) + {u'_{[2]}}^2(S,t) + {u'_{[3]}}^2(S,t).
\end{aligned}$$

Accordingly, the term $\star\star$ in relation (A.8) can be expanded up to the second order. If the equilibrium configuration of the cable can be approximated with a parabola, then $x'_{[1]\mathrm{eq}} \gg x'_{[2]\mathrm{eq}}$ (*cf.* section 6.2.3) and we can consider $x'_{[2]\mathrm{eq}} = \mathcal{O}(\|\boldsymbol{u}\|)$. Using this latter assumption, equation (A.7) can be approximated in the three directions as

$$EA_\mathrm{R}\left[u'_{[1]} + \frac{1}{x'_{[1]\mathrm{eq}}}\left(x_{[2]\mathrm{eq}}u'_{[2]} + \frac{1}{2}u'^2_{[2]} + \frac{1}{2}u'^2_{[3]\mathrm{eq}}\right)\right]' = \rho_\mathrm{R}\ddot{u}_{[1]}, \tag{A.9}$$

$$EA_\mathrm{R}\left[\frac{x'_{[1]\mathrm{eq}}-1}{x'_{[1]\mathrm{eq}}}u'_{[2]} + \frac{x'_{[2]\mathrm{eq}}+u'_{[2]}}{x'_{[1]\mathrm{eq}}}\left(u'_{[1]} + x_{[2]\mathrm{eq}}u'_{[2]} + \frac{1}{2}u'^2_{[2]} + \frac{1}{2}u'^2_{[3]\mathrm{eq}}\right)\right]' = \rho_\mathrm{R}\ddot{u}_{[2]}, \tag{A.10}$$

$$EA_\mathrm{R}\left[\frac{x'_{[1]\mathrm{eq}}-1}{x'_{[1]\mathrm{eq}}}u'_{[3]} + \frac{u'_{[2]}}{x'_{[1]\mathrm{eq}}}\left(u'_{[1]} + x_{[2]\mathrm{eq}}u'_{[2]} + \frac{1}{2}u'^2_{[2]} + \frac{1}{2}u'^2_{[3]\mathrm{eq}}\right)\right]' = \rho_\mathrm{R}\ddot{u}_{[3]}, \tag{A.11}$$

where we have not specified the variables for brevity sake.

The above system of equations can be simplified by applying the so-called static condensation, *i.e.* by making the assumption that the frequencies of interest are close to the first eigenfrequencies $\omega_j$ of the transverse eigenvalue problem associated to taut strings (*cf.* subsection (6.3.1)). With this hypothesis, for metallic cables, the variation of the excitation in time is too slow to activate the longitudinal dynamics of the cable. Accordingly, the inertial term in equation (A.9) can be neglected. Moreover, due to the parabolic approximation, we can assume that

$$x_{[1]\mathrm{eq}}(S) \approx 1 + \frac{\check{F}_{[1]\mathrm{eq}}}{EA_\mathrm{R}}$$

and thus at first order:

$$x'_{[1]\mathrm{eq}}(S) \approx 1 \quad \text{and} \quad \frac{x'_{[1]\mathrm{eq}}(S)-1}{x'_{[1]\mathrm{eq}}(S)} \approx \frac{\check{F}_{[1]\mathrm{eq}}}{EA_\mathrm{R}} \quad \forall S. \tag{A.12}$$

It follows that equation (A.9) becomes

$$\left[u'_{[1]}(S,t) + \left(x_{[2]\mathrm{eq}}(S)u'_{[2]}(S,t) + \frac{1}{2}u'^2_{[2]}(S,t) + \frac{1}{2}u'^2_{[3]\mathrm{eq}}(S,t)\right)\right]' = [f(t)]' = 0, \tag{A.13}$$

where $f$ is a function independent from the spatial variable. Using relations (A.12) and (A.13) in equations (A.10) and (A.11), one obtains:

$$F_{[1]\mathrm{eq}} u''_{[2]}(S,t) + EA_{\mathrm{R}}(\boxed{x''_{[2]\mathrm{eq}}(S)} + u''_{[2]}(S,t))f(t) = \rho_{\mathrm{R}} \ddot{u}_{[2]}(S,t), \tag{A.14}$$

$$F_{[1]\mathrm{eq}} u''_{[3]}(S,t) + EA_{\mathrm{R}} u''_{[3]}(S,t)f(t) = \rho_{\mathrm{R}} \ddot{u}_{[3]}(S,t). \tag{A.15}$$

The boxed term is due to the initial sag of the static equilibrium configuration.

From equation (A.14), considering only the linear terms and relation (6.42) for $x_{[2]\mathrm{eq}}(S)$, one obtains the first of equations (6.45).

For this section, we have followed the derivation from the work of Nayfeh et al. (2008).

# Bibliography


Lamb, H. (1881). "On the Vibrations of an Elastic Sphere". In: *Proc. London Math. Soc.* s1-13.1, pp. 189–212. DOI: 10.1112/plms/s1-13.1.189 (cited on page 170).

Floquet, G. (1883). "Sur les équations différentielles linéaires à coefficients périodiques". In: *Ann. Sci. l'École Norm. supérieure* 12, pp. 47–88. DOI: 10.24033/asens.220 (cited on page 17).

Bloch, F. (1929). "Über die Quantenmechanik der Elektronen in Kristallgittern". In: *Zeitschrift für Phys.* 52.7-8, pp. 555–600. DOI: 10.1007/BF01339455 (cited on page 17).

Kronig, R. d. L. and W. G. Penney (1931). "Quantum mechanics of electrons in crystal lattices". In: *Proc. R. Soc. London A* 130.814, pp. 499–513. DOI: 10.1098/rspa.1931.0019 (cited on page 3).

Brillouin, L. (1946). *Wave Propagation in Periodic Structures - Electric Filters and Crystal Lattices*. 1st ed. McGraw - Hill Book Company, Inc., p. 248 (cited on pages 19, 27).

Anderson, P. W. (1958). "Absence of Diffusion in Certain Random Lattices". In: *Phys. Rev.* 109.5, pp. 1492–1505. DOI: 10.1103/PhysRev.109.1492 (cited on page 74).

Eringen, A. C. and E. S. Suhubi (1974). *Elastodynamics*. Academic Press, p. 1003 (cited on pages 14, 170).

Henohold, W. and J. Russell (1976). "Equilibrium and natural frequencies of cable structures (a nonlinear finite element approach)". In: *Comput. Struct.* 6.4-5, pp. 267–271. DOI: 10.1016/0045-7949(76)90001-8 (cited on page 119).

Irvine, H. M. and J. H. Griffin (1976). "On the dynamic response of a suspended cable". In: *Earthq. Eng. Struct. Dyn.* 4.4, pp. 389–402. DOI: 10.1002/eqe.4290040406 (cited on page 135).

Bensoussan, A., J.-L. Lions, and G. Papanicolaou (1978). *Asymptotic analysis for periodic structures*. North-Holland Pub. Co., p. 700 (cited on pages 6, 34, 35, 38).

Reed, M. and B. Simon (1978). *Methods of modern mathematical physics. IV, Analysis of operators*. New York, NY: Academic Press, p. 325 (cited on page 77).

Sanchez-Palencia, E. E. (1980). *Non-Homogeneous Media and Vibration Theory*. Vol. 127. Lecture Notes in Physics. Berlin, Heidelberg: Springer Berlin Heidelberg, p. 398. DOI: 10.1007/3-540-10000-8 (cited on page 35).

Irvine, M. (1981). *Cable structures*. Cambridge: The Massachusetts Institute of Technology, p. 259 (cited on page 121).

Auriault, J.-L. and G. Bonnet (1985). "Dynamique des composites élastiques périodiques". In: *Arch.Mech.* 37.February, pp. 269–284 (cited on pages 3, 7, 35, 37).

Sanchez-Palencia, E. and A. Zaoui, eds. (1987). *Homogenization Techniques for Composite Media*. Vol. 272. Lecture Notes in Physics. Berlin, Heidelberg: Springer Berlin Heidelberg. DOI: 10.1007/3-540-17616-0 (cited on page 48).

Desai, Y., N. Popplewell, A. Shah, and D. Buragohain (1988). "Geometric nonlinear static analysis of cable supported structures". In: *Comput. Struct.* 29.6, pp. 1001–1009. DOI: 10.1016/0045-7949(88)90326-4 (cited on page 119).

Bakhvalov, N. and G. Panasenko (1989). *Homogenisation: Averaging Processes in Periodic Media*. Vol. 36. Mathematics and its Applications. Dordrecht: Springer Netherlands. DOI: 10.1007/978-94-009-2247-1 (cited on page 35).

Bohm, D. (1989). *Quantum theory*. New York, NY: Dover Publications, p. 646 (cited on page 80).

Dautray, R. and J.-L. Lions (1990). *Mathematical Analysis and Numerical Methods for Science and Technology: spectral theory and applications*. Paris: Masson, p. 541 (cited on page 44).

Sigalas, M. M. and E. N. Economou (1992). "Elastic and acoustic wave band structure". In: *J. Sound Vib.* 158.2, pp. 377–382 (cited on page 2).

Kuchment, P. (1993). *Floquet Theory for Partial Differential Equations*. Basel: Birkhäuser Basel. DOI: 10.1007/978-3-0348-8573-7 (cited on page 2).

Kushwaha, M. S., P. Halevi, L. Dobrzynski, and B. Djafari-Rouhani (1993). "Acoustic band structure of periodic elastic composites". In: *Phys. Rev. Lett.* 71.13, pp. 2022–2025. DOI: 10.1103/PhysRevLett.71.2022 (cited on page 2).

Auriault, J.-L. (1994). "Acoustics of heterogeneous media: Macroscopic behavior by homogenization". In: *Curr. Top. Acoust. Res.* 1.January 1994, pp. 63–90 (cited on page 3).

Figotin, A. and A. Klein (1994a). "Localization of electromagnetic and acoustic waves in random media. Lattice models". In: *J. Stat. Phys.* 76.3-4, pp. 985–1003. DOI: 10.1007/BF02188695 (cited on page 74).

Figotin, A. and A. Klein (1994b). "Localization phenomenon in gaps of the spectrum of random lattice operators". In: *J. Stat. Phys.* 75.5-6, pp. 997–1021. DOI: 10.1007/BF02186755 (cited on page 74).

Conca, C., J. Planchard, and M. Vanninathan (1995). *Fluids and periodic structures*. Paris: J. Wiley & Sons/Masson (cited on page 11).

Martínez-Sala, R., J. Sancho, J. V. Sánchez, V. Gómez, J. Llinares, and F. Meseguer (1995). "Sound attenuation by sculpture". In: *Nature* 378.6554, pp. 241–241. DOI: 10.1038/378241a0 (cited on page 2).

Nayfeh, A. H. and D. T. Mook (1995a). *Nonlinear oscillations*. Wiley, p. 720 (cited on page 118).

Nayfeh, S. A., A. H. Nayfeh, and D. T. Mook (1995b). "Nonlinear Response of a Taut String to Longitudinal and Transverse End Excitation". In: *J. Vib. Control* 1.3, pp. 307–334. DOI: 10.1177/107754639500100304 (cited on page 151).

Sigalas, M. M. and E. N. Economou (1995). "Comment on acoustic band structure of periodic elastic composites". In: *Phys. Rev. Lett.* 75.19, p. 3580. DOI: 10.1103/PhysRevLett.75.3580 (cited on page 2).

Figotin, A. and P. Kuchment (1996a). "Band-gap structure of spectra of periodic dielectric and acoustic media. I. Scalar model". In: *SIAM J. Appl. Math.* 56.1, pp. 68–88. DOI: 10.1137/S0036139994263859 (cited on page 2).

Figotin, A. and P. Kuchment (1996b). "Band-Gap Structure of Spectra of Periodic Dielectric and Acoustic Media. I. Scalar Model". In: *SIAM J. Appl. Math.* 56.1, pp. 68–88. DOI: 10.1137/S0036139994263859 (cited on page 2).

Figotin, A. and A. Klein (1996c). "Localization of classical waves I: Acoustic waves". In: *Commun. Math. Phys.* 180.2, pp. 439–482. DOI: 10.1007/BF02099721 (cited on pages 74, 75).

Royer, D. and E. Dieulesaint (1996). *Elastic waves in solids I*. Berlin, Heidelberg: Springer Berlin Heidelberg (cited on pages 58, 63).

Åberg, M. and P. Gudmundson (1997). "The usage of standard finite element codes for computation of dispersion relations in materials with periodic microstructure". In: *J. Acoust. Soc. Am.* 102.4, pp. 2007–2013. DOI: 10.1121/1.419652 (cited on page 65).

Conca, C. and M. Vanninathan (1997). "Homogenization of Periodic Structures via Bloch Decomposition". In: *SIAM J. Appl. Math.* 57.6, pp. 1639–1659. DOI: 10.1137/S0036139995294743 (cited on pages 11, 17).

Figotin, A. and A. Klein (1997a). "Localization of Classical Waves II: Electromagnetic Waves". In: *Commun. Math. Phys.* 184.2, pp. 411–441. DOI: 10.1007/s002200050066 (cited on page 75).

Figotin, A. and A. Klein (1997b). "Localized classical waves created by defects". In: *J. Stat. Phys.* 86.1-2, pp. 165–177. DOI: 10.1007/BF02180202 (cited on pages 76–78).

Sigalas, M. M. (1997). "Elastic wave band gaps and defect states in two-dimensional composites". In: *J. Acoust. Soc. Am.* 101.3, pp. 1256–1261. DOI: 10.1121/1.418156 (cited on page 78).

Dahlen, F. A. and J. Tromp (1998). *Theoretical global seismology*. Princeton University Press, p. 944 (cited on page 170).

Klein, A. and A. Figotin (1998). "Midgap Defect Modes in Dielectric and Acoustic Media". In: *SIAM J. Appl. Math.* 58.6, pp. 1748–1773. DOI: 10.1137/S0036139997320536 (cited on pages 77, 78).

Sigalas, M. M. (1998). "Defect states of acoustic waves in a two-dimensional lattice of solid cylinders". In: *J. Appl. Phys.* 84.6, pp. 3026–3030. DOI: 10.1063/1.368456 (cited on page 78).

Rega, G., W. Lacarbonara, A. Nayfeh, and C. Chin (1999). "Multiple resonances in suspended cables: direct versus reduced-order models". In: *Int. J. Non. Linear. Mech.* 34.5, pp. 901–924. DOI: 10.1016/S0020-7462(98)00065-1 (cited on page 139).

Pendry, J. B. (2000). "Negative Refraction Makes a Perfect Lens". In: *Phys. Rev. Lett.* 85.18, pp. 3966–3969. DOI: 10.1103/PhysRevLett.85.3966 (cited on page 2).

Wu, F., Z. Hou, Z. Liu, and Y. Liu (2001). "Point defect states in two-dimensional phononic crystals". In: *Phys. Lett. Sect. A Gen. At. Solid State Phys.* 292.3, pp. 198–202. DOI: 10.1016/S0375-9601(01)00800-3 (cited on page 78).

Goffaux, C., J. Sánchez-Dehesa, A. L. Yeyati, P. Lambin, A. Khelif, J. O. Vasseur, and B. Djafari-Rouhani (2002). "Evidence of Fano-like interference phenomena in locally resonant materials". In: *Phys. Rev. Lett.* 88.22, pp. 225502/1–225502/4. DOI: 10.1103/PhysRevLett.88.225502 (cited on page 3).

Nayfeh, A. H., H. N. Arafat, C.-M. Chin, and W. Lacarbonara (2002). "Multimode Interactions in Suspended Cables". In: *J. Vib. Control* 8.3, pp. 337–387. DOI: 10.1177/107754602023687 (cited on page 139).

Khelif, A., A. Choujaa, B. Djafari-Rouhani, M. Wilm, S. Ballandras, and V. Laude (2003). "Trapping and guiding of acoustic waves by defect modes in a full-band-gap ultrasonic crystal". In: *Phys. Rev. B* 68.21, p. 214301. DOI: 10.1103/PhysRevB.68.214301 (cited on page 78).

Sheng, P., X. X. Zhang, Z. Liu, and C. T. Chan (2003). "Locally resonant sonic materials". In: *Phys. B Condens. Matter* 338.1-4, pp. 201–205. DOI: 10.1016/S0921-4526(03)00487-3 (cited on page 2).

Gattulli, V., L. Martinelli, F. Perotti, and F. Vestroni (2004). "Nonlinear oscillations of cables under harmonic loading using analytical and finite element models". In: *Comput. Methods Appl. Mech. Eng.* 193.1-2, pp. 69–85. DOI: 10.1016/j.cma.2003.09.008 (cited on page 119).

Kittel, C. (2004). *Introduction to Solid State Physics*. 8th ed. New York: John Wiley & Sons, p. 704 (cited on pages 15, 65).

Wu, F., Z. Liu, and Y. Liu (2004). "Splitting and tuning characteristics of the point defect modes in two-dimensionalphononic crystals". In: *Phys. Rev. E - Stat. Physics, Plasmas, Fluids, Relat. Interdiscip. Top.* 69.6, p. 4. DOI: 10.1103/PhysRevE.69.066609 (cited on page 78).

Sakoda, K. (2005). *Optical Properties of Photonic Crystals*. Vol. 80. Springer Series in Optical Sciences. Berlin, Heidelberg: Springer Berlin Heidelberg. DOI: 10.1007/b138376 (cited on page 2).

Fang, N., D. Xi, J. Xu, M. Ambati, W. Srituravanich, C. Sun, and X. Zhang (2006). "Ultrasonic metamaterials with negative modulus". In: *Nat. Mater.* 5.6, pp. 452–456. DOI: 10.1038/nmat1644 (cited on page 2).

Milton, G. W., M. Briane, and J. R. Willis (2006a). "On cloaking for elasticity and physical equations with a transformation invariant form". In: *New J. Phys.* 8.10, pp. 248–248. DOI: 10.1088/1367-2630/8/10/248 (cited on page 3).

Milton, G. W. and N.-A. P. Nicorovici (2006b). "On the cloaking effects associated with anomalous localized resonance". In: *Proc. R. Soc. A Math. Phys. Eng. Sci.* 462.2074, pp. 3027–3059. DOI: 10.1098/rspa.2006.1715 (cited on page 3).

Phani, A. S., J. Woodhouse, and N. A. Fleck (2006). "Wave propagation in two-dimensional periodic lattices". In: *J. Acoust. Soc. Am.* 119.4, pp. 1995–2005. DOI: 10.1121/1.2179748 (cited on page 65).

Anton, S. R. and H. A. Sodano (2007). "A review of power harvesting using piezoelectric materials (2003–2006)". In: *Smart Mater. Struct.* 16.3, R1–R21. DOI: 10.1088/0964-1726/16/3/R01 (cited on page 4).

Milton, G. W. and J. R. Willis (2007). "On modifications of Newton's second law and linear continuum elastodynamics". In: *Proc. R. Soc. A Math. Phys. Eng. Sci.* 463.2079, pp. 855–880. DOI: 10.1098/rspa.2006.1795 (cited on page 3).

Priya, S. (2007). "Advances in energy harvesting using low profile piezoelectric transducers". In: *J. Electroceramics* 19.1, pp. 167–184. DOI: 10.1007/s10832-007-9043-4 (cited on page 4).

Joannopoulos, J. D., S. G. Johnson, J. N. Winn, and R. D. Meade (2008). *Photonic Crystals: Molding the Flow of Light (Second Edition)*. Princeton University Press, p. 446 (cited on page 2).

Nayfeh, A. H. and P Frank Pai (2008). *Linear and nonlinear structural mechanics*. Wiley\, p. 763 (cited on pages 119, 175).

Yao, S., X. Zhou, and G. Hu (2008). "Experimental study on negative effective mass in a 1D mass–spring system". In: *New J. Phys.* 10.4, p. 043020. DOI: 10.1088/1367-2630/10/4/043020 (cited on page 28).

Huang, H. H. and C. T. Sun (2009). "Wave attenuation mechanism in an acoustic metamaterial with negative effective mass density". In: *New J. Phys.* 11, p. 013003. DOI: 10.1088/1367-2630/11/1/013003 (cited on page 28).

Lu, M.-H., L. Feng, and Y.-F. Chen (2009). "Phononic crystals and acoustic metamaterials". In: *Mater. Today* 12.12, pp. 34–42. DOI: 10.1016/S1369-7021(09)70315-3 (cited on page 1).

Priya, S. and D. J. Inman (2009). *Energy Harvesting Technologies*. Boston, MA: Springer US, pp. 1–517. DOI: 10.1007/978-0-387-76464-1 (cited on page 3).

Wu, L. Y., L. W. Chen, and C. M. Liu (2009a). "Acoustic energy harvesting using resonant cavity of a sonic crystal". In: *Appl. Phys. Lett.* 95.1, p. 013506. DOI: 10.1063/1.3176019 (cited on page 5).

Wu, L.-Y., L.-W. Chen, and C.-M. Liu (2009b). "Experimental investigation of the acoustic pressure in cavity of a two-dimensional sonic crystal". In: *Phys. B Condens. Matter* 404.12-13, pp. 1766–1770. DOI: 10.1016/j.physb.2009.02.025 (cited on pages 5, 78).

Wu, L. Y. and L. W. Chen (2010). "Wave propagation in a 2D sonic crystal with a Helmholtz resonant defect". In: *J. Phys. D. Appl. Phys.* 43.5, p. 055401. DOI: 10.1088/0022-3727/43/5/055401 (cited on pages 6, 79).

Erturk, A. and D. J. Inman (2011). *Piezoelectric Energy Harvesting*. Chichester, UK: John Wiley & Sons, Ltd. DOI: 10.1002/9781119991151 (cited on page 3).

Nazarov, S. A. (2011a). "Asymptotic expansions of eigenvalues in the continuous spectrum of a regularly perturbed quantum waveguide". In: *Theor. Math. Phys.* 167.2, pp. 606–627. DOI: 10.1007/s11232-011-0046-6 (cited on page 76).

Nazarov, S. A. (2011b). "Localized elastic fields in periodic waveguides with defects". In: *J. Appl. Mech. Tech. Phys.* 52.2, pp. 311–320. DOI: 10.1134/S0021894411020192 (cited on page 76).

Auriault, J.-L. and C. Boutin (2012). "Long wavelength inner-resonance cut-off frequencies in elastic composite materials". In: *Int. J. Solids Struct.* 49.23-24, pp. 3269–3281. DOI: 10.1016/j.ijsolstr.2012.07.002 (cited on pages 7, 35).

Carrara, M, M. R. Cacan, J Toussaint, M. J. Leamy, M Ruzzene, and A Erturk (2013). "Metamaterial-inspired structures and concepts for elastoacoustic wave

energy harvesting". In: *Smart Mater. Struct.* 22.6, p. 065004. DOI: 10.1088/0964-1726/22/6/065004 (cited on page 4).

Deymier, P. A., ed. (2013). *Acoustic Metamaterials and Phononic Crystals*. Vol. 173. Springer Series in Solid-State Sciences. Berlin, Heidelberg: Springer Berlin Heidelberg (cited on page 3).

Elvin, N. and A. Erturk (2013). *Advances in Energy Harvesting Methods*. Ed. by N. Elvin and A. Erturk. Vol. 9781461457. New York, NY: Springer New York, pp. 1–455. DOI: 10.1007/978-1-4614-5705-3 (cited on page 3).

Kaina, N., M. Fink, and G. Lerosey (2013). "Composite media mixing Bragg and local resonances for highly attenuating and broad bandgaps". In: *Sci. Rep.* 3.1, p. 3240. DOI: 10.1038/srep03240 (cited on page 28).

Lv, H., X. Tian, M. Y. Wang, and D. Li (2013). "Vibration energy harvesting using a phononic crystal with point defect states". In: *Appl. Phys. Lett.* 102.3, pp. 2013–2016. DOI: 10.1063/1.4788810 (cited on pages 5, 6).

Yang, A., P. Li, Y. Wen, C. Lu, X. Peng, J. Zhang, and W. He (2013). "Enhanced Acoustic Energy Harvesting Using Coupled Resonance Structure of Sonic Crystal and Helmholtz Resonator". In: *Appl. Phys. Express* 6.12, p. 127101. DOI: 10.7567/APEX.6.127101 (cited on page 6).

Marigo, J.-J. (2014). *Mécanique des Milieux Continus I*, p. 340 (cited on page 131).

Zigoneanu, L., B.-I. Popa, and S. A. Cummer (2014). "Three-dimensional broadband omnidirectional acoustic ground cloak". In: *Nat. Mater.* 13.4, pp. 352–355. DOI: 10.1038/nmat3901 (cited on page 2).

Gazzola, F. (2015). *Mathematical Models for Suspension Bridges*. Vol. 15. MS&A. Milan: Springer International Publishing. DOI: 10.1007/978-3-319-15434-3 (cited on page 130).

Laude, V. (2015). *Phononic Crystals*. Berlin, München, Boston: DE GRUYTER (cited on page 3).

Borthwick, D. (2016). *Introduction to Partial Differential Equations*. Universitext. Cham: Springer International Publishing. DOI: 10.1007/978-3-319-48936-0 (cited on page 44).

Kulkarni, P. P. and J. M. Manimala (2016). "Longitudinal elastic wave propagation characteristics of inertant acoustic metamaterials". In: *J. Appl. Phys.* 119.245101. DOI: 10.1063/1.4954074 (cited on page 28).

Qi, S., M. Oudich, Y. Li, and B. Assouar (2016). "Acoustic energy harvesting based on a planar acoustic metamaterial". In: *Appl. Phys. Lett.* 108.26, p. 263501. DOI: 10.1063/1.4954987 (cited on page 6).

Tol, S., F. L. Degertekin, and A. Erturk (2016a). "Gradient-index phononic crystal lens-based enhancement of elastic wave energy harvesting". In: *Appl. Phys. Lett.* 109.6, p. 063902. DOI: 10.1063/1.4960792 (cited on page 4).

Tol, S., F. Degertekin, and A. Erturk (2016b). "Piezoelectric power extraction from bending waves: Electroelastic modeling, experimental validation, and performance enhancement". In: *Wave Motion* 60, pp. 20–34. DOI: 10.1016/j.wavemoti.2015.08.008 (cited on page 4).

Ammari, H., B. Fitzpatrick, D. Gontier, H. Lee, and H. Zhang (2017). "Sub-wavelength focusing of acoustic waves in bubbly media". In: *arXiv*. arXiv: 1706.08113 (cited on page 7).

Delourme, B., S. Fliss, P. Joly, and E. Vasilevskaya (2017). "Trapped modes in thin and infinite ladder like domains. Part 1: Existence results". In: *Asymptot. Anal.* 103.3, pp. 103–134. DOI: 10.3233/ASY-171422 (cited on page 76).

Limonov, M. F., M. V. Rybin, A. N. Poddubny, and Y. S. Kivshar (2017). "Fano resonances in photonics". In: *Nat. Photonics* 11.9, pp. 543–554. DOI: 10.1038/NPHOTON.2017.142 (cited on page 3).

Oudich, M. and Y. Li (2017). "Tunable sub-wavelength acoustic energy harvesting with a metamaterial plate". In: *J. Phys. D. Appl. Phys.* 50.31, p. 315104. DOI: 10.1088/1361-6463/aa779d (cited on page 6).

Tol, S., F. L. Degertekin, and A. Erturk (2017a). "Phononic crystal Luneburg lens for omnidirectional elastic wave focusing and energy harvesting". In: *Appl. Phys. Lett.* 111.1, p. 013503. DOI: 10.1063/1.4991684 (cited on page 4).

Tol, S., F. L. Degertekin, and A. Erturk (2017b). "Low-Frequency Elastic Wave Focusing and Harvesting via Locally Resonant Metamaterials". In: *Vol. 1 Dev. Charact. Multifunct. Mater. Mech. Behav. Act. Mater. Bioinspired Smart Mater. Syst. Energy Harvest. Emerg. Technol.* Vol. 1. American Society of Mechanical Engineers. DOI: 10.1115/SMASIS2017-3957 (cited on page 4).

Ammari, H., B. Fitzpatrick, E. O. Hiltunen, and S. Yu (2018). "Subwavelength Localized Modes for Acoustic Waves in Bubbly Crystals with a Defect". In: *SIAM J. Appl. Math.* 78.6, pp. 3316–3335. DOI: 10.1137/18M1178748. arXiv: 1804.00756 (cited on page 79).

Comi, C. and L. Driemeier (2018). "Wave propagation in cellular locally resonant metamaterials". In: *Lat. Am. J. Solids Struct.* 15.4. DOI: 10.1590/1679-78254327 (cited on page 65).

Comi, C, M Moscatelli, and J.-J. Marigo (2019). "Two scale homogenization in ternary locally resonant metamaterials". In: *Mater. Phys. Mech.* 44, pp. 8–18. DOI: 10.18720/MPM.4412020_2 (cited on page 35).

Moscatelli, M., R. Ardito, L. Driemeier, and C. Comi (2019). "Band-gap structure in two- and three-dimensional cellular locally resonant materials". In: *J. Sound Vib.* 454, pp. 73–84. DOI: 10.1016/j.jsv.2019.04.027 (cited on page 65).

Romero-García, V. and A. C. Hladky-Hennion (2019). *Fundamentals and Applications of Acoustic Metamaterials*. Wiley, pp. 1–300. DOI: 10.1002/9781119649182 (cited on page 3).

Borthwick, D. (2020). *Spectral Theory*. Vol. 284. Graduate Texts in Mathematics. Cham: Springer International Publishing, p. 338. DOI: 10.1007/978-3-030-38002-1 (cited on page 145).

Comi, C. and J.-J. Marigo (2020). "Homogenization approach and Bloch-Floquet theory for band-gap prediction in 2D locally resonant metamaterials". In: *J. Elast.* 139.1, pp. 61–90. DOI: 10.1007/s10659-019-09743-x (cited on pages 11, 35, 55, 61, 65, 170).

De Ponti, J. M., A. Colombi, R. Ardito, F. Braghin, A. Corigliano, and R. V. Craster (2020). "Graded elastic metasurface for enhanced energy harvesting". In: *New J. Phys.* 22.1, p. 13013. DOI: 10.1088/1367-2630/ab6062 (cited on page 4).

Delourme, B., S. Fliss, P. Joly, and E. Vasilevskaya (2020). "Trapped modes in thin and infinite ladder like domains. Part 2: Asymptotic analysis and numerical application". In: *Asymptot. Anal.* 119.1-2, pp. 117–152. DOI: 10.3233/ASY-191573 (cited on page 76).

Ma, K.-J., T. Tan, F.-R. Liu, L.-C. Zhao, W.-H. Liao, and W.-M. Zhang (2020). "Acoustic energy harvesting enhanced by locally resonant metamaterials". In: *Smart Mater. Struct.* 29.7, p. 075025. DOI: 10.1088/1361-665X/ab8fcc (cited on page 6).

Moscatelli, M., C. Comi, and J.-J. Marigo (2020a). "Energy Localization through Locally Resonant Materials". In: *Materials (Basel).* 13.13, p. 3016. DOI: 10.3390/ma13133016 (cited on page 98).

Moscatelli, M., C. Comi, and J.-J. Marigo (2020b). "Locally Resonant Materials for Energy Harvesting at Small Scale". In: *Proc. XXIV AIMETA Conf. 2019*. September. Rome: Springer, pp. 606–626. DOI: 10.1007/978-3-030-41057-5_50 (cited on page 98).

De Ponti, J. M., L. Iorio, E. Riva, F. Braghin, A. Corigliano, and R. Ardito (2021). "Enhanced Energy Harvesting of Flexural Waves in Elastic Beams by Bending Mode of Graded Resonators". In: *Front. Mater.* 8.November, pp. 1–7. DOI: 10.3389/fmats.2021.745141 (cited on page 4).

Hu, G., L. Tang, J. Liang, C. Lan, and R. Das (2021). "Acoustic-elastic metamaterials and phononic crystals for energy harvesting: a review". In: *Smart Mater. Struct.* 30.8, p. 085025. DOI: 10.1088/1361-665X/ac0cbc (cited on page 4).

Ma, K., T. Tan, Z. Yan, F. Liu, W.-H. Liao, and W. Zhang (2021). "Metamaterial and Helmholtz coupled resonator for high-density acoustic energy harvesting". In: *Nano Energy* 82, p. 105693. DOI: 10.1016/j.nanoen.2020.105693 (cited on page 5).

Moscatelli, M., C. Comi, and J.-J. Marigo (2021). "On the dynamic behaviour of discrete metamaterials: From attenuation to energy localization". In: *Wave Motion* 104, p. 102733. DOI: 10.1016/j.wavemoti.2021.102733 (cited on pages 12, 74).

ECOLE DOCTORALE

**Titre :** Métamatériaux pour la récupération d'énergie à petite échelle

**Mots clés :** métamatériaux, propagation des ondes, homogénéisation périodique, récupération d'énergie

**Résumé :** L'exigence croissante des petits capteurs et dispositifs électroniques autonomes en énergie à faible puissance a propulsé l'émergence de technologies de récupération d'énergie basées sur les vibrations ambiantes, en tant que domaine d'intérêt majeur pour la recherche.
Pour une récupération efficace de l'énergie, il est nécessaire de développer des systèmes capables de transmettre et de piéger les vibrations (et l'énergie qu'elles entraînent) dans un domaine à support compact.
Les cristaux phononiques et les matériaux périodiques localement résonnants, s'ils sont correctement conçus, peuvent être utilisés pour développer des systèmes de récupération d'énergie basés sur les vibrations, en exploitant la présence de bandes interdites dans leur spectre, c'est-à-dire des intervalles de fréquences correspondant à des ondes atténuées.
A l'aide d'un cristal de masse-en-masse, nous identifions d'abord les rôles des principaux paramètres du problème de la propagation des ondes dans ces deux classes de métamatériaux. Ensuite, nous utilisons une technique d'homogénéisation à deux échelles pour dériver leur comportement effectif à une échelle sous-longueur d'onde. En particulier, les matériaux localement résonnants sont analysés, étant caractérisés par la présence de bandes interdites déjà à un régime sous-longueur d'onde.
Visant à focaliser l'énergie mécanique dans une zone confinée aux basses fréquences, nous introduisons une cavité dans des matériaux localement résonnants, jouant le rôle d'un défaut de périodicité et aboutissant à la formation de modes localisés à des fréquences à l'intérieur d'une bande interdite. Nous montrons que les ondes mécaniques traversant ces métamatériaux défectueux peuvent être piégées dans le défaut, où l'énergie s'accumule et se concentre.
Dans la dernière partie du manuscrit, en utilisant un câble avec des masses attachées périodiquement, nous montrons comment ce système se comporte comme un métamatériau et nous validons expérimentalement les effets d'atténuation et de localisation.
Nos résultats fournissent de nouvelles informations sur le comportement dynamique des milieux périodiques défectueux à utiliser dans les systèmes de récupération d'énergie, ce qui rend ce travail pertinent à la fois pour les domaines théoriques et pratiques.

**Title :** Metamaterials for energy harvesting at small scale

**Keywords :** metamaterials, wave propagation, periodic homogenization, energy harvesting

**Abstract :** The increasing demand of low-power energy-autonomous small electronic sensors and devices has propelled the emergence of energy harvesting technologies based on ambient vibrations, as a prominent area of interest for research.
For an efficient harvesting of energy, it is required to develop systems that are able to convey and trap the vibrations (and the energy they carry with them) in a compactly-supported domain.
Phononic crystals and periodic locally resonant materials, if properly designed, can be used to develop vibration-based energy harvesting systems, by exploiting the presence of band gaps in their spectrum, i.e. intervals of frequencies corresponding to attenuated waves.
Using a mass-in-mass crystal, we first individuate the roles of the main parameters of the problem of wave propagation in these two classes of metamaterials. Then, we employ a two-scale homogenization technique to derive their effective behavior at a sub-wavelength scale. In particular, locally resonant materials are analyzed, being characterized by the presence of band gaps at a sub-wavelength regime.
Aiming to focus the mechanical energy in a confined area at low frequencies, we introduce a cavity in locally resonant materials, acting as a defect of periodicity and resulting in the formation of localized modes at frequencies inside a band gap. We show that mechanical waves traveling through these defective metamaterials can be trapped in the defect, where the energy piles up and focus.
In the final part of the manuscript, by employing a cable with periodically attached masses, we show how this system behaves as a metamaterial and we experimentally validate the attenuation and localization effects.
Our results provide new insights on the dynamic behavior of defective periodic media to be used in energy harvesting systems, which makes this work relevant to both theoretical and practical fields.

**Institut Polytechnique de Paris**
91120 Palaiseau, France